E-687

A STUDY OF THE DECAYS $D^o \rightarrow K^o_s\pi^+\pi^-$ AND $D^o \rightarrow K^o_sK^+K^-$ IN HIGH ENERGY PHOTOPRODUCTION

A Dissertation

Submitted to the Graduate School
of the University of Notre Dame
in Partial Fulfillment of the Requirements
for the Degree of

Doctor of Philosophy

by

Robert William Gardner, Jr.

Randal C. Ruchti

Randal C. Ruchti, Director

Department of Physics
Notre Dame, Indiana

April, 1991

ATA62641

A STUDY OF THE DECAYS

$D^o \to K^o_s\pi^+\pi^-$ AND $D^o \to K^o_s K^+ K^-$

IN HIGH ENERGY PHOTOPRODUCTION

Abstract

by

Robert William Gardner, Jr.

Measurements of the relative branching fractions for two decay modes of the D^o meson are described. The events were produced in hadronic photon interactions with a Beryllium target, with an average photon beam momentum of 220 GeV/c. A common feature of the two decay modes is that each contains a K^o_s meson plus two additional charged tracks; the similar event topologies figure prominently in the analysis. For the $D^o \to K^o_s K^+ K^-$ decay, the relative branching fractions were measured:

$$\begin{aligned} \mathrm{Br}(D^o \to \overline{K}^o K^+ K^-)/\mathrm{Br}(D^o \to \overline{K}^o \pi^+\pi^-) &= 0.198 \pm 0.057 \pm 0.078 \\ \mathrm{Br}(D^o \to \overline{K}^o \phi)/\mathrm{Br}(D^o \to \overline{K}^o \pi^+\pi^-) &= 0.121 \pm 0.057 \pm 0.090 \\ \mathrm{Br}(D^o \to \overline{K}^o (K^+K^-)_{\mathrm{non}-\phi})/\mathrm{Br}(D^o \to \overline{K}^o \pi^+\pi^-) &= 0.136 \pm 0.042 \pm 0.068 \end{aligned}$$

where for each ratio the first error is statistical and the second is systematic. For the $D^o \to K^o_s\pi^+\pi^-$ decay, the fit fractions and relative phases of the $K^{*-}\pi^+$, $\overline{K}^o\rho^o$, and $\overline{K}^o\pi^+\pi^-_{\mathrm{nonres}}$ amplitudes were determined from a maximum likelihood fit to the Dalitz plot.

The data sample was collected by the E687 Collaboration at the Fermilab Wide Band Laboratory during the 1987-88 fixed target running period. Results are com-

pared to other experiments and to predictions from phenomenological models of charmed meson decay.

This dissertation is dedicated to my parents, Robert and Ann and to my grandparents, Mildred and David.

TABLE OF CONTENTS

LIST OF FIGURES

LIST OF TABLES

ACKNOWLEDGEMENTS

It is hardly possible to thank or recognize all the individuals whose contributions made the first run of E687 a success. I am very grateful to have been permitted to participate in this experiment, and for that a collective thanks to everyone in the collaboration.

I would like to especially thank my research director Randy Ruchti for his help and encouragement during all phases of my graduate studies. I'd also like to thank Neal Cason for his help with the data analysis. Jerome Busenitz provided a model I will never be able to emulate, but I thank him just the same for that. On E687 I was very much influenced and guided by Joel Butler, Jim Wiss, John Cumalat, Luigi Moroni and Silvano Sala. I also benefited from the vee analysis of Jeff Wilson and Eric Mannel, and the Monte Carlo development by Karen Lingel. I would like to thank those who worked on the SFT detector development: Alan and Barry Baumbaugh, Kelley Knickerbocker, Ray Mountain and Jim Bishop.

At Notre Dame there were many people upon whose friendship I relied to keep graduate school in perspective, most importantly John Cunningham (my roommate and confidant) and Danilo Pušeljić. Dan Shibata always provided the laughs as did Zeid Ayer. C.W. Bogart from Colorado was always an ally.

Thanks Mom and Dad, Chris, Kim, and Di. I would like to thank other friends that have inspired and helped me all along: Walter, Winston, and Alan—thanks for everything. Finally, while working on E687 I was lucky to meet Doni...I can't thank the Milano group enough for this fortune.

CHAPTER 1

INTRODUCTION

In the past several years much progress has been made, both theoretically [1] and experimentally [2], toward increasing our understanding of weak decay mechanisms of D mesons.[1] However, the situation is rather complicated and much work remains in understanding the complete picture of D meson decays. Particularly troublesome are the non-leptonic channels in which the D meson decays to a final state consisting only of hadrons. In this case, a framework containing both the weak and strong interactions must be developed. A wide range of theoretical models have been put forth to explain the experimental findings which include the differences in lifetime of the D^+ and D^o mesons, their differing semileptonic decay rates, as well as observation of unexpectedly large decay rates (eg. $D^o \rightarrow \overline{K}^o\phi$). Most of these models require as input experimentally measured branching ratios, and in some cases observed decay rates may serve to either validate or contradict proposed hypotheses. In this chapter, we review some of the leading models and point out their main features.

Historically, the measurements of D meson branching ratios have been dominated by e^+e^- experiments [3]. Many of the two-body decays D$\rightarrow$ PP, PV and VV (P = pseudoscalar meson, V = vector meson) have been observed and their decay rates have been well measured. However, good measurements of relative branching fractions for D meson decays are now becoming available from fixed target experiments [2, 4]. The

[1] By D meson we refer collectively to the mesons containing charm quarks, $D^o(c\bar{u})$, $D^+(c\bar{d})$, $D_s^+(c\bar{s})$, and throughout this thesis the charge-conjugate particle is implied unless otherwise noted.

data from these experiments will provide new results in a different setting and may confirm, and in some cases complement, the body of results already obtained from the e^+e^- colliders. In any case it is clear that much more serious work concerning D meson decays is needed to account for all of the possible decay modes.

1.1 Models of D Meson Decay

1.1.1 Spectator Model

The simplest model of charm quark decay involves treating the charm quark inside the D meson as a quasi-free particle, allowing it to decay without concern for effects due to the light quark ($\bar{u}$ or $\bar{d}$), which is assumed to act only as a "spectator". In Fig. 1.1a the weak decay of the D meson is described by the emission of a W-boson from the charm quark which is changed into a strange quark. The W-boson can decay to either of two lepton doublets $l\bar{\nu}$, or to one of three color combinations of quark-pairs ($u\bar{d}$). In this picture, the "color-aligned" amplitude shown in Fig. 1.1b is suppressed by a factor of three (corresponding to three quark colors) or 1/9 in the decay rate relative to the W-emission diagram, owing to the need to form a color singlet.

A number of predictions can be made from the simple scheme outlined here. The first is that lifetimes for D^o and D^+-mesons (as well as the D_s^+-meson and Λ_c^+ baryon) should be equal. An estimate by analogy to the weak decay $\mu^- \rightarrow e^-\bar{\nu}_e\nu_\mu$ yields [5]

$$\frac{1}{\tau_c} = \Gamma_c \simeq \Gamma_\mu\left(\frac{m_c}{m_\mu}\right)^5 \cdot 5 \simeq 10^{12}\ sec^{-1} \qquad (1.1)$$

resulting in lifetimes of order one picosecond. A second prediction is that of equal semileptonic branching ratios, of 20%, obtained by considering again the possible decay modes of the W-boson. Since 1974, when these predictions were first made,

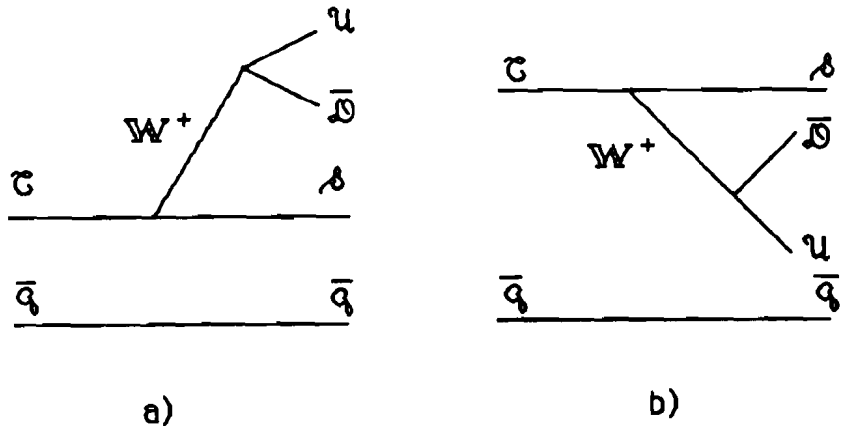

Figure 1.1. The spectator diagrams for heavy quark decay: a) W-emission, and b) color-aligned.

numerous experiments, have shown that the lifetimes of the D^0 and D^+ differ [6]:

$$\frac{\tau_{D^+}}{\tau_{D^0}} = 2.45 \pm 0.09 \tag{1.2}$$

as do their semileptonic branching fractions

$$\frac{\mathrm{Br}(D^+ \to e^+ X)}{\mathrm{Br}(D^0 \to e^+ X)} = 2.3 \pm 0.5. \tag{1.3}$$

Some physicists have attempted to account for these differences by considering additional quark decay diagrams, for example those depicted in Fig. 1.2. The W-exchange and W-annihilation diagrams, if they are indeed operative, may enhance the D^0 decay rate (thus reducing its lifetime) relative to the D^+ decay since for the latter, the contribution would be Cabbibo-suppressed at the final W-vertex. The differences in both lifetimes and semileptonic branching fractions for the D^0 and D^+ mesons suggest differing decay dynamics in the non-leptonic sector. Measurements of non-leptonic

branching fractions may provide some insights into the strengths of the diagrams in Fig. 1.2, and thus shed some light on the observed lifetime differences.

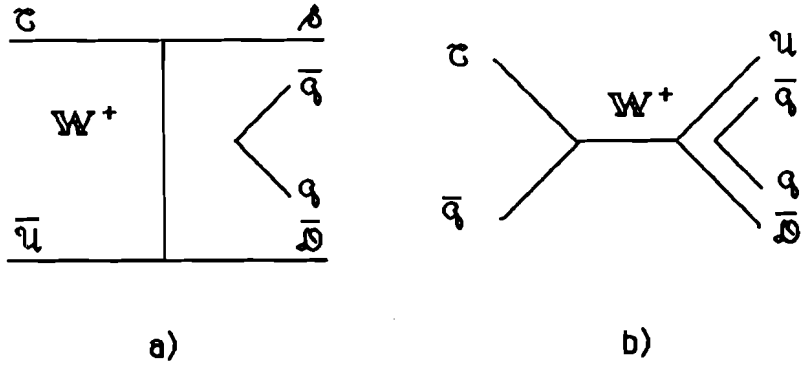

Figure 1.2. Additional valence quark diagrams: a) W-exchange and, b) W-annihilation diagrams.

In this context, the decay $D^o \to \overline{K}^o\phi$ was first suggested by Bigi and Fukugita [7] as clear evidence for the W-exchange process of Fig. 1.2a. The corresponding diagram for the decay $D^o \to \overline{K}^o\phi$ is illustrated in Fig. 1.3, which they argued was the only allowed diagram for this decay process. They estimated the decay rate, taking into account a suppression factor for the formation of an $s\bar{s}$ pair from the vacuum, to scale relative to the spectator processes by:

$$\frac{\mathrm{Br}(D^o \to \overline{K}^o\phi)}{\mathrm{Br}(D^o \to \overline{K}^o\rho^o)} \simeq 0.23 - 0.46 \tag{1.4}$$

$$\frac{\mathrm{Br}(D^o \to \overline{K}^o\phi)}{\mathrm{Br}(D^o \to K^{*-}\pi^+)} \simeq 0.10 - 0.20 \tag{1.5}$$

which, assuming for example $\mathrm{Br}(D^o \to K^{*-}\pi^+) \sim 1$–2%, leads to the branching fraction estimate $\mathrm{Br}(D^o \to \overline{K}^o\phi) \simeq .1$–1%. They noted that ordinary charm decay dia-

grams such as those of Fig. 1.1 are OZI suppressed [8] and would thus give a relative branching ratio $\mathrm{Br}(\mathrm{D}^{\circ} \to \overline{\mathrm{K}}^{\circ}\phi)/\mathrm{Br}(\mathrm{D}^{\circ} \to \overline{\mathrm{K}}^{\circ}\rho^{\circ}) \sim 10^{-1}$. Finally they pointed out that the decay has distinctive features, such as the narrow mass width of the ϕ, which make it experimentally less difficult to observe. Subsequent observations of this mode [9, 10, 11] yielded an average branching ratio of $\simeq 1\%$, seemingly validating the W-exchange dominance hypothesis. However, effects from final state interactions, which are discussed next, may also contribute to the decay rate.

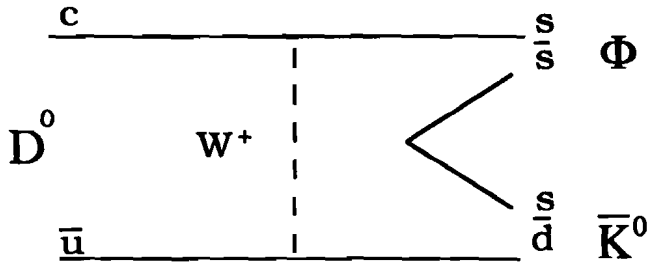

Figure 1.3. W-exchange process for the decay $\mathrm{D}^{\circ} \to \overline{\mathrm{K}}^{\circ}\phi$.

1.1.2 Final State Interactions

Final state interactions (FSI) provide alternate mechanisms for D meson decays. Effects owing to the strong interaction can cause internal hadronic states to rescatter, or mix in such a way that the underlying quark decay schemes become difficult, if not impossible, to verify [12]. The fact that the D° mass lies in an energy region which is known to exhibit resonance structure suggests that strong interaction effects between the outgoing particles from the decay must be considered.

The general mechanism for rescattering [13] can be illustrated for the decay $D^o \to \overline{K}^o\phi$. In Fig. 1.4a the D^o meson decays to an intermediate state, $K^{*o}\eta$, which can be reached through the normal W-emission graph of Fig. 1.1a. However, this intermediate state may be connected to the $\overline{K}^o\phi$ state through use of the $s\bar{s}$ component of the η wavefunction (even though it was produced with the $u\bar{u}$ component). This occurs when the $s\bar{s}$ component is selected in a rescattering process, and the quarks in the final state are rearranged in a simple way to produce $\overline{K}^o\phi$, as depicted in Fig. 1.4b.

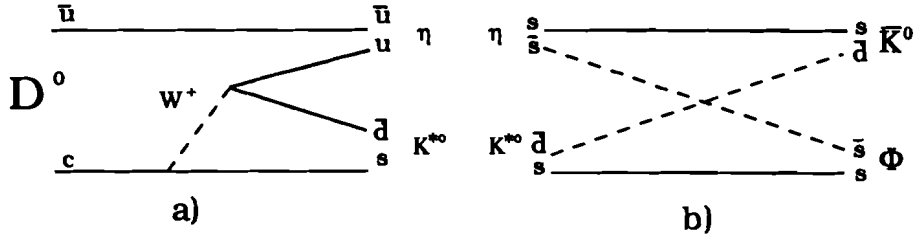

Figure 1.4. Final state rescattering model for $D^o \to \overline{K}^o\phi$ [13]: a) W-emission for producing $D^o \to K^{*o}\eta$; b) quark exchange leading to rescattering.

Sorting through the data to determine how such effects complicate the picture of D meson decays is one goal in the study of the non-leptonic decays. To see which modifications these long range effects can have, we first discuss the attempts to describe decays in which only the short distance strong effects are accounted for.

1.1.3 *Effective Weak Hamiltonian*

Without strong interactions, the effective weak Hamiltonian for hadronic decay of charm at the valence quark level is given, for Cabbibo-favored decays, by [5]:

$$\mathcal{H}_{eff} = \frac{G_F}{\sqrt{2}} cos^2\theta_c \Big[(\bar{u}d)_L(\bar{s}c)_L\Big] \tag{1.6}$$

where G_F is the Fermi coupling constant, $cos^2\theta_c$ is the Cabbibo factor relating the weak and mass eigenstates, and $(\bar{q}q')_L \equiv \bar{q}\gamma_\mu(1-\gamma_5)q'$ are the left-handed hadronic currents which for the moment are assumed to be color singlets.

This Hamiltonian can be modified to take into account short distance strong interactions consisting of hard gluon exchanges by introducing coefficients $c_\pm$ and rewriting the above as [14]

$$\mathcal{H}_{eff} = \frac{G_F}{\sqrt{2}} cos^2\theta_c \Big\{c_+O_+ + c_-O_-\Big\} \tag{1.7}$$

with the operators $O_\pm$ defined as

$$O_\pm = \frac{1}{2}\Big[(\bar{u}d)_L(\bar{s}c)_L \pm (\bar{u}c)_L(\bar{s}d)_L\Big]. \tag{1.8}$$

This expression is identical to Eqn. 1.6 when $c_\pm = 1$. The first term in each of the operators $O_\pm$ corresponds to the charged current decay which describes $c \to s$. The second term can be understood as an effective neutral current since it describes the transition $c \to u$. Taking into account color factors, the Cabbibo-favored hadronic decay rate is proportional to $(2c_+^2 + c_-^2)$ and the 20% semileptonic branching ratio, proportional to $1/(2+2c_+^2+c_-^2)$, is recovered when $c_\pm = 1$. The quantities $c_\pm$ are the renormalized Wilson coefficients and are calculated within QCD [14]. They depend

on the normalization scale μ, and satisfy $c_+^2 c_- = 1$. At the charm quark mass scale ($\simeq$ 1.5 GeV), the values are computed to be $c_+ = .7, c_- = 2.0$, which from the above imply a semileptonic branching ratio of 14%. Thus, the expression leads to an enhancement in the non-leptonic decays and can be interpreted as the population of "color suppressed" states via the effective neutral current interaction. Eqn. 1.7 can be rewritten by defining

$$c_1 = \frac{c_+ + c_-}{2} \quad \text{and} \quad c_2 = \frac{c_+ - c_-}{2} \tag{1.9}$$

which allows writing

$$\mathcal{H}_{eff} = \frac{G_F}{\sqrt{2}} cos\theta_c^2 \Big\{ c_1(\bar{u}d)_L(\bar{s}c)_L + c_2(\bar{s}d)_L(\bar{u}c)_L \Big\} \tag{1.10}$$

so that the "effective neutral current" is proportional to c_2, and in the absence of QCD corrections $c_2 = 0$ and the term vanishes. This formulation of the effective weak Hamiltonian is the starting point for the phenomenological framework termed factorization, which is discussed next.

1.1.4 Factorization Approximation

The approach of Stech and co-workers [15] has been to deal with non-leptonic two-body decays by replacing the quark currents with effective hadron currents representing the mesons involved. The assumption of the model is that the complete amplitude for the decay of a D meson, expressed as $D \rightarrow h_1 h_2$, can be approximated by *factorization* of the amplitude into one-particle matrix elements which are more easily calculated. Thus, taking as an example the D^o decay channel $K^{*-}\pi^+$ and

assuming factorization, the analog of Eqn. 1.10 becomes

$$\begin{aligned} < \mathrm{K}^{*-}\pi^{+}|\mathcal{H}_{eff}|\mathrm{D}^{o} > &= \frac{G_F}{\sqrt{2}} cos^2\theta_c \Big[a_1 < \pi^{+}|(\bar{u}d)_L|0 >< \mathrm{K}^{*-}|(\bar{s}c)_L|\mathrm{D}^{o} > \\ &+ a_2 < \mathrm{K}^{*-}\pi^{+}|(\bar{s}d)_L|0 >< 0|(\bar{u}c)_L|\mathrm{D}^{o} > \Big] \end{aligned} \tag{1.11}$$

where the quantities a_1 and a_2 are defined by

$$a_1 = c_1 + \xi c_2 \quad \text{and} \quad a_2 = c_2 + \xi c_1. \tag{1.12}$$

The color mix-up factor ξ weights the contributions to final states which are not color singlets. It can be determined from color counting, in the most naive case, to be $\xi \simeq 1/N_{colors} = \frac{1}{3}$. However, it is left as a free parameter in the model and can be determined, or partially so, from the experimental data. The origin of this parameter differs from the quantities $c_{\pm}$ which were calculated from short distance QCD effects. Its origin is due more to long distance effects which may include final state interactions and rescattering. It is hoped that such effects may be absorbed into ξ, though there exists no fundamental reason to expect them to.

The authors of this model have attempted to incorporate effects due to final state interactions through use of an isospin analysis. They noted that the bare amplitudes, as would be calculated by Eqn. 1.11 above, must be modified according to

$$A = S^{1/2}A^{o} \tag{1.13}$$

where S is the strong interaction S-matrix for hadron-hadron scattering and A^o is the decay amplitude in the absence of long range strong interactions. Unfortunately, $S^{1/2}$ cannot be reliably estimated. One can, however, perform an isospin analysis to

gain some idea of the effects involved. For D→Kπ decays, the isospin decomposition relating the I=1/2 and I=3/2 amplitudes is

$$\begin{aligned} A(\mathrm{D}^o \to \mathrm{K}^-\pi^+) &= \frac{1}{\sqrt{3}}\left(\sqrt{2}A_{1/2} + A_{3/2}\right) \\ A(\mathrm{D}^o \to \bar{\mathrm{K}}^o\pi^o) &= \frac{1}{\sqrt{3}}\left(-A_{1/2} + \sqrt{2}A_{3/2}\right) \\ A(\mathrm{D}^+ \to \bar{\mathrm{K}}^o\pi^+) &= \sqrt{3}A_{3/2} \end{aligned} \tag{1.14}$$

where the amplitudes are complex, and parameterized by phases as

$$A_I = |A_I|\exp(i\delta_i). \tag{1.15}$$

They were able to obtain a fit to the Mark III data [3] to find

$$\begin{aligned} |A_{3/2}| &\simeq (3.35 \pm 0.19)\cdot 10^{-6}\ \mathrm{GeV} \\ |A_{1/2}| &\simeq (0.99 \pm 0.38)\cdot 10^{-6}\ \mathrm{GeV} \\ \delta_{1/2} - \delta_{3/2} &\simeq (77 \pm 11)^o \end{aligned} \tag{1.16}$$

Using these results, and calculations similar to 1.11, they obtained estimates for the two parameters a_1 and a_2 by fitting a substantial number of two-body D meson branching ratios:

$$a_1 \simeq 1.3 \pm 0.1 \quad \text{and} \quad a_2 \simeq -0.55 \pm 0.1 \tag{1.17}$$

The result seems to indicate that the color mix-up factor $\xi \approx 0$, which differs significantly from the QCD expectation of 1/3. This scheme can also be applied to the

decay rate for $D^o \to \overline{K}^o\phi$. In the factorization approximation, the amplitude is a pure annihilation amplitude, thus proportional to a_2 and hence small. However, if channel mixing (or rescattering as discussed above) occurs, the rate may receive contributions from channels with stronger amplitudes. This is illustrated in Fig. 1.5 in which states with weak coupling proportional to a_1, $K^-\rho^+$ and $K^{*-}\pi^+$, mix with $\overline{K}^o\phi$.

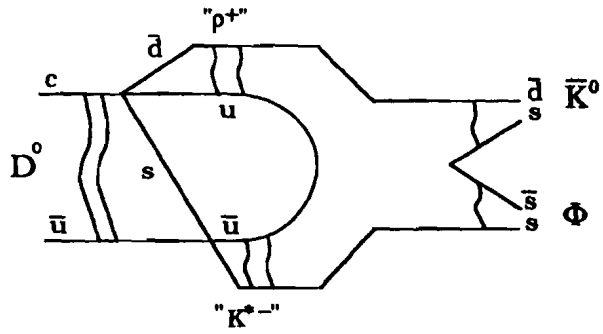

Figure 1.5. Final state interaction in $D^o \to \overline{K}^o\phi$ [15] .

The above discussion indicates that a large number of topics remain unresolved in charm decays, most notably in the non-leptonic decays. There are numerous approaches, not discussed here, that may eventually provide adequate descriptions of D meson decays. One of them [16], based on an expansion parameter $1/N_c$ where N_c is the number of colors, avoids ad-hoc assumptions made in the factorization model.

1.2 Scope of this Thesis

In this thesis measurements are presented which can aid in the understanding of some of the above mentioned problems. The work was carried out at the fixed target, high

energy photoproduction experiment E687, at Fermilab.[2] The experiment is described in Chapter 2. In Chapter 3, the development of a project designed to detect heavy flavor decays using scintillating fiber tracking techniques is described. Though the data from this tracking device were not employed in the analysis, the techniques developed have implications for vertex and tracking detectors under design for the SSC [18]. In Chapter 4 the data processing and analysis techniques used to extract the D meson signals is presented. In Chapter 5 the decay $D^o \rightarrow K^o_s\pi^+\pi^-$ is analyzed to determine the resonant and non-resonant decay fractions, as well as interference effects between the decay amplitudes. In Chapter 6 the decay $D^o \rightarrow K^o_sK^+K^-$ is analyzed specifically to determine the branching fraction $\overline{K}^o\phi$. The results are summarized, and a concluding discussion is given in Chapter 7.

[2]Fermi National Accelerator Laboratory, Batavia Illinois.

CHAPTER 2

THE E687 EXPERIMENT

A very detailed description of the E687 spectrometer, as it was used for the 1987-88 data taking run, can be found in reference [19]. Presented here is a review of the features and components important for the analysis of this thesis. In the first section, a general description of the E687 spectrometer and beamline is given. In subsequent sections some of the detectors are described in more detail.

2.1 Beam and Spectrometer Layout

The E687 experiment was carried out in the Wideband Photon Laboratory, which is located in the Proton East area on the Fermilab site. Construction for the experiment began in March of 1984, and a new beamline (PB East) was installed to replace the existing Broadband beam. The new beam, commissioned during the summer of 1985, is discussed first.

2.1.1 The Wideband Photon Beam

Before describing how the beam was generated, and what its properties are, it is worth reviewing some motivations driving the choice of the photon as the beam particle. First, though the cross section for producing charm is only 1% of the total hadronic cross section as compared to 40% of the production continuum in e^+e^- experiments, the overall rate of production can be quite large using high luminosity

photon beams. Second, its use as a probe to create charm and beauty final states is relatively "clean": typical mean charged particle multiplicities are of order 8 to 10, while that for hadron beams is 12 to 14. This lessens the complexity of separating tracks belonging to the charm vertex from those belonging to the primary vertex. Third, photon interactions are in themselves very interesting: production models based on QCD, and the (older) Vector Meson Dominance Model can be tested and studied. Finally, since the heavy quark cross sections are known to rise with increasing photon beam energy, the Tevatron accelerator can be exploited to generate a photon beam of the highest energy and intensity, providing an opportunity to collect a high statistics charm sample. There are some disadvantages associated with photon beams, however, and these will be discussed in the paragraphs below.

The generation of the photon beam, which was of the bremsstrahlung type, is derived from the protons accelerated by the Tevatron. Here is an outline of the steps leading from the primary proton beam to the photons used at the experimental target (see Fig. 2.1):

1. Protons extracted from the Tevatron were steered to the Wideband beamline where they were directed onto a beryllium target, 18" in length, representing one interaction length of material. This creates many types of reaction products, including charged and neutral hadrons, and importantly π^o mesons which promptly decay to two photons.

2. All of the charged particles emerging from this primary production target are removed from the beamline by a set of sweeping magnets. The neutral particles, γ, n, and K^o_L are allowed to continue straight down the beam pipe.

3. The next step is to convert the neutral beam to an electron beam. The photons are converted to e^+e^- pairs (through the pair production process) using a one-radiation length thick lead converter. The positrons and electrons are steered

away from the beam centerline; the remaining neutrals to go into another beam dump. The electrons, which are swept to the east of beam centerline, are captured by a conventional charged particle transport system which takes them through a "double-dogleg" bend around the neutral dump, returning them to the undeflected beam direction. The positrons were not used during this period of operation of the beam.

4. Since the electrons emerging from the lead converter have varied momenta, the negative beam transport system must have a large momentum acceptance if high fluxes are to be obtained. The currents in these magnets could be varied to select a central transport momentum, which for the 1987-88 run was 350 GeV/c. In order to achieve a high flux, a $\pm 15\%$ spread in momentum was tolerated. This is the origin of the "wideband" terminology, which means large momentum bite.

5. The electrons having the selected momenta impinge on a lead foil which was effectively 27% of a radiation length, creating photons by the bremsstrahlung process. The recoil electrons were deflected into an electromagnetic calorimeter (discussed below) by a string of six dipole sweeping magnets, while the radiated photons traveled directly to the experimental target.

About 1.2×10^{-5} electrons were created per primary proton. During the 1987-88 run, a typical value for the number of protons per twenty second spill duration was 2×10^{12} so that the number of electrons striking the lead foil radiator was approximately 2.5×10^{7} per spill.

A problem with photon beams is that other neutral particles can mimic a photon interaction, and thus neutral hadrons must be carefully filtered from the beam to prevent contamination. The Wideband beam does this quite well with the implementation of the neutral dump and double-dogleg. However, one source occurs when

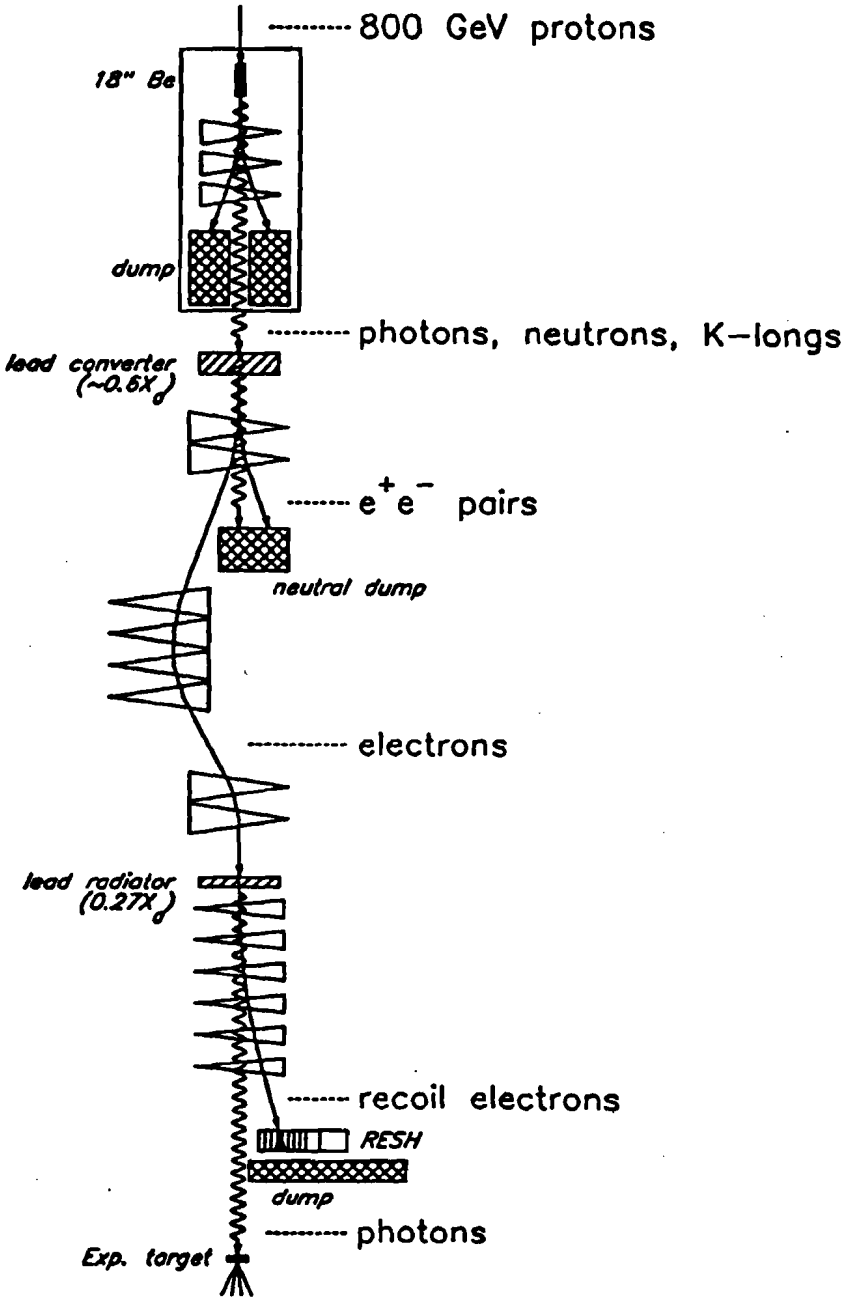

Figure 2.1. The Wideband photon beam generation.

neutral hadrons react in the lead converter, making π^- mesons which can be captured by the electron beam transport. A small number of these will interact in the lead foil radiator creating neutral hadrons, and some of these will interact in the experimental target. This background was estimated from Monte Carlo beam simulations to be less than 1.3×10^{-5} neutral hadrons/photon.

One last difficulty was the spatial extent of the beam at the experimental target. Due to the large momentum bite accepted, the spot size of the beam at the target was rather large, about 0.8 cm horizontally and 0.4 cm vertically. This created difficulties in monitoring the beam profile for the purpose of cross section measurements since much of the beam missed the target.

Photon Energy and Luminosity

If the incident electron beam energy is known, then the energy of the photon produced by the bremsstrahlung process can be tagged by measuring the energy of the recoil electron after the radiator. This was accomplished with a recoil electron shower hodoscope (RESH) which consisted of 10 segmented electromagnetic calorimeter modules oriented transverse to the photon beam direction as shown in Fig. 2.2. The modules consist of 23 lead-Lucite layers, each of 1/4" thickness representing about 24 radiation lengths. The range of measurable photon energies was $E_\gamma \sim 138$ GeV (recoil electron strikes the module closest to the beam) to $E_\gamma \sim 310$ GeV (module furthest from the beam is struck). The photon energy is given according to

$$E_\gamma = E_{beam} - E_{recoil} - E_{BGM} \tag{2.1}$$

where E_{beam} is the incident electron beam energy, E_{recoil} is the measured electron recoil energy, and E_{BGM} is the energy of the photons produced when the incident electron beam undergoes multiple-bremsstrahlung scatters. The energy of the "multi-

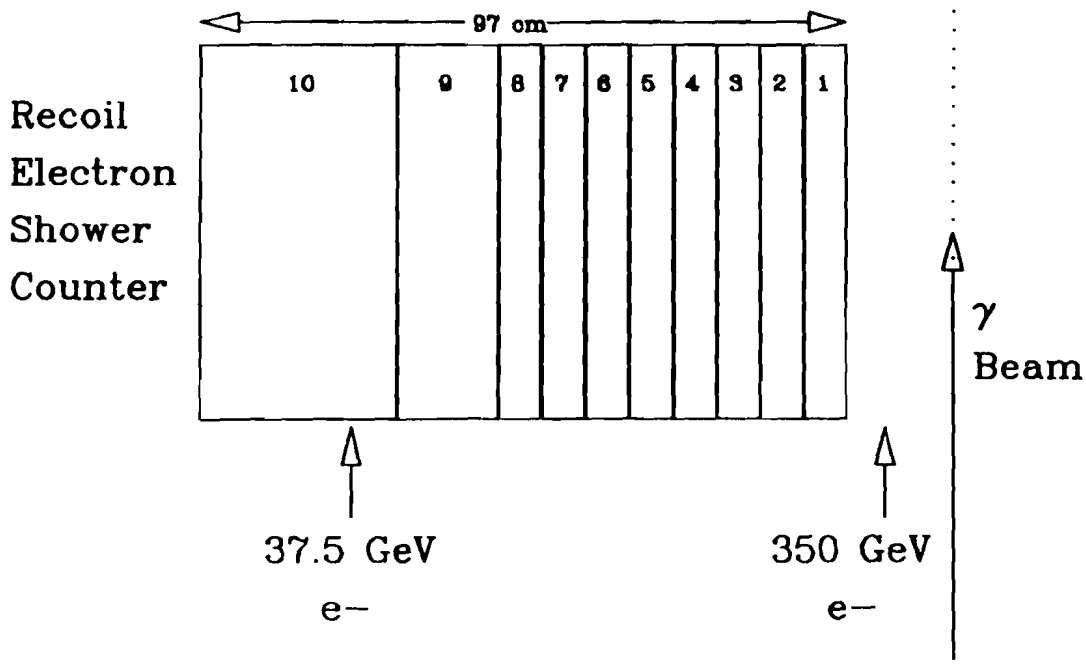

Figure 2.2. The recoil electron shower counter (RESH).

brem" photons, as well as the other non-interacting photons, is measured by a 'beam gamma monitor' (BGM), located at the downstream end of the hadron calorimeter and centered on the photon beam. The energy of the photon could not be measured better than ±50 GeV, since the E_{beam} was not known to within this value (due to the momentum bite and lack of momentum definition before the radiator foil).

The BGM detector was also used as a scale of the luminosity. The counter consisted of 45 layers of 1/8" lead-lucite planes of transverse dimension $9"_x \times 10"_y$, representing 24 radiation lengths. The light produced by all of the scintillator layers was collected into a single photomultiplier tube. The signal from the counter was discriminated allowing electromagnetic energy measurements of 133 GeV and greater. The counter was scaled during the data taking, and the value recorded for each spill was written to tape. While the counter does not directly measure the number of photons impinging on the experimental target, it can still serve as an indirect measure of the luminosity if the incident beam profile, the electron beam spectrum

and the bremsstrahlung process can be accurately modelled to gauge the response of the BGM. This work in this thesis did not require precise knowlege of the beam luminosity, although the scaled BGM detector counts were used as a measure of the luminosity to study the K_s^o yield variation over the running period (Chapter 4).

2.1.2 The E687 Spectrometer

A schematic drawing of the plan view of the apparatus is shown in Fig. 2.3. Designed for large acceptance and high rate capability, the main components of the E687 spectrometer are a microstrip detection system, two vertically-bending analysis magnets, a proportional wire chamber system, a Čerenkov particle identification system, a muon detection system, an electromagnetic calorimetry system which covered a substantial fraction of the center of mass solid angle, and hadronic calorimeters for event energy measurement and triggering.

Wideband Hall Fire

On October 3, 1987 the experiment suffered a fire which completely destroyed the IE, P4, and H×V detectors, and damaged sections of the hadron calorimeter. It took nearly three months to rebuild or replace the damaged detectors and return the spectrometer to running conditions. Up to this time, the experiment had recorded approximately 10^7 events, which came to be known as "pre-fire" data. All of the data used in this thesis came from the "post-fire" data sample.

2.2 The Targets

There were three principal targets in use during the experiment. Most of the data was taken with either of two beryllium target configurations. A third target was a silicon wafer target, which was used for about 10% of the running time. In addition, a relatively small amount of data was taken with a scintillating glass target, the

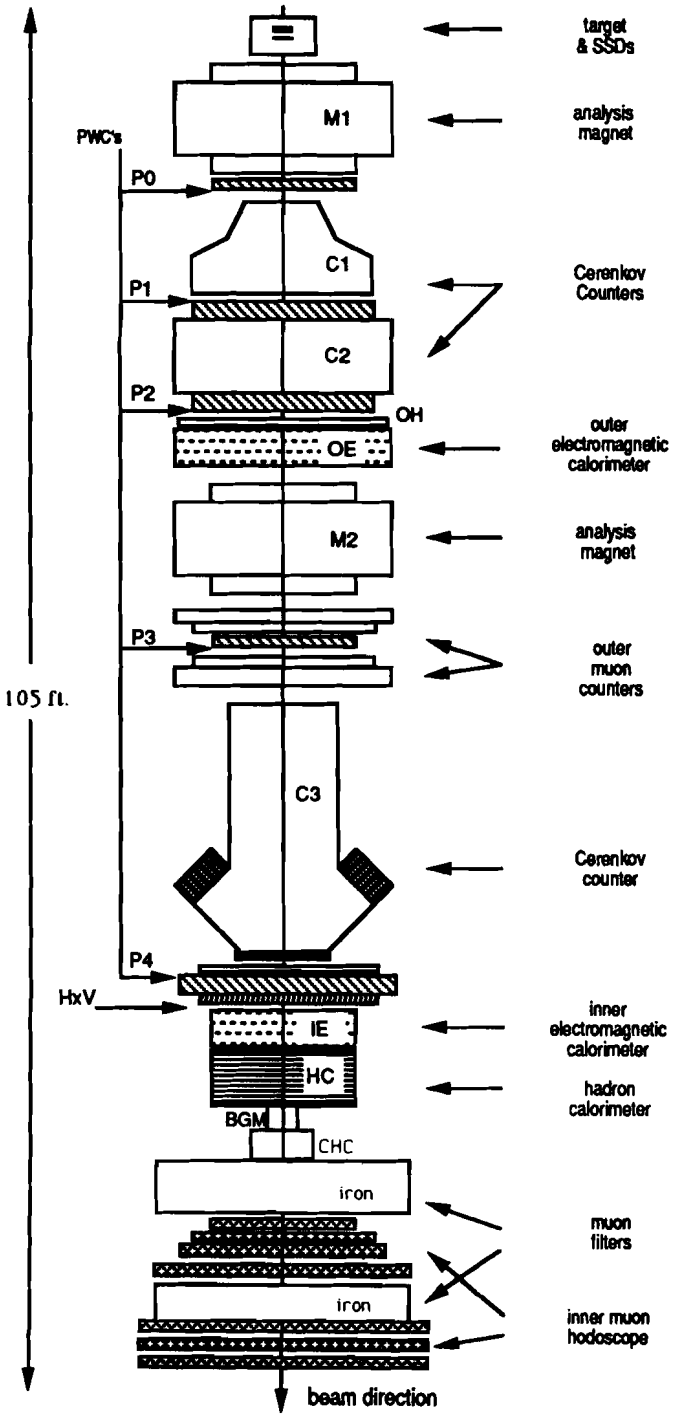

Figure 2.3. The E687 spectrometer (plan view).

development of which is the subject of the next chapter.

2.2.1 Beryllium Segments

Two configurations of beryllium segments were used: one with four segments and one with five segments. A diagram of the five segment target is shown in Fig. 2.4. The large segments are 2.54 cm square, rotated by 45^o with respect to the vertical direction, and about 0.8 cm thick. The smaller segments measured 1.0 cm on a side, and were hexagonally cut to optimize the number of interactions occurring in the region covered by the high resolution sections of the microstrip detectors. The larger segments were designed to cover the beam profile without adding too much material longitudinally so that multiple coulomb scattering effects would be minimized. The target was about 4.5 cm in length, and represented 10% of an interaction length while introducing 11.5% of a radiation length. The target was located about 7 cm upstream of the microstrip detectors, and was used for about 60% of the running time. The four segment target was identical with the exception of having one less large segment.

2.2.2 Silicon Wafer Target

Data were also taken with an active target consisting of 29 instrumented silicon wafers, each having 220 μm thickness, and interleaved with 300 μm beryllium slabs which added to the total interaction length. Following these segments were 19 additional silicon wafers, each 250 μm thick. The target represented 4.7% of an interaction length and 14.4% of a radiation length. The silicon wafers were instrumented to collect ionization charge which could be used to reconstruct a longitudinal profile of the event. The "jumps" in pulse height corresponding to sudden track mulitiplicity increases could be used as a seed in locating the primary interaction vertex. However, this feature was not utilized in the present analysis. The properties of the main targets

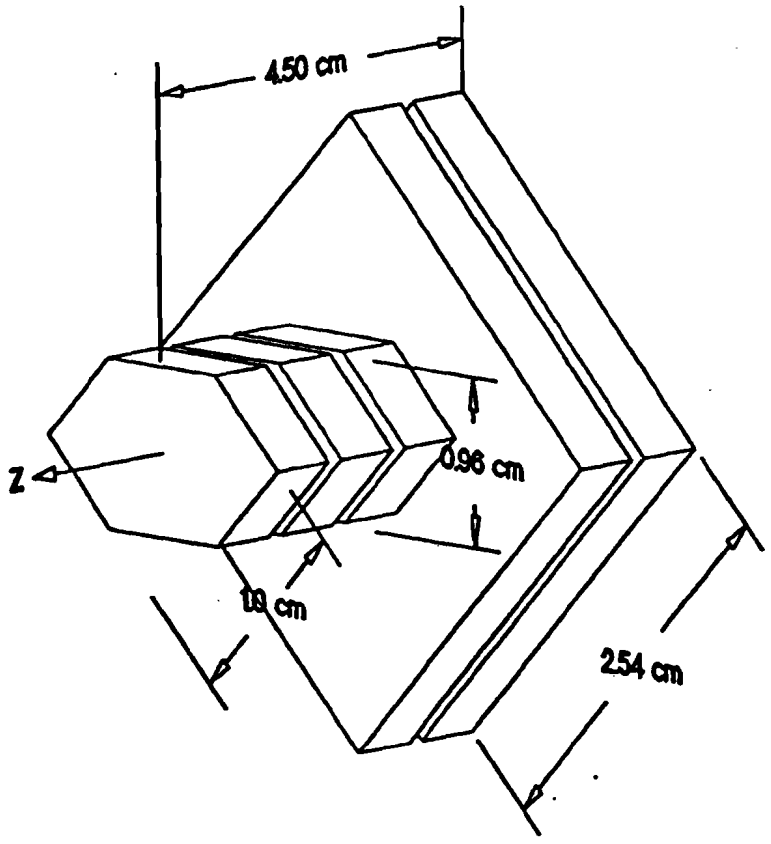

Figure 2.4. The 5-segment beryllium target.

are summarized in Table 2.1.

2.3 Tracking

The tracking of charged particles produced in the interactions was accomplished with two separate systems: the silicon microstrip detectors (SSDs) and the multiwire proportional chambers (PWCs).

Table 2.1. Characteristics of targets.

Target:	5-segment Be	4-segment Be	silicon wafers
length	4.5 cm	3.7 cm	2.3 cm
radiation length	11.5%	9.2 %	14.4%
interaction length	10%	8%	4.7%

2.3.1 *Silicon Strip Detectors*

The silicon microstrip detector system provided all of the tracking information upstream of the first analysis magnet. The importance of the information from this system cannot be understated, as it was absolutely essential for resolving charm decay vertices. The system provided high quality tracking information with twelve planes of microstrips, organized as three views in four separate stacks. A schematic diagram of the arrangement is shown in Fig. 2.5. The views were oriented along coordinate directions i,j,k defined respectively by rotation angles of $-135°$, $-45°$, and $-90°$ with respect to the horizontal plane (see Fig. 2.6 for SSD and E687 main spectrometer coordinate system definitions). Each plane was divided into two regions: an "outer" region and an "inner" region, which had a resolution twice as good as the outer region. The inner regions of the three downstream stacks had strips of 50 μm pitch, while the outer regions were 100 μm. The most upstream stack had 25 μm and 50 μm pitch for the inner and outer regions, respectively. Also, each plane contained 688 readout strips and was 300 μm thick. As such, all planes added, the SSDs represented 20% of a radiation length, and thus introduced complications arising from multiple coulomb scattering. This will be discussed in more detail in Chapter 4. Table 2.2 summarizes the properties of the microstrip stacks.

2.3.2 *Proportional Wire Chambers*

The tracking of charged particles through the main spectrometer was provided by a system of five proportional wire chambers which recorded hit information in four views X,Y,U,V. These chambers are depicted in Fig. 2.3 by the symbols P0–P4. The X and Y-views correspond to the main spectrometer coordinate directions as indicated in Fig. 2.6 while the U and V coordinate directions were rotated at angles $\theta = \pm 11.3$ degrees with respect to the X-axis. The system consisted of two types of chambers

Table 2.2. Microstrip detector properties.

Detectors:	stack #1	stack #2	stack #3	stack #4
No. channels	2,064	2,064	2,064	2,064
active area	3.5 × 2.5 cm^2	5.0 × 5.0 cm^2	5.0 × 5.0 cm^2	5.0 × 5.0 cm^2
center region	3.5 × 1.0 cm^2	5.0 × 2.0 cm^2	5.0 × 2.0 cm^2	5.0 × 2.0 cm^2
pitch(inner)	25 μm	50 μm	50 μm	50 μm
pitch(outer)	50 μm	100 μm	100 μm	100 μm
Z-position†	4.6 cm	10.6 cm	16.6 cm	28.6 cm

†Position measured relative to supporting granite block.

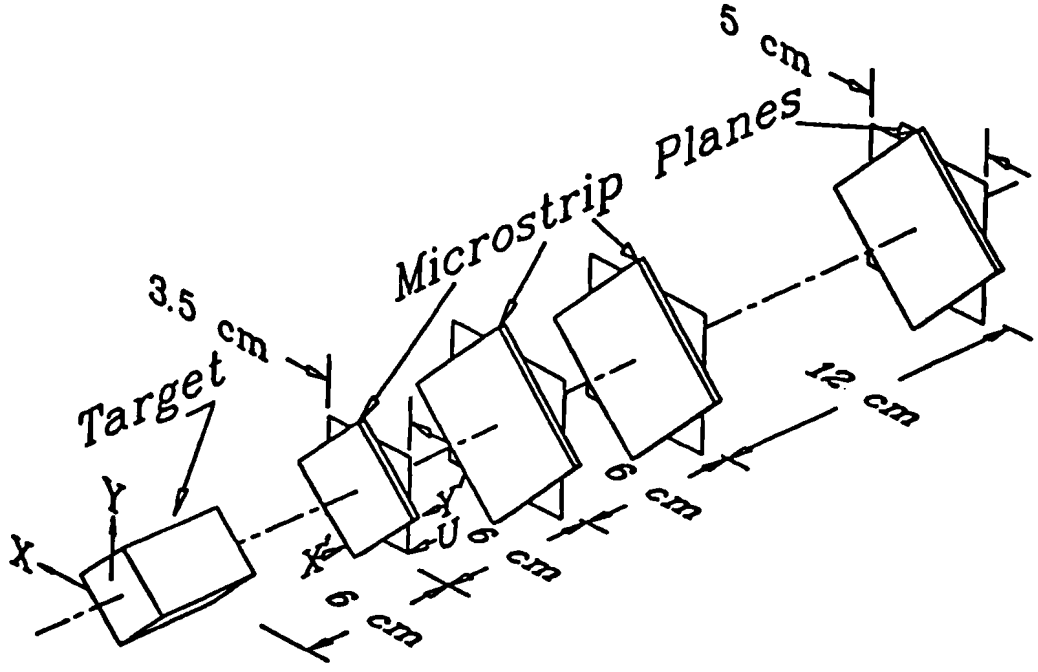

Figure 2.5. The silicon microstrip system: X', Y' and U correspond to coordinate directions i,j,k in Fig. 2.6.

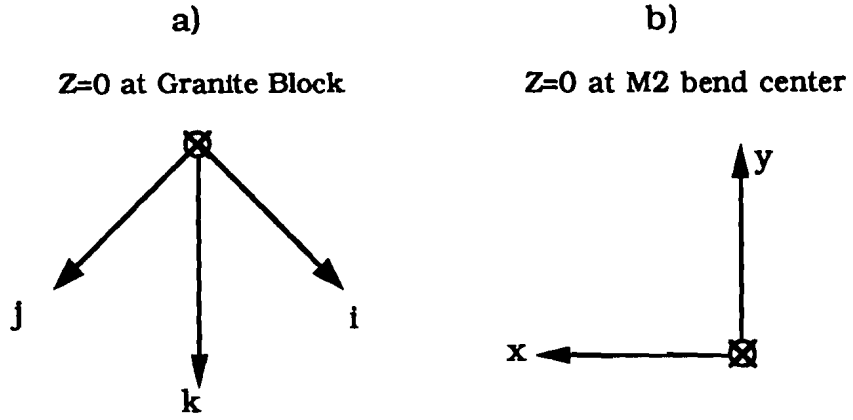

Figure 2.6. E687 coordinate systems: a) microstrip system; b) main spectrometer system.

corresponding to large and small aperture coverage. The first type (P0,P3) covered a transverse area of 30" × 50" and was instrumented by ~ 2300 wires of 2 mm spacing. The second type (P1,P2) had a transverse aperture of 60" × 90" and was instrumented by ~ 2900 wires of 3 mm spacing. The pre-fire P4 chamber was of this second type as well. The replacement P4, salvaged from an older experiment, had only three planes in the views X,V,U with an an aperture 40" × 60" and was instrumented with ~ 1900 wires of 3 mm (X) and 2 mm (U,V) spacings. The chambers were operated at atmospheric pressure with a 65% argon and 35% ethane mixture, and with typical voltages of 3.0 to 3.5 kilovolts. Struck wires were readout with time-to-digital converters (TDCs), recording both wire address and drift time, though the drift timings were not used in the off-line track reconstruction program.

Two large vertically-bending dipole magnets, M1 and M2, provided the deflections necessary to measure the momenta of the charged particles in the event. The first magnet, M1, provided a transverse momentum impulse of about 0.4 GeV/c while the

Table 2.3. Parameters of the analysis magnets.

Magnet:	M1	M2
p_t kick	0.40 GeV/c	-0.85 GeV/c
aperture	30"×50"	30"×50"
current	1020 amps	2000 amps
field	6.6 kilogauss	12.7 kilogauss

second magnet, M2, had opposite polarity and an impulse of -0.8 GeV/c. These values were chosen so that charged particles deflected by M1 would be refocused to their original undeflected positions (in the Y-view) at the IE detector. This arrangement thus provided that e^+e^- pairs created in the target would be spread apart vertically by M1, but redirected to the strike the BGM monitor at the end of the HC detector. The magnet parameters are summarized in Table 2.3.

2.4 Čerenkov Detectors

Particle identification was in part accomplished by system of three multicell Čerenkov counters, indicated by C1,C2 and C3 in Fig. 2.3. The cells were instrumented with photomultiplier tubes in order to view the Čerenkov radiation caused by particles travelling faster than the speed of light through the refractive gases. The Čerenkov light was reflected off mirrors, located at the downstream ends of the counters, into light collection cones which captured and directed the light to PMTs, mounted safely away from the beam region. These counters were operated in "threshold" mode, meaning that the presence of light in the counter, as determined through the recorded ADC pulse heights of the cells, and the momenta of the particles were used to derive possible particle hypotheses. A portion of the first counter, C1, was originally designed to image the ring diameter of the Čerenkov light cone, but this feature has not been

Table 2.4. Čerenkov detector properties.

Counter:	C1	C2	C3
No. cells	90	110	100
aperture (inches)	$50_x \times 80_y \times 71_z$	$90.5_x \times 100_y \times 74_z$	$60_x \times 93.25_y \times 277_z$
gas mixture	He-N_2	N_2O	He
mirror type	planar & spherical	planar	spherical
$P_{\pi^\pm}^{thresh}$ GeV	6.6	4.5	17.2
$P_{K^\pm}^{thresh}$ GeV	23.3	15.9	60.8
$P_{p^\pm}^{thresh}$ GeV	44.3	30.2	115.5
<photoelectron yield>	2.6	8	9

implemented. A summary of the properties of each of the counters, including the characteristic threshold momenta, is given in Table 2.4.

2.5 *Calorimeters*

In E687, both electromagnetic and hadronic calorimetry were implemented. The electromagnetic calorimetry was divided into an "inner" region and an "outer" region. The inner region was instrumented by the IE detector (see Fig. 2.3), which was located just downstream of the H×V trigger hodoscope. Wide angle particles going into the outer region were covered by the OE detector. Both calorimeters employed lead-scintillator configurations and were segmented to allow analysis of shower profiles for π^o, γ, and, $e^\pm$ reconstruction during the offline analysis.

The hadron calorimeter, as shown in Fig. 2.7, served two main purposes:

1. to provide a trigger for hadronic event energy above a specified threshold value and thus reject electromagnetic events.

2. to measure individual hadron energies of in multi-hadronic events.

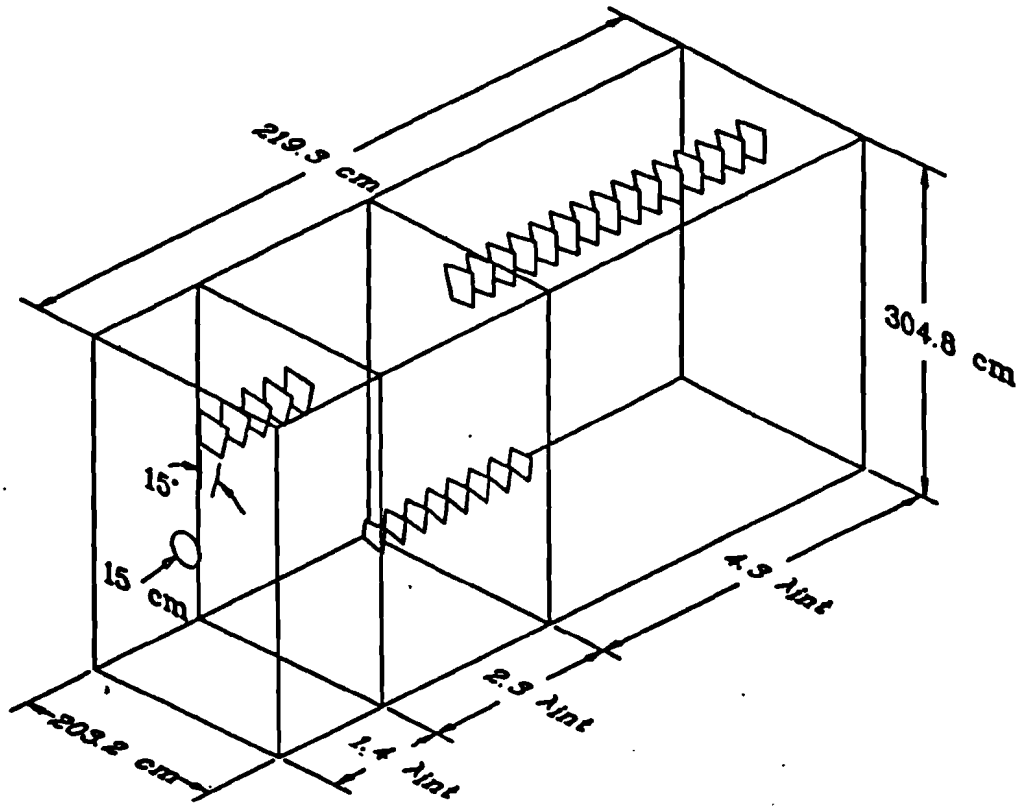

Figure 2.7. E687 hadron calorimeter.

The detector consisted of 28 iron plates of dimension $82"_x \times 120"_y \times 1.75"_z$ representing 8 interaction lengths. Between these plates were active sense planes constructed of extruded aluminum proportional tubes and copper sensing pads, as shown in Fig. 2.8. The proportional tubes used a gas mixture of 50% argon and 50% ethane, and charged particles passing through them produce signals at the sense wires which were sampled capacitively by the copper sensing pads. The readout signals of these pads were grouped together to form a "tower geometry"[20].

In addition, since there was a hole in the calorimeter of 6 inch radius, another small calorimeter, the Central Hadron Calorimeter (CHC) was installed just behind the BGM counter to provide coverage for hadrons filling this region. The detector consisted of 6 interaction lengths composed of sixteen depleted uranium slabs alternating with scintillators for readout. The CHC was also used in the hadronic energy triggering, as will be discussed below.

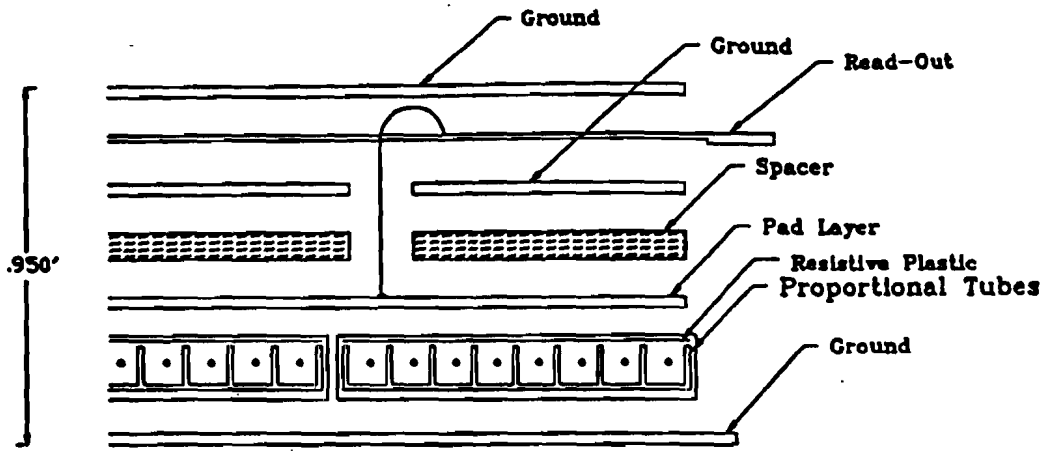

Figure 2.8. Sense pad cross section for hadron calorimeter.

2.6 The Triggers

In order to study detection biases and to collect interesting physics signals, several triggers were employed in the experiment. The triggering system consisted of two levels: a fast, pre-trigger named the master gate, and a higher level trigger which used information from various parts of the spectrometer, called the second level trigger.

2.6.1 Master Gate

The purpose of the master gate was to detect the presence of two charged tracks in the spectrometer while suppressing events with only e^+e^- pair conversions. About 90% of the electromagnetic events were vetoed with this trigger, and studies from Monte Carlo simulations show that this trigger did not compromise the charm acceptance ($\geq$ 85% for the decay $D^o \rightarrow K^o_s\pi^+\pi^-$). The counters used in the master gate were (see Fig. 2.9):

1. A0. This was a small scintillator counter placed directly in the beam line to veto against charged particles in the beam.

2. AM, TM. The AM counter consisted of 24 scintillator paddles (25.4 cm by 58.4 cm) mounted to a fence separating the beamline tunnel and the experimental hall, about 8 meters upstream of the experimental target. The TM counters had dimension 45.7 cm by 61 cm and were placed approximately 2.5 m upstream of the target. The purpose of these counters was to provide a veto against muons associated with beam halo.

3. TR1, TR2. These scintillator counters were intended to detect the presence of a charged particle from the target passing through the microstrip detectors. TR1 was a small counter, 3.5 cm by 2.5 cm, and was mounted directly in front of the first stack of microstrip planes. TR2 was larger and placed just downstream of the last stack of microstrip detectors.

4. HxV hodoscope. These scintillator paddles were designed to detect the presence of one or more charged tracks outside of the pair-region. The array was mounted just downstream of P4, and consisted of 24 horizontal paddles and 12 vertical paddles in two sections. These sections were separated horizontally by 7 cm in order to avoid firings from unwanted pairs. The signals from these counters were fed to a logic module which interpreted the pattern of hit paddles for consistency with one or two track crossings.

5. OH. This was a plane of 24 scintillator paddles mounted on the upstream face of the OE detector. Its purpose was to trigger on wide angle tracks not passing through the aperture of M2.

Signals from these counters were combined logically to preselect events having two charged tracks outside the main pair region, while vetoing beam related background

muons:

$$MG = T \cdot \left(H \times V_{\geq 1body} \cdot OH + H \times V_{\geq 2body} \right) \tag{2.2}$$

where

$$T \equiv TR1 \cdot TR2 \cdot \overline{\left(A0 + AM + TM \right)} \tag{2.3}$$

In this way, two tracks which passed through the "inner" spectrometer, or one which passed through the "outer" region while the other passed through the inner region fired the trigger. During the 1987-88 run, typically 10^5 master gates were generated during each spill cycle.

2.6.2 Second Level Trigger

If it had been possible, the experiment would have recorded every event satisfying the master gate, saving all the selection decisions for offline analysis programs. Of course, detector dead times, data acquisition rate limitations, processing times, and storage requirements prevented us from realizing this ideal. The solution is to require one of several "second level" trigger requirements which are likely to select events containing charm without introducing significant biases.

In E687, several second level triggers were used, involving such factors as detected event energy in the hadron calorimeter, the presence of energy in the RESH counter, prescaled e^+e^- pairs, two-muons detected, etc. Events which generated a master gate caused the pulse height information from some of the detectors to be processed and latched into "buslines"–signals from which higher level logical selections could be made. Combinations of signals were selected through use of programmable "pin-logic" modules. One pin-logic module, corresponding to a minimum bias energy trigger, required that the following conditions be satisfied:

a) event hadronic energy: sum of HC and CHC energy > 35 GeV.

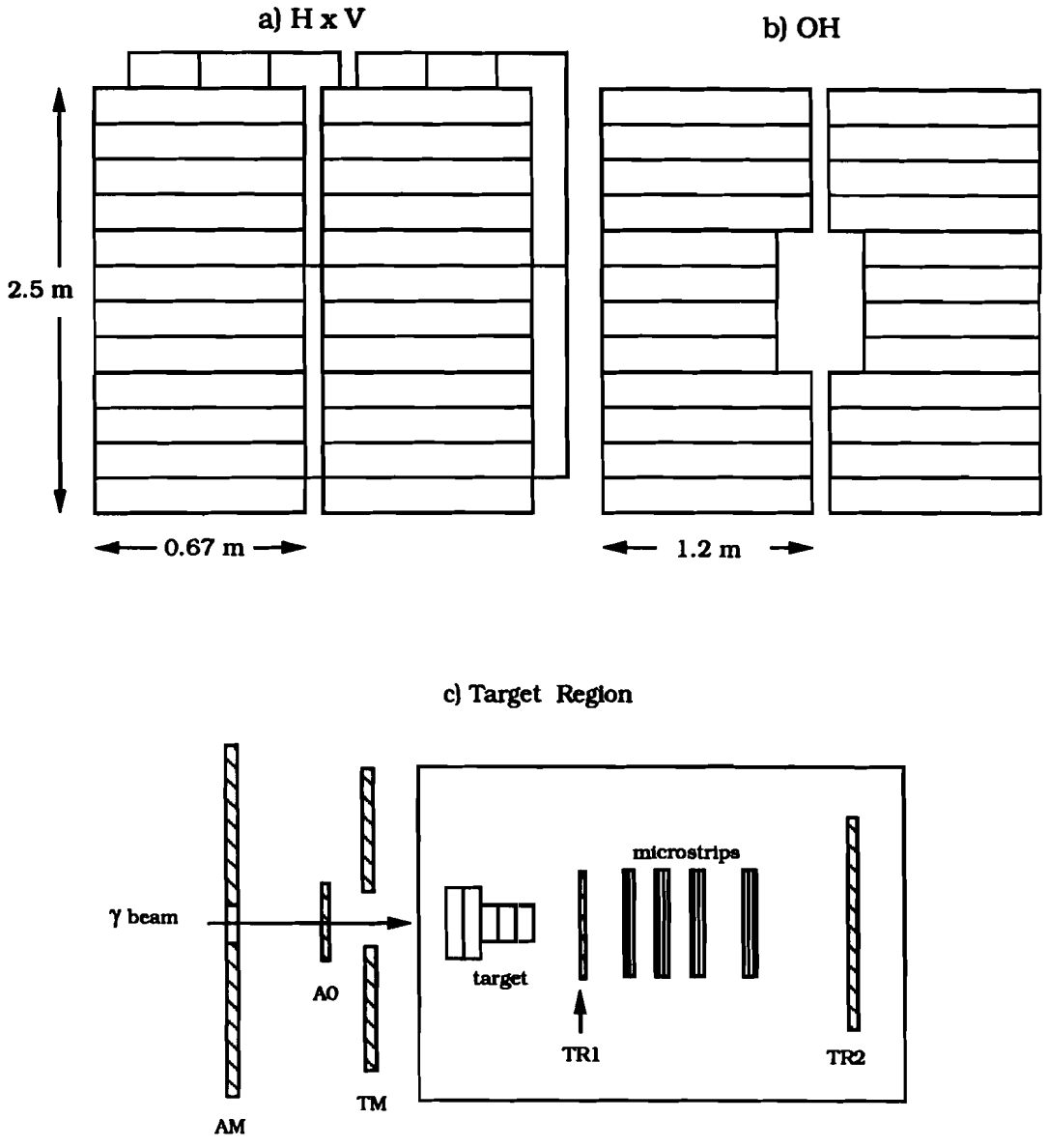

Figure 2.9. Master gate trigger counters.

b) minimal presence of RESH energy.

c) multiplicity: at least one hit outside the central pair region in P0 (X-view).

The RESH requirement insured that a valid photon energy could be reconstructed from the RESH counters, corresponding to a minimal photon energy of approximately 140 GeV. Most of the events of the 1987-88 sample were recorded under this energy trigger.

2.7 Data Acquisition

The analog signals from the detectors were recorded by LeCroy 1185 ADCs, LeCroy TDCs, Milano MIDA ADCs, and latches made by Fermilab. After the firing of a master gate, a hold off of about 1 μs was generated to allow the fast trigger electronics to make the second level trigger decision. If the second level logic was not satisfied, a fast clear was sent out to all recording modules. If an event satisfied the second level trigger, then all the detector responses were digitized and read out into four Fastbus memory buffers. The contents of these buffer memories were transferred to 6250 bpi magnetic tapes by a PDP 11/45 computer. Typically, about 2000 events were written to tape during every 20 second beam spill. The total deadtime incurred by the trigger-event reading cycles was about 25%. During the data taking, monitoring, run control, and online event display programs were run on a VAX 11/780 computer.

CHAPTER 3

SFT DETECTOR DEVELOPMENT

The Scintillating Fiber Target (SFT) was implemented to do short-range charged particle tracking and vertex identification in the vicinity of the primary interaction. A prototype device was installed for two brief periods during the 1987-88 data taking run during which time approximately 200 thousand events were logged to tape using both π^- meson and photon beams.

3.1 System Overview

The SFT design [21] was based upon scintillating fiber optic wave guides stacked into a coherent array (longitudinally, with respect to the fiber axes) to serve as both target and detection material. This orientation is depicted in Fig. 3.1, along with the fiber stacking arrangement of the SFT used with the prototype system. The scintillation photons trapped in the fibers by total internal reflection are collected at the end to record coordinates along a track projection. This light, as it reaches the face of the SFT, is called an image.

The light levels produced in this target were very low ($\sim$ few photons per fiber) as the number of scintillation photons detected depended upon many factors such as the energy deposited per unit length in the material (dE/dx), the fiber trapping efficiency, and the attenuation of light by the glass material itself. In order to record the light from the struck fibers, the image was amplified with sufficient gain to be viewed by

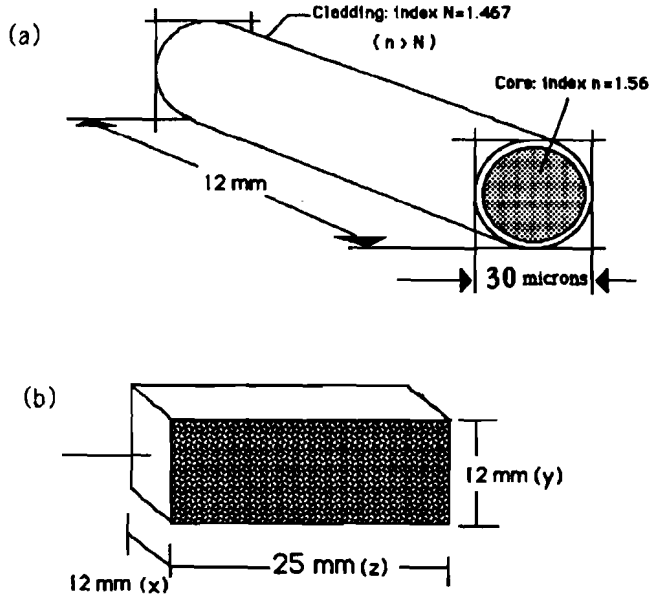

Figure 3.1. Scintillating fiber target: a) single Cerium-doped glass fiber with dimensions; b) SFT: stacked array of approximately 1×10^6 fibers.

an image sensor. This was accomplished with a two-stage, electrostatically focused image intensifier coupled to a microchannel plate intensifier. After the image was amplified it was sensed and recorded for later viewing and analysis. A SIT VIDICON camera was used for this purpose.[1] The arrangement of the target assembly, image tubes, and SIT VIDICON is shown in the simplified drawing of Fig. 3.2, and the geometrical specifications are shown in Fig. 3.3.

In Fig. 3.4 a block schematic diagram of the SFT system is shown in which the system is divided into the following functional groups:

- targeting and image detection
- fast image recording
- higher level data acquisition

The image detection system was installed in the region just upstream of the microstrip detectors, while the fast image recording and higher level data acquisition systems

[1]SIT is an abbreviation for Silicon Intensifier Target, discussed in detail below.

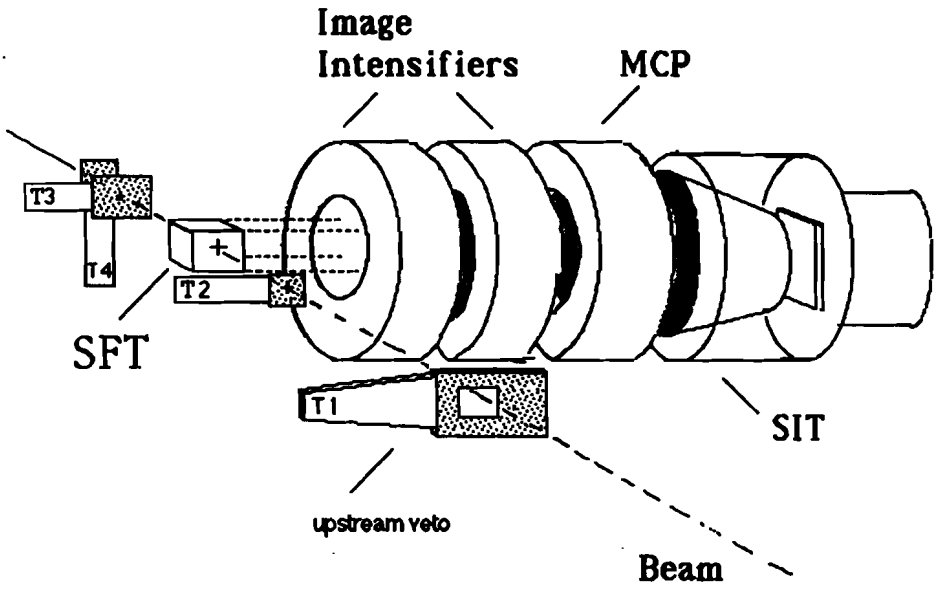

Figure 3.2. SFT schematic layout: the orientation of the SFT, image tubes, SIT camera and trigger counters.

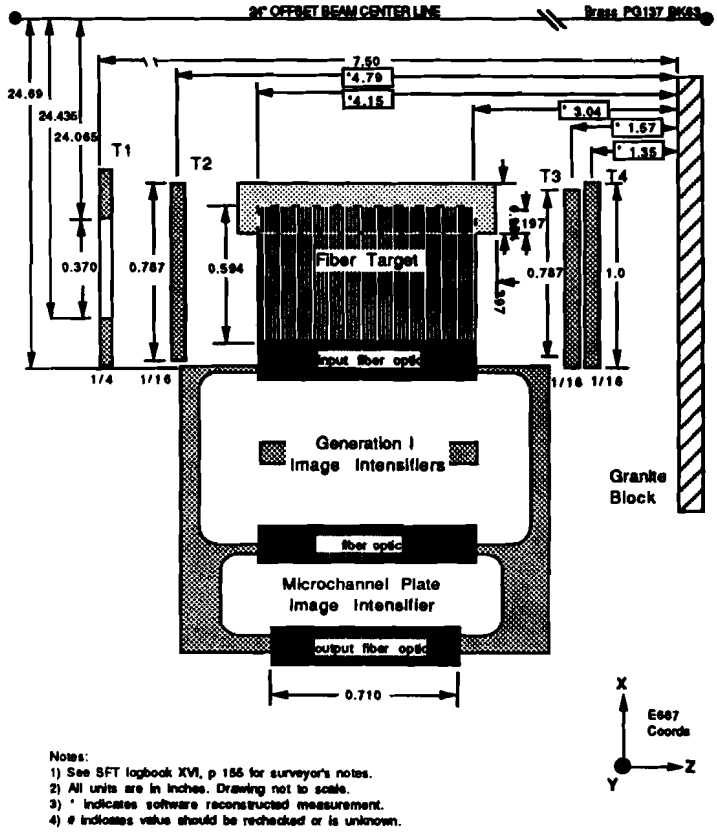

Figure 3.3. SFT geometry specifications.

were located in the counting room. The latter two systems [22][23] were developed out of the necessity of handling large volumes of image data generated by typical event sizes, which ranged between 25-50 kilobytes.

3.2 *Targeting and Image Detection*

The general flow of the image information from the target to the digitizing device is a rather complicated one, and each subsystem is worthy of some discussion.

3.2.1 Fiber Target

As already indicated in Fig. 3.1, the target consisted of a stacked array of approximately 1×10^6 square fibers of 29 μm $\times$ 29 μm cross section. Each fiber consisted of a core glass material, GS1 [25], with refractive index $n_{core} = 1.56$, surrounded by a thin cladding material [24] with refractive index $n_{clad} = 1.467$. The active scintillation agent was a Cerium oxide dopant (C_2O_3) added to the raw glass stock in low concentration [25]. The glass was fabricated into a large boule ($\sim$ 1 inch square), which was subsequently drawn with the cladding material into fibers of reduced cross sectional size ($\sim 1mm^2$) [26]. At this intermediate step, fifty or so fibers were grouped into a "multi-fiber", which was drawn still further, fusing the fibers in the drawing process. Later, multi-fibers were stacked with an epoxy glue and drawn again. In the last step an optical surface was cut and polished to form a final target. The physical dimensions of the detector are listed in Table 3.1.

The composition of the core material used is broken down in Table 3.2. This choice of targeting material was dictated in part by the availability of scintillators which could be drawn to such small diameters while retaining optical integrity. The fabricated target was radiation resistant, as is necessary for targeting high intensity beams. An important consideration of the fiber material is its fluorescence emission and absorption characteristics. The GS1 glass has a fluorescence emission spectrum

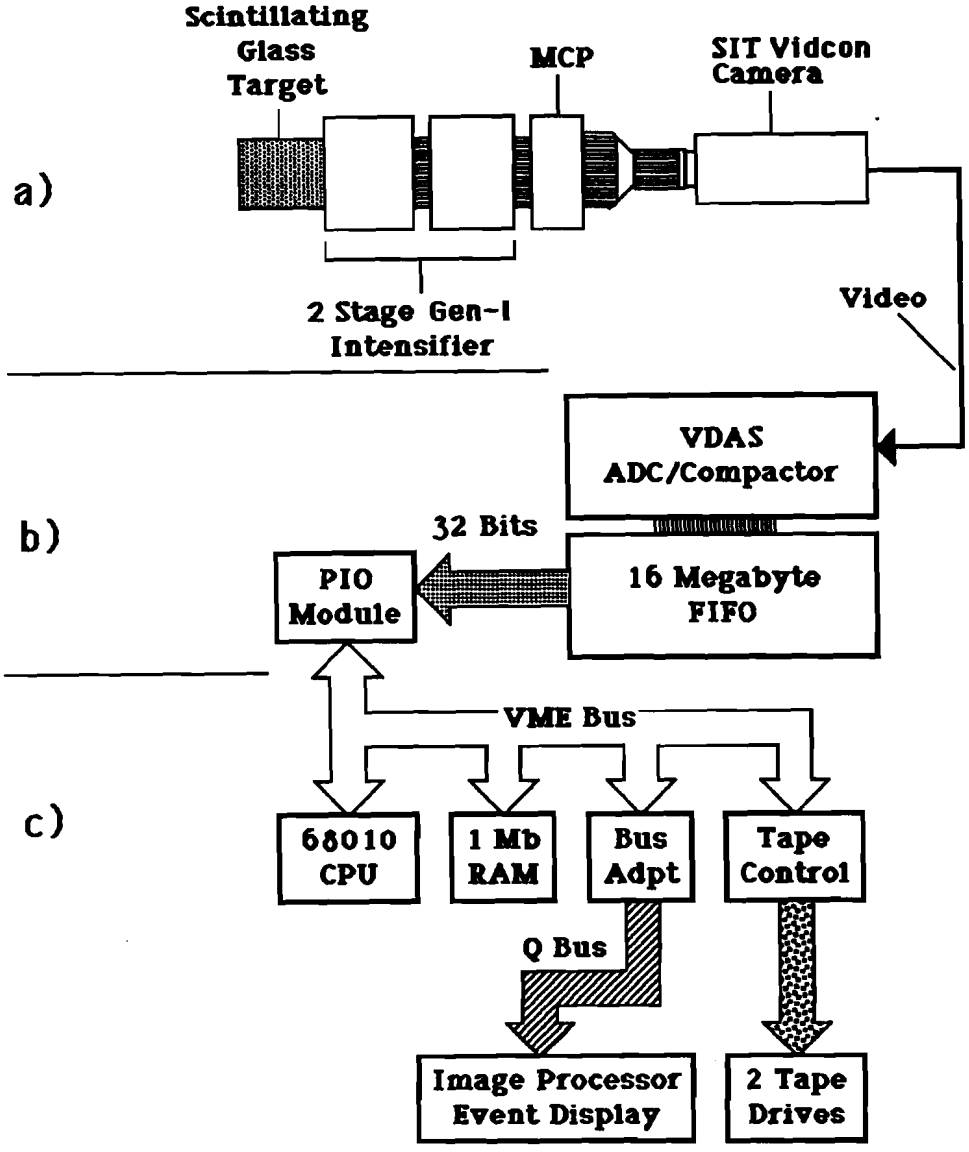

Figure 3.4. SFT system block diagram: the functional groups are a) targeting and image detection; b) fast image recording; c) higher level data acquisition.

Table 3.1. SFT dimensions.

Measure	E687 direction	(cm)
bulk thickness	X	1.509
bulk height	Y	2.715
bulk length	Z	2.713
active thickness	X	1.509
active height	Y	2.540
active length	Z	2.527
precision	all	$\pm$ 0.08

which peaks near 390 nanometers and separated by 30 *nm* from the absorption spectrum peak at 360 nanometers (see Fig. 3.5). This led to a significant attenuation of the light from tracks traversing deep within the target. Another disadvantage was the large ratio of radiation length to interaction length (5 compared to $\sim$1 for beryllium), which causes added production of unwanted e^+e^- pairs when a photon beam is used.

3.2.2 Image Intensifiers

A diagram of the two-stage image intensifying assembly employing electrostatically focused GEN-I[2] type devices and the microchannel plate intensifier (MCP) is given in Fig. 3.6. The light output from the target was collected by a direct optical coupling to a 25 mm input faceplate, itself a fiber-optic array of 7 μm glass fibers of low numerical aperture, which connected the target face and the photocathode window. Each GEN-I intensifier was operated with a 15 kV potential difference between the photocathode and phosphor screen, resulting in approximately a factor of ten gain. The light output from the second GEN-I phosphor screen was directed to the photocathode of the MCP

[2]Commonly used acronym for "first generation" image intensifiers.

Table 3.2. SFT material composition (GS1 glass [25]).

element	percentage
SiO_2	55
MgO	24
Al_2O_2	11
Li_2O	6
Ce_2O_3	4
radiation length	25%
interaction length	4.9%

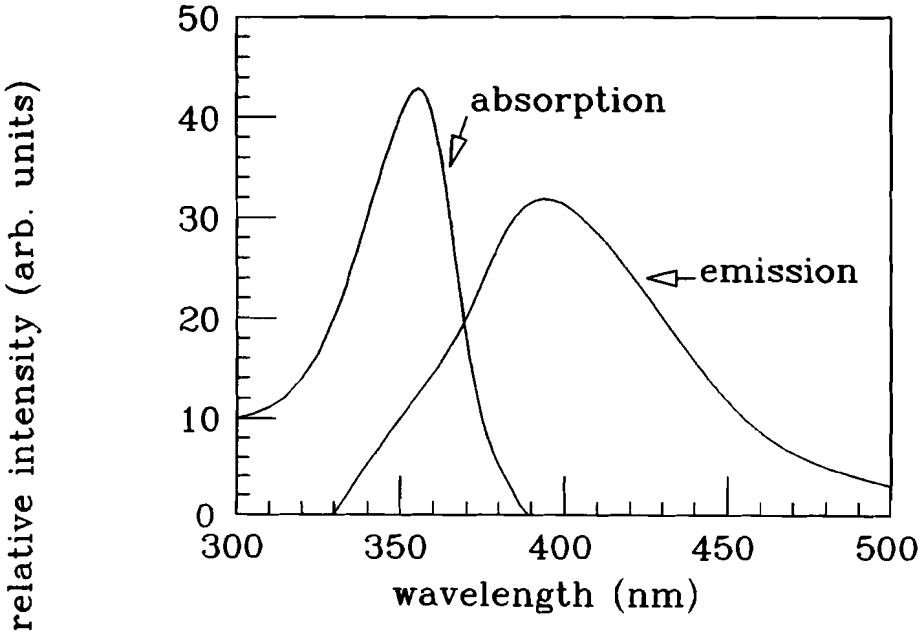

Figure 3.5. SFT fluorescence and emission spectra (GS1 silicate glass).

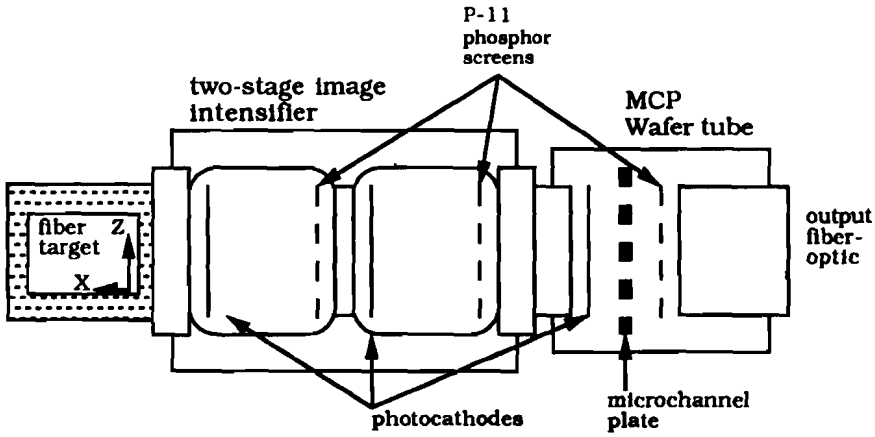

Figure 3.6. Image intensifier/MCP schematic.

which provided additional gain and triggerability. When the MCP was forward biased, photoelectrons were accelerated across 300 volts to a specially designed plate pierced with 12 μm pores which acted as multipliers creating small electron showers. The voltage across the plate was typically tuned around 700 volts. Electrons emerging from the plate were accelerated to the anode across 5.2 kV, striking a phosphor screen. The output fiber optic faceplate of the MCP was 18 mm in diameter. The combined luminous gain from the three intensifiers was approximately 6×10^5. As will be seen below, the system gain could be boosted further by taking advantage of the intrinsic gain characteristics of the SIT VIDICON.

3.2.3 Trigger and Image Gating

As mentioned above, the MCP was operated in a gated mode in which it was normally reversed-biased, becoming forward biased when an external trigger condition was satisfied. Thus the system operated in a *dark field* mode in which the image sensor (i.e. the SIT VIDICON) normally viewed a blank screen while waiting for an event to

occur. The target, of course, as well as the two GEN-I image intensifiers were always *active*, meaning they were constantly sensitive to beam crossings, pair interactions, subsequent hadronic interactions, etc. The phosphors used on the GEN-I devices were the P-11 type, which have decay time constants of 10-20 μs, measured as an intensity attenuation to 10% of the initial peak value after excitation. In this way, they served to store the light information while a trigger decision was being made. Obviously this time was overly long and thus was a source of event pile-up. The phosphor screen of the MCP was also of the P-11 type. The time constants of the phosphor screens contribute to both the pile-up and the dead-time of the system. The triggering sequence of events was roughly the following:

1. An interaction occurs in target, pulses trigger counters.
2. Target light is amplified by the GEN-I intensifiers, and excites phosphor screens.
3. Trigger logic activates the MCP gate, forward biasing the tube.
4. The readout commences on the next vertical retrace of the SIT camera.

The SFT trigger for the π^- meson beam running was designed to indicate the presence of charged tracks emerging downstream of the target, with the beam entering the target in a good fiducial region. This was specified by setting voltage thresholds for the photomultiplier tube signals from the T-counters (see Fig. 3.2) and specifying the following trigger logic:

$$T = \overline{T_1} \cdot T_2 \cdot T_3 \cdot T_4$$

The trigger was formed locally to the target with a custom trigger processor utilizing ECL electronics [27]. The phototube anode signals were fed directly into dual channel discriminators followed by programmable comparators. In this way, coincident "on"

or veto conditions could be selected, as could threshold levels on all the trigger counters. The reversed-biased condition was realized by holding the input cathode of the MCP to +320 volts; the MCP was switched on by dropping this voltage to ground. The formation time of this trigger was less than 70 nanoseconds. The gating time was set to 500 μs to collect as much light out of the first two intensifiers as possible; this was necessitated by the long persistence tails of the P-11 phosphor screens.

As it was necessary to forward-bias the MCP as soon as possible after the event interaction, the trigger electronics modules were mounted in close proximity to the target; signal cables leading to the experiment control room were pulsed to initiate the SFT and E687 DAQ reading cycles. Since no other trigger information from the spectrometer was used, this "SFT trigger" became the equivalent of the master gate and second level triggers (see Section 2.6).

3.2.4 SIT VIDICON Camera

The output image of the MCP was viewed by a variable resolution and image format scanning device know as a SIT VIDICON camera. The output faceplate of the MCP was fiber optically coupled to the SIT camera. Photoelectrons produced at the photocathode of the SIT camera were accelerated across 6 kV and targeted onto a photodiode array. The target surface was a matrix of p-n junction diodes which were read-out by a scanned electron beam. The diodes were spaced 12 μm by 12 μm which set the limit for the intrinsic resolution of the device. As the beam was electrostatically deflected across the target surface, the charge created by the photoelectrons impinging on the diode sites was collected by an integrating amplifier. The pulses were in turn fed to a video signal generator, producing a video scene viewable by a television-like monitor. Using a SIT camera, an additional gain of several hundred can be realized, providing an advantage over non-intensified cameras.

The device was configured to scan the photosensitive area of 15 mm by 30 mm,

with a sampling of format of 1179_y by 784_z. Here, the first numbers refer to the direction transverse to the (experiment) beam direction (see Fig. 2.6) while the second refer to the direction longitudinal to the beam. The effective "pixel size" was 18 μm by 54 μm. The reason for the smaller transverse pixel size was to improve the transverse track resolvability in the forward interaction cone. The readout of the SIT camera typically involved scans of one or more "fields". This was due to an effect called "lag" which occurs when charge remnants from previous scans are not completely removed from the active diode sites. These lags could constitute charge collections of up to 30% of the originally deposited charge. To avoid sampling old charge, one or sometimes two additional field scans were made after an event had been digitized. The SIT camera was read at a sampling rate of 8 MHz, and thus a three-field scan corresponded to a dead time of approximately 120 milliseconds. During the two running periods in which the SFT was installed, the event collection rate was approximately six to eight frames per second, although much higher readout rates were in principle possible.

Overall Device Resolution

Having specified all the detector elements, one can attempt to estimate the overall photoelectron spot resolution. The contributing factors are many, but consist mainly in the following:

1. Target center-to-center fiber spacing: 29 μm.
2. Alignment and diffractive effects at the coupling junctions of each stage: 10 μm.
3. The point spatial function of the GEN-I image intensifiers: 15 μm.
4. MCP pore diameter and spatial function: 19 μm.
5. Effective SIT camera beam resolution: 22 μm(Y), 55 μm(Z).

The spot resolution estimate can be taken as quadrature sum of these resolutions assuming correlations between these quantities are small. Doing this one finds $\sigma_y^{spot} =$ 44 μm, $\sigma_z^{spot} = 67$ μm. These resolutions represent the spatial spreading of the single photoelectron response through the system. This resolution could be improved with offline analysis of the pulse height distribution.

3.3 Fast Image Capture

There are two basic to be problems addressed in the recording of interaction images within a high rate environment. First, the potential event size is extremely large by high energy physics standards; the image frame of 1179 by 784 pixels represents 924 thousand detector elements per event to either read in and store, or to encode. Second, the system obviously needed to be be triggerable, which is not a common feature among video camera systems. The solution to these problems required development of a video data acquisition system (VDAS), a block diagram of which is illustrated in Fig. 3.7. The major components consist of a flash ADC, a high speed data compactor, and a 16 megabyte first-in-first-out (FIFO) buffer memory. An important design feature was the programmability of the video controller to accommodate camera architectures differing in image format and pixel rates. This permitted use of a CCD camera during initial tests, and variable sampling formats for the SIT camera during data taking. The FIFO buffer size was chosen keeping in mind the beam spill cycle, the anticipated event size, and event rate. The device was designed to process image data at rates of up to 30 million pixels per second, which can be compared to the standard camera rate (and the rate at which the prototype device operated) of 8 MHz.

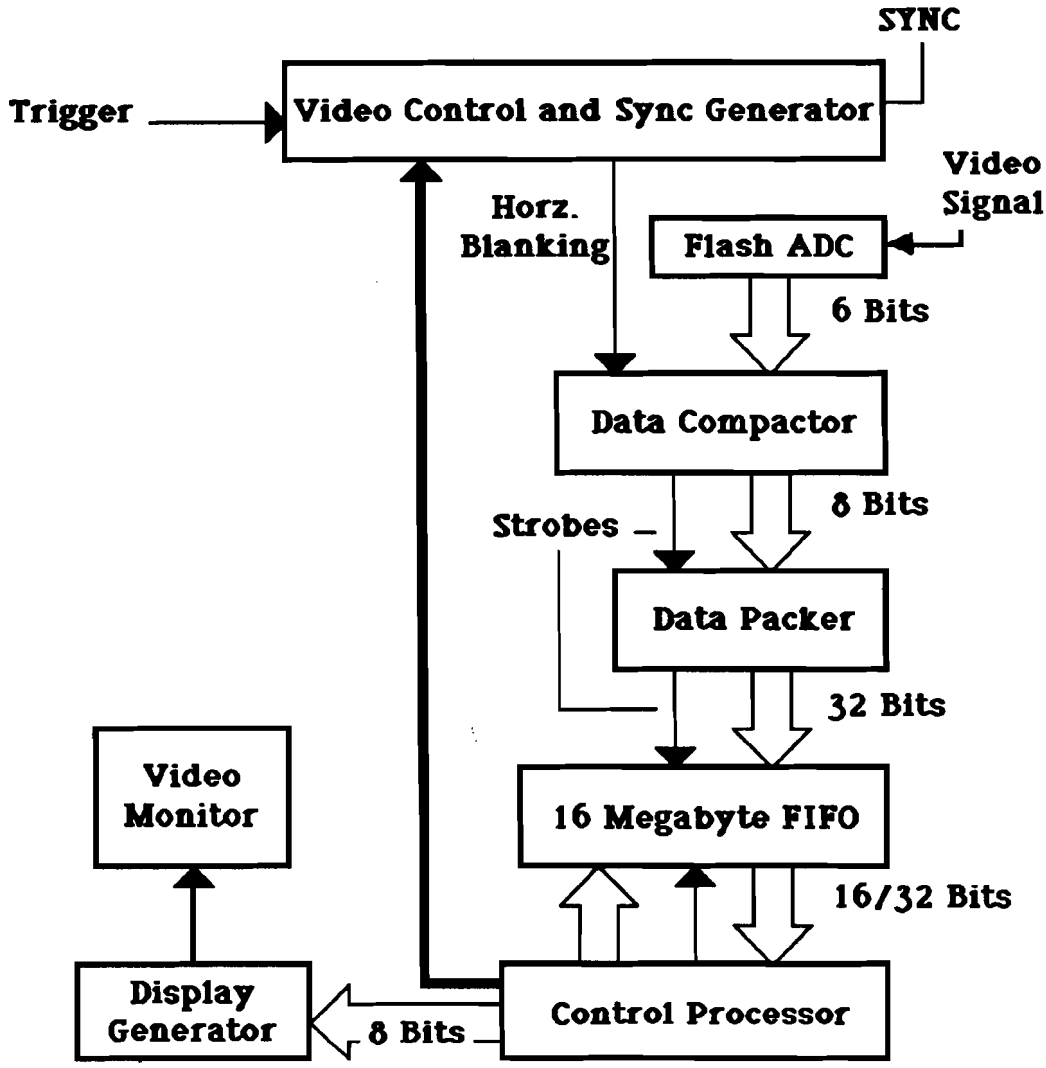

Figure 3.7. VDAS block diagram.

3.3.1 Image Compaction

The video signal from the SIT camera was fed into a six bit flash ADC, with lower and upper reference voltages tuned to optimize the video signal sampling. The digitization of the pixels into 64 gray levels was suitable for target images. The six bit data word was transferred to a data compactor module which compressed the image by discarding, in a reconstructable way, pixels below a programmed reference threshold. This threshold was determined by the operating conditions such as the gain settings of the image intensifiers. The method of image compaction deserves special attention.

Compaction Scheme

As mentioned, the amount of information contained in a single event is enormous (~900 kilobytes) so that online compaction of the image was necessary to reduce I/O bottlenecks at later stages of the data acquisition and transfer. Since target images were usually sparcely populated with active pixels (typically 2 - 10% of the pixels for a given frame), the idea was to record only the active pixels, but in such a way that their location within the image could be recovered. This was done by an encoding scheme employing pixel counting. The horizontal scanline and vertical "column" positions of the sampled surface were encoded into the data stream itself by counting "off" pixels. As the video signal was digitized, the pixel pulse heights below the threshold value caused a "zero" counter to increment. This would continue until either an "on" pixel was encountered, the zero counter registered a value of 127, or the end of the scanline was reached. If an "on" pixel was encountered, the value of the zero counter (with a special code attached—see below) was written into the data sample followed by the pulse height value of the "on" pixel. In addition, special status flags, or "C-flags", were encoded to mark horizontal and vertical sync markers (which are needed for the offline software reconstruction of the event), as well as flags indicating that bytes following correspond to run, spill and event numbers. A schematic of the electronics module

Table 3.3. Compactor data byte codes.

meaning	bit assignments	Interpretation
data	10nnnnnn	6 bit pulse height
zero count	0nnnnnnn	No. consecutive "off" pixels
C0 Status	11000000	Horizontal synch fiducial
C3 Status	11000011	Run No. tag
C4 Status	11000100	Event No. tag
C5 Status	11000101	Frame byte count tag
C6 Status	11000110	Frame No. tag
C7 Status	11000111	Spill No. tag

which performed this task is shown in Fig. 3.8. All of the component electronics were ECL-type, chosen for fast clocking speeds though individual gates. The compacted data is formed into 32 bit words before being transferred to the FIFO buffer memory.

3.3.2 FIFO Architecture

Even with the compression of event images, the (variable) amounts of data generated are still rather large, ranging between 5 to 50 kilobytes. In order to provide a smooth transfer of the events to magnetic tape, a large buffer memory was designed into which the events could be temporarily stored. During the spill period, the rapidly filling buffer could be read nearly simultaneously, and of course, data reads could continue during the interspill period as well. The FIFO was organized as four separate memory modules with each holding four megabytes. Each module can be visualized as a matrix of bits 512 wide by 256K deep, as pictured in Fig. 3.9. The sequencing of the compactor output into and out of the FIFO memory was the key to its speed. Each 32-bit wide longword from the compactor was latched in a series of shift registers by

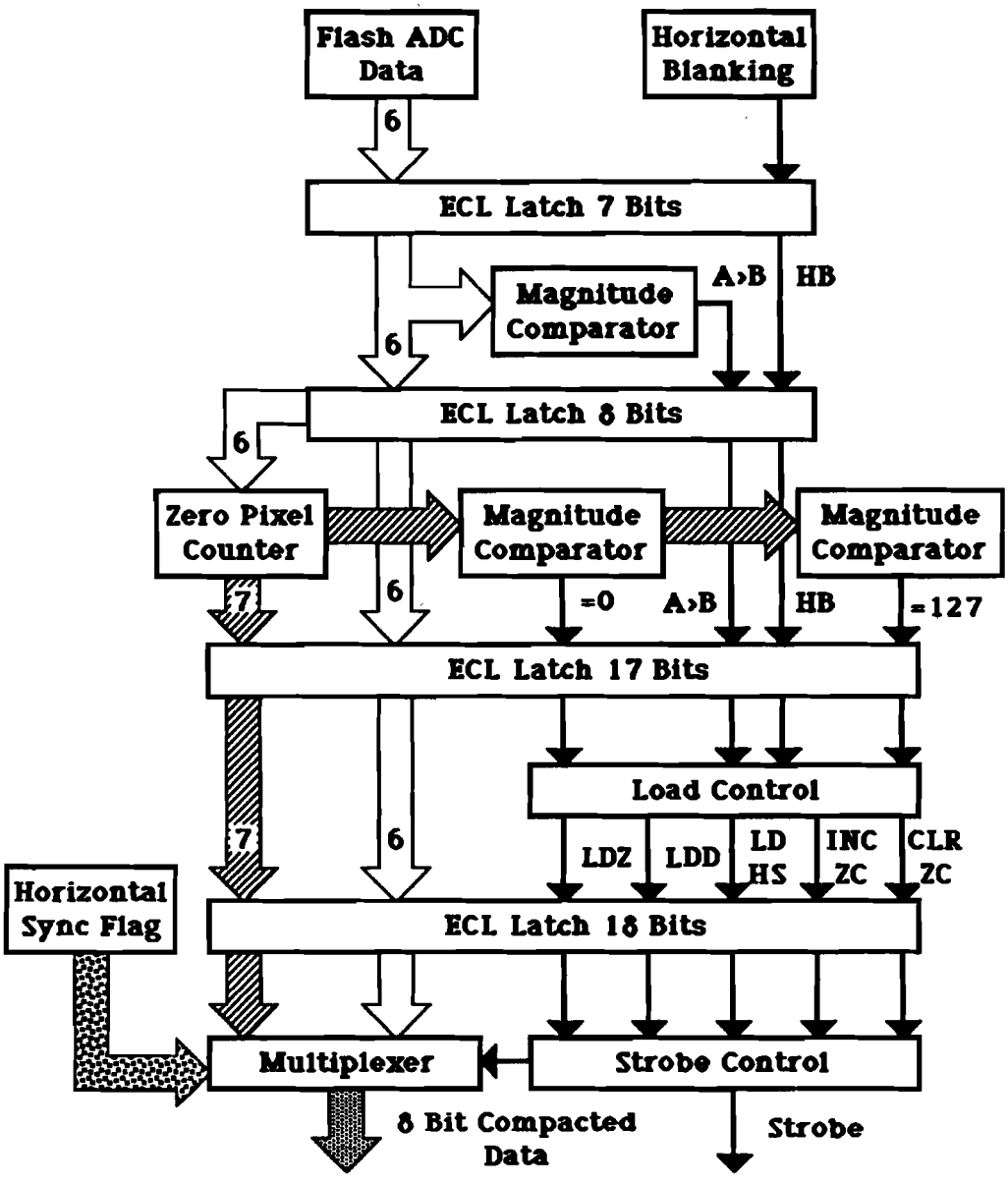

Figure 3.8. Data compactor as implemented in VDAS. For magnitude comparisons, "A" refers to data, while "B" refers to the threshold value.

presenting the data at the inputs and applying "FIFO write" strobes. After sixteen FIFO writes the data were transferred into an input storage register where, upon the next memory cycle, it would be strobed into a memory array of dimension 256K by 512 bits. The separation between the staging of data bytes and the actual transfer to the memory chips allowed the internal memory cycles to run at a rate sixteen times slower than the FIFO write rate. Thus, cheaper memory chips having lower power consumption could be used while external latching electronics were standard TTL logic chips.

While the rate of data transfers through the FIFO was determined by the ADC compactor board to be 30 million bytes per second, the FIFO itself was bench-tested to be operational at rates of up to 100 million bytes per second. It was also possible to expand the memory size of the FIFO in four megabyte increments to a maximum of 256 megabytes, though this was not necessary for the prototype SFT configuration. The addition of extra memory allows even more FIFO write strobes to occur for each memory control cycle (since only the input latches are affected), thus even faster memory *filling* rates can be achieved, limited only by the TTL latching speed ($\approx$ 50 MHz). The problem of the data transfer out of the buffer memory to a long term storage media still remains, however, and is discussed in the following section.

3.4 VMEbus Data Acquisition System

Once the image data for the SFT was buffered into the VDAS memories, the job still remained of transferring the data to mass storage. For this purpose the data were written to two conventional streaming tape drives controlled from a system resident in VMEbus, chosen for its fast throughput (10 MHz clock cycle) and module flexibility. In Fig. 3.10 the system layout is shown in which the main components are specified. The transfer of data buffered by the FIFO is accomplished with a commercially available parallel I/O card adhering to VMEbus standards. The system

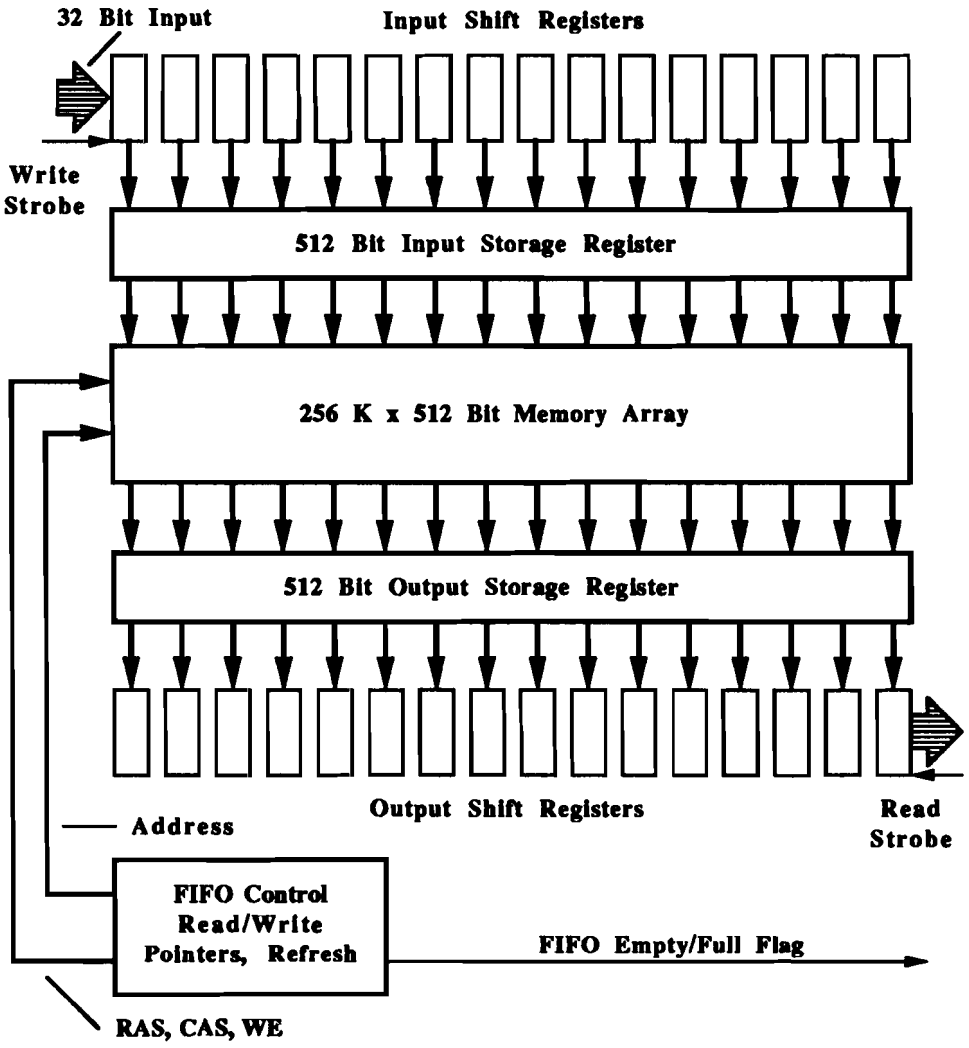

Figure 3.9. FIFO architecture implemented in VDAS.

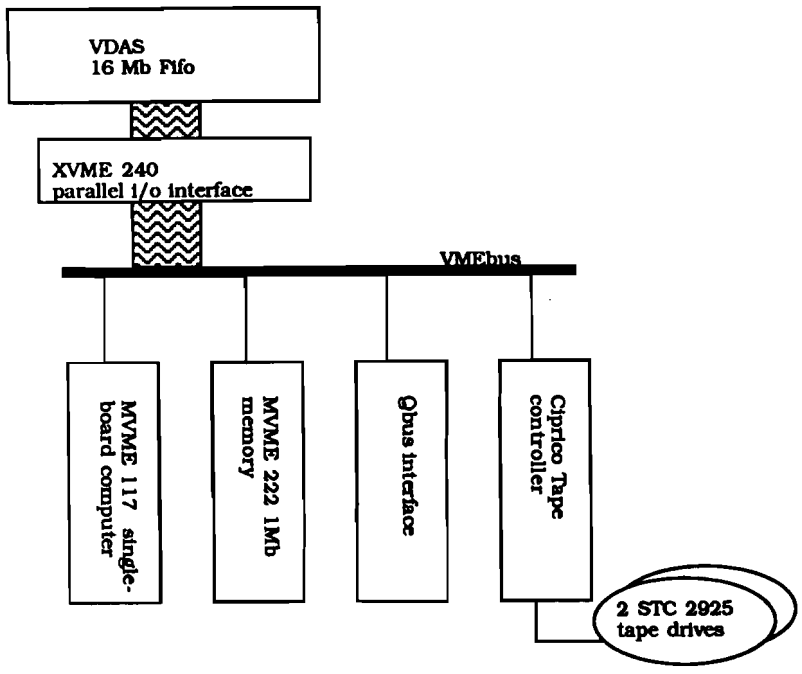

Figure 3.10. VMEbus data acquisition system.

is controlled with a single board computer in which a task coordinates all aspects of the data acquisition flow.

3.4.1 Functional Description

The general transfer sequence was initiated by the FIFO with an interrupt to the software task running on the VME computer indicating that data was available for transfer. The task would then commence reading the FIFO data into a buffer memory addressable from the VMEbus. The data were organized into fixed length blocks of 16 kilobytes each. After a certain number of these blocks were filled, a transfer of the data to the magnetic tape drives was initiated. This was done by constructing a command parameter block which specified the transfer addresses for the DMA (Direct Memory Access) controller of the tape-writing module. After requesting the DMA transfer for the buffered data, the process waited for an interrupt signal indicating completion. Upon receiving this signal more buffers were filled with data read from the FIFO, and the cycle repeated. This would continue as long as the FIFO contained

data to be read.

As the data were being written to the tape drive, the controlling task kept a count of the number of bytes and events written. If the total byte count exceeded 135 megabytes, the output was directed without interruption to a second drive. The SFT data tapes usually contained a few thousand events, depending on the running conditions.

The data speeds through the system were limited mainly by the VDAS-VME parallel I/O interface, which necessitated the use of programmed data transfers rather than direct memory accesses. The speed was measured to be 480 kilobytes per second, which matched the limiting speeds of the tape drives, but clearly was far below the operating speed of the FIFO.

3.4.2 Event Identification System

In order to match events recorded by the SFT to those recorded by the spectrometer, an event tagging system was developed. The system was designed to reside in a specially modified CAMAC-type crate, as is shown in Fig. 3.11. Event information, consisting of the run, spill and event numbers, was generated uniquely in one location and distributed to both data streams for off-line cross referencing. At the beginning of each run, the main E687 DAQ program downloaded the current run number into a sixteen bit latch, where it could be distributed over a modified dataway to modules dedicated to various data streams. NIM and TTL trigger inputs for both spill and event pulses were provided so that two resident counters could increment on these triggers. Just as for the run number, the counter outputs were latched and fanned out onto the dataway for distribution.

One module latched the run and spill numbers into a set of external identification latches in the VDAS system. These numbers needed to be loaded at most once per spill. In addition, 24 bits of the 32 bit event counter were connected to a special input

latch which inserted the event number into the FIFO data stream following the event data. The three bytes were grouped with a "C-flag", as discussed above, so that it could be identified during the software event reconstruction.

The run, spill and event numbers were also inserted into the main E687 data pathway via latch modules built by the University of Illinois. Ideally, these numbers would have been inserted via hardware modules into every distinct data pathway, such as the LeCroy 1892 memories, in order to provide an extra check for data synchronicity.

3.5 Data Sample

The prototype device, as described in the preceeding discussion, was installed and operated for two separate running periods. The first tests were made January 17-19, 1988. During this period about 60 thousand events using a 350 GeV photon beam were recorded, as well as 110 thousand events using π^- meson beams of 350 GeV and 450 GeV. The original intention was to run solely with a photon beam, but triggering on photon-induced hadronic events proved to be too difficult without use of the hadron calorimeter information. Most of the events using the photon beam turned out to be electromagnetic showers developing in the target or surrounding magnetic shielding material. The target was installed again for another brief period on February 14-15, 1988. During this run 72 thousand events using a π^- meson beam at 350 GeV were recorded.

To get an idea of the typical response of the system, consider Fig. 3.12 in which a π^- meson beam particle is incident from the right and strikes a target nucleus. The dots on the image are drawn using the scanline and column positions as directly read out from the SIT, and thus have not been rescaled to the physical lengths. The intensity of the dots are scaled according to the ADC pulse heights as digitized by the VDAS system, and hence represent observed light intensity. A very dark spot at the primary interaction indicates a nuclear breakup, as do the heavy fragment

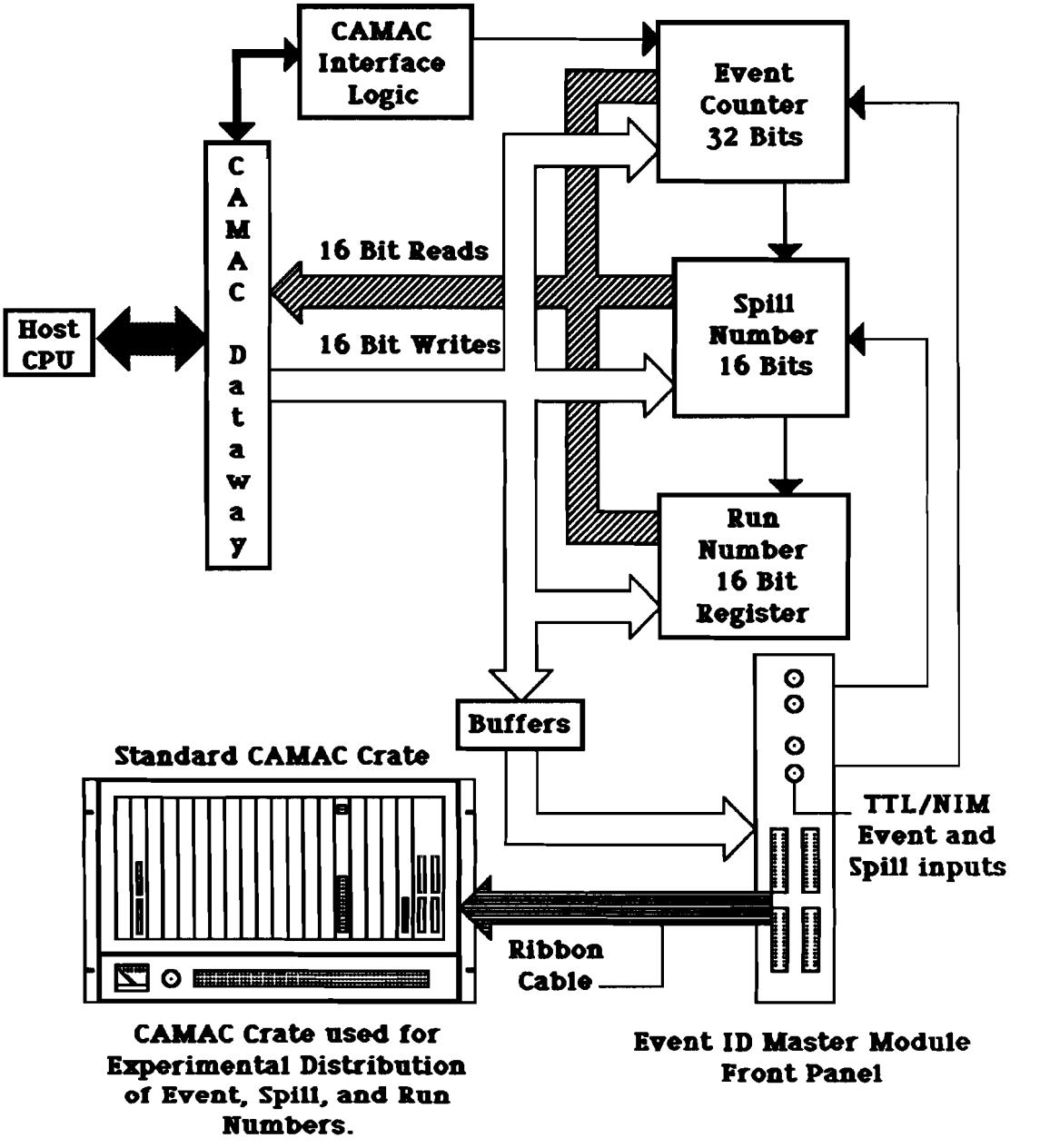

Figure 3.11. E687 event identification system.

tracks emerging at wide angles. There are as well several tracks contained in the forward cone. In this event only one hit can be seen for the beam track, indicating the interaction took place deep within the target (away from the input fiber-optic of the first image intensifier). This is consistent with a study of single track events which showed that the nominal hit density for the system was $\simeq 1.5$ hits per millimeter along the beam path.

A study of single track events also showed good correlation with tracks reconstructed by the microstrip detectors. In Fig. 3.13 the y-intercepts at the center of the SFT target for tracks reconstructed by both the SFT and SSD systems are shown. This was first done as a check that SFT and SSD events were matched between the main spectrometer data tapes and the SFT tapes. The SFT tracks were reconstructed by fitting hits to a straight line hypothesis. The hits were first subjected to a pulse height analysis to determine their spatial centroids. Distortions owing to the "pincushion" focusing of the image intensifiers were neglected. In Fig. 3.14 the results of a vertex correlation study are shown as z-coordinates of vertices found by both the SFT and SSD are plotted. SSD vertices are determined by a "stand alone" vertexing algorithm, VERTIC, which is described in Section 4.2. Events having only one vertex found by the microstrip detectors were analyzed for SFT vertices. The SFT image was scanned visually and a vertex was determined by recording the SIT-coordinates of the electronically displayed image. The vertices from the two detection systems were again correlated to within the vertex z-coordinate error of the SFT device.

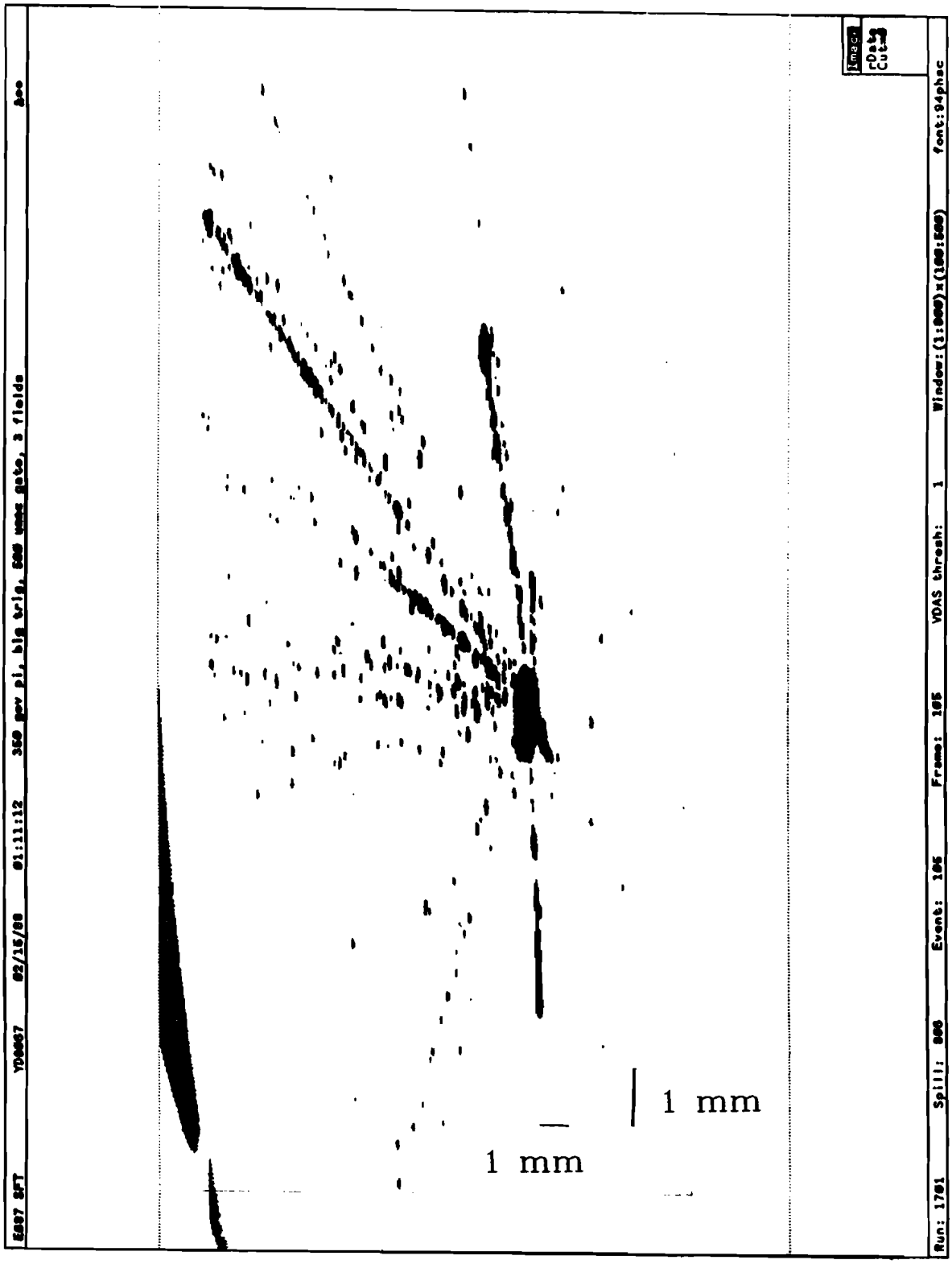

Figure 3.12. 350 GeV π^- meson–target nucleus interaction.

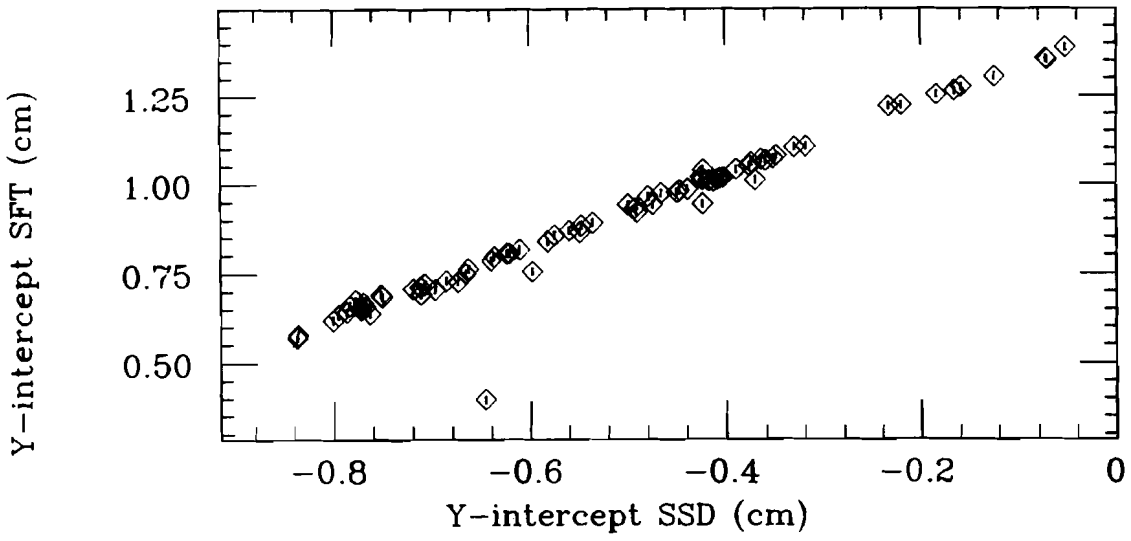

Figure 3.13. SFT and SSD intercept correlation. The the y-intercepts were defined at the SFT target center. The units of the SSD tracks are E687 M2 bend center units, while the SFT units are in cm from the bottom edge of the SIT-scanned target area.

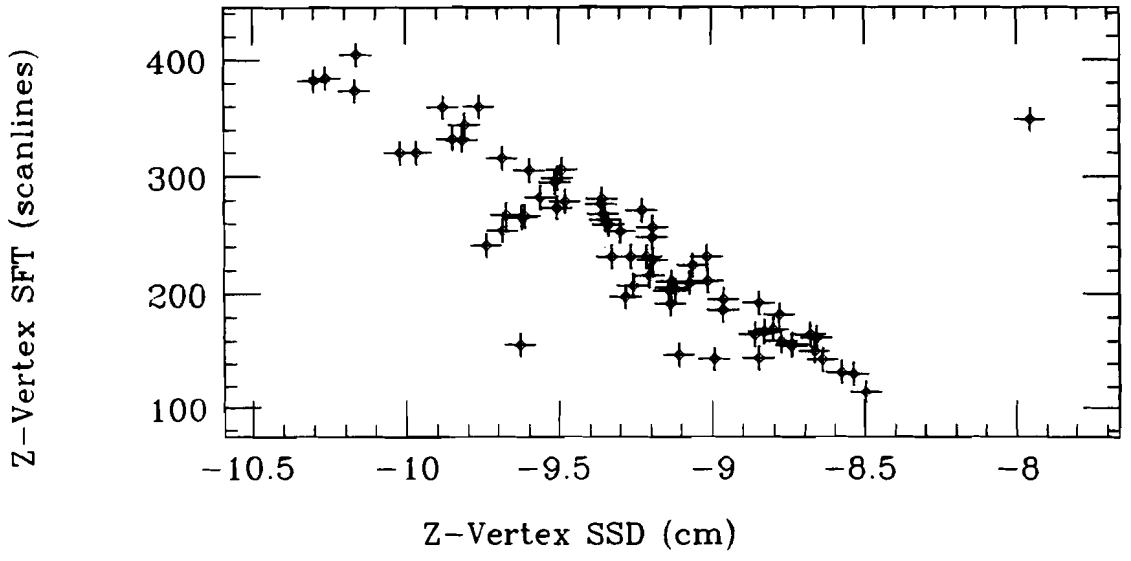

Figure 3.14. SFT and SSD vertex correlation. The the z-coordindates of SSD and SFT vertices for one vertex events. An SFT scanline unit represents approximately 60 μm, and is measured from the upstream edge of the SIT-scanned target area. The SSD z-coordinate is measured relative to the granite support block (See Chapter 2).

CHAPTER 4

DATA REDUCTION

This chapter contains a description of the analysis and reduction of the "post-fire" data sample leading to the isolation of the D^o candidate events. The data were recorded from December 1987 to mid-February 1988. During this time approximately 60 million events were written onto about 1200 data tapes. Each event contained the digitized detector responses such as ADC pulse heights, TDC information and latched trigger bits. The general analysis scheme consisted in first processing the "raw" data tapes into "reconstructed" ones in which particle trajectories, momenta, and identification codes were written. The package of routines which performed the task, PASS1, was functionally divided into charged particle tracking, momentum analysis, vertex finding, neutral vee finding, and Čerenkov analysis. The package was executed on the Fermilab ACP computer farms [28] from May until September of 1989. About 45 million events were successfully reconstructed and written to about 2400 new tapes. Not all of the information provided by the program was utilized in the present analysis, and the sections that follow discuss only the necessary routines.

After reconstruction, it was necessary to reduce the event sample to a manageable size. This was was performed during a "skimming" phase in which various physics states and charm topologies were edited from the reconstructed event sample and written to new sets of analysis tapes. Following this phase was the physics analysis using highly compressed data summary tapes (DSTs).

4.1 *Track Reconstruction*

The starting point of the analysis began with the selection of reconstructed tracks in the spectrometer. The reconstruction was achieved through a multi-step process utilizing the high quality tracking information from two separate detection systems: the four stacks of SSDs and the five-chamber PWC system. The detector responses from each of these systems were first analyzed independently, and at a later stage the fitted track parameters were linked, where possible, to provide complete trajectory specifications for charged particles passing through the apparatus. The major points are discussed below.

4.1.1 SSD Tracking

The microstrip ADC responses were analyzed with an independent tracking program functionally divided into three main parts [29]:

1. charge sharing analysis
2. projection pattern recognition
3. three dimensional space track fitting

The charge sharing algorithm was performed to assign optimal coordinate positions to the track intersection points with the struck planes, and to resolve, in the case of adjacent hits, single track crossings and multiple track crossings. For isolated hits, the centroid of the hit strip was used. For two adjacent hits resolved as one track crossing, the centerline between the strips was used as the coordinate. For three adjacent hits resolved as two track crossings, either the two centerlines between the strips were used, or the centerline between two of the strips and the centroid of the third was used. Clusters of more than three adjacent hits were not analyzed.

The next step was to use the resolved coordinate information to search for projected tracks, i.e. aligned hits along each of the (i,j,k) coordinate directions as indicated in Fig. 2.6. Each projection was required to have three out of four hits, and pass a χ^2 test on a least squares fit to the hits. In order to reduce biases stemming from the order of the projection search, hit sharing was allowed among the projections, with the exception that the three downstream hits of four-station projections were not made available to projections having only three hits.

Following the pattern recognition, three dimensional space tracks could be formed by matching the newly found projections. Two projections were grouped, say one from each of the i and j views, and a third was searched for from the k view to complete a space-point triplet. This was accomplished by computing their planar intersection points at the second and eleventh planes and imposing a maximum separation cut. The twelve coordinate positions associated with the four grouped triplets were subjected to another least squares fit and the final candidates were required to pass a χ^2 cut of < 8. The parameters returned by the fit were the slopes and intercepts of the tracks. In addition, tracks sharing projections in i and j were arbitrated on the basis of their χ^2 values, and clusters of closely spaced tracks were combined into a single track when possible.

The efficiency of track reconstruction using this method was studied in Monte Carlo and found to be about 96% efficient overall for charm events, while tracks with momentum greater than 10 GeV were correctly reconstructed nearly 99% of the time. The level of "spurious" tracks (fake tracks drawn from accidental association of hits) was less than 3%.

Since the routine operated without the benefit of the downstream tracking information, no knowledge of the track momentum was used during the fitting process. Thus the internal cuts were set particularly wide so as to avoid loss of efficiency resulting from multiple coulomb scattering (MCS), which is an important factor due

to the material introduced by the silicon strips themselves. This choice was motivated by the desire to keep CPU time requirements to a minimum. However, during later stages in the analysis, for example when computing vertex positions, accurate knowledge of track covariance matrices becomes important. The transverse position resolution for tracks extrapolated to the center of the target were computed as (for the high resolution regions only) [30]:

$$\sigma_x = 11\mu m\sqrt{1+\left(\frac{17.5\ GeV}{P}\right)^2} \tag{4.1}$$

$$\sigma_y = 7.7\mu m\sqrt{1+\left(\frac{25.0\ GeV}{P}\right)^2} \tag{4.2}$$

where the second term under each square root indicates the momentum below which MCS effects dominate. These formulas were checked in the data by comparing the projected miss distances of the tracks at the z location of the primary vertex, and dividing by the anticipated error. The resulting distributions could be fit with Gaussian functions with widths very close to one, indicating that the errors are calculated correctly.

4.1.2 PWC Tracking

Tracks reconstructed by the PWC system fell into two major classes specified by the number of chambers the track passed through: 1) 5 or 4-chamber tracks, and 2) 3-chamber tracks (commonly referred to as "stubs"). All tracks were required to have hits in the first wire chamber, P0. The three chamber stubs were formed from hits in the first three chambers, P0, P1, P2. These tracks were usually of low momentum (ranging roughly between 3 and 10 GeV) and either missed the aperture of the second

bending magnet or were swept clear of the P3 chamber by M2.

The philosophy of the tracking program was similar to that used for the SSD tracking, and consisted in the formation of view projections (except now four views are used: X, Y, U, V) followed by a matching of the projections to form three dimensional space track candidates. These candidates were fit to the 20 measured coordinates, followed by a χ^2 cut. In each case, projections in the non-bend (X) view were searched for by extending the X-projections of tracks already reconstructed by the microstrip detectors. These projections were the first ones used to combine together with the U, V, and Y-projections to form the space tracks. X-hits not selected by the extended microstrip tracks were then used in additional X-projection searches to be combined with the remaining U, V, Y-projections. The list of tracks passing with minimal χ^2 cuts were also required not to have more than four missing hits, and no more than two in any chamber. The parameters of the fit were again the x and y slopes and the intercepts, and for the case of 4 and 5-chamber tracks, the bend angle through M2. As before, arbitration between tracks with shared projections had to be performed. The overall efficiency for track reconstruction was determined from Monte Carlo to be $\simeq$98% for tracks with momentum greater than 5 GeV, and spurious tracks were returned less than 1% of the time. Finally, the number of reconstructed tracks possible for an event was limited to 30. This reduced the CPU time consumption of the algorithm so that very high multiplicity events, or those containing chamber oscillations, did not cause the program to compute endlessly.

4.1.3 Linking and Momentum Analysis

The process of matching the results of the two tracking procedures is called linking. This becomes important since the tracks reconstructed by the PWCs are not of high enough spatial resolution to resolve charm decay vertices, while the very precise SSD tracks have no momentum assignments and thus cannot be used to calculate such

quantities as invariant mass products. Neither, it turns out, do 3-chamber stubs since they also do not have tracking information on opposite sides of either analysis magnet, M1 or M2. As was pointed out earlier, knowledge of the track momentum is necessary for assigning errors which account for MCS. An added objective to the linking process is to determine which tracks are *unlinked.* Such tracks are useful indicators of neutral vee[1] particles decaying downstream of the microstrips.

The linking proceeds basically by looping over all possible combinations of tracks from the two systems and projecting them to the bend plane of M1. At this location, differences between slopes and intercepts (for x and y-views) between the two tracks are computed. The windows for the link were specified to be a certain number of wire spacings in each view. Combinations falling within the specified windows had their SSD and PWC hits subjected to a global 32 plane fit. Those passing a certain χ^2 cut had their track parameters replaced by the refitted ones resulting from the link comparison. The algorithm allowed an SSD track to link to two PWC tracks, but PWC tracks could only link to a single SSD track. This allowed for proper linkage of Bethe-Heitler pairs created in the target or microstrip detectors.

The momentum of a charged particle was determined by measuring its deflection through either M1 or M2. For linked tracks, the more precise determination is made using M1 due to the higher resolution tracking provided by the SSDs. For unlinked, 5-chamber tracks, M2 is used. For unlinked stubs, the momentum was determined by constraining the stub to point back to a vertex identified using other microstrip tracks in the event. The momentum resolution using M1 is [30]

$$\frac{\sigma}{P} = 1.4\%\left(\frac{P}{100\ GeV}\right)\sqrt{1+\left(\frac{23\ GeV}{P}\right)^2} \tag{4.3}$$

[1] We use the term *vee* to indicate pairs of oppositely charged tracks which form a probable vertex, and emerge from the target region. Such objects are candidates for K°_s and Λ° decays.

where the momentum below which MCS becomes important is 23 GeV. This high figure indicates that a large fraction of tracks from charm decays are very susceptible to MCS within the microstrips. For 5-chamber tracks measured by M2 the resolution was computed by:

$$\frac{\sigma}{P} = 3.4\%\left(\frac{P}{100\ GeV}\right)\sqrt{1+\left(\frac{17\ GeV}{P}\right)^2} \tag{4.4}$$

where again the momentum below which MCS effects dominate was 17 GeV.

4.2 Stand Alone Vertex Finding

Tracks reconstructed by the microstrips were used to search for primary and secondary decay vertices. The algorithm operated in a "stand-alone" fashion as none of the downstream information such as the momentum of linked PWC tracks was used. A least squares fit to a hypothesized vertex using all the tracks was performed and a χ^2 computed. Tracks which had the greatest contribution to this χ^2 were discarded and the remaining set refitted. This continued until enough tracks were discarded such that the vertex passed a suitable χ^2 cut. The entire procedure would then be repeated on the set of discarded tracks to find additional vertex candidates.

As mentioned above, these vertices were useful for momentum analysis of un-linked, 3-chamber stubs. Since this category of tracks has tracking information only between the two magnets, a vertex identified in the target region could be used to provide *probable* upstream intercept coordinates. The assumption here is that the stub originated at the primary vertex, which is tolerable in the absence of all other information. This procedure was known as "un-stubbing".

Reference Primary Vertex

Another important use these topologically identified vertices was was to provide

an approximate reference primary vertex for the vee finding routines. Actually, the notion of primary vertex identification is complicated since there really is no unambiguous set of criteria to apply to events in which multiple SSD vertices are found. Studies [31] have shown that for SSD vertices having at least one linked track, a strong correlation exists between the most upstream and the most populated vertices, especially when such vertices are required to lie within the target region. The implication is that either of these criteria would be a suitable. The implementation choice for the reference vertex was as follows:

1. If no SSD vertex was found in the event, the nominal target center was used.

2. If only one SSD vertex was found, it was used regardless of whether or not it contained linked tracks.

3. If more than one SSD vertex was found, the most upstream having at least one linked track was chosen.

The requirement that one of the vertex track members be linked was imposed as an additional validity check on the vertex. As will be seen below, the reference primary vertex was useful for computing vee detachment and p_t balance variables for SSD vees. Fig. 4.1 shows the distribution of reference primary vertices used for un-stubbing and vee finding.

Finally, secondary decay vertices found by the "stand-alone" algorithm were useful in isolating charm decays directly, and were also used as an isolation cutting tool for SSD vees. This is discussed in Section 4.6.3.

4.3 Neutral Vee Detection

The purpose of this section is to review the methods used to detect the neutral vee decays in the E687 spectrometer. The most common of these, and the most important

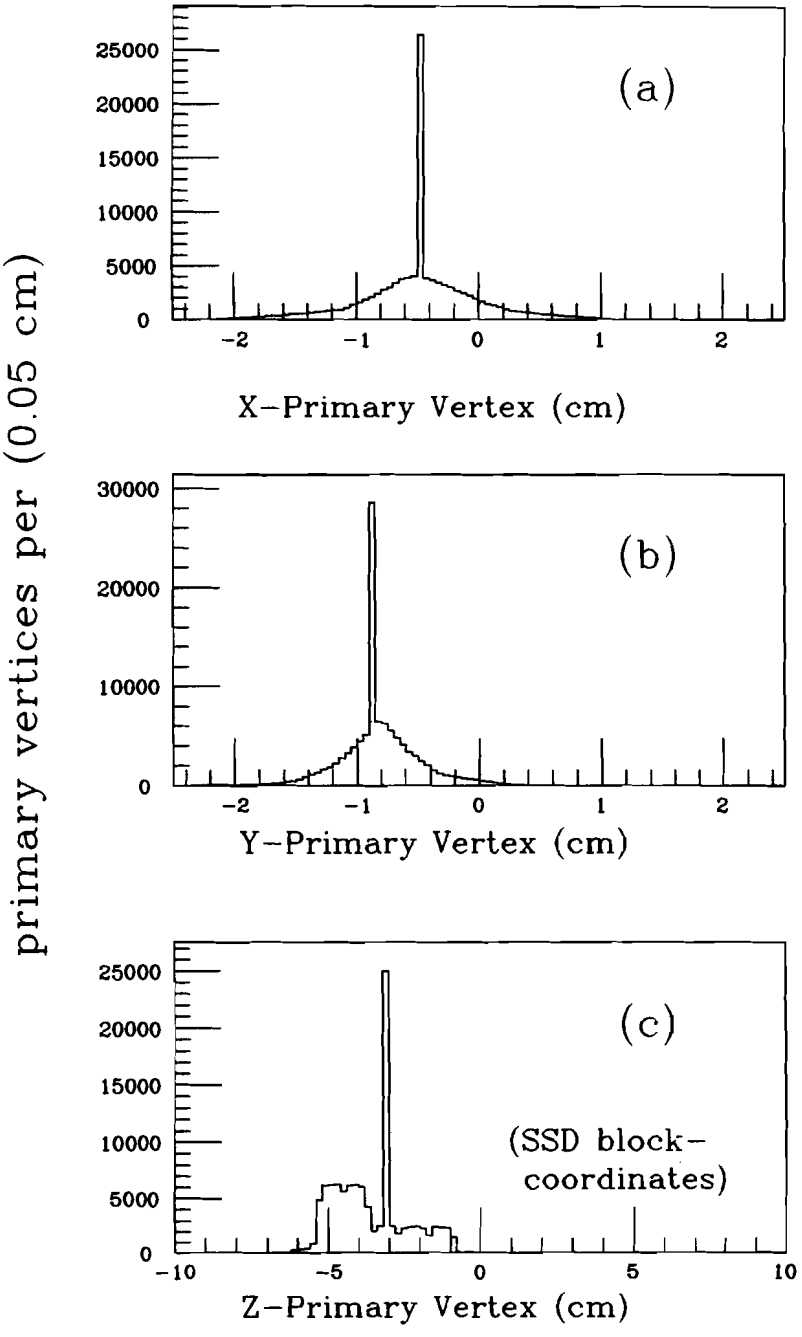

Figure 4.1. Reference primary vertex distributions: a),b) are the x and y-coordinate distributions; c) the profile of the z-coordinates of reference vertices measured relative to the SSD system. The large spike reflects events in which no SSD vertex was found and the approximate target center was used.

for the analysis presented here, is the decay $K_s^o \rightarrow \pi^+\pi^-$, though the methodology is very nearly the same for the decay $\Lambda^o \rightarrow p\pi^-$. The production and decay of these particles provide an important tool not only for isolating charm events, but also for studying the performance of the detector apparatus and algorithms. This is in part due to their copious production (about 1000 per data tape) and clear signals. We will direct our focus to the K_s^o decays.

The K_s^o candidates were detected in various topologies as a consequence of their decay point. The topologies for reconstructed K_s^o events were defined in terms of the reconstructed track types of the daughters:

1. SSD: two linked SSD-PWC tracks.
2. MIC: two unlinked PWC tracks extended into the SSD chamber system using hits leftover by the microstrip tracking algorithm.
3. TT: "track-track"; two 5-chamber, unlinked PWC tracks.
4. TS: "track-stub"; one unlinked 5-chamber PWC track, and one unlinked 3-chamber PWC track.
5. SS: "stub-stub"; two unlinked 3-chamber PWC tracks.
6. RECON: "reconstruction vees"; unused PWC hits for K_s^o decays between P0 and P2.

Fig. 4.2 shows the histogramed $M_{\pi^+\pi^-}$ invariant mass for each of the categories. There are obvious differences in the mass distributions which are related to the mass resolution effects of the particular decay topologies and the degree to which clean up cuts could be applied. In Fig. 4.3 the proper lifetime distribution,

$$t = L/\gamma v \tag{4.5}$$

for the events in Fig. 4.2 is plotted, where L is the decay flight distance measured from the vee decay point to the reference primary vertex, γ is the K_s^o Lorentz boost factor, and v is the velocity measured in the laboratory frame. The plot gives a qualitative feeling for the proper time behavoir of the measured K_s^o decays and has not been corrected for acceptance or background. The average value was measured from the plot to be 80 ± 5 ps, not far from the known value of 89.2 ± 0.2 ps. The lower value obtained is a result of not subtracting the (smaller lifetime) background events as well as not accounting for the longer-lived K_s^o decays which fall out of the acceptance of the PWC chamber system.

4.3.1 Microstrip Region K_s^o

Two types of K_s^o candidates were reconstructed by the microstrip detectors: those consisting of fully reconstructed and linked tracks, and those which decayed within the microstrip detector volume and thus escaped being found by main microstrip reconstruction program. These comprise two topologies, the SSD and MIC type vees.

SSD Type K_s^o

All linked pairs of SSD tracks, of net zero charge, were considered as SSD vee candidates. A vertex was calculated by minimizing the miss distance between the tracks. The corresponding PWC track was not allowed to be linked to another SSD track. The two tracks were assumed to emerge from a common vertex, calculated by minimizing a χ^2 with respect to the (x_v, y_v, z_v) of the intersection point:

$$\chi^2 = \sum_{i=1}^{2\ tracks} \left\{ \omega_{x_i}(x_i - x_v)^2 + \omega_{y_i}(y_i - y_v)^2 \right\} \tag{4.6}$$

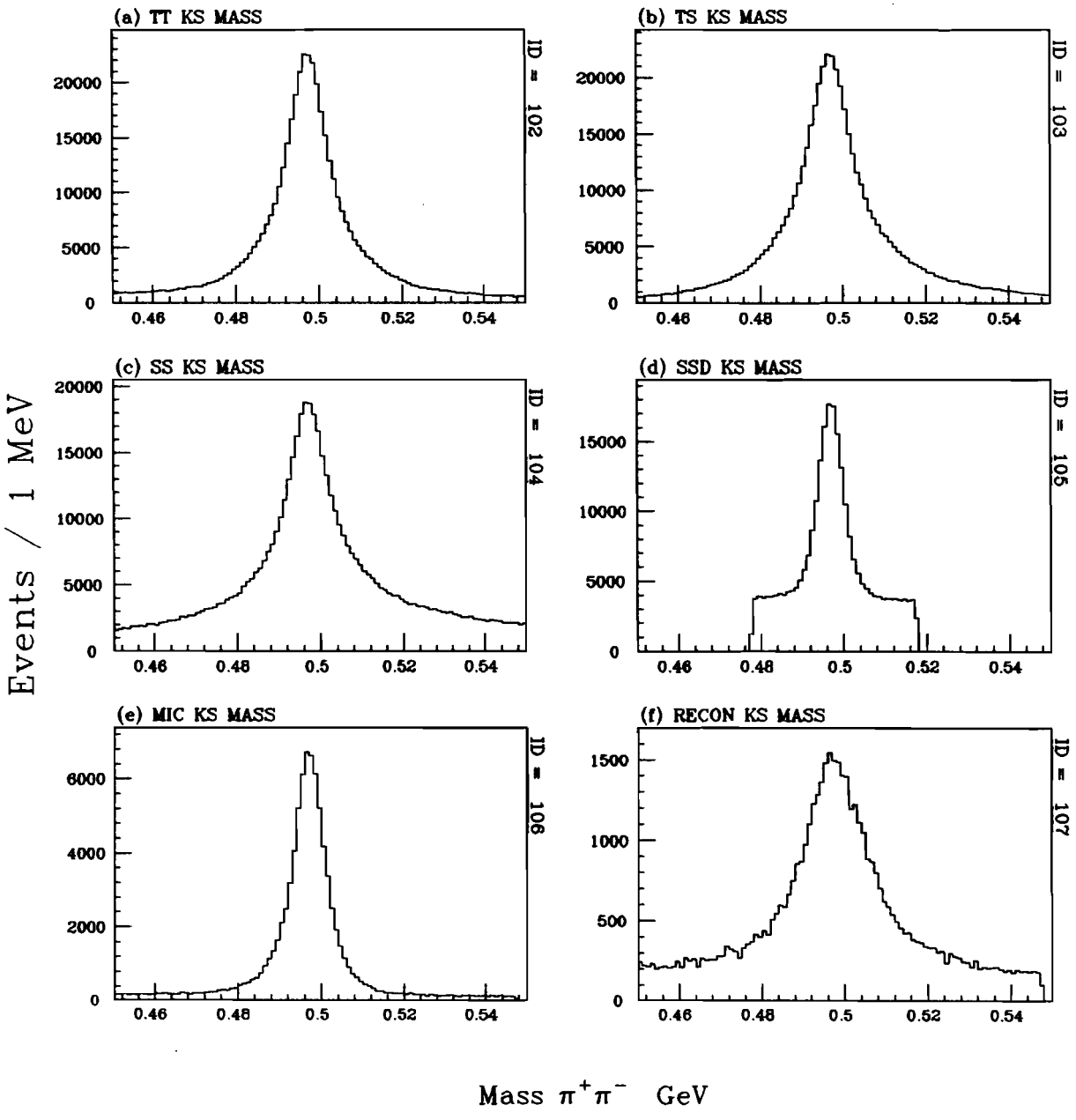

Figure 4.2. Reconstructed K_s^0 decays by topology: a) track-track; b) track-stub; c) stub-stub; d) SSD; e) MIC; f) RECON. These events were subjected to clean up cuts described in Section 4.6.1, and represent the entire data set.

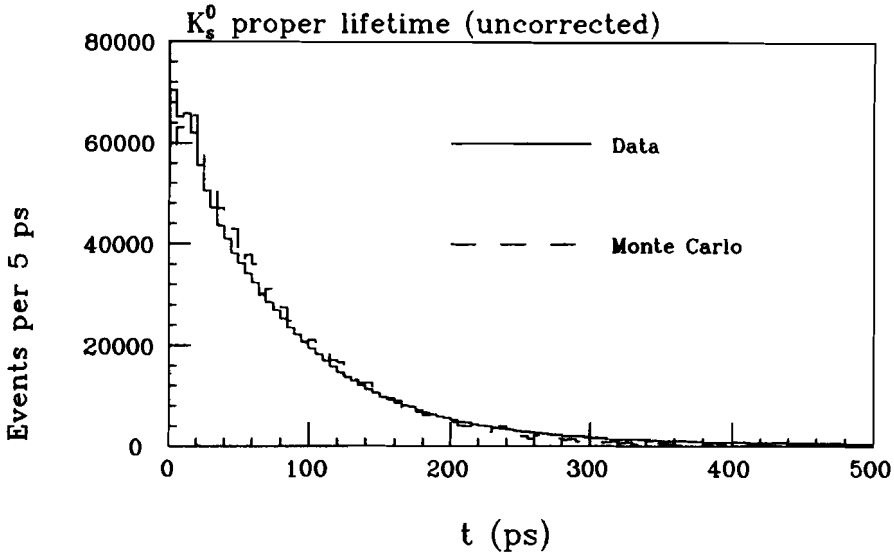

Figure 4.3. Proper lifetime distribution for reconstructed K_s^0 decays.

where the usual track equations are given by,

$$x_i = x_{oi} + (z_v - z_o)x_i^{'}$$

$$y_i = y_{oi} + (z_v - z_o)y_i^{'}.$$

The sum is carried over the indices of the two linked microstrip tracks, and the weights, ω_i, are ideally inversely proportional to the square of the extrapolated transverse errors, σ_{x_i}, given in a standard approximation in terms of the SSD track covariance matrix elements by (eg. σ_{x_i}):

$$\sigma_{x_i} = cov(x_{0i}, x_{0i}) + 2(z_v - z_0)cov(x_{0i}, x_i^{'}) + (z_v - z_0)^2 cov(x_i^{'}, x_i^{'}).$$

To avoid excessive CPU usage, the algorithm uses a fixed value of 15 μm which is

effectively the low resolution strip pitch divided by $\sqrt{12}$. An approximate error in the z-coordinate of the vee decay vertex is calculated according to

$$\sigma_{zv} = \frac{15\ \mu m}{\theta_v}$$

where θ_v is the vee opening angle. Several quantities are calculated from the fit results and are used as preliminary cutting tools for vee candidates. The first is a distance of closest approach (DCA) between the daughter tracks, evaluated at the z-plane of the vertex returned from the fit. This was required to be less than 120 μm. The second is a significance of detachment ratio, SD, defined as the normalized z-separation between the vee vertex and the primary vertex:

$$SD = \frac{z_v - z_{prim}}{\sigma_{z_v}} \tag{4.7}$$

which was required to be greater than 20. The reference primary vertex here was defined in the previous section. This large figure was required to throw out the large number of SSD track pairs from the primary vertex which can easily be formed into two-track vertices. A miss distance variable, RV, is defined by projecting the vee candidate back along the direction of its momentum vector, passing through the vee vertex, and computing the impact parameter at the primary vertex. This is used to throw out combinations which do not loosely point to the primary vertex.[2] Finally, a K_s^0 invariant mass is calculated by assigning the pion mass to each of the daughter tracks and applying a liberal cut. The cuts for potential SSD K_s^0 candidates are summarized in Table 4.1.

[2]Obviously for charm decays the K_s^0-meson should point to the secondary vertex, not the primary vertex. However, at this point in the analysis the charm decay topology has not yet been solved, and the requirement is needed to reject false combinations of tracks forming "good" vertices.

Table 4.1. SSD K_s^o candidate cuts.

variable	cut value
DCA	$< 120\ \mu m$
SD	> 20
RV	$< 1\ mm$
$M_{K_s^o}$	$0.45 < M_{\pi^+\pi^-} < 0.55\ \mathrm{GeV/c^2}$

MIC type K_s^o

Additional K_s^o candidates were recovered through use of hits left unused by the microstrip track reconstruction routine. These hits could be considered as consistent with a K_s^o decaying within the volume of the microstrip system itself, for example, downstream of the second or third stacks. This type of search was possible in part due to the low level of spurious firing of strips. Unlinked PWC tracks were used to seed the search of hits associated with K_s^o daughter pions, beginning with the most downstream stack. If such matches were found, the track parameters were recalculated using the matched triplet from the fourth stack as an additional hit. The search was then continued by extending the newly fitted track to the z plane of the third microstrip stack. All possible pairs of oppositely charged extended tracks were tested for neutral vee consistency by imposing a DCA cut of 500 μm. In some instances these candidates overlapped with the unlinked magnet region vees (discussed below). This occurred in about 5% of the events containing vees. In those cases, the extended vee was retained for further analysis, and the magnet region vee was deleted from the list of vee candidates. As an illustration of the improvement in mass resolution by using the extended vees, Fig. 4.4 shows the reconstructed K_s^o mass before and after successful extension.

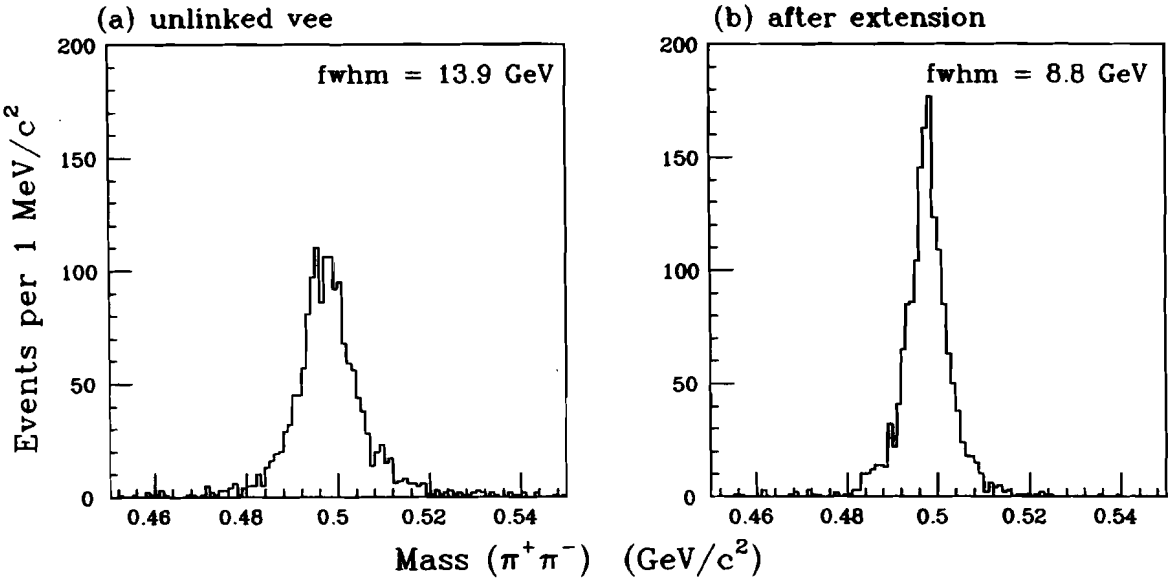

Figure 4.4. Mass resolution improvement after extension: a) unlinked TT K_s^o mass; b) TT K_s^o mass after extension to SSD hits.

4.3.2 Magnet Region K_s^o

Magnet region K_s^o comprise the largest category of vee candidates. The decay volume is occupied mainly by the first analysis magnet, extending from the first set of wire chambers, P0, to the target region. All oppositely charged pairs of track-track, track-stub, and stub-stub combinations were looped over and considered as K_s^o candidates. In each sub-class, the X-projections of the component tracks were intersected to obtain an initial Z-coordinate estimate of the vee vertex. Since this occurs most often inside the magnet, the Y-coordinate of the vertex is determined by employing a magnetic tracing algorithm using the downstream track parameters and momentum as initial input. A new Z-coordinate of the vee vertex can be determined using the two Y positions, and the procedure can be iterated until a convergence condition specified by a cut on successive shifts in the vee Z-coordinate is satisfied. Candidate combinations not meeting this condition were discarded. For combinations containing

stubs, an added constraint was that the vee point to the reference primary vertex.

The next step in the analysis was to subject the two vee candidate tracks to a fit [32] assuming the hypothesis of a neutral vee originating in the target and decaying somewhere before P0. There were nine parameters to be determined in the fit:

- X, Y, Z-coordinates of the vee decay vertex
- X, Y-slopes of the tracks at the vee decay vertex
- the momentum of each track

During each iteration, the parameter estimates were used to predict downstream parameters to be compared with those measured by the chambers and the upstream primary vertex as measured by the SSDs. The fit incorporated the full covariance matrices of the track parameters which included multiple coulomb scattering corrections. The χ^2 also included a requirement that the vee point back to the primary vertex. As will be seen in Section 4.6.1 below, the χ^2 quantity was an important variable in the final selection of events for the D^o meson analysis. Fig. 4.5a shows the fit χ^2 distribution for TS vees having two degrees of freedom.

An important feature of the fit was that it returned a predicted mass error for each event. The mass error was calculated using the vee parameter covariance matrix:

$$\sigma_M^2 = D_i < \delta V_i \delta V_j > D_j \tag{4.8}$$

where $D_i = \partial M / \partial V_i$, and the V_i correspond to the nine vee parameters. The importance can be appreciated by realizing that the correct mass determination is highly sensitive to the decay kinematics of the K_s^o (eg., the orientation of the decay plane with the magnet bend direction), and the Z-coordinate of the K_s^o vertex, which determines the amount of magnet field the K_s^o will experience. Studies [32] from K_s^o decays

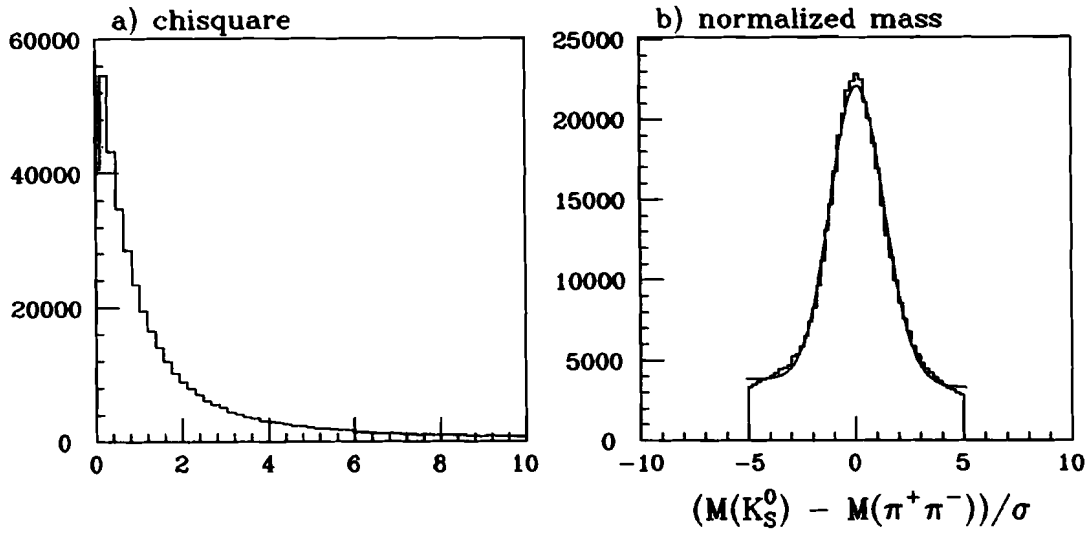

Figure 4.5. Track-stub K^o_s vee fit results: a) computed χ^2 distribution; b) normalized K^o_s mass.

in Monte Carlo as well as in real data, which compared the measured widths to predicted widths, have shown that the errors are understood reasonably well. This provides an addtional criterion on which to select clean samples of K^o_s events. In Fig. 4.5b the normalized mass difference, given by

$$(M_{\pi^+\pi^-} - M_{K^o_s})/\sigma_M \tag{4.9}$$

indicates this large spread very well accounted for. The fitted curve on the histogram is a Gaussian with a straight line for the background. The Gaussian width determined by the fit was 1.24 ± 0.03.

4.3.3 Downstream Region K^o_s

A final category of vees [33] could be recovered for those which decayed between chambers P0 and P2. These were termed "reconstruction vees" because the algo-

rithm constructed the vee candidates from chamber hits rather than reconstructed tracks. The topologies considered were three or four chamber vees with hits in P1, P2, P3, P4, or two chamber vees with hits in chambers P2 and P3. In each case only hits left over from the main tracking reconstruction algorithm were considered. The general scheme of the vee finding involved, again, pattern recognition of aligned hits in the X-projection. Forming track candidates by pairing two good X-projections, and matching with clusters of V, U, Y views using the geometrical conditions between the views. The present analysis did not utilize these vee topologies.

4.4 Particle Identification

The main source of particle identification employed by the present work was that provided by the Čerenkov analysis [34]. Charged tracks were characterized as electrons, pions, kaons, or protons on the basis of light left in each of the Čerenkov counters C1, C2, and C3. Each of these particles cause light to be emitted in the counters when they reach a certain characteristic momentum, determined by the properties of the gas used in the counter.

The first step in the analysis was to examine the cells of a given counter to determine their on/off status. The ADC pulse heights were compared to a cut value chosen to be a suitable level above pedestal, but not too large in order to avoid cutting into the single photoelectron peak. The next step was determining each counter's response to a given track. The track parameters were used to evaluate the particle's intercept at the image plane of each counter, and thus determine into which cells the Čerenkov light would be focused. For each of these cells, the anticipated light yield was calculated, taking into account the track momentum, a particle hypothesis, and the overlap of the Čerenkov light cone with the cell. If the principal cell or any of the adjacent cells were on and the yield calculation predicted light for them, the track was registered as "on" by the counter. If the cells were off while some light was

predicted, the track was registered as "off". Tracks which failed to satisfy either of these conditions were labelled "confused".

Once each of the counter responses had been determined, the particle identities with which the track could be deemed consistent were assigned. The degree to which a track could unambiguously be identified was a function of its momentum and the particle type threshold momenta of the three counters, which were given in Table 2.4. Identification flags for each counter's response were encoded by the algorithm in the following way: a four bit status word for each counter was assigned in which each bit tagged the consistency determination for each of the hypothesized particle types. These were determined by comparing the expected on/off status (based on the particle hypothesis and momentum) with the on/off status returned by the algorithm as described above. A bit set to 1 meant the counter's response was consistent with that particle identity, while a bit set to 0 meant it was inconsistent. For confused tracks all bits were set to 1. The bit assignments for the status words were made as follows:

bit 0: electron consistency

bit 1: pion consistency

bit 2: kaon consistency

bit 3: proton consistency

The individual status words for each counter were then subjected to a bit-by-bit logical "and" to form a complete response for the system. This response was loaded into a variable called ISTATP. The interpretation of this variable would be made, for example, when applying particle consistency requirements during event selection. For example, a track with ISTATP = 3 would have bits 0 and 1 set, and would thus be interpreted as being consistent with an electron or pion. An ISTATP = 4 would

have bit 2 set to one with all others zero, meaning the system's response was that of definite kaon identification. Table 4.2 lists the possible particle interpretations returned by the algorithm.

Table 4.2. Čerenkov ISTATP Codes.

ISTATP	Interpretation
0	inconsistent
1	electron
2	pion
3	electron / pion
4	kaon
7	electron / pion / kaon
8	proton
12	kaon / proton
14	pion / kaon / proton
15	electron / pion / kaon / proton

The efficiency of the Čerenkov system was studied in data using the decays:

$$\phi \rightarrow K^+K^- \text{ and } K^o_s \rightarrow \pi^+\pi^-.$$

A ϕ sample was useful as a measure of the kaon consistent efficiency [35]: events were selected using kinematical cuts and by requiring one of the kaons to be "kaon definite", or ISTATP = 4. The identification efficiency for the opposite kaon was determined by binning the ISTATP codes of events in the ϕ signal region as well as two sideband regions away from the signal. The background ISTATP codes were subtracted from the signal bins to get the number of kaons satisfying ISTATP = 4

or 8. The overall efficiency for identifying kaons after requiring they are detected as "kaon definite" (ISTATP = 4) or "kaon/proton ambiguous" (ISTATP = 14) was 78%.

The efficiency for pion consistency using K_s^o decays was studied by fitting the $M_{\pi^+\pi^-}$ invariant mass distributions to determine the signal and background contributions. In Fig. 4.6 the normalized mass distributions for K_s^o decays into the magnet region topolgies is plotted. In Fig. 4.6a there are no Čerenkov requirements while in Fig. 4.6b the pions were required to be *inconsistent* with either the kaon or proton hypothesis, i.e., ISTATP $\neq$ 4, 8, 12. A pion satisfying this identification requirement was termed "not heavy". The ratio of the fitted Gaussian yields gives an overall efficiency of $\simeq$ 95% for this dual-identification requirement.

4.5 *Monte Carlo Simulations*

Monte Carlo simulations were used for a variety of reasons, an important one being the calculation of the spectrometer acceptance for the D^o decay modes studied in this analysis. The Monte Carlo program used in this analysis was developed and extensively tested at the University of Illinois [35][36], and consisted of two packages, termed GENERIC and ROGUE, for the purpose of event generation and spectrometer simulation, respectively. Thus, a two-step process was followed in all Monte Carlo studies, which is briefly discussed below.

4.5.1 Event Generation

First, hypothetical charm events were generated according to a photon-gluon fusion cross section model to produce charm/anti-charm quark pairs in which one member subsequently hadronized into a D^o meson while the other was allowed to hadronize other D mesons. The D^o was forced to decay to the final state of interest, eg. $D^o \rightarrow K_s^o\pi^+\pi^-$, with the option of specifying the particular decay matrix element.

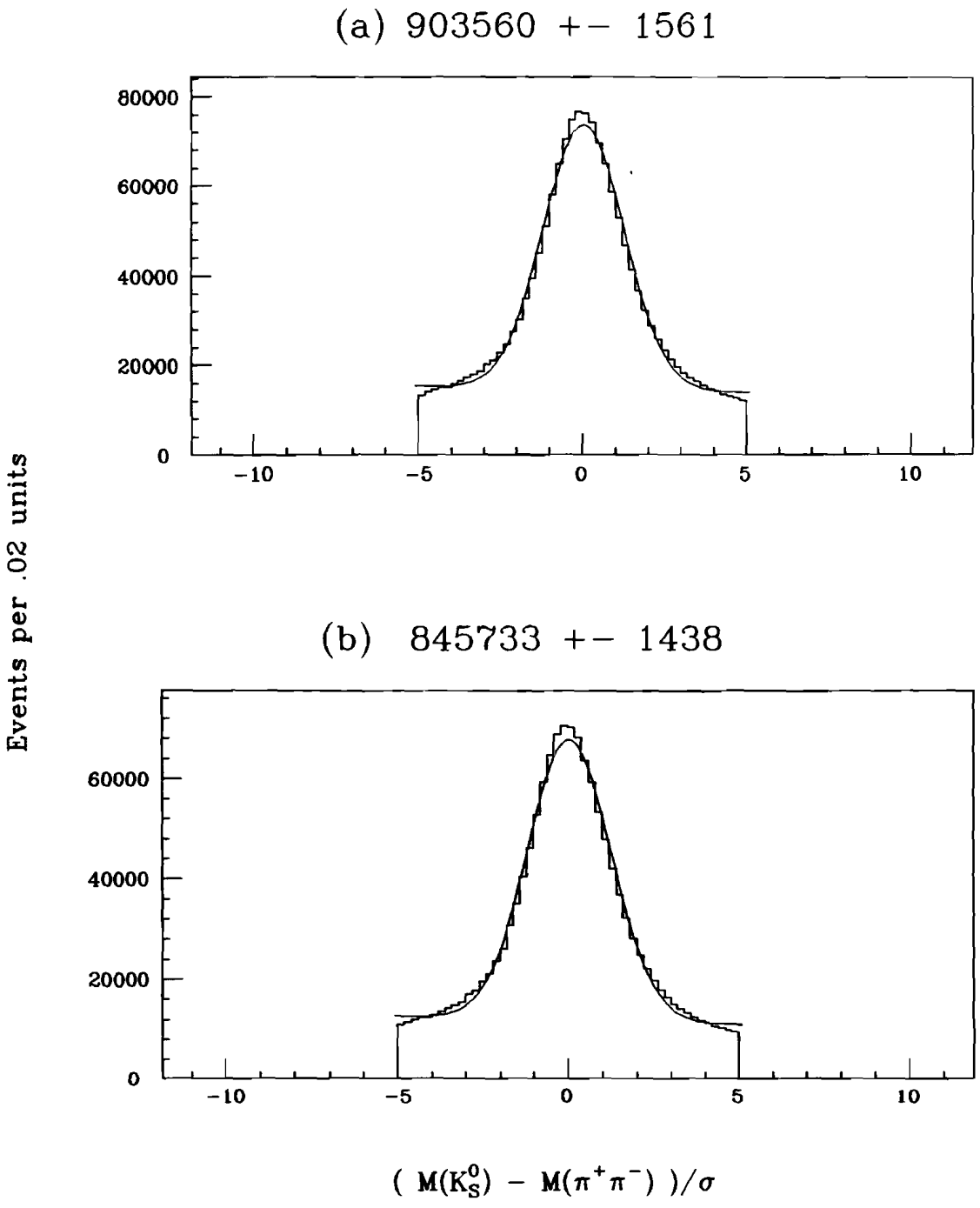

Figure 4.6. Čerenkov ID efficiency for pions: a) the decay $K_s^o \rightarrow \pi^+\pi^-$ with no Čerenkov ID; b) the same, only requiring ISTATP $\neq$ 4, 8, 12 for both tracks.

The opposing particle was allowed to decay to modes weighted according current Particle Data Group branching ratios [40]. In cases where a resonant final state was of interest, eg. the decay $D^o \rightarrow K^o_s\phi$, the decay matrix element was specified to be consistent with angular momentum conservation for a pseudoscalar $\rightarrow$ pseudoscalar + vector decay. In the generation process, the Wideband photon beam was simulated using a parameterized form of the measured electron beam momentum spectrum, and a shower model was used for the bremsstrahlung process in the thick lead radiator. The latter was important for the correct simulation of "multi-bremsstrahlung" events which were embedded in the real data. Also, effects owing to various targeting conditions were included, such as which target was used and the locations of the nominal beam spot centroid (which was known to undergo small shifts during the course of the entire running period). In most studies, generated events for each of the different configuration periods were weighted by the recorded luminosity for that configuration. In this way, "mini-E687 runs" could be generated so as to automatically average over these complications.

4.5.2 Apparatus Simulation

The next step was the actual simulation of the spectrometer responses to the fake charm events. Charged particles were propagated according to their generated charge and momentum, as well as their "birth" (and sometimes "death") coordinates. The particles were traced through the magnets using the measured field moments, and all materials introduced by the spectrometer were properly simulated in terms of their interaction and radiation lengths. Thus, effects due to MCS were simulated, as were run-dependent PWC chamber inefficiencies, spurious noise simulations, hadron calorimeter efficiency, and in-flight decays of charged pions and kaons. Simulated ADC pulse heights, trigger counter responses, etc., were packed into buffer arrays in the same fashion as the data, and fake data tapes were produced to emulate the raw

data tapes.

Typically Monte Carlo data tapes were analyzed in much the same way as the real data with regard to running of the reconstruction programs. Using these Monte Carlo tapes, the integrated effects such as geometrical acceptance, multiple scattering, and detector as well as algorithm inefficiencies could be studied for particular charm decay topologies and modelled to correct the data. This is especially important in the calculation of relative branching ratios.

4.6 The Data Skims

As mentioned, the number of reconstructed PASS1 output tapes numbered about 2400, which is a collection quite unwieldy for analysis purposes. In order to reduce the data set to manageable event samples, several editing schemes (or "skims") were devised in which sub-samples of events containing fewer background events were created while saving as many of the charm events as possible. Some of these methods were decay topology dependent, focusing on one or a few specific final states. Others were completely general schemes in which background events could be rejected by cutting on "charm-like" indicators such as decay length separations. The skim strategy keyed on in this work was a simple K_s^o meson selection.

The package of skimming routines was executed on the Fermilab Amdahl computers from August to December of 1989. The process was actually carried out in two stages. The first, termed "Skim1", contained the following set of skims:

1. Two-"heavy" particles: events with KK, Kp, pp particles (as identified through Čerenkov analysis) were selected.

2. Global vertex χ^2: topology independent lifetime skim based on the selection of events which exhibited a low probability of having all tracks emerge from a common vertex.

3. D-Meson skim: various Cabibbo-favored and suppressed D-meson decays with K and π daughters were selected based on invariant mass restrictions, the correct charge-strangeness correlations for charm decays, and mild vertex requirements.

4. Constrained vertex, and "stand alone"-vertex based skims.

5. Neutral vee skim: events containing K_s^o and Λ^o decay candidates were selected.

As the data for these skims became available, bugs were uncovered in some analysis codes and others were deemed unsatisfactory (for various reasons, such as one which skimmed too many events). In addition, certain runs from the PASS1 output were re-processed after refinements were made to the magnetic geometry parameters. Therefore, Skim1 was halted and replaced by a new, but reduced package of routines which was termed "Skim1.5".

The K_s^o selection algorithm ran during both Skim1 and Skim1.5 stages, and thus spanned the complete data taking run. The selected K_s^o data consisted in about 2.5×10^6 events and the output was written to approximately 250 data tapes. To further aid in the analysis, the data were highly compressed into a DST format containing only the necessary information for all subsequent physics analyses. The data compression reduced the amount of storage required by over a factor of 10, and so the final K_s^o data set was contained on 20 tapes. Even at later stages, for instance during the Dalitz plot analysis, fewer variables could be stored in disk files for rapid access from computer analysis codes.

4.6.1 K_s^o Data Selection Criteria

The analysis of the decay modes $D^o \rightarrow K_s^o\pi^+\pi^-$ and $D^o \rightarrow K_s^oK^+K^-$ was performed on events selected through use of an algorithm which considered all of the vee parameters describing the candidate. The routine employed very liberal cuts on the K_s^o candidates

while selecting only a small fraction of the unbiased PASS1 output events. The events were subjected to the following cuts according to decay topology:

1. SSD vees:

   (a) An invariant mass cut of $0.477 < M_{\pi^+\pi^-} < 0.517$ GeV.

   (b) Both tracks had to be attached to the same SSD vertex

   –or–

   satisfy the "point back" condition: RV $< 150\ \mu m$.

2. MIC vees: An invariant mass cut of $0.450 < M_{\pi^+\pi^-} < 0.550$ GeV.

3. Magnet Region vees:

   (a) A normalized mass cut of $\Delta M/\sigma_M < 5$.

   (b) χ^2 of the fit to the neutral vee hypothesis of < 50.

4. RECON vees: An invariant mass cut of $0.450 < M_{\pi^+\pi^-} < 0.550$ GeV.

The selection algorithm was studied in Monte Carlo and found to be $82 \pm 2\%$ efficient in keeping $D^o \rightarrow K^o_s\pi^+\pi^-$ events in which the K^o_s vee candidates were reconstructed, and less than 5% of the total PASS1 reconstructed events were selected by these requirements.

4.6.2 K^o_s Yield Study

The uniformity of the K^o_s yield over the data sample was studied by dividing the run into certain experimental running periods and counting the number of K^o_s mesons detected, normalized to the recorded luminosity for the run period. Divisions between these periods were identified by dates in which significant changes in the running conditions occurred. These changes corresponded to events such as the installation

of a new target, or to periods when the trigger efficiency might have been low due to instabilities in the hadron calorimeter. The luminosity was computed by summing the scaled beam gamma monitor (BGM) counts for each of the runs and correcting for targeting effects, such as the drift of the beam centroid with respect to the experimental target [37]. The resulting K_s^o yields, scaled by the corrected luminosity measurement, are plotted in Fig. 4.7 for both the total K_s^o yield and by vee topology. There obviously were significant fluctuations in the normalized yield over time while the fractions into each topology tended to remain constant. The precise origin of these shifts in normalized yields was not understood.

4.6.3 Tighter K_s^o Selection

At later points in the analysis, it became desirable to place more restrictive cuts on the K_s^o candidates. This was done at the DST-level through use of a routine which imposed the following extra set of cuts:

1. SSD: Both tracks had to be attached to the same SSD vertex, and this vertex was required have no other tracks attached to it.

2. MIC: An invariant mass cut $0.480 < M_{\pi^+\pi^-} < 0.520$ GeV.

3. Magnet region:

   (a) A normalized mass cut of $\Delta M/\sigma_M < 2.5$.

   (b) A $\chi^2 < 3$ requirement for the vee hypothesis fit.

Application of these cuts reduced the number of vee candidates by 23%, while the efficiency for retaining the decays $D^o \rightarrow K_s^o\pi^+\pi^-$ was found from a Monte Carlo study to to be 84 $\pm$ 2%. This might not appear to be such an effective restriction for background reduction if the background and signal are discarded at approximately

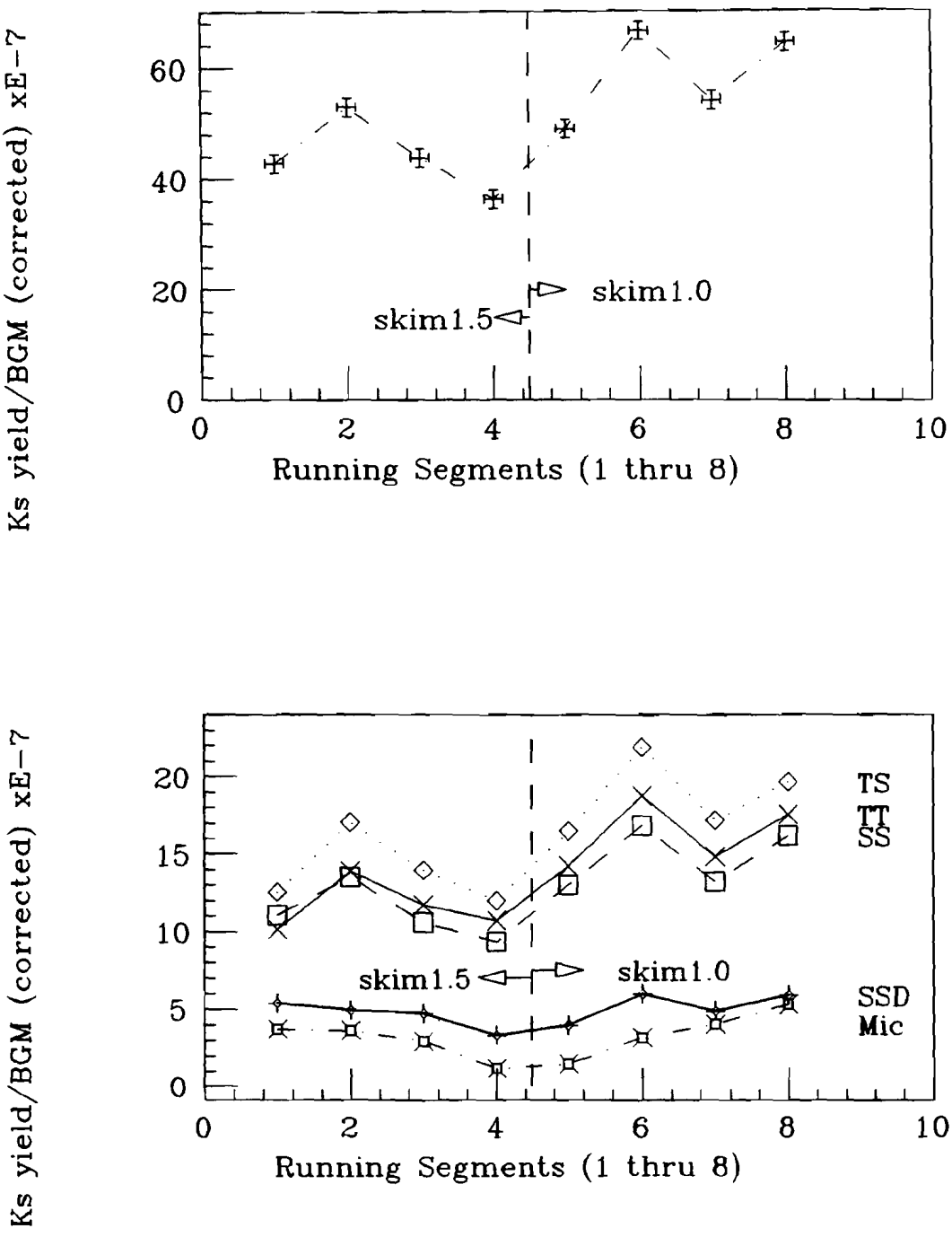

Figure 4.7. Luminosity normalized K_s^o yields: a) all topologies; b) by topology fraction.

equal rates. However, the signal to background ratio for events in the K_s^o peak region is improved significantly for all categories, as shown in the invariant mass histograms of Fig. 4.8.

The SSD vertex attachment restriction on the SSD vee candidates is illustrated in Fig. 4.9 for vees occuring in real data. Recall that these vertices were determined by the "stand alone" method of Section 4.2, and thus were found without information regarding the K_s^o decay. In Fig. 4.9a the invariant mass is plotted for all SSD vee candidates before any background reducing cuts are applied. In Fig. 4.9b the invariant mass for SSD vee candidates with each daughter track attached to the same vertex, which indicates an efficiency of $\simeq$ 75%. However, the background can be further reduced without much greater loss in efficiency by requiring the multiplicity of the vertex to be exactly two, so that candidates which form good vertices with other tracks are removed. These turn out to be mostly background events, as is indicated in Fig. 4.9c. Thus, the effect of requiring the vertex multiplicity to be exactly two is equivalent to a topological isolation cut on the vertex candidates. This study indicates this added restriction is quite efficient (95%) and results in an improvement in the signal to background ratio of $3 \rightarrow 20$. Figs. 4.10a-b illustrate that the signal discarded by these restrictions is roughly divided into two categories: vees in which only one track was attached to a fitted vertex, and vees in which neither track was attached to a found SSD vertex. Fig. 4.10c shows that the "stand alone" technique virtually never assigns the K_s^o daughter tracks to two different vertices.

4.7 D^o Event Selection

The tapes containing the selected K_s^o events were analyzed to search for the D^o events decaying according to $D^o \rightarrow K_s^o\pi^+\pi^-$ and $D^o \rightarrow K_s^oK^+K^-$. All possible combinations of oppositely charged PWC tracks were grouped with the K_s^o candidates passing the tighter requirements outlined in Section 4.6.3 to form the initial sample of candidates.

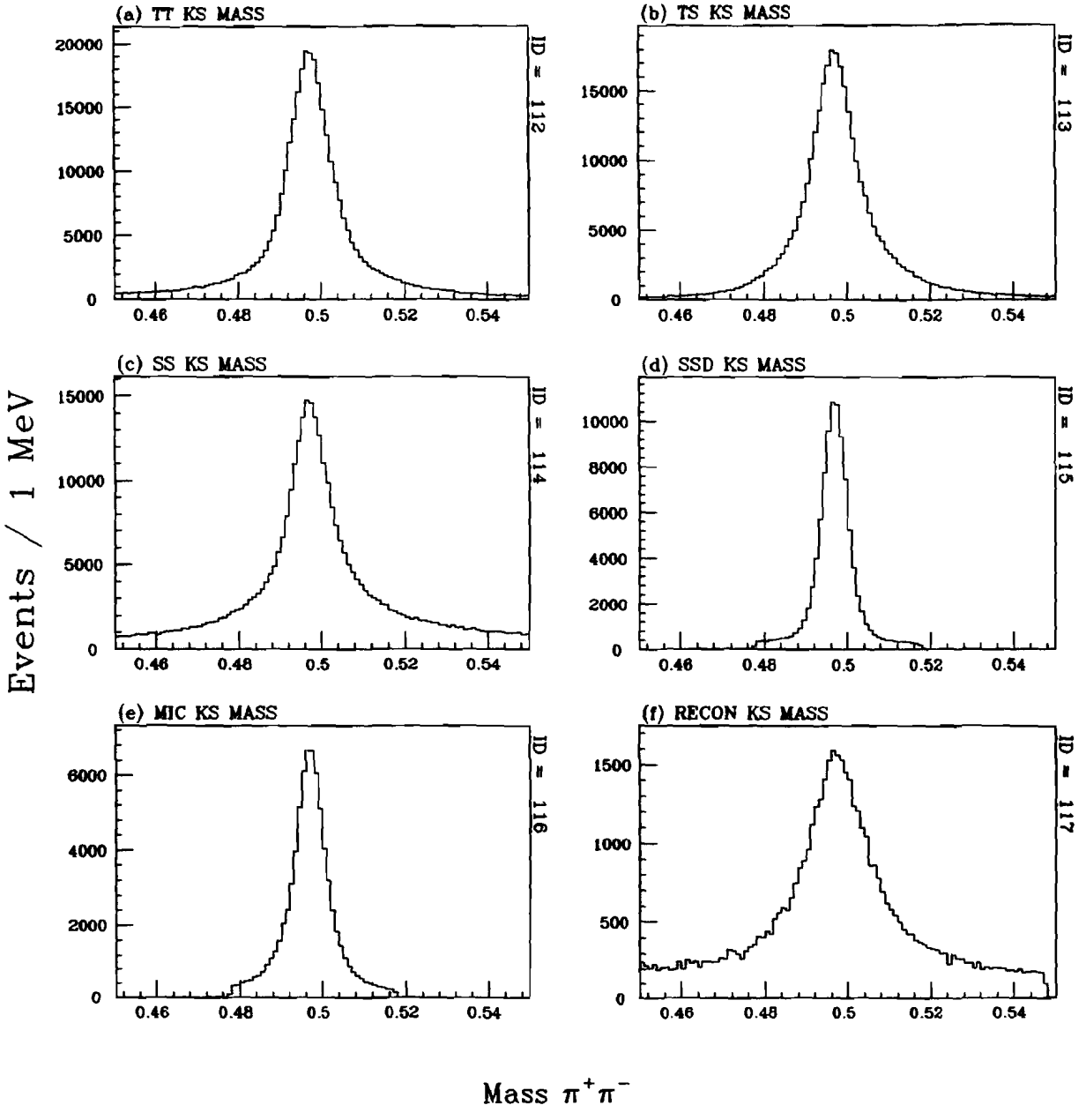

Figure 4.8. K_s^o decays with tighter restrictions: a) track-track; b) track-stub; c) stub-stub; d) SSD; e) MIC; f) RECON. These events were subjected to clean up cuts described in Section 4.6.3, and represent the entire data set.

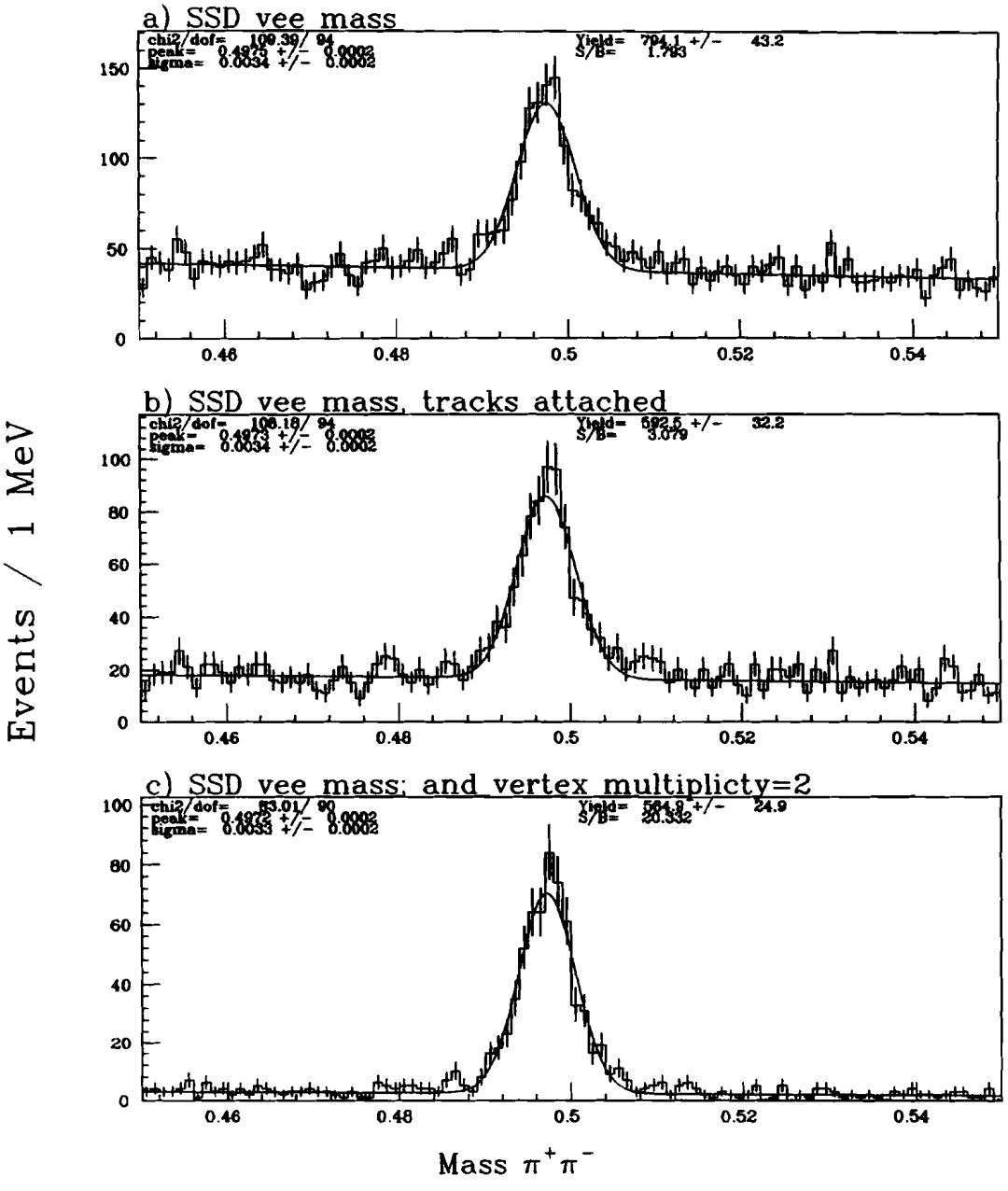

Figure 4.9. SSD vee vertex attachment: a) un-cut K^0_s invariant mass; b) both tracks attached to same SSD vertex; c) and, require vertex multiplicity to be 2 .

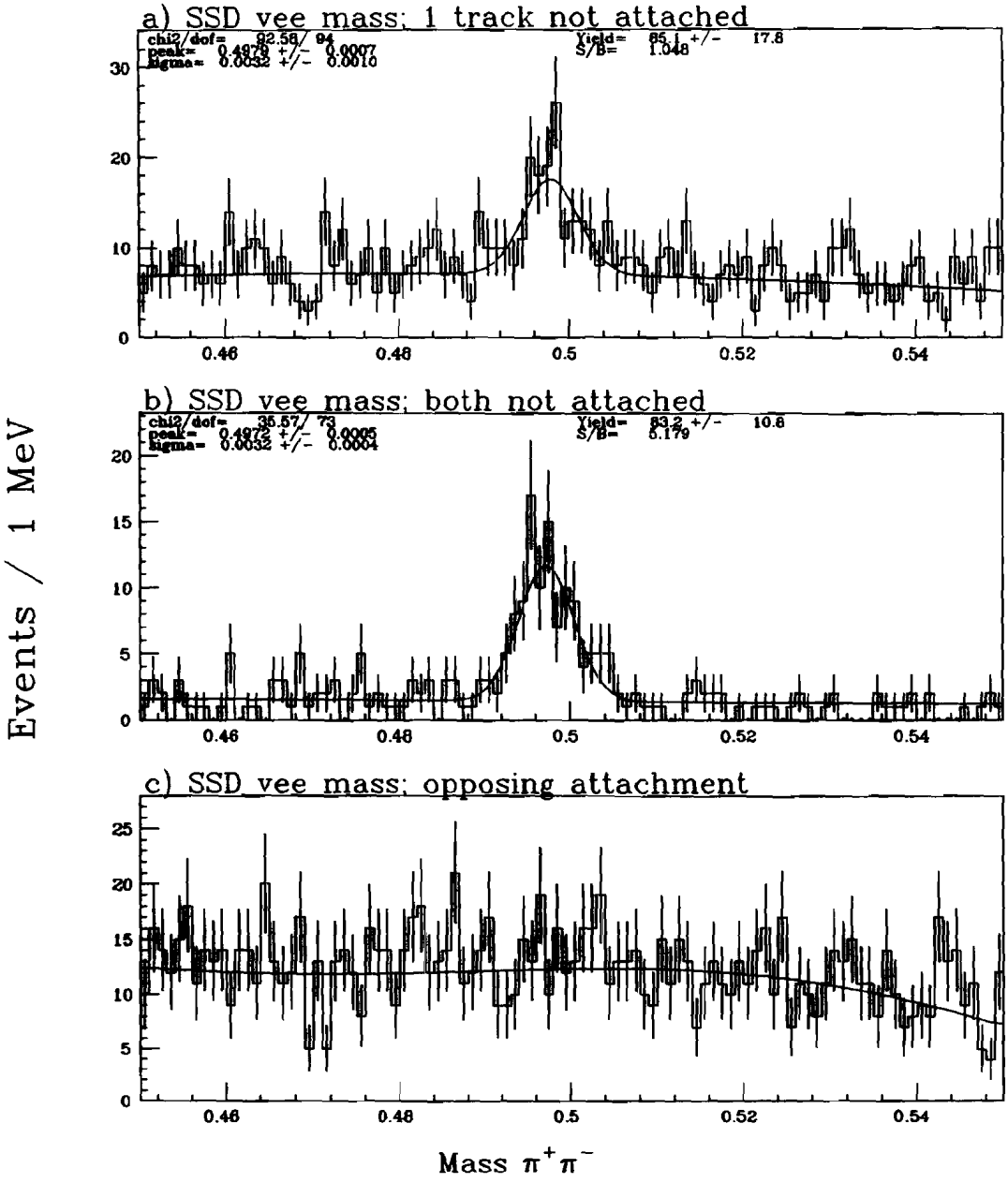

Figure 4.10. SSD K^o_s unattachment: a) one track unassigned; b) both tracks not attached to any SSD vertex; c) both tracks attached to different SSD vertices.

In order that a vertex analysis could be performed at a later stage, these PWC tracks were required to be linked to SSD tracks. A three body mass calculation was performed using the momentum vectors of the two selected tracks, the K_s^o momentum vector, and the appropriate mass assignments. The mass assigned to the "K_s^o track" was the nominal value of 497.67 MeV rather than that which was returned from the vee fit. Combinations which fell within the mass range of 1.6 GeV to 2.1 GeV were advanced to the vertex analysis, which is discussed next.

4.7.1 Candidate-Driven Vertexing

A very useful background reduction tool in fixed-target charm production experiments is the decay length (or equivalently, the proper time) separation of the secondary decay vertex from which the charm daughters emerge, from the production, or primary vertex. Owing to the relatively strong Lorentz boost the D-mesons experience from their rest frame to the lab frame, their short mean lifetimes (of order one picosecond) span decay lengths of order millimeters. These separations are well within the resolvability of the microstrip detectors. However, one is faced with deciding which tracks should be selected for the D-candidate and which should be used for the primary vertex from which the separation is measured.

One solution to this problem is to exploit the fact that the charm candidate should point to the primary vertex. Thus, a "candidate-driven" vertexing algorithm [38] was employed which uses the information from the set of tracks comprising the D-candidate (chosen on the basis of kinematics, charge-strangeness correlation for Cabbibo-allowed decays, and/or particle identification) to form a new track, i.e. a "D-track". Such a track would be consistent with emerging from the primary vertex. Thus, the very interesting utility of the D-track is that it can be used to "seed" the selection of tracks consistent with forming the primary vertex. The algorithm proceeds in the following steps. First, the transverse track errors extrapolated to

the center of the target are computed at the beginning of the event. These errors are specified as full covariance matrices which account for the MCS in both the spectrometer and target. A special consideration is made for the K_s^o-track since in most cases microstrip tracking information is not present: the transverse errors are set to arbitrarily large values so that they do not contribute to the fit, and thus the vertex minimization is dominated by the two microstrip tracks. Microstrip tracks not belonging to the D-track are considered as primary vertex candidate tracks. Each of these tracks is combined with the D-track to form a 2-track vertex. Those tracks which when fitted with the D-track result in poor χ^2 values are discarded. The remaining set are grouped into all possible 2-track combinations and combined with the D-track to form 3-track vertices. The one which has the best χ^2 is selected, and additional attempts are made to add more tracks while returning an acceptable χ^2. In this work, the primary vertex was required to have at least two tracks in addition to the D-track. After the best set of tracks was chosen, the D-track was removed from the primary vertex track list, and the remaining group refit.

The results of the fit are the D-meson and primary vertex positions (as well as covariance matrices), a fitted decay length L and its error σ_L, as well as the fit χ^2 values for each of the quantities. The significance of detachment L/σ_L behaves differently for signal and background events. Nearly all of the background events consist of tracks emerging from the primary vertex, and thus the expected L/σ_L distribution should reflect the finite resolution of the microstrips. The distribution for the D^o signal, on the other hand, should reflect not only the finite position resolution but also the proper time distribution of the D^o, and thus follow an exponential decay law. Thus, cutting on successively larger values of this significance of detachment should favor keeping the signal events at the expense of the background. As will be seen below, this indeed is the case.

The efficiency of the algorithm for finding primary vertices was tested on real

data [38] by using a D*-meson event sample in which a signal could be observed on a kinematical basis only, thus avoiding use of any vertex cuts. The two decay topologies studied were $D^{*\pm} \rightarrow (K^{\mp}\pi^{\pm})\pi^{\pm}, (K^{\mp}\pi^{\pm}\pi^{\pm}\pi^{\mp})\pi^{\pm}$. The efficiency of the algorithm in successfully finding a primary vertex (without decay length cuts) for the two modes was 92% and 85%, respectively. If, however, the D-candidate contains a K_s^o-track, one would expect the efficiency to be degraded somewhat due to the poorer slope information provided by the K_s^o-tracks. Unfortunately, signals for charm states involving K_s^o-tracks could not be observed without the use of vertex cuts.

One estimate of the efficiency for the $D^o \rightarrow K_s^o\pi^+\pi^-$ decay is to compare the Monte Carlo results for the D* meson modes above to Monte Carlo results for the $K_s^o\pi^+\pi^-$ mode. The Monte Carlo efficiencies obtained for each of the modes are listed in Table 4.3, in which the $K_s^o\pi^+\pi^-$ algorithm efficiency for finding a primary vertex is at least 5% lower than that with the all charged track modes. The difference in efficiencies between real data and Monte Carlo for the all charged-track modes indicate that the efficiency of finding the primary vertex for the $D^o \rightarrow K_s^o\pi^+\pi^-$ decay mode in real data may well be 6 to 10% lower than the value in Table 4.3. Regardless, this result can be used to set a level of systematic uncertainty associated with correcting event yields for the primary vertex selection.

Table 4.3. Candidate-vertex algorithm efficiency. The efficiencies (from a Monte Carlo study) are for finding the primary vertex.

Mode	Efficiency (Monte Carlo)[38]
$D^{*\pm} \rightarrow (K^{\mp}\pi^{\pm})\pi^{\pm}$	.956
$D^{*\pm} \rightarrow (K^{\mp}\pi^{\pm}\pi^{\pm}\pi^{\mp})\pi^{\pm}$.	.970
$D^o \rightarrow K_s^o\pi^+\pi^-$	.890

4.7.2 *The Decay $D^o \rightarrow K^o_s\pi^+\pi^-$*

The vertexing scheme discussed above was essential in finding the $D^o \rightarrow K^o_s\pi^+\pi^-$ decays. From the sample of 1.6×10^6 events in which the K^o_s candidates passed the tighter selection requirements, approximately 1.3×10^6 $K^o_s\pi^+\pi^-$ mass combinations between 1.6 GeV and 2.1 GeV are considered for further vertex cuts. In Fig. 4.11 the steps in background reduction are illustrated. In Fig. 4.11a the combinations in which a primary vertex was found, and the secondary decay vertex was downstream of the primary vertex by at least three standard deviations are plotted. In Fig. 4.11b the same distribution is plotted after requiring the following extra cuts: 1. confidence levels of greater than 2% for each of the vertex fits, as well as the decay length fit; 2. that the primary vertex have at least two tracks (excluding the D-candidate track); 3. that the combinations have a momentum in the range $45 < P(D^o) < 160$ GeV/c. This resulted in a background reduction of a factor of 10. In Fig. 4.11c the secondary is required to be more than five standard deviations downstream of the primary vertex. Similarly, Figs. 4.12a-c show the effect of background reduction in increasing steps in L/σ_L . In each step in L/σ_L the background is seen to decrease at a faster rate that the signal. In terms of physics analysis of the signal, the tradeoff between high signal-to-background ratio and adequate event statistics must be judged carefully. Fig 4.13a illustrates the uncorrected signal yield in successive steps in L/σ_L while Fig 4.13b shows the variation of signal to noise ratio. For the $K^o_s\pi^+\pi^-$ mode, the event sample chosen for further analysis was selected with the following cuts:

1. $L/\sigma_L > 10.0$
2. the confidence level was greater than 2% for each of the primary and secondary vertex fits, as well as the decay length fit.

3. at least two tracks were included in the primary vertex (in addition to the D-candidate track).

4. no Čerenkov particle identification requirements were imposed on any of the daughter tracks.

5. The D-candidate momentum was required to be in the range $45 < P(\mathrm{D}^o) < 160$ GeV/c. (This is discussed below).

4.7.3 *The Decay* $D^{*\pm} \rightarrow (K^o_s\pi^+\pi^-)\pi^\pm$

Decays resulting from the decay sequence $\mathrm{D}^{*\pm} \rightarrow (\mathrm{K}^o_s\pi^+\pi^-)\pi^\pm$ were isolated by using the D^*–D^o mass difference constraint:

$$143 \ \mathrm{MeV/c^2} < \mathrm{M}_{(\mathrm{K}^o_s\pi^+\pi^-)\pi^\pm} - \mathrm{M}_{\mathrm{K}^o_s\pi^+\pi^-} < 148 \ \mathrm{MeV/c^2} \qquad (4.10)$$

which is approximately ± 2.5 MeV/c^2 about the known mass difference [40] of 145.45 MeV/c^2. After $\mathrm{D}^o \rightarrow \mathrm{K}^o_s\pi^+\pi^-$ candidate events were isolated using the background reduction requirements outlined above, the remaining tracks in the event were added to the D^o candidate combinations, and the computed invariant mass was tested against Eqn. 4.10. In Fig. 4.14 the resulting D^*-tagged candidates are plotted in steps of L/σ_L . These events were useful for the Dalitz plot analysis as a consistency check for the analysis of the inclusive decays due to their overall better signal-to-background ratio.

4.7.4 *The Decay* $D^o \rightarrow K^o_s K^+ K^-$

For the $\mathrm{K}^o_s\mathrm{K}^+\mathrm{K}^-$ mode, the Čerenkov identification plays a much more crucial role, resulting in a reduction factor of 50 for the $L/\sigma_L > 3$ sample. The evolution of the

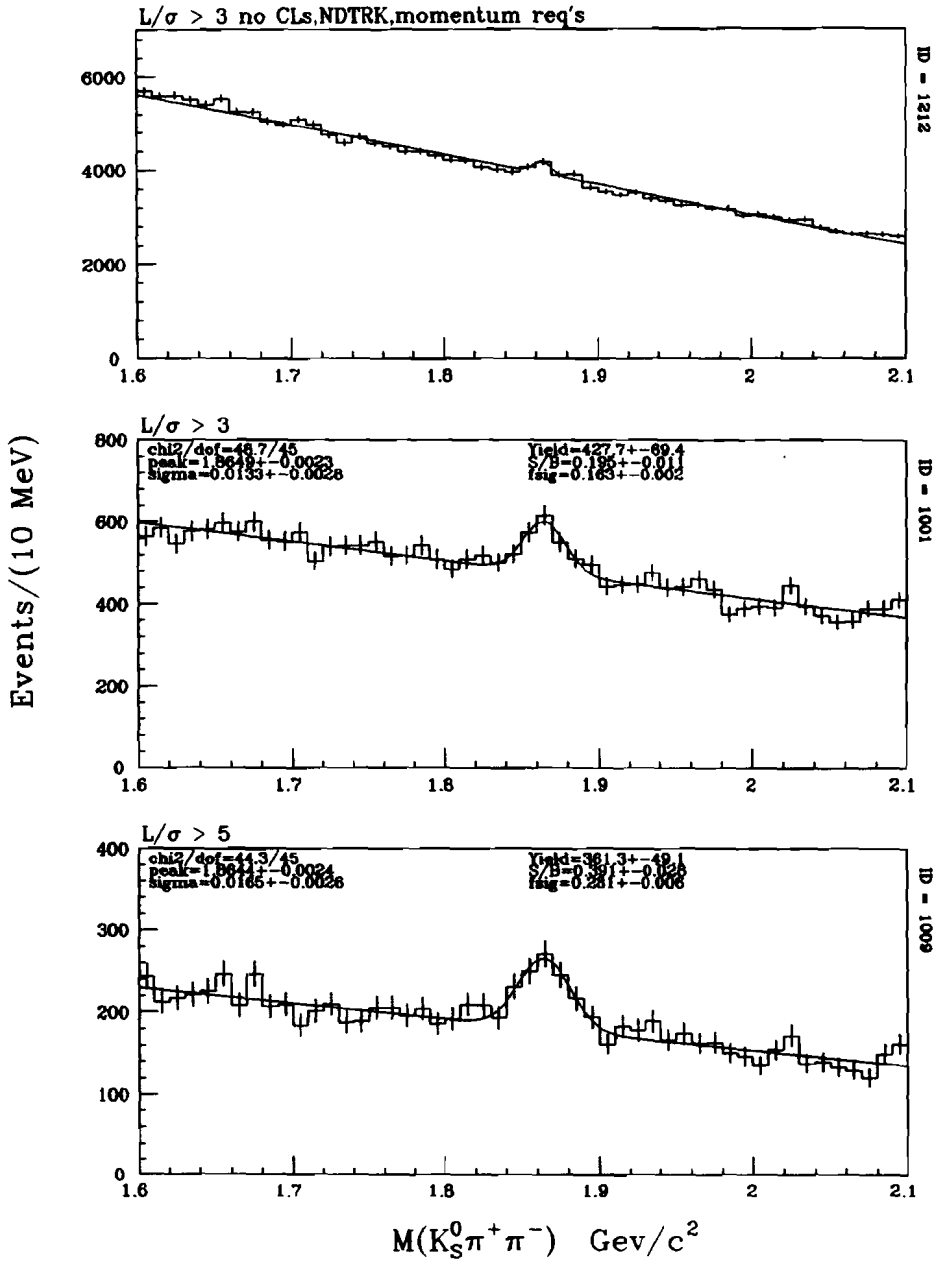

Figure 4.11. Background reduction for $D^o \rightarrow K^o_s \pi^+ \pi^-$.

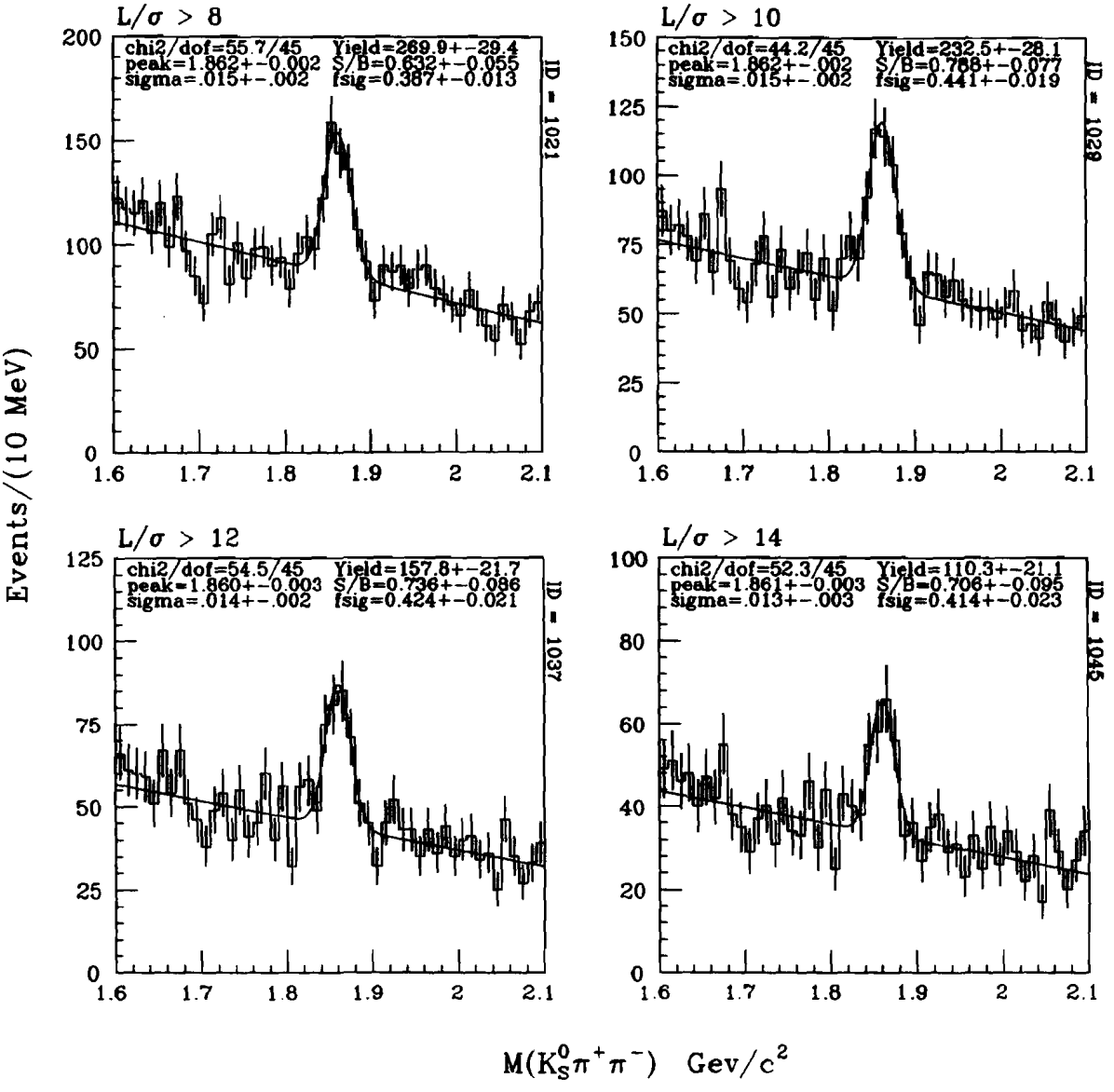

Figure 4.12. Further background reduction for $D^o \rightarrow K^o_s\pi^+\pi^-$.

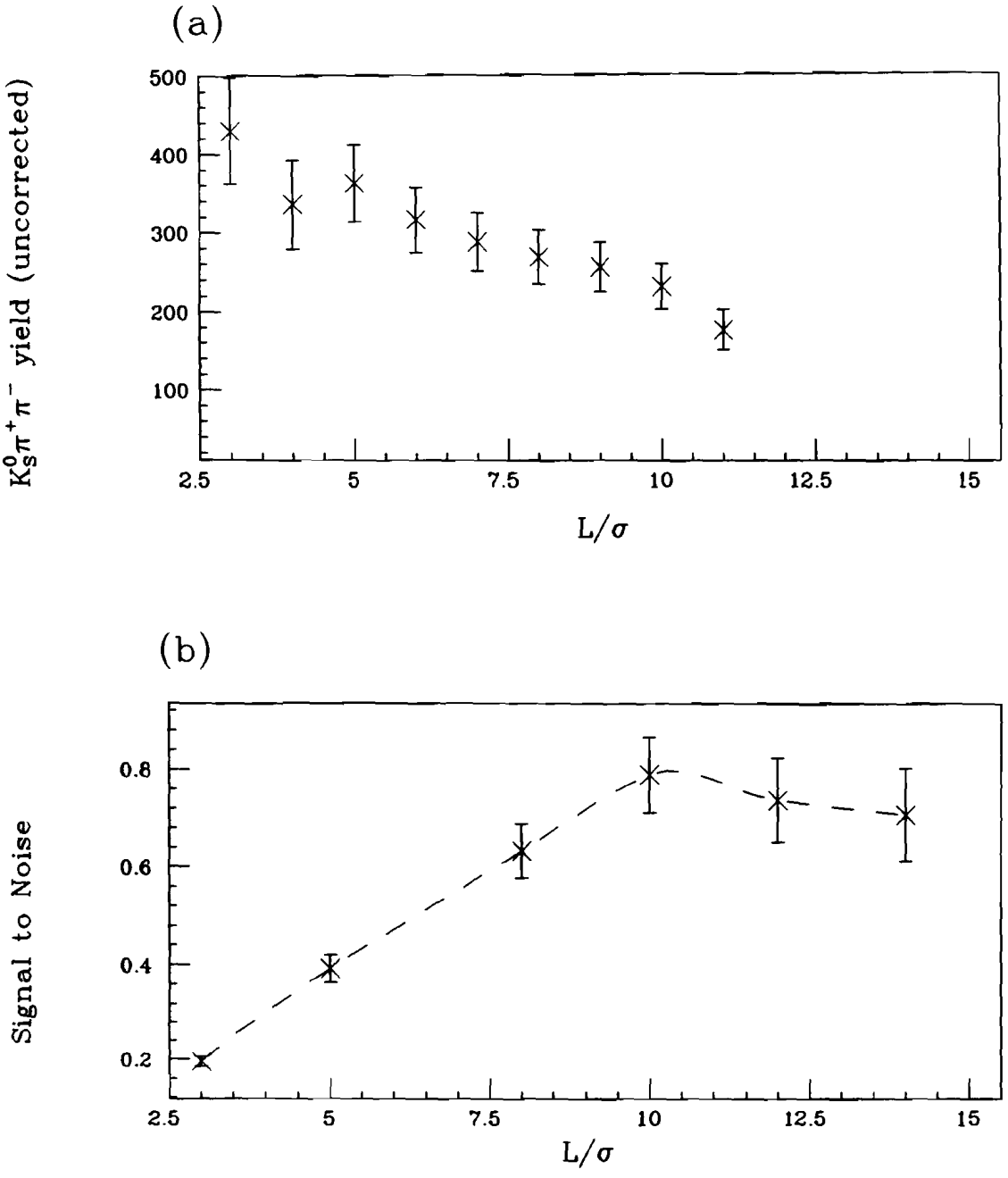

Figure 4.13. $K^0_s\pi^+\pi^-$ Event yield and signal to noise: a) yield of events vs. L/σ_L ; b) signal-to-noise ratio vs. L/σ_L .

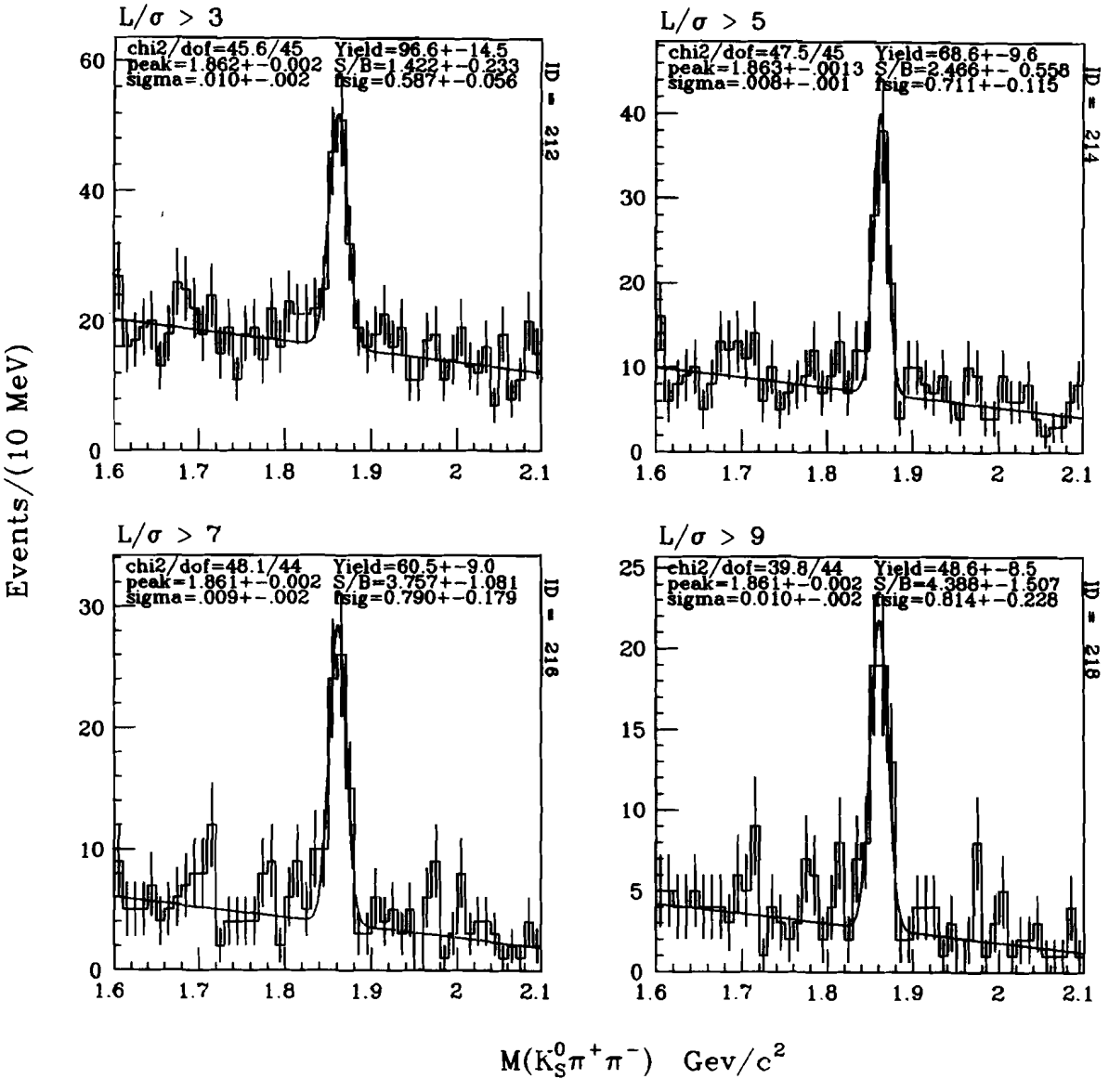

Figure 4.14. $D^{*\pm} \rightarrow (K^0_S \pi^+ \pi^-)\pi^\pm$ candidates vs. L/σ_L .

signal under increasing L/σ_L cuts is shown in Fig. 4.15. For the $K^o_s K^+ K^-$ mode, the signal retained for further analysis had the following cuts applied:

1. $L/\sigma_L > 3.0$
2. the confidence level was greater than 5% for both the secondary vertex and decay length fits, and greater than 2% for the primary vertex fit.
3. at least two tracks were included in the primary vertex (in addtion to the D-candidate track).
4. each kaon was required to be Čerenkov identified with ISTATP codes of 4, 12, or 7 (if $P_{K^\pm} > 60$ GeV/c).
5. The D-candidate momentum was required to be in the range $45 < P(D^o) < 160$ GeV/c.

The Čerenkov identification condition of ISTATP = 7 (if $P_{K^\pm} > 60$ GeV/c) allows identification kaons which have momentum greater than the kaon threshold of C3. The momentum restriction $45 < P(D^o) < 160$ GeV/c ensured that candidates have a momentum in the region where the spectrometer acceptance was good and well described by an acceptance function, which will be discussed in more detail in the Chapter 6. A summary of selected signal parameters is given in Table 4.4.

Table 4.4. Selected D^o signal parameters

parameter	$D^o \to K^o_s \pi^+ \pi^- (L/\sigma_L > 10)$	$D^o \to K^o_s K^+ K^- (L/\sigma_L > 3)$
Yield	232 ± 28	39 ± 8
Mass	1862 ± 2 MeV/c^2	1867 ± 2 MeV/c^2
Width	15 ± 2 MeV/c^2	7 ± 2 MeV/c^2
Signal/Noise	0.8	1.1

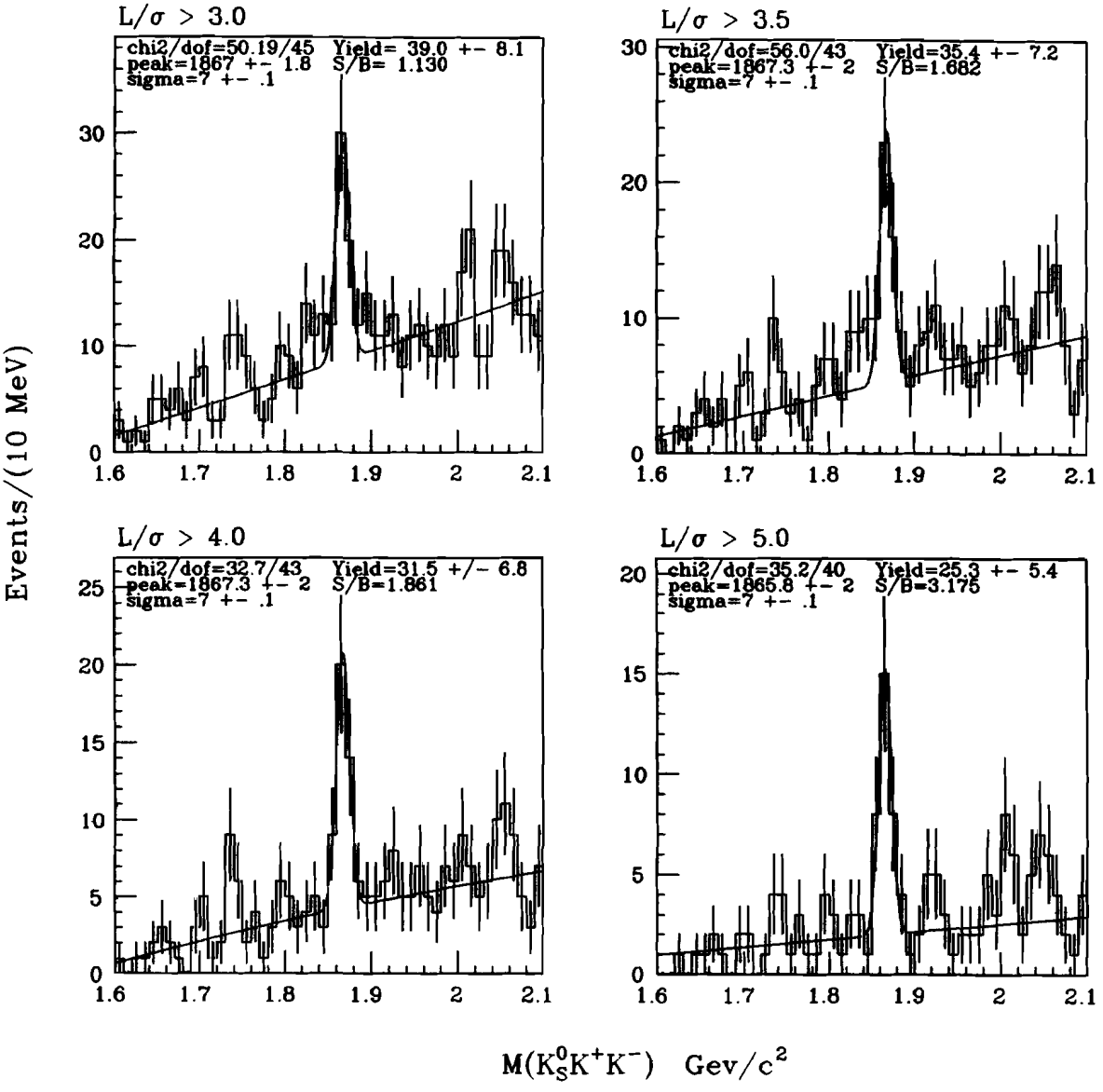

Figure 4.15. Background reduction for $D^o \rightarrow K^o_s K^+ K^-$.

CHAPTER 5

THE $D^o \rightarrow K^o_s\pi^+\pi^-$ DALITZ PLOT

The goal of the present analysis was to study the nature of the weak hadronic decay mechanism of the D^o meson using the selected K^o_s data collected by the E687 spectrometer. For reasons mentioned earlier, the analysis was restricted to the decay topology of a K^o_s meson plus two additional charged tracks; thus a complete and consistent picture using all $K\pi\pi$ decay modes, for instance, was not obtainable in this analysis. Nevertheless, the D^o signals presented in the previous chapter were used to directly measure several relative branching ratios. In this chapter the focus is directed to the decay $D^o \rightarrow K^o_s\pi^+\pi^-$.

5.1 Introduction

In order to determine the branching fractions of the resonant and non-resonant contributions to the $\overline{K}^o\pi^+\pi^-$ decay rate, the Dalitz plots were studied in terms of non-uniform population densities—deviations from pure phase space. For the Dalitz plot analysis, an additional restriction for the inclusive $D^o \rightarrow K^o_s\pi^+\pi^-$ decays was imposed in order to improve the signal to background ratio. Events in which either of the two tracks labeled as pions had a consistent kaon or proton definition were rejected. In Fig. 5.1 the inclusive and D^*-tagged signals are displayed, along with correpsonding mass selection windows for the signal regions and sideband regions. In Fig. 5.2 the corresponding Dalitz plots are displayed. Also shown are projections onto the three

possible invariant mass pairings. These plots exhibit many prominent features which can be understood as resulting from intermediate states. For example, the large clustering of events in the vertical and diagonal bands corresponding to $m^2_{K^o\pi} \approx 0.65$ GeV^2 is due to $K^{*-}\pi^+$ couplings; the effect is pronounced in the mass projection histograms. Not so evident are possible $\overline{K}^o\rho^o$ features, which would be most visible in the $m^2_{\pi^+\pi^-}$ projection. In addition, there are many points which appear to be randomly distributed and can be understood, in a simple way, as three-body non-resonant decays. Measurement of the fractional contributions and possible interference effects of hypothesized final states is the goal of the Dalitz plot fits.

The following sections contain a discussion of a fitting procedure, based on the maximum likelihood method, which attempts to model the Dalitz plot population by incoherent, partially coherent, and completely coherent sums of decay amplitudes which, for the intermediate resonances, consist of vector decay matrix elements and complex Breit-Wigner factors. Background contributions, important due to the relatively low signal to background ratios of the signals, were parameterized from fits made to the sidebands. Also presented are results from sensitivity tests made on Monte Carlo samples, and the method of efficiency correction. Following this, the results from the fits to the data sample are presented.

5.2 *Dalitz Plot Likelihood*

The motivation for the Dalitz fit approach is clear after some consideration of the decay rate expression for $D^o \to K^o_s\pi^+\pi^-$:

$$d^9\Gamma = \frac{(2\pi)^4}{2m_D}|\mathcal{M}|^2 d^9\Phi \tag{5.1}$$

where m_D is the D^o mass, $|\mathcal{M}|$ is the decay matrix element, and $d^9\Phi$ is the differential Lorentz invariant phase space factor. For three-body decays of a spinless particle into

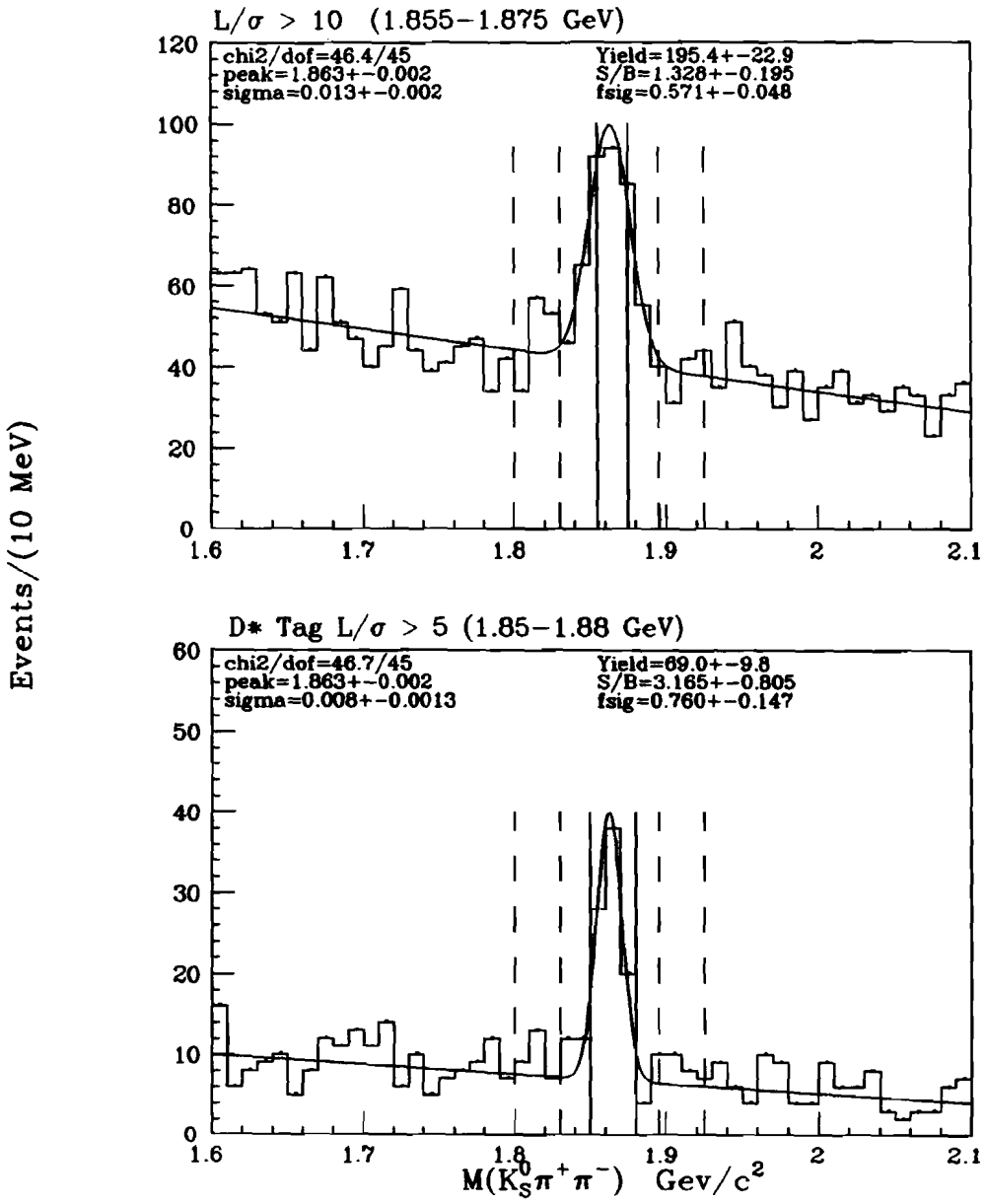

Figure 5.1. Event selections for Dalitz plot analysis: a) inclusive $L/\sigma_L > 10$, and b) D*-tagged $L/\sigma_L > 5$.

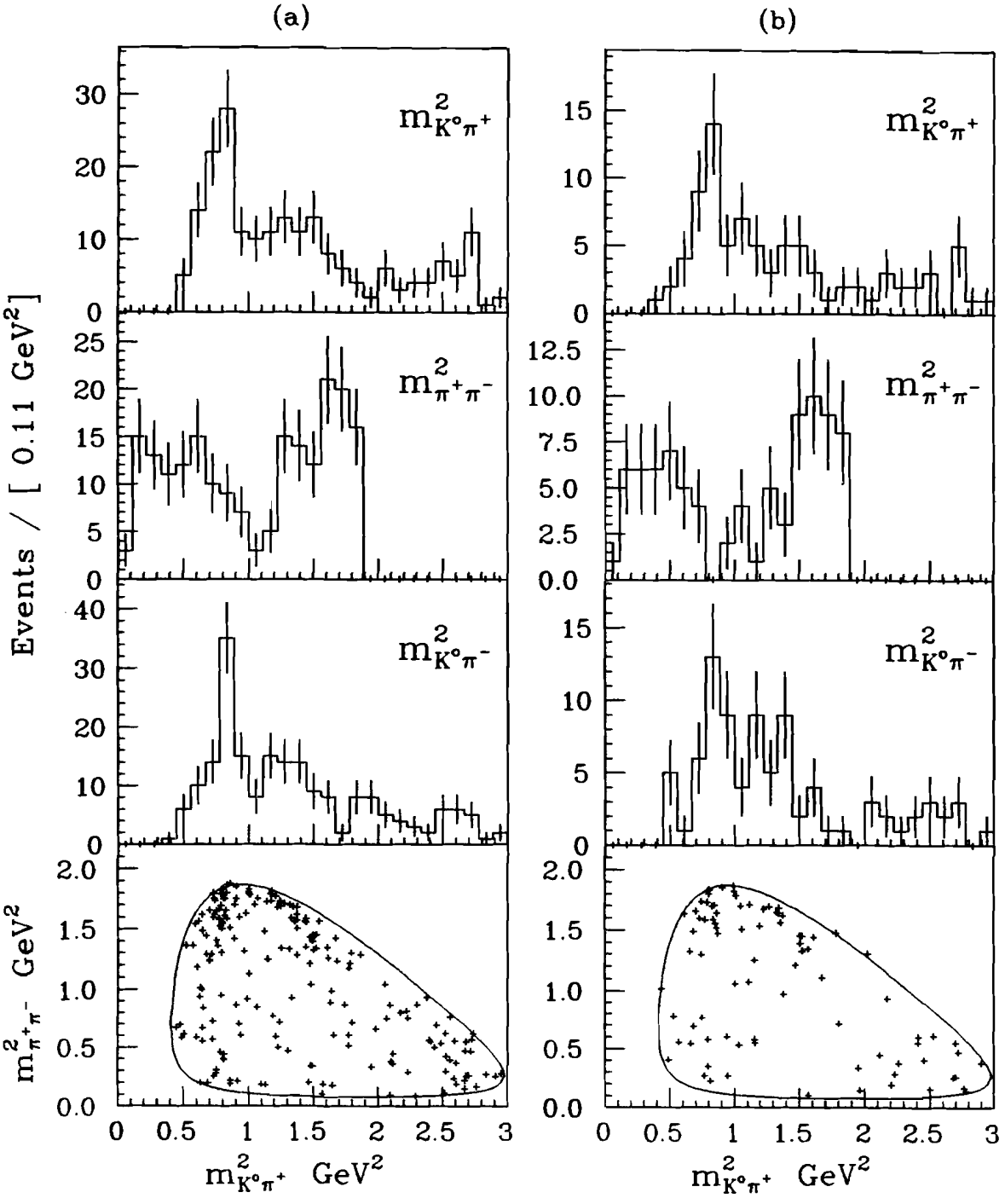

Figure 5.2. Dalitz plots for the $D^0 \to K^0_s\pi^+\pi^-$ events: a) inclusive $L/\sigma_L > 10$, and b) D^*-tagged $L/\sigma_L > 3$.

three pseudoscalars, the dimension of $d^9\Phi$ can be reduced to two, and $d^2\Phi$ can be expressed in terms of differentials of the invariant mass products $m^2_{K^\circ\pi}$ and $m^2_{\pi\pi}$. These quantities can readily be computed from the reconstructed momenta of the K°_s and $\pi^\pm$ tracks. The decay rate expressed as

$$d^2\Gamma = \frac{|\mathcal{M}|^2}{(2\pi)^3 32 m_D^3} dm^2_{K^\circ\pi} dm^2_{\pi\pi} \tag{5.2}$$

indicates that if a sample of D^o meson decays evenly populate the total available phase space, meaning the matrix element is a constant, then a flat distribution of the space of $m^2_{K^\circ\pi}$ and $m^2_{\pi\pi}$ results.

The fit to the Dalitz plot involved modelling the observed density with phenomenological amplitudes describing the decay processes. A continuous likelihood function for the Dalitz plot density was constructed from the assumed model, and maximized on an event-by-event basis using the MINUIT [39] minimization package. For the signal events, the probability function for the observed Dalitz plot density was chosen to be expressed as a coherent sum of the form:

$$\mathcal{L}^{\mathcal{S}} = \frac{\sum_{i=1}^{n}\sum_{j=1}^{n} \epsilon \cdot \sqrt{f_i^s f_j^s}\exp\left[i(\theta_i - \theta_j)\right]\tilde{A}_i^s \tilde{A}_j^{s\star}}{\mathcal{N}^{\mathcal{S}}}. \tag{5.3}$$

Each summation is over all decay channels contributing to the observed signal. The factor $\epsilon = \epsilon(m^2_{K^\circ\pi}, m^2_{\pi\pi})$ is the correction due to acceptance and reconstruction efficiency, and is discussed in Section 5.6. The f_i^s are the fit coefficients for each channel, and the exponential factors parameterize the relative phases between decay channels. These phases are related to dynamical effects in the decay process, about which we need not have *a priori* knowlege. The $\tilde{A}_i^s$ are complex, normalized amplitudes which model the decay by exploiting two facts: first, that total angular momentum will be

conserved, and second, that effects caused by intermediate states containing strong resonances can be parametrized with use of Breit-Wigner functions. In addition, in order that $\mathcal{L}^S$ retains its purpose as a probability density, the normalization factor, $\mathcal{N}^S$, is computed by integrating the double summation term in Eqn. 5.3 over all phase space, or Dalitz plot limits ($\mathcal{DP}$):

$$\mathcal{N}^S = \sum_{i=1}^{n}\sum_{j=1}^{n}\sqrt{f_i^s f_j^s}\exp\left[i(\theta_i-\theta_j)\right]\int_{\mathcal{DP}}\epsilon\cdot\tilde{A}_i^s\tilde{A}_j^{s\star}dm^2_{K^\circ\pi}dm^2_{\pi\pi}. \tag{5.4}$$

The integrals can be performed independent of the fitting parameters, and stored in a file for reading at the beginning of the fit procedure. In this way, the normalization factor can be rapidly computed for each iteration in the fit.

Because not all of the signal events in the real data sample could be isolated from background events, a model for the background combinations was also constructed. The sidebands were used to describe the distribution of background events falling within the signal region. The form of the background probability function, $\mathcal{L}^B$, was taken as an incoherent sum of non-resonant and resonant terms:

$$\mathcal{L}^B = \frac{\sum_{i=1}^{n} f_i^b|\tilde{A}_i^b|^2}{\mathcal{N}^B} \tag{5.5}$$

where the background normalization is simply

$$\mathcal{N}^B = \sum_{i=1}^{n} f_i^b. \tag{5.6}$$

As will be explicitly shown below, the description included only the mass dependencies for the resonant backgrounds.

The likelihood for the Dalitz plot, including both signal and background events,

thus can be expressed as a product of probabilities of all events:

$$L = \prod_{n=1}^{nevt} \left\{ f_{sig}\mathcal{L}^S + f_{bkg}\mathcal{L}^B \right\} \tag{5.7}$$

As discussed, the terms $\mathcal{L}^S$ and $\mathcal{L}^B$ are individually normalized, and the constants f_{sig} and f_{bkg}, representing the fraction of signal and background events respectively, are constrained by fitting the invariant mass histogram of the D^o candidates. In a photoproduction experiment of this kind, signal events are in principle completely distinguishable from background events, and are treated as such in these expressions.

Summarizing, given below is a general outline of the procedure followed in the Dalitz plot fit analysis:

- The data were studied to determine which decay channels were the most prominent contributors to the signal and background events.
- Amplitudes were constructed for each of the decay channels considered.
- A probability function was formulated in terms of the complex amplitudes, fit coefficients, and phases for each of the decay channels in question.
- The fit coefficients and phases were varied in order to find the maximum value assumed by the likelihood of the observed Dalitz Plot. This was accomplished by minimizing the quantity $-ln(L)$, where L is given by Eqn. 5.7.

In the sections that follow, the details of the each step of the fitting process are discussed.

5.3 Decay Matrix Elements

As mentioned, combinations of amplitudes were selected through consideration of structures seen in the Dalitz plots; these structures were compared to expectations

using Monte Carlo generated events. For the $K^{\circ}_{s}\pi^{+}\pi^{-}$ signal, the channels considered were the $K^{*-}(892)\pi^{+}$, $\overline{K}^{\circ}\rho^{\circ}$, and the three-body non-resonant $\overline{K}^{\circ}\pi^{+}\pi^{-}$ final states. (An amplitude for the channel $K^{*-}_{\circ}(1430)\pi^{+}$ was also considered, and is discussed separately in Sec. 5.7.) A description of each amplitude is in order.

5.3.1 Three-Body Non-Resonant Decays

The simplest decay matrix element is that of the three-body non-resonant decay, which is taken as a constant. Thus,

$$\tilde{A}^{s}_{nr} = \frac{1}{\sqrt{\int_{DP} dm^{2}_{K^{\circ}\pi} dm^{2}_{\pi\pi}}}. \tag{5.8}$$

The integral over the available phase space is a constant for the decay specified, and can be computed numerically by summing the area enclosed by the Dalitz plot boundary. Events which decay into the non-resonant mode simply populate the Dalitz plot uniformly in the case where the detector acceptance and efficiency is flat. The projections, however, have a characteristic shape, as will be illustrated in the Section 5.4.

5.3.2 Vector Decay Matrix Elements

To model the resonant final states, we construct amplitudes from the available parameters in the decay.[1] For the $K^{*-}\pi^{+}$ final state, these consist of the K^{*-} spin and momentum, and the π^{+} momentum. For the present problem, the description of a P-wave decay of the pseudoscalar D° meson can be achieved by taking the scalar product between the covariant spin vector for the K^{*-} and the energy-momentum four-vector of the recoiling π^{+}, each evaluated in the D° rest frame. This is equivalent to requiring

[1] The present work is patterned largely after the work in reference [41], in which use is made of Zemach tensors [42].

that the K^{*-} have zero helicity, as is necessary for angular momentum conservation. Below, explicit formulas for the $K^{*-}\pi^+$ final state are developed; the $\overline{K}{}^{*0}\rho^0$ final state is completely analogous.

The total decay amplitude is written symbolically as

$$A^s_{K^{*-}} = (t_{K^{*-}} \cdot p_{\pi^+})\mathrm{BW}(K^{*-}) \tag{5.9}$$

where $\mathrm{BW}(K^{*-})$ is the Breit-Wigner function (see below) describing the strong resonance between the K^0_s and π^- particles. The quantity $t_{K^{*-}}$ is the polarization or spin vector of the K^{*-}, defined in its rest frame by $(0, \vec{p}^{\,*}_{K^0} - \vec{p}^{\,*}_{\pi^-})$. By defining new covariant four-vectors

$$\tilde{p}_{K^0} = p_{K^0} - X\frac{(p_{K^0} \cdot X)}{m_X^2}$$
$$\tilde{p}_{\pi^-} = p_{\pi^-} - X\frac{(p_{\pi^-} \cdot X)}{m_X^2}$$

in which $X = X_{K^0\pi^-}$ refers to a momentum four-vector for the $(K^0_s\pi^-)$ system, and p_{K^0} and p_{π^-} are four-vectors evaluated in an arbitrary frame, $t_{K^{*-}}$ becomes

$$t_{K^{*-}} = \tilde{p}_{K^0} - \tilde{p}_{\pi^-}. \tag{5.10}$$

In the rest frame of the K^{*-} this reduces to $(0, \vec{p}^{\,*}_{K^0} - \vec{p}^{\,*}_{\pi^-})$, as required. Now $t_{K^{*-}}$ can be evaluated directly in the D^0 rest frame where the scalar product is computed:

$$t_{K^{*-}} \cdot p_{\pi^+} = p_{K^0} \cdot p_{\pi^+} - p_{\pi^-} \cdot p_{\pi^+} + \frac{(m^2_{K^0} - m^2_{\pi^-})}{m^2_{K^0\pi^-}}(p_{K^0} \cdot p_{\pi^+} - p_{\pi^-} \cdot p_{\pi^+}). \tag{5.11}$$

The advantage of this expression is that it can be written entirely in terms of the invariant mass quantities $m^2_{K^0\pi^-}$, $m^2_{\pi^+\pi^-}$, $m^2_{K^0\pi^+}$—i.e., the variables of the Dalitz

plot. Remembering that only two of these are independent, related through

$$m^2_{\mathrm{K^\circ}\pi^-} + m^2_{\pi^+\pi^-} + m^2_{\mathrm{K^\circ}\pi^+} = m^2_{\mathrm{D^\circ}} + m^2_{\mathrm{K^\circ}} + m^2_{\pi^+} + m^2_{\pi^-},$$

this part of the amplitude can be written (suppressing a factor of 1/2):

$$\begin{aligned} t_{\mathrm{K}^{*-}} \cdot p_{\pi^+} &= (m^2_{\mathrm{D^\circ}} - m^2_{\mathrm{K^\circ}\pi^-} - m^2_{\pi^+\pi^-} + m^2_{\mathrm{K^\circ}})\Big(\frac{m^2_{\mathrm{K^\circ}} - m^2_{\pi^-}}{m^2_{\mathrm{K^\circ}\pi^-}} + 1\Big) \\ &+ (m^2_{\pi^+\pi^-} - m^2_{\mathrm{K^\circ}} - m^2_{\pi^+})\Big(\frac{m^2_{\mathrm{K^\circ}} - m^2_{\pi^-}}{m^2_{\mathrm{K^\circ}\pi^-}} - 1\Big). \end{aligned} \tag{5.12}$$

A three dimensional plot of $|t_{\mathrm{K}^{*-}} \cdot p_{\pi^+}|^2$ is shown in Fig.5.3a. The most dramatic dependence is seen in the $m^2_{\pi^+\pi^-}$ dimension, in which the familiar "$\cos^2\Theta_{\mathrm{helicity}}$" behavior is evident. There also is a smaller dependence on $m^2_{\mathrm{K^\circ}\pi^-}$, but as will be seen shortly it is quite small compared to the strong resonance effect.

5.3.3 *Breit-Wigner Functions*

To parameterize the strong resonance, the P-wave formulation is used (again, using the K* as the example) [43]:

$$\mathrm{BW(K^*)} = \frac{\sqrt{m_{K^*}\Gamma(m_{K\pi})}}{m^2_{K^*} - m^2_{K\pi} - i m_{K^*}\Gamma(m_{K\pi})}$$

with

$$\Gamma(m_{K\pi}) = \Big(\frac{p_{K\pi}}{p_{K^*}}\Big)^3 \Gamma_{K^*}.$$

The quantities m_{K^*} and Γ_{K^*} are the mass and width of the K*, and were taken as 891.83 MeV/c^2 and 49.8 MeV/c^2 respectively [40]. The quantity $p_{K\pi}$ is the decay momentum for the $K\pi$ system; p_{K^*} is the value it assumes at the resonance mass. While

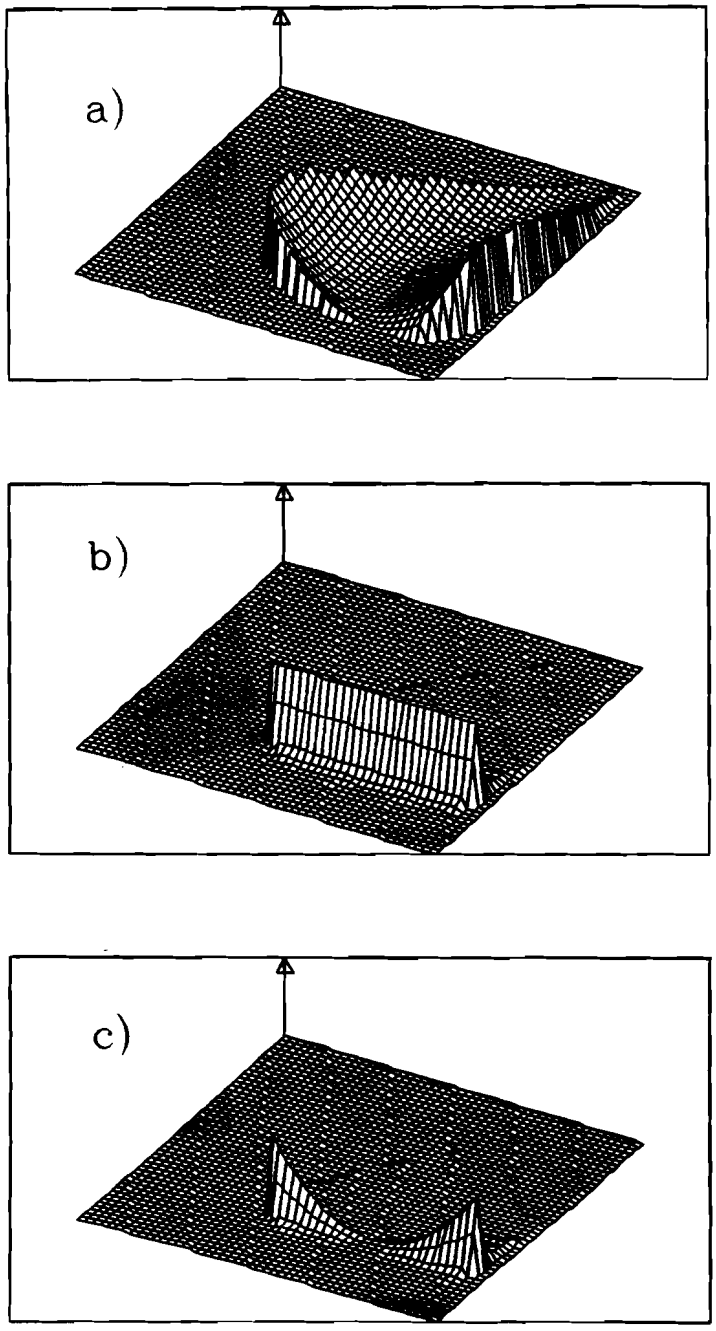

Figure 5.3. The $|(t_{K^{*-}} \cdot p_{\pi^+})BW(K^{*-})|^2$ distribution: a) the quantity $|t_{K^{*-}} \cdot p_{\pi^+}|^2$; b) the Breit-Wigner function $BW(K^{*-})$; c) the complete intensity $|A^s_{K^{*-}}|^2$.

doing the analysis, different forms for the parameterization were attempted. For example, one such form scaled the width $\Gamma(m_{K\pi})$ by the mass ratio $m_{K^0\pi}/m_{K^*}$. Results from fits to the real data sample of Fig. 5.2 showed little sensitivity to the particular form used, mostly due its limited statistics. The shape of the parameterization across the plot is given in Fig. 5.3b and also along the $m^2_{K^0\pi^-}$ projection in Fig. 5.4. As the Brieit-Wigner function BW(K^{*-}) depends only on $m^2_{K^0\pi^-}$, the complete amplitude for the decay is a function of two variables, $A^s_{K^{*-}} = A^s_{K^{*-}}(m^2_{K^0\pi^-}, m^2_{\pi^+\pi^-})$, and the corresponding intensity is plotted in Fig. 5.3c. Again, the amplitude for the fitting was normalized by numerical integration over the Dalitz plot:

$$\bar{A}^s{}_{K^{*-}} = \frac{A^s_{K^{*-}}}{\sqrt{\int_{DP} |A^s_{K^{*-}}|^2 dm^2_{K^0\pi} dm^2_{\pi\pi}}}.$$

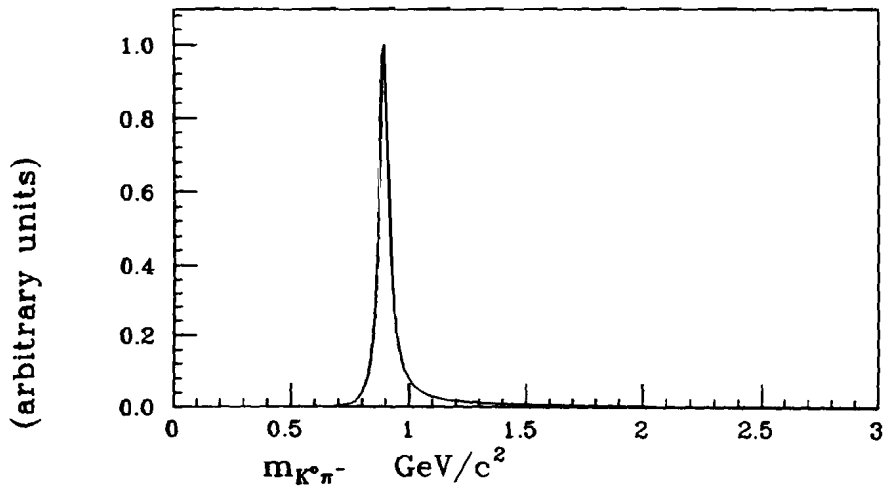

Figure 5.4. The Breit-Wigner function for the K* resonance. Relativistic P-wave formulations were used for both the K* and ρ^0 resonances.

5.3.4 D^o-$\overline{D}^o$ Detection Ambiguity

One more important point must be made concerning the form of the probability density function $\mathcal{L}^S$ of Eqn. 5.3: it assumes the correct pairing of the K^o_s and π^+ or π^-. Experimentaly, of course, the strangeness of the K^o_s is not determined for the inclusive decays, and so neither is the charm/anti-charm quantum number of the D^o candidate. (For D^* decays the charge of the bachelor pion can be used as a tag for the D^o or $\overline{D}^o$, but was not in this analysis.) Thus, $\mathcal{L}^S$ must describe an event sample in which the decays go into both $K^{*-}\pi^+$ and $K^{*+}\pi^-$ states. The following replacement correctly describes the expected probability density:

$$\mathcal{L}^S(m^2_{K^o\pi^-}, m^2_{\pi^+\pi^-}) \rightarrow f_D \cdot \mathcal{L}^S(m^2_{K^o\pi^-}, m^2_{\pi^+\pi^-}) + (1 - f_D) \cdot \mathcal{L}^S(m^2_{K^o\pi^+}, m^2_{\pi^+\pi^-}). \quad (5.13)$$

A new parameter f_D, which specifies the fraction of D^o mesons detected, was introduced in order to avoid the assumption of equal rates of $D^o/\overline{D}^o$ production in the experiment. The effect of the detection ambiguity on the observed Dalitz plot density is illustrated in Fig. 5.5. In addition, the Dalitz plot projections will have different shapes implied by this ambiguity. A similar replacement to Eqn. 5.13 is made for the background probability density $\mathcal{L}^B$ of Eqn. 5.5.

Having specified the ingredients of the amplitudes, it is instructive to write out the explicit expression used for signal events. $\mathcal{L}^S$ of Eqn. 5.3 can be written:

$$\begin{aligned}
\mathcal{L}^S(m^2_{K^o\pi^-}, m^2_{\pi^+\pi^-}) &= \frac{\epsilon(m^2_{K^o\pi^-}, m^2_{\pi^+\pi^-})}{\mathcal{N}^S}\Big[f^s_{nr}|\tilde{A}^s_{nr}|^2 + f^s_{K^*}|\tilde{A}^s_{K^{*-}}|^2 + f^s_{\rho^o}|\tilde{A}^s_{\rho^0}|^2 \\
&+ 2\mathrm{Re}\Big(\sqrt{f^s_{nr} f^s_{K^*}}\exp\left[i(\theta_{nr} - \theta_{K^*})\right]\tilde{A}^s_{nr}\tilde{A}^{s\star}_{K^{*-}}\Big) \\
&+ 2\mathrm{Re}\Big(\sqrt{f^s_{nr} f^s_{\rho^o}}\exp\left[i(\theta_{nr} - \theta_{\rho^o})\right]\tilde{A}^s_{nr}\tilde{A}^{s\star}_{\rho^o}\Big) \\
&+ 2\mathrm{Re}\Big(\sqrt{f^s_{K^*} f^s_{\rho^o}}\exp\left[i(\theta_{K^*} - \theta_{\rho^o})\right]\tilde{A}^s_{K^{*-}}\tilde{A}^{s\star}_{\rho^o}\Big)\Big]. \qquad (5.14)
\end{aligned}$$

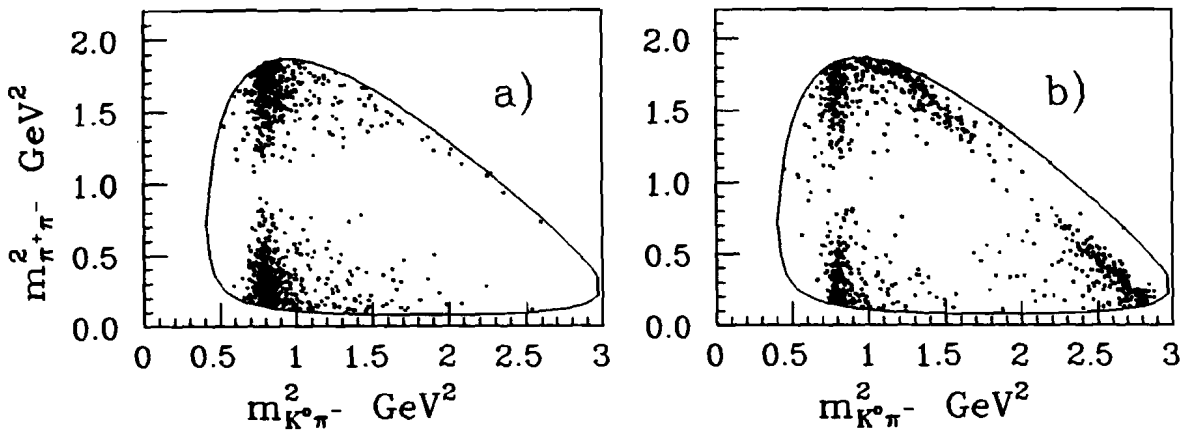

Figure 5.5. Effect of D^0–$\overline{D}^0$ detection ambiguity for $K^{*-}\pi^+$. Dalitz plots for a) D^0 events only; b) D^0–$\overline{D}^0$ mixed events.

Again, remembering also that the replacement specified by Eqn. 5.13 is required, this is the expression which allows for full interference among the decay channels. If, however, the decays were thought to proceed incoherently, or with partial coherence, the modification to $\mathcal{L}^S$ would be dropping the appropriate cross terms between the amplitudes. The next section illustrates some of these points in more detail.

5.4 *Monte Carlo Tests*

To test and study the forms of the amplitudes, as well as the fitting procedure itself, mock samples of events decaying according to one of the final states in question, for example the $\overline{K}^0\rho^0$ decay mode, were created. This was done by generating events which were evenly distributed over the total available phase space, and then weighting them by the assumed decay amplitude. These studies were made independent of the spectrometer simulations so that acceptance corrections could momentarily be ignored; thus, the overall efficiency factor $\epsilon(m^2_{K^0\pi^-}, m^2_{\pi^+\pi^-})$ was set to 1. In some of the studies the phase space events were weighted by combinations of amplitudes

which allowed for interference by specifying fit coefficients and phases in accord with Eqn. 5.14.

5.4.1 *Incoherent Decays*

As a first test of the fitting procedure, four samples of incoherent D^0 decays into pure $K^{*-}\pi^+$, $\overline{K}^0\rho^0$, and three-body non-resonant states, as well as a mixture of each, were generated and run through the fitting procedure. The pure samples, each consisting of 1000 events, are shown in Fig. 5.6(a,b) and Fig. 5.7a. The mixed sample was generated with fit fractions of 33% $\overline{K}^0\pi^+\pi^-_{\rm nonres}$, 55% $K^{*-}\pi^+$, and 12% $\overline{K}^0\rho^0$ which are approximately consistent with the previously reported branching ratios [40].

The fit for incoherent decays is very simple. The complicated expression for the probability density of Eqn. 5.14 reduces to a simple one:

$$\mathcal{L}^S(m^2_{K^0\pi^-}, m^2_{\pi^+\pi^-}) = \frac{f^s_{nr}|\tilde{A}^s_{nr}|^2 + f^s_{K^*}|\tilde{A}^s_{K^{*-}}|^2 + f^s_{\rho^0}|\tilde{A}^s_{\rho^0}|^2}{\sum_{i=1}^{3} f^s_i}. \qquad (5.15)$$

A two or three-parameter fit can be performed to extract the fractions for each of the samples. In doing the fit, the normalization can be fixed by expressing one of the fit fractions in terms of the remaining ones:

$$f^s_{nr} = 1 - f^s_{K^*} - f^s_{\rho^0}.$$

Alternative methods allowed all three parameters to vary, or fixing the most dominant fraction to 1.0 and allowing the remaining two to vary. To evaluate the fit results, the predictions of the fit are compared to data in each of the three possible projections in the following manner. For a given bin of a projection, the probablity function $\mathcal{L}^S$ is integrated between the bin limits and over the opposite mass-squared variable to get

the predicted number of events for the bin. The integrated quantity is normalized so that the integral of $\mathcal{L}^S$ over the entire projection is equal to the number of events in the plot. In Fig. 5.6 and Fig. 5.7, the fit result is plotted as a histogram, while the Monte Carlo data are plotted as points with error bars representing $\sqrt{N(\text{bin entries})}$ statistical errors. In each case the resultant fit fractions, listed in Table 5.1, were determined to within a few percent of the generated values. The reported errors on the fit parameters were calculated within the MINUIT fitting package by varying each fit parameter separately until the negative log-likelihood, $-ln(L)$ of Eqn. 5.7, increased by one half from its minimum, corresponding to one standard deviation error. At this point correlations between the fit parameters are ignored.

Table 5.1. Incoherent Monte Carlo Dalitz plot fit results.

Sample	f_{nr}	$f_{K^\star}$	f_{ρ^o}
$D^o \to \overline{K}^o\pi^+\pi^-_{nonres}$	0.98 ± 0.01	0.10 ± 0.01	0.01 ± 0.02
$D^o \to K^{\star-}\pi^+$	0.08 ± 0.02	0.92 ± 0.01	0.00 ± 0.01
$D^o \to \overline{K}^o\rho^o$	0.00 ± 0.01	0.00 ± 0.01	1.00 ± 0.04
33% 55% 12% mixture	0.34 ± 0.04	0.54 ± 0.02	0.12 ± 0.02

To evaluate the goodness of these fits, three χ^2 per degree of freedom quantities, corresponding to each of the projections, were determined by summing the squared deviations between observed and fit-predicted values for each bin. The number of degrees of freedom for each projection requires some consideration. It would not be correct to subtract all degrees of freedom, because some of the informational content of the fitting function may not be related to a given projection, and is lost when the integration is carried out. One method to account for this is to subtract instead the number of degrees of freedom divided by 3, which though arbitrary should give a better χ^2 estimator. Thus, accounting also for the normalization of $\mathcal{L}^S$ to the number

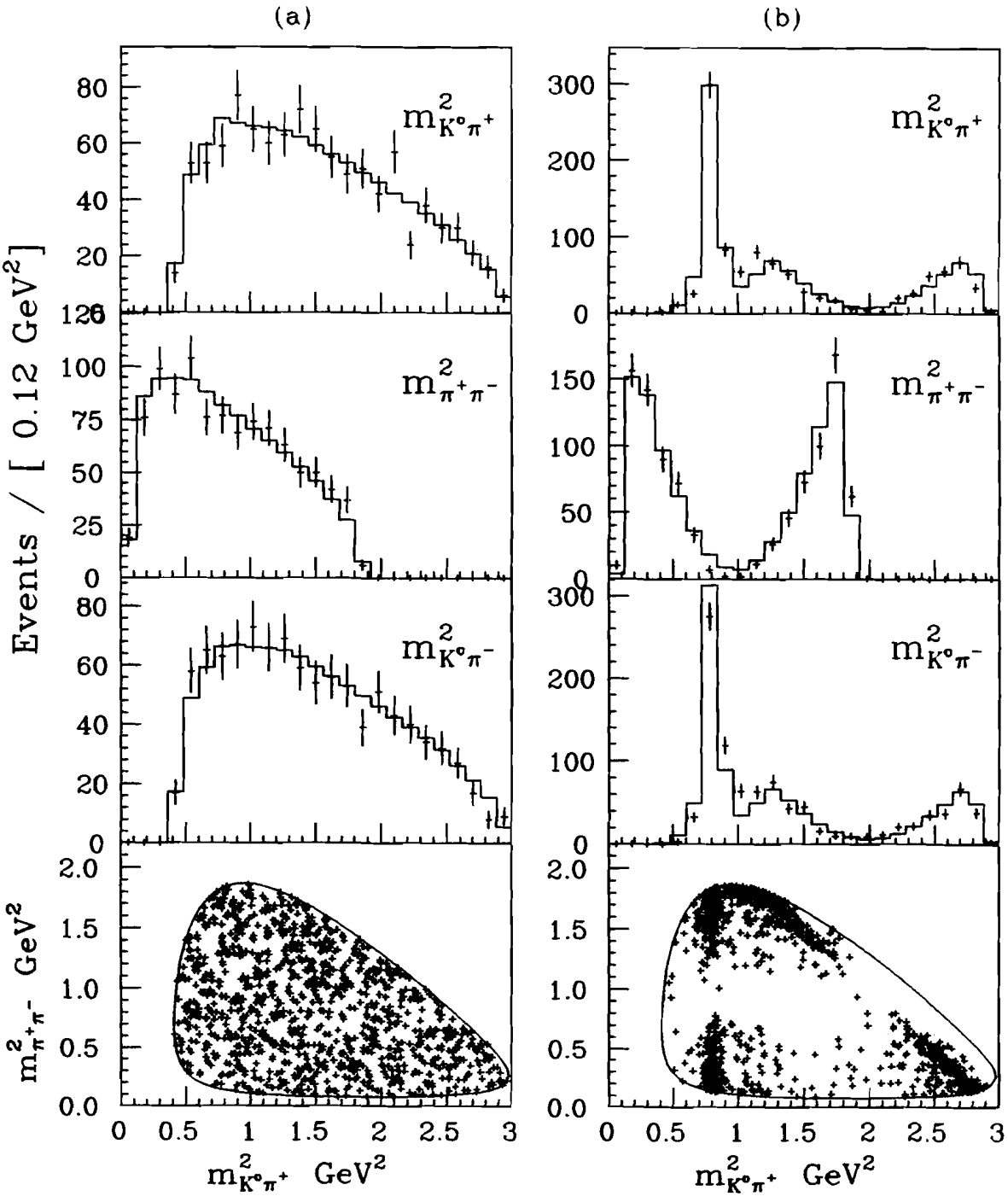

Figure 5.6. Monte Carlo Dalitz plot fits for a) $\overline{K}^0\pi^+\pi^-_{\text{nonres}}$, and b) $K^{*-}\pi^+$ final states.

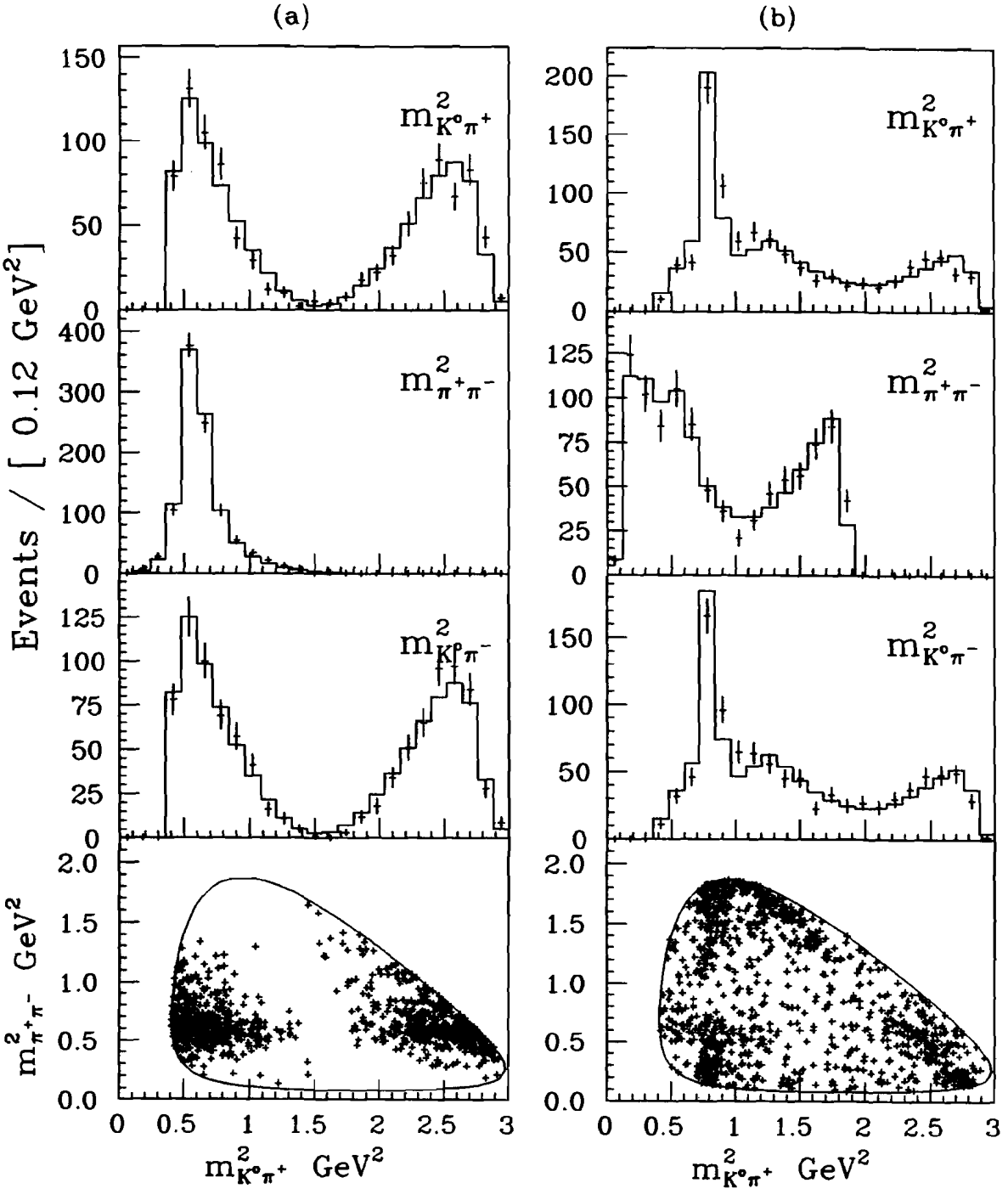

Figure 5.7. Monte Carlo Dalitz plot fits for a) $\overline{K}^0\rho^0$, and b) a mixture of each of the three final states in question. See the text for the fit fractions.

of events in the data sample, the number degrees of freedom for each projection was taken as:

$$N_{dof} = N(\text{kinematically allowable bins}) - \frac{N(\text{fit parameters})}{3} - 1.$$

Another method is to calculate a two-dimensional χ^2 which removes all ambiguities concerning the number of degrees of freedom. This method does not have the same visual effectiveness as the direct comparison of the projections, which is quite useful for finding mistakes or causes for lack of agreement between the model and the data. Both indicators were useful during the analysis. Table 5.2 lists the goodness of fit indicators for each of the incoherent Monte Carlo fits.

Table 5.2. Monte Carlo goodness of fit indicators.

Sample	$\chi^2(m^2_{K^0\pi^+})$	$\chi^2(m^2_{\pi^+\pi^-})$	$\chi^2(m^2_{K^0\pi^-})$	χ^2(2D)
$D^0 \to \overline{K}^0\pi^+\pi^-_{nonres}$	1.10	0.80	0.85	1.47
$D^0 \to K^{*-}\pi^+$	1.16	1.49	2.28	0.98
$D^0 \to \overline{K}^0\rho^0$	1.72	1.88	1.82	1.19
33% 55% 12% mixture	0.54	0.84	0.87	0.71

5.4.2 Coherent Decays and Interference

To study the structure introduced into the Dalitz plot from coherence, we consider the case of $K^{*-}\pi^+$ and $\overline{K}^0\rho^0$ amplitudes interfering, with the three-body non-resonant state contributing incoherently. This choice is arbitrary, and is intended only for illustrative purposes. In this case, interference arises from two sources: (1) the complex overlap of the two Breit-Wigners, and (2) phase differences between the D^0 meson de-

cay amplitudes into the individual channels. The interference piece of the probability function, taken from the appropriate cross term of Eqn. 5.14, can be written:

$$2\sqrt{f^s_{K^*} f^s_{\rho^0}}|\bar{A}^s{}_{K^{*-}}||\bar{A}^{s\star}_{\rho^0}|cos(\phi_{K^*} - \phi_{\rho^0} - \theta)$$

where $\theta = \theta_{\rho^0} - \theta_{K^*}$ is the relative phase. The ϕ variable for each represents the Breit-Wigner phase, the tangent of which is equal to the imaginary part over the real part of the amplitude:

$$\phi_{K^*} = tan^{-1}\sqrt{\frac{m_{K^*}\Gamma(m_{K\pi})}{m^2_{K^*} - m^2_{K^0\pi^-}}}. \tag{5.16}$$

Fig. 5.8a shows the $cos(\phi_{K^*} - \phi_{\rho^0} - \theta)$ modulation for the case of $\theta = 0^o$. The figure only indicates the familiar change in sign of the real part of the resonance amplitude passing through its pole mass, but in this case for two resonances at once. Fig. 5.8b shows the attenuation due to the product of the Breit-Wigner and angular portions of the amplitude, excluding the phase modulation of Fig. 5.8a. Fig. 5.8c shows behavior of the total interference amplitude, and Fig. 5.8d shows the same for the case of $\theta = 90^o$. The size of the interference amplitude can be substantial in the regions where the Breit-Wigner amplitudes overlap apreciably, and as can be seen in Fig. 5.8d, the interference term can act destructively in some locations depending on the relative phase. The net contributions of the interference depend on the branching fractions into each mode, the extent to which the bands of the resonances overlap, and on the relative phase between amplitudes. One point worth noting is that in this analysis the relative phase between the amplitudes is assumed not to depend on position in the Dalitz plot.

To get a clearer picture of the role played by the interference terms between the

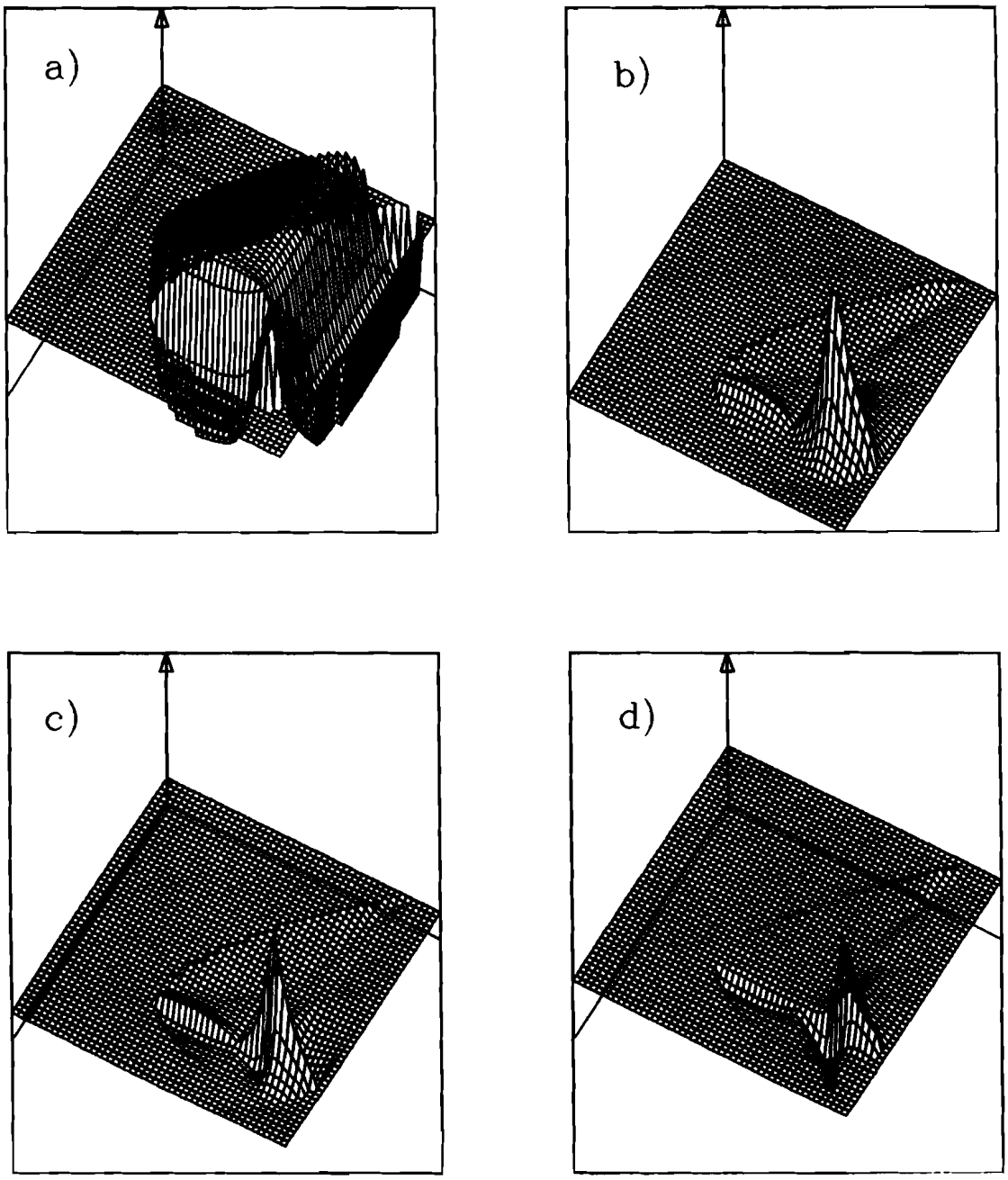

Figure 5.8. Interference effects between amplitudes: a) cosine of Breit-Wigner phases $cos(\phi_{K^*} - \phi_{\rho^0} - \theta)$; b) $|\tilde{A}^s{}_{K^*+}||\tilde{A}^{s^*}{}_{\rho^0}|$ moduli overlap; c) the product of a) and b); d) the same, but with the relative phase $\theta = 90^\circ$.

$K^{*-}\pi^+$ and $\overline{K}^0\rho^0$ amplitudes of our example, it is instructive to see the effect on the invariant mass-squared projections. In Fig. 5.9 the integrated interference terms onto the $m^2_{K^0\pi^-}$ and $m^2_{\pi^+\pi^-}$ projections as a function of increasing steps in the phase angle θ are plotted. These intensities are added to the probability density function on the same footing as the "normal" incoherent terms, and so either constructively or destructively add to the expected projection histograms. For this particular case of interference, the normalization factor of Eqn. 5.4 becomes:

$$\mathcal{N}^S = f^s_{nr} + f^s_{K^*} + f^s_{\rho^0} + 2\sqrt{f^s_{K^*} f^s_{\rho^0}} I,$$

where the interference integral is given by:

$$I = \frac{\int_{DP} |A^s_{K^{*-}}||A^{ns}_{\rho^0}| cos(\phi_{K^*} - \phi_{\rho^0} - \theta) dm^2_{K^0\pi} dm^2_{\pi\pi}}{\sqrt{\int_{DP} |A^s_{K^{*-}}|^2 dm^2_{K^0\pi} dm^2_{\pi\pi} \int_{DP} |A^s_{\rho^0}|^2 dm^2_{K^0\pi} dm^2_{\pi\pi}}}.$$

The quantity I can be used as a measure of the amount of interference between amplitudes. If it is zero, then the incoherent case is recovered. However, as the mass-squared projection histograms of Fig. 5.9 show, it is not likely to integrate to zero regardless of the relative phase. Note also that the fit coefficients defined in this way no longer satisfy the constraint of summing to one. Again, this only occurs when the interference term integrates to zero.

In order to study the power of the fitter in resolving these interference effects, event samples were generated as a coherent mixtures of of $K^{*-}\pi^+$ and $\overline{K}^0\rho^0$ decays. As before, detector acceptances were not included in the study. The interference was specified by setting the phases of the amplitudes to arbitrary values. As an example, a sample with 1000 events having 4.6%, 74%, and 13.9% for the three-body non-resonant, $K^{*-}\pi^+$, and $\overline{K}^0\rho^0$ amplitudes respectively, along with phase angles of 0.,

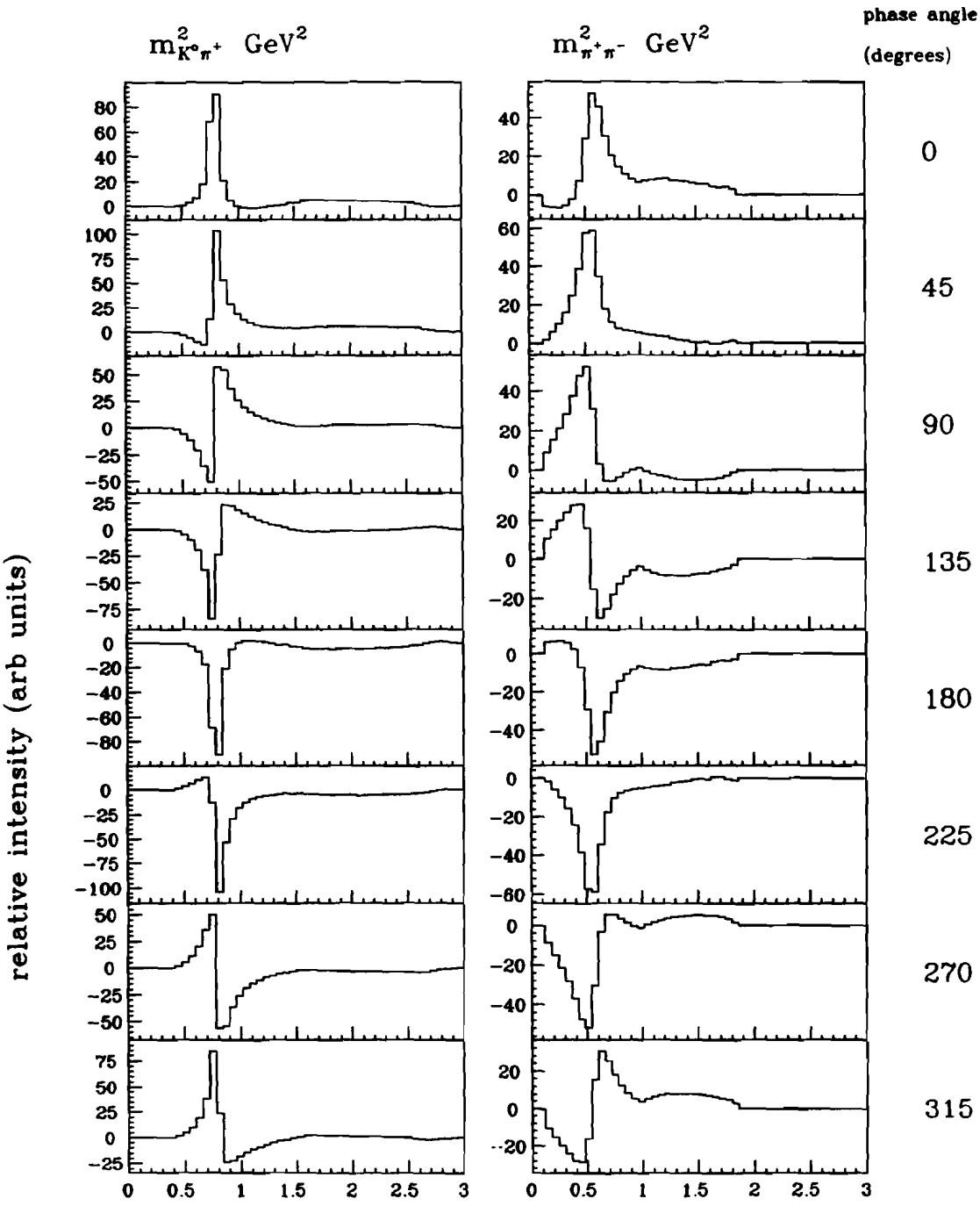

Figure 5.9. Interference projections for $K^{*-}\pi^+$—$\overline{K}^0\rho^0$ amplitudes. The projections correspond to the $K^{*-}\pi^+$-$\overline{K}^0\rho^0$ interference and are expressed as a function of the relative phase angle $\theta = \theta_{\rho^0} - \theta_{K^{*-}}$.

4.7, and 3.0 radians was fitted and verified to return the correct values to within statistical errors, as shown in Fig 5.10.

5.5 *Background Parameterization*

In order to do a realistic fit to the data, the distribution of background events across the Dalitz plot must also be adequately described. This becomes increasingly important with diminishing signal to background ratio. The sources of background are not always easy to understand, much less model. One source, perhaps the simplest, is that due to the combinatoric background. These are events composed of random combinations of tracks which, although passing all charm-selection cuts, are not related to charm candidates of any kind. These combinations, apart from possible detection biases, should result in invariant mass products $m^2_{K^o\pi^+}$, $m^2_{\pi^+\pi^-}$, $m^2_{K^o\pi^-}$ which are uncorrelated; thus, they should populate the Dalitz plot evenly. Other sources are photoproduced vector mesons, namely $K^*(892)$ and $\rho^o(770)$ mesons and perhaps others coupling to $K^o\pi^\pm$ and $\pi^\pm\pi^\mp$, which can result when two tracks from the primary vertex combine with a third to mimick a charm vertex.

Whatever the true source of background, it is not neccessary to accurately specify its content or measure, say, the fraction of each type of contributing source. One only has to construct a model for it, and implement that model into the overall likelihood function. To get an idea of the behavior of the background, several sideband studies were made. In Fig. 5.11 the Dalitz plot and projections are shown for lower and upper sidebands for one such selection from the inclusive D^o signal. The corresponding plots for the D^*-tagged sample are similar. The sideband mass regions were defined as :

$$\text{low sideband :} \quad 1.800 < M(K^o_s\pi^+\pi^-) < 1.830 \text{ GeV/c}^2$$

$$\text{high sideband :} \quad 1.895 < M(K^o_s\pi^+\pi^-) < 1.925 \text{ GeV/c}^2.$$

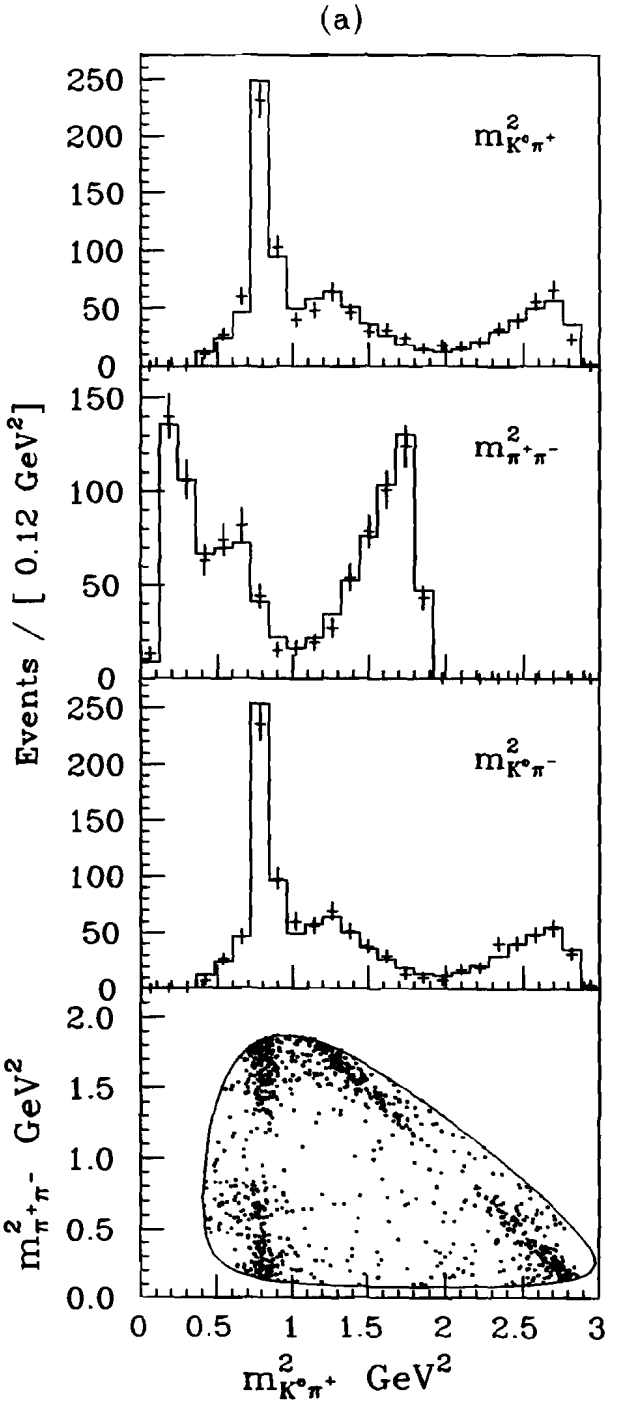

(b)

f(3−body) = 5.7 +− 1.8 %

f($K^{*-}\pi^+$) = 74.8 +− 9.4 %

f($K^0\rho^0$) = 13.2 +− 2.2 %

θ(3−body) = 0.00 (fixed)

θ($K^{*-}\pi^+$) = 4.81 +− 0.19

θ($K^0\rho^0$) = 3.06 +− 0.18

$\chi^2(m^2_{K^0\pi^+})$ = 1.53 conf.= 7%

$\chi^2(m^2_{\pi^+\pi^-})$ = 0.77 conf.= 69%

$\chi^2(m^2_{K^0\pi^-})$ = 1.05 conf.= 40%

χ^2(2−dim) = 1.09 conf.= 33%

Figure 5.10. Coherent Monte Carlo Dalitz plot fits: a) data (points) and plotted fit result (histograms) to the mixture described in the text; b) returned fit parameters and goodness of fit indicators.

The Dalitz boundries drawn on each plot correpond to central mass values of the respective sideband selection. Also shown in the figure is the predicted population from a model which was constructed with the following terms:

1. A constant term for the uncorrelated combinatoric background (analogous to "three-body non-resonant").

2. An amplitude for background $K^{*\pm}(890)$ events.

3. An amplitude for background $\rho^{o}(770)$ events.

For the resonance terms the same Breit-Wigner functions as before were used. In each projection, the model adequately describes the background as being mostly uncorrelated, though a significant fraction of the events are consistent with photoproduced K^{*} events. For the inclusive signal, there was no evidence for any photoproduced ρ^{o} events passing the selection cuts, and so the sideband events were re-fitted removing the ρ^{o} amplitude. However, for the D^{*}-tagged lower sideband, a fit allowing ρ^{o} events determined a fraction of ρ^{o} background of 7 ± 9 %. Even so, the χ^2/dof of the projections improved slightly when the ρ^{o} amplitude was removed, and so the parameterization without its contribution was used. Table 5.3 lists the resulting fit fractions, and the goodness of fit indicators are listed in Table 5.4. Both the lower and upper sidebands are consistent with a K^{*} fraction from a few percent up to 20%. This becomes a source of systematic error on the fit coefficients as will be seen below.

5.6 *Acceptance and Reconstruction Efficiency*

If the efficiency of the spectrometer reconstruction is not flat across the Dalitz plot, the amplitude functional forms alone are insufficient to determine the branching fractions. The effects are usually apparent when the mass-squared projections are studied to

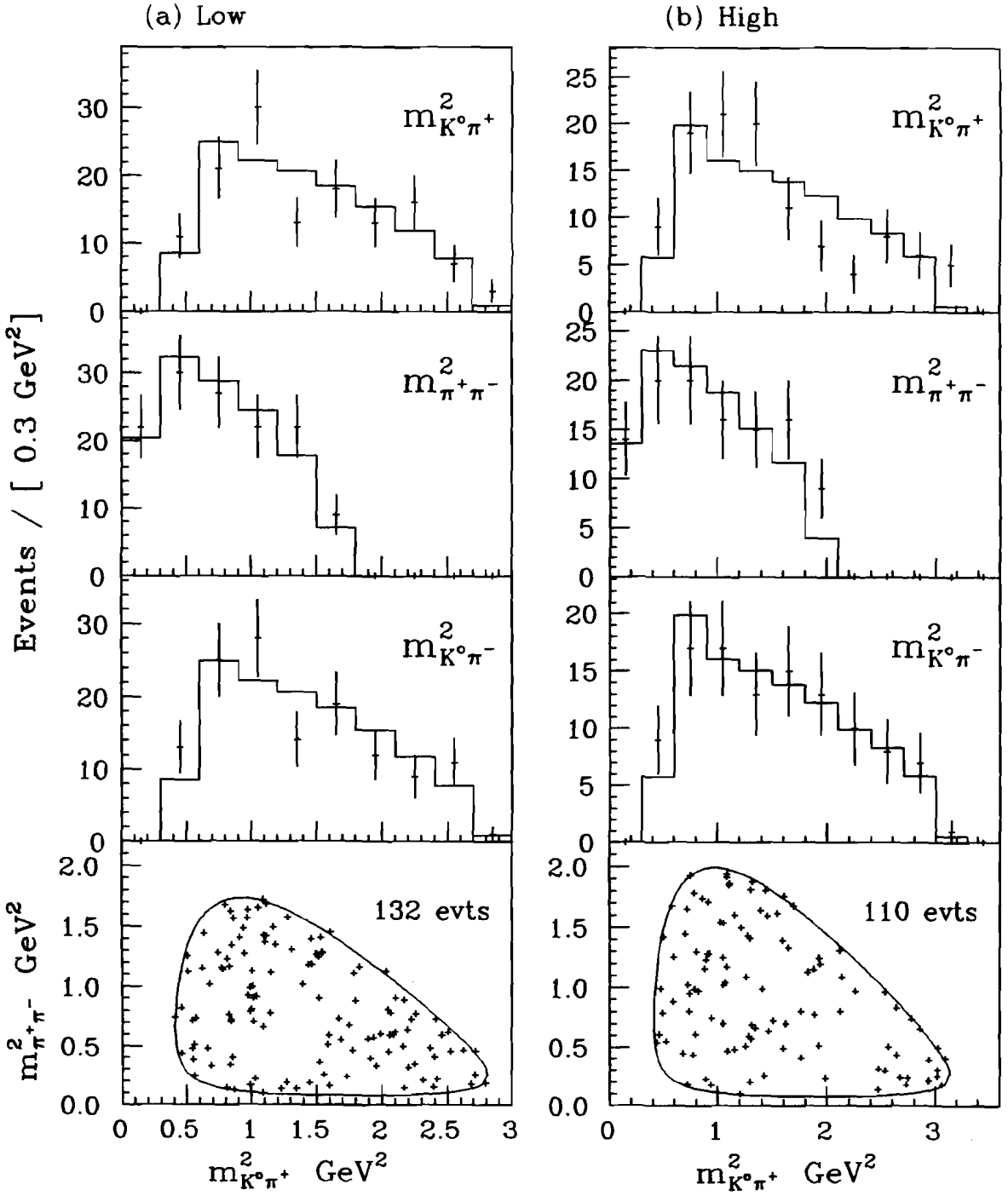

Figure 5.11. Sideband Dalitz plots: a) low sideband $1.800 < M(K^0_s\pi^+\pi^-) < 1.830$ GeV/c²; b) high sideband $1.895 < M(K^0_s\pi^+\pi^-) < 1.925$ GeV/c².

Table 5.3. Background fit parameters.

Data Sample	f^b_{nr}	$f^b_{K^*}$
$D^o \to K^o_s\pi^+\pi^-$ (low)	0.91 ± 0.10	0.08 ± 0.06
$D^o \to K^o_s\pi^+\pi^-$ (high)	0.85 ± 0.11	0.15 ± 0.12
$D^{*\pm} \to (K^o_s\pi^+\pi^-)\pi^\pm$ (low)	0.80 ± 0.10	0.20 ± 0.10
$D^{*\pm} \to (K^o_s\pi^+\pi^-)\pi^\pm$ (high)	0.83 ± 0.10	0.17 ± 0.10

Table 5.4. Background goodness of fit indicators.

Data Sample	$\chi^2(m^2_{K^o\pi^+})$	$\chi^2(m^2_{\pi^+\pi^-})$	$\chi^2(m^2_{K^o\pi^-})$
$D^o \to K^o_s\pi^+\pi^-$ (low)	1.56	0.48	1.25
$D^o \to K^o_s\pi^+\pi^-$ (high)	2.63	1.01	0.32
$D^{*\pm} \to (K^o_s\pi^+\pi^-)\pi^\pm$ (low)	1.02	3.15	0.47
$D^{*\pm} \to (K^o_s\pi^+\pi^-)\pi^\pm$ (high)	1.10	0.42	0.63

evaluate the goodness of the fit results. The inability of the likelihood function with $\epsilon = 1$ to describe the data was, in fact, a motivatition for studying the acceptance and reconstruction efficiency in detail.

5.6.1 Fit Function for $\epsilon(m^2_{K^o\pi^-}, m^2_{\pi^+\pi^-})$

A check was made for variation in spectrometer acceptance and reconstruction efficiency, and to determine the function $\epsilon(m^2_{K^o\pi^-}, m^2_{\pi^+\pi^-})$. A sample of $\simeq$ 200 thousand Monte Carlo events was generated, with the D^o-meson decaying according to phase space, and passed through the reconstruction package for this purpose. The Dalitz plot for the sample of events passing all analysis cuts is shown in Fig. 5.12a, with the projections represented by the plotted points with error bars. The over-plotted

histograms are the predictions for unit efficiency. There appears to be a relative depletion of events in the low $m^2_{\pi^+\pi^-}$ projection, which is also indicated by the relatively poor χ^2= 4.21. An attempt was made to parameterize the efficiency effects using the distribution of the mass-squared variables $m^2_{K^\circ\pi^-}$ and $m^2_{\pi^+\pi^-}$. A sample of events was subjected to a maximum likelihood fit to a cubic polynomial, symmetric in the two variables $m^2_{K^\circ\pi^-}$ and $m^2_{\pi^+\pi^-}$. The results of the fit, which returned better χ^2 values in each projection and reduced the negative log-likehood considerably, are plotted over the projections in Fig. 5.12b. Note that the observed dip in the $m^2_{\pi^+\pi^-}$ projection at low mass is correctly modelled by the function. A plot of the function as a surface, illustrated in Fig. 5.13, shows very little acceptance variation along the $m^2_{K^\circ\pi^-}$ direction while the $m^2_{\pi^+\pi^-}$ projection is seen to be steadily rising with $m^2_{\pi^+\pi^-}$. The variation is about a factor of two from $m^2_{\pi^+\pi^-} \simeq$ .01 GeV^2 to 1.8 GeV^2. The relatively large corrections implied by the resulting fits prompted concern for the validity of the procedure. Thus an investigation was initiated to determine the cause of the uneven efficiency.

The variation in reconstruction efficiency along the $m^2_{K^\circ\pi}$ and $m^2_{\pi\pi}$ projections was found to vary with the decay length detachment cut L/σ_L . As was depicted in Fig. 5.12, a clear trend in the efficiency degradation at low $m^2_{\pi\pi}$ was observed as L/σ_L increased from 0 to 10. When averaged over the $m^2_{K^\circ\pi}$ projections, however, the depletions were less dramatic. These effects can again be understood as resulting from the D$^\circ$ decay kinematics and the method of the secondary vertex fit. In Fig. 5.14 are shown the average L, σ_L, and L/σ_L as a function of the projection mass-squared variables $m^2_{K^\circ\pi}$ and $m^2_{\pi\pi}$. In each projection, the average decay length is roughly constant ($\simeq 4mm$). This is not surprising since L scales with the D$^\circ$ meson momentum, which is not a function of position in the Dalitz plot. The error in L, σ_L, however depends on the opening angles between the particles and thus Dalitz plot position. In Fig. 5.14b the dependence of σ_L on $m^2_{\pi\pi}$ is consistent with expectations: increasing

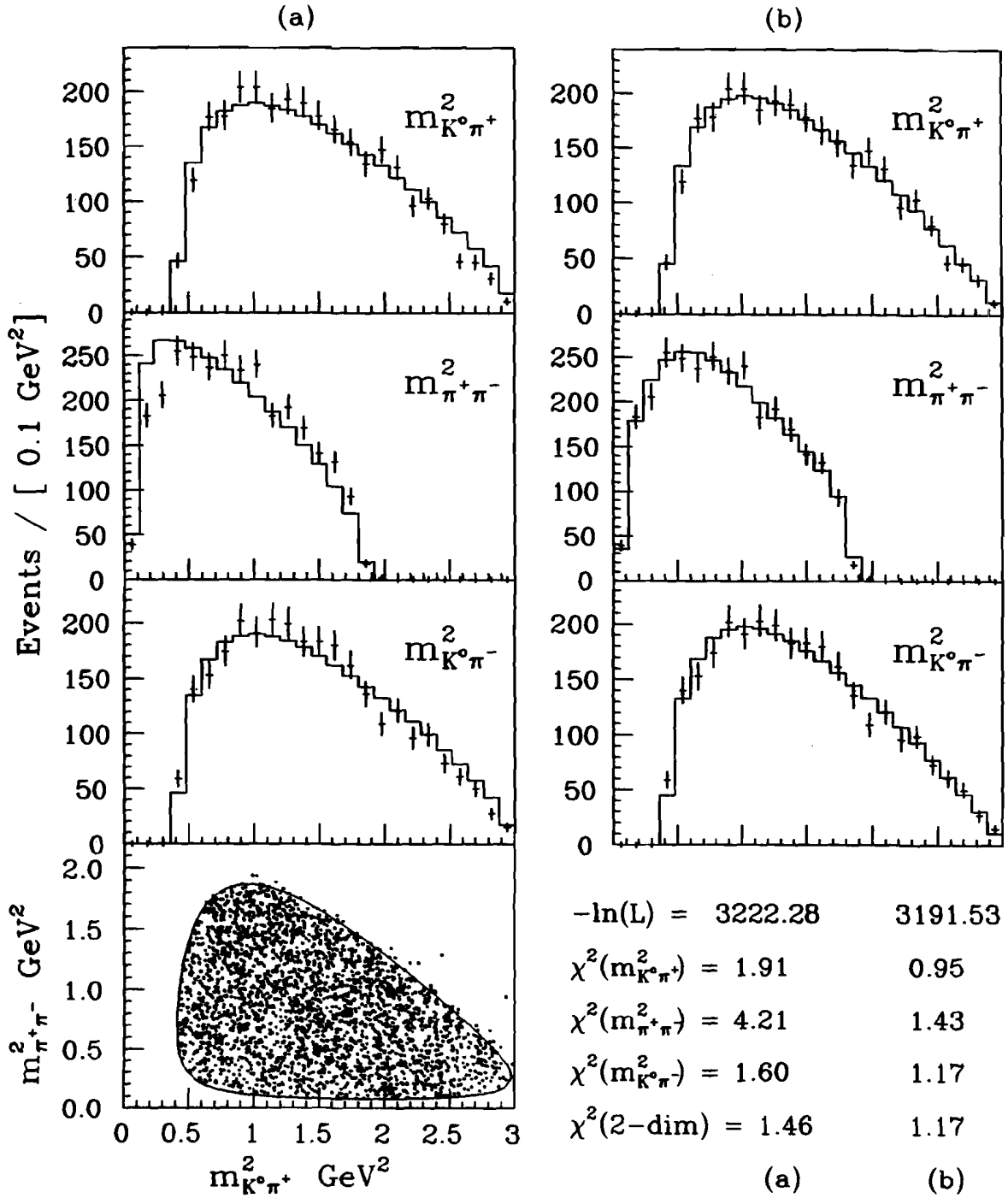

Figure 5.12. Dalitz plot for reconstructed phase space events: a) Dalitz plot and mass-squared projections. In the projections, the reconstruted events are given by the points with error bars, and the prediction for flat acceptance by the histogram. In b) the histogram is the result of a cubic polynomial fit.

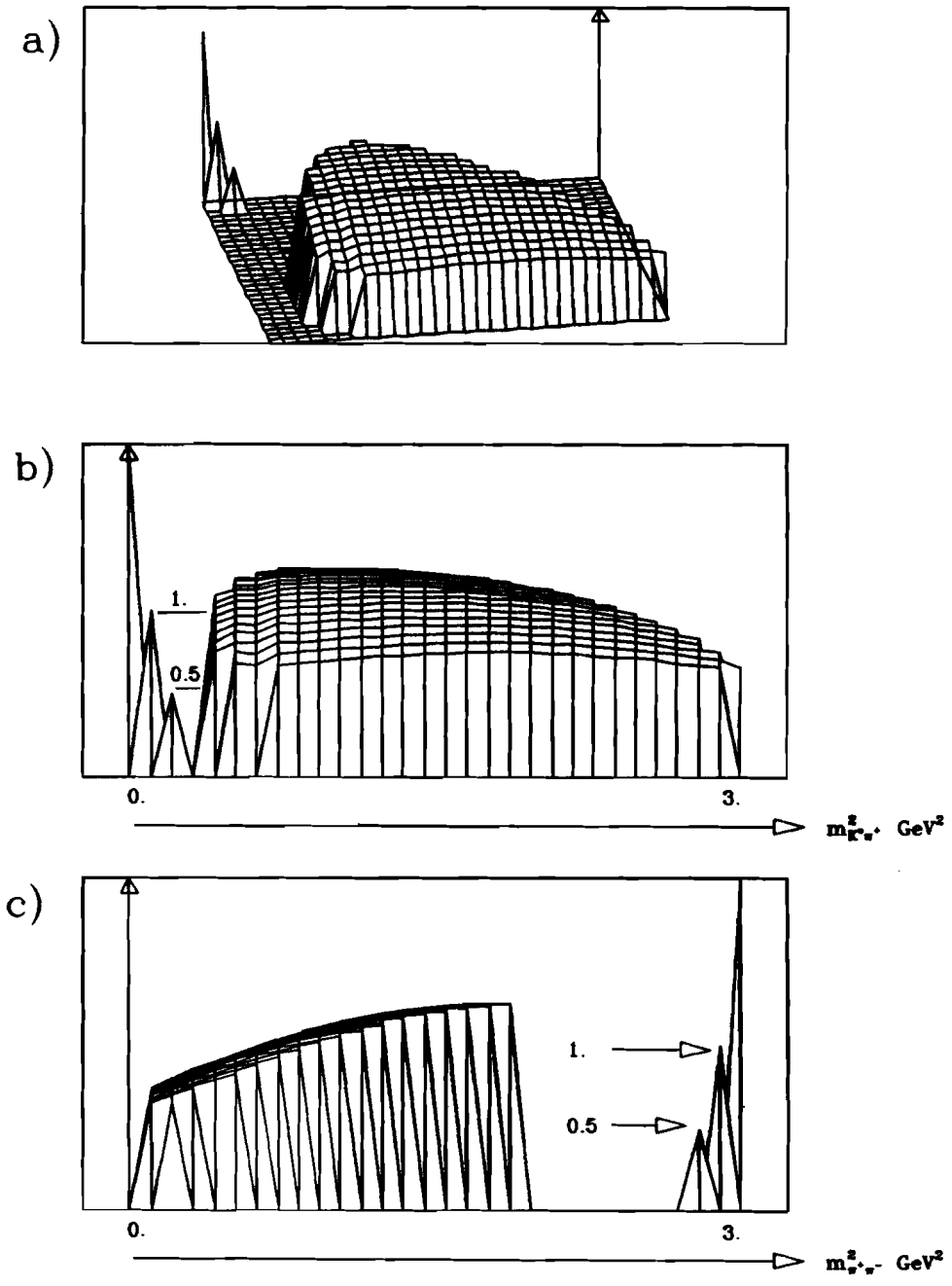

Figure 5.13. Normalized three dimensional efficiency function: a) the fitted function $\epsilon(m^2_{K^\circ\pi}, m^2_{\pi\pi})$ is normalized to have an average value of 1. b) the variation viewed along the $m^2_{K^\circ\pi}$ projection, and c) along the $m^2_{\pi\pi}$ projection.

the opening angle improves the determination of L. Together with the flat dependence in L, Fig. 5.14c shows the behavoir of L/σ_L along the $m^2_{\pi\pi}$ projection. The variation of about a factor of two corresponds to the fit result displayed in Fig. 5.13c. However, Fig. 5.14e for σ_L vs. $m^2_{K^\circ\pi}$ seems somewhat curious: one expects to see a similar dependence to that in Fig. 5.14b. The distribution is a direct consequence of the secondary vertex fit (see Section 4.7.1): the error in vertex position (and thus the decay length) is determined solely by the π^+-π^- track combination. Thus, the variation of σ_L with $m^2_{K^\circ\pi}$ is understood after examining the average π^+-π^- opening angle as a function of $m^2_{K^\circ\pi}$, as shown in Fig. 5.15. This dependence, along with the flat distribution in L along $m^2_{K^\circ\pi}$, explains the curvature of the efficiency in Fig. 5.14f, and shows consistent agreement with the fit result of Fig. 5.13b.

The above discussion illustrates that the efficiency across the plot is reasonably well understood, and can be parameterized with a function of the mass-squared variables. However, one caution should be given: as with the background modelling, the fitted function for the efficiency may introduce systematic biases due to its intrinsic smoothing attributes. Therefore, a second technique using binned correction factors was pursued, and is outlined below.

5.6.2 Bin-by-Bin Efficiency Correction

An alternate means of correcting for efficiency is a "bin-by-bin" correction method, in which the generated and reconstructed events are histogramed in bins of the mass-squared variables $m^2_{K^\circ\pi^-}$ and $m^2_{\pi^+\pi^-}$. The efficiency is taken as the ratio of the number of reconstructed events to the number generated in a particular $(m^2_{K^\circ\pi^-}, m^2_{\pi^+\pi^-})$ bin. Fig. 5.16 shows the efficiency correction factors in bins of 0.2 GeV^2 by 0.2 GeV^2. Although clearly the bin-by-bin statistics are limited in this plot, the same general trend of increasing efficiency with increasing $m^2_{\pi^+\pi^-}$ mass is likewise observed. The weighting factors used for the efficiency correction to the data sample are shown in

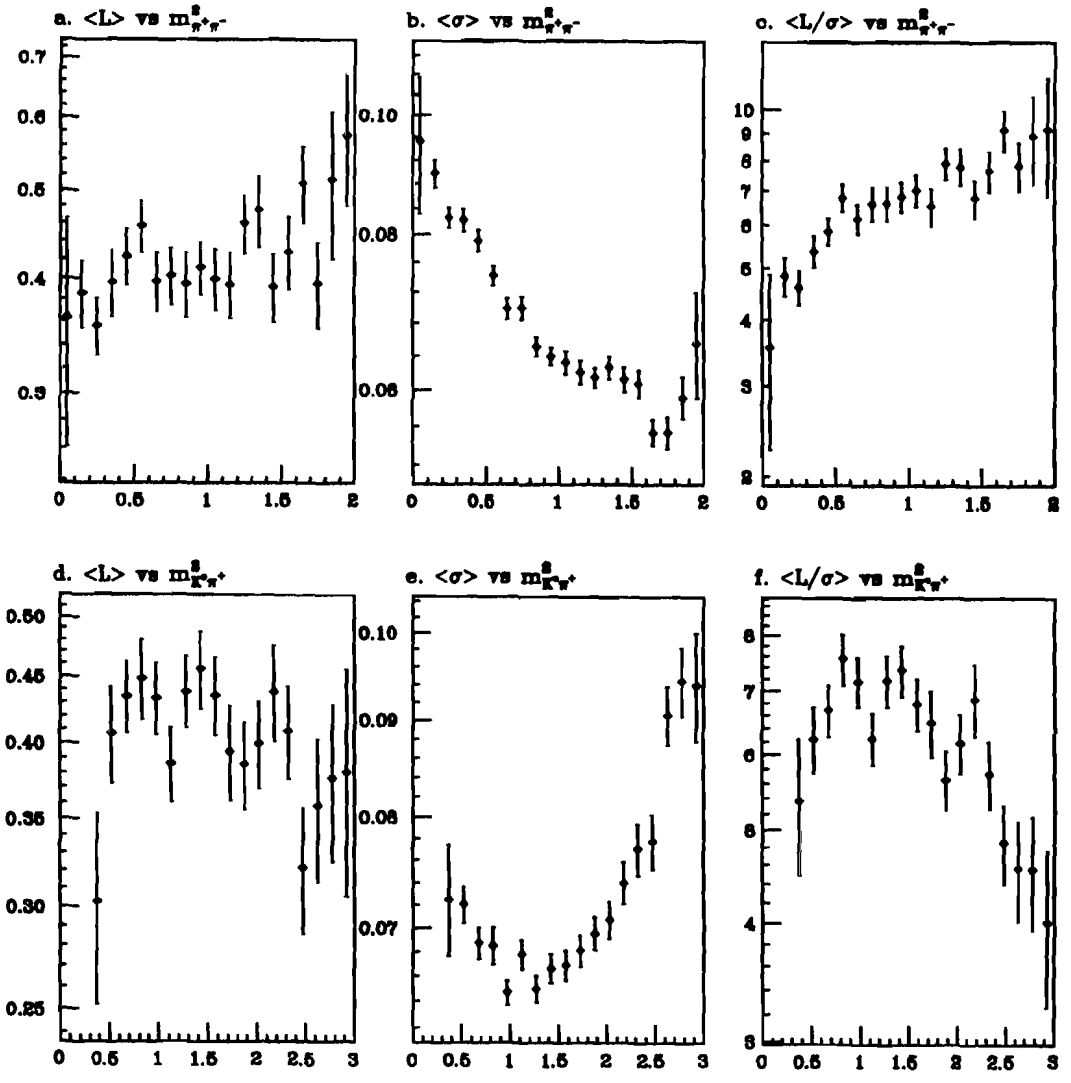

Figure 5.14. Average L, σ_L, and L/σ_L vs. $m^2_{K^0\pi}$ and $m^2_{\pi\pi}$. L and σ are measured in centimeters and the mass-squared variables are in GeV^2.

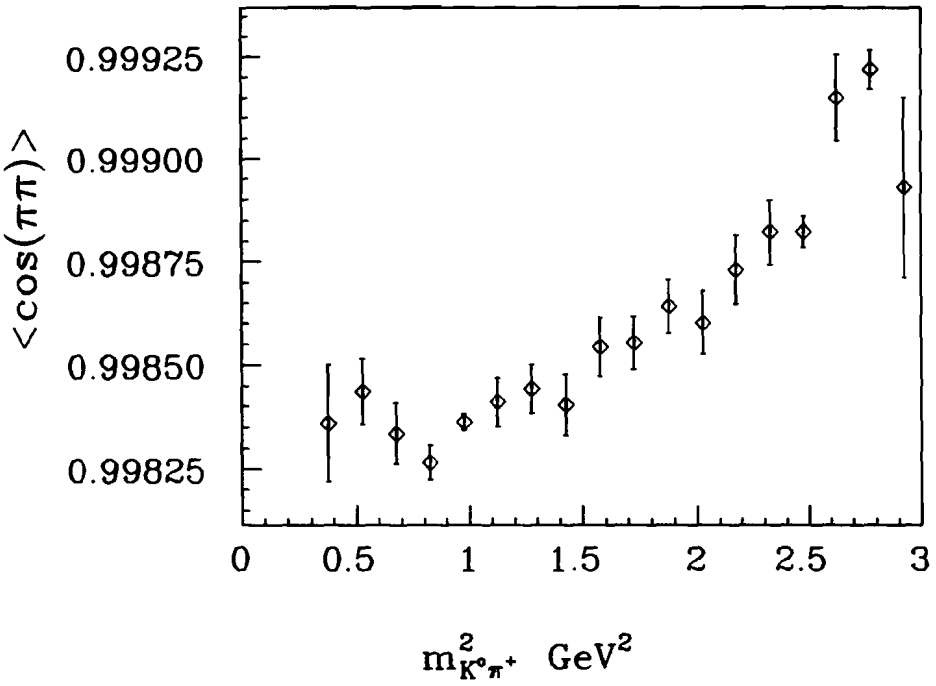

Figure 5.15. Average cosine π^+–π^- opening angle vs. $m^2_{K^\circ\pi}$.

Fig. 5.17.

Each efficiency correction method was applied to the data. The obvious advantage of the bin-by-bin method is there are no assumptions to make about the variation of the efficiency across the plot, and smoothing effects, for instance at the boundary of the plot, are avoided. The disadvantage is that much more computer time is required to get factors which will not be dominated by Monte Carlo statistics. In Section 5.7 the results using each method are discussed.

5.6.3 Spectrometer Mass Resolution

Next, a check for mass resolution effects was undertaken. For this study, the residuals between reconstructed masses and Monte Carlo generated masses were studied for events passing all of the analysis cuts used on the data sample. In particular, the mass differences $(m^{gen}_{K^\circ\pi} - m^{recon}_{K^\circ\pi})$ and $(m^{gen}_{\pi\pi} - m^{recon}_{\pi\pi})$ were studied as a function of position, or "region", on the Dalitz plot as defined in Fig. 5.18. The regions correspond

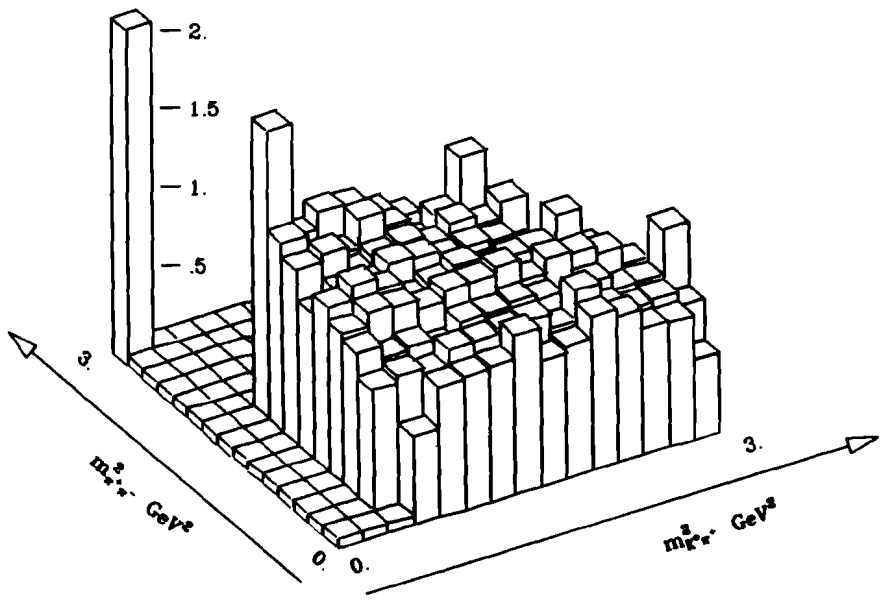

Figure 5.16. Bin-by-bin efficiency correction. The reference bin at left corresponds to a relative correction factor of 2.

to vertical (horizontal) bands in the $m^2_{K^0\pi}$ ($m^2_{\pi\pi}$) variable. In Fig. 5.19 the measured residuals for each of the bands are plotted in order of increasing mass-squared. The residuals are seen to grow increasingly worse for increasing $m^2_{K^0\pi^-}$ mass (σ=4.1 MeV $\rightarrow$ 10 MeV), corresponding to regions R1($m^2_{K^0\pi}$) to R5($m^2_{K^0\pi}$). Similarly, for for increasing $m^2_{\pi^+\pi^-}$ mass, corresponding to regions R1($m^2_{\pi\pi}$) to R4($m^2_{\pi\pi}$), the residual varys as σ=4.4 MeV $\rightarrow$ 8.2 MeV.

These effects can be understood by noting that the errors in the mass-squared variables depend on the measurement errors of the momenta of the daughter particles and the opening angles between pairs of tracks. In Fig. 5.20 the average cosine of the opening angles between the two pion tracks, and the kaon and pion tracks for the Monte Carlo events are plotted. As expected, lower values of invariant mass correspond to smaller average opening angles. Plotted on the same graphs are the mass errors for the corresponding mass-squared bins. The errors shown translate into worst case shifts of $\simeq$ 0.04 GeV^2 in the mass-squared variables. Thus even in the R4 or R5 bands the resolution is still very good when compared to typical binning

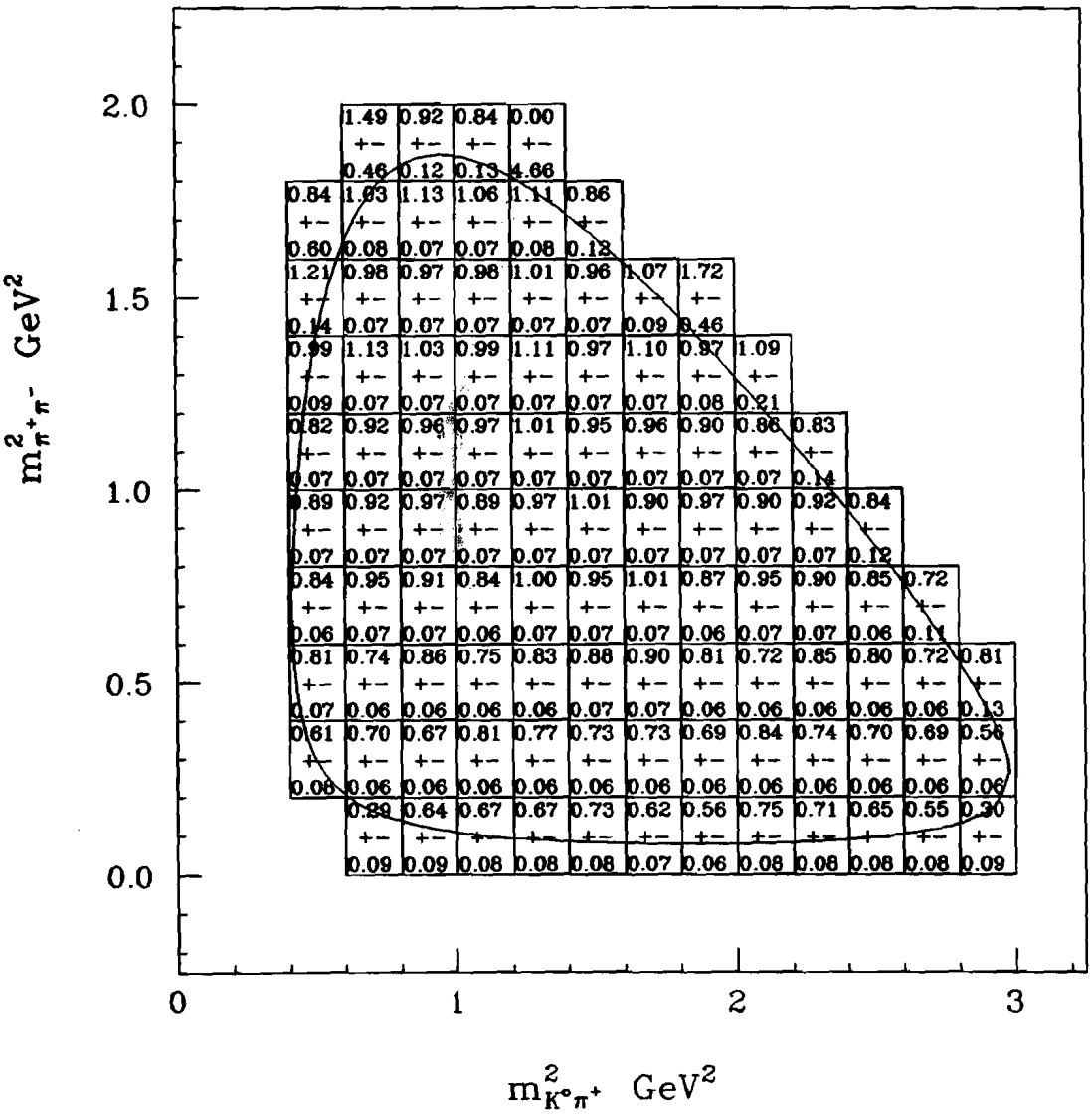

Figure 5.17. Bin-by-bin efficiency correction factors.

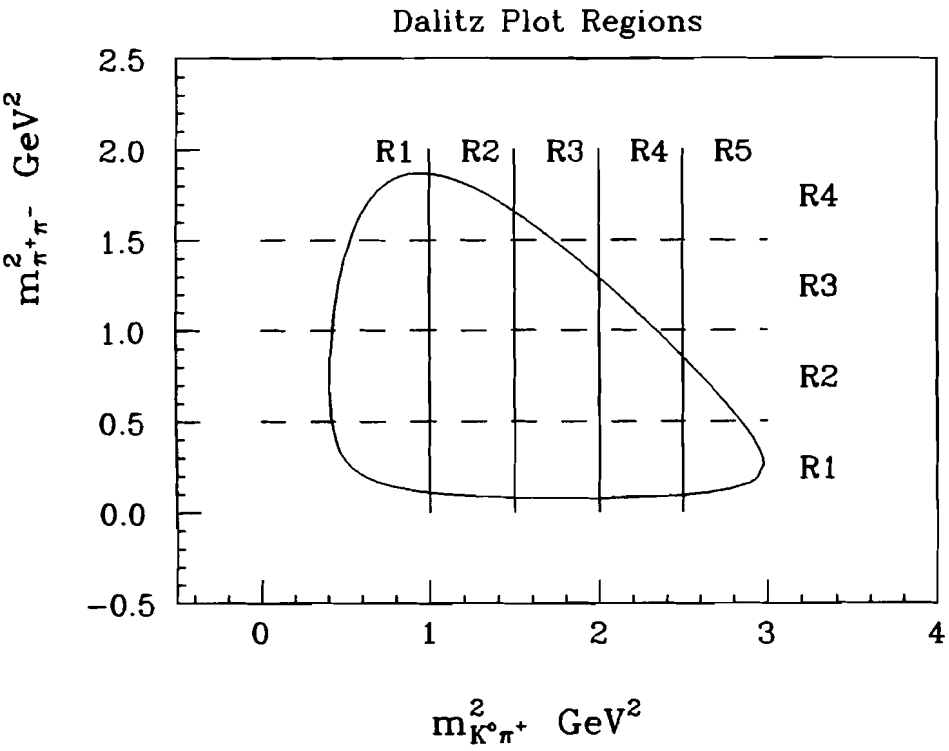

Figure 5.18. Dalitz plot regions for resolution studies.

sizes in the projection histograms (made during the fit comparisions but not for the fit itself), and when compared to the widths of the resonances in the decays.

Another way to observe the effect of the finite mass resolution is to measure the total shift in both $m^2_{K^\circ\pi}$ and $m^2_{\pi\pi}$ and count the number events shifting above a threshold limit of 0.03 GeV^2—one third of a bin width for the fit comparisions with the projection histograms. A sample of approximately 14 thousand Monte Carlo events passing all the analysis cuts was analyzed to determine the shifts in the mass-squared variables from the theoretical (i.e. generated) positions. Only 3.7% of the events experience shifts of greater than 0.03 GeV^2 upon reconstruction. This is plotted with arrows pointing from the generated to the reconstructed positions in Fig. 5.21 below. Note the regions of the Dalitz plot where the shifts are more likely to occur are in the higher mass-squared regions as was observed in Fig. 5.19.

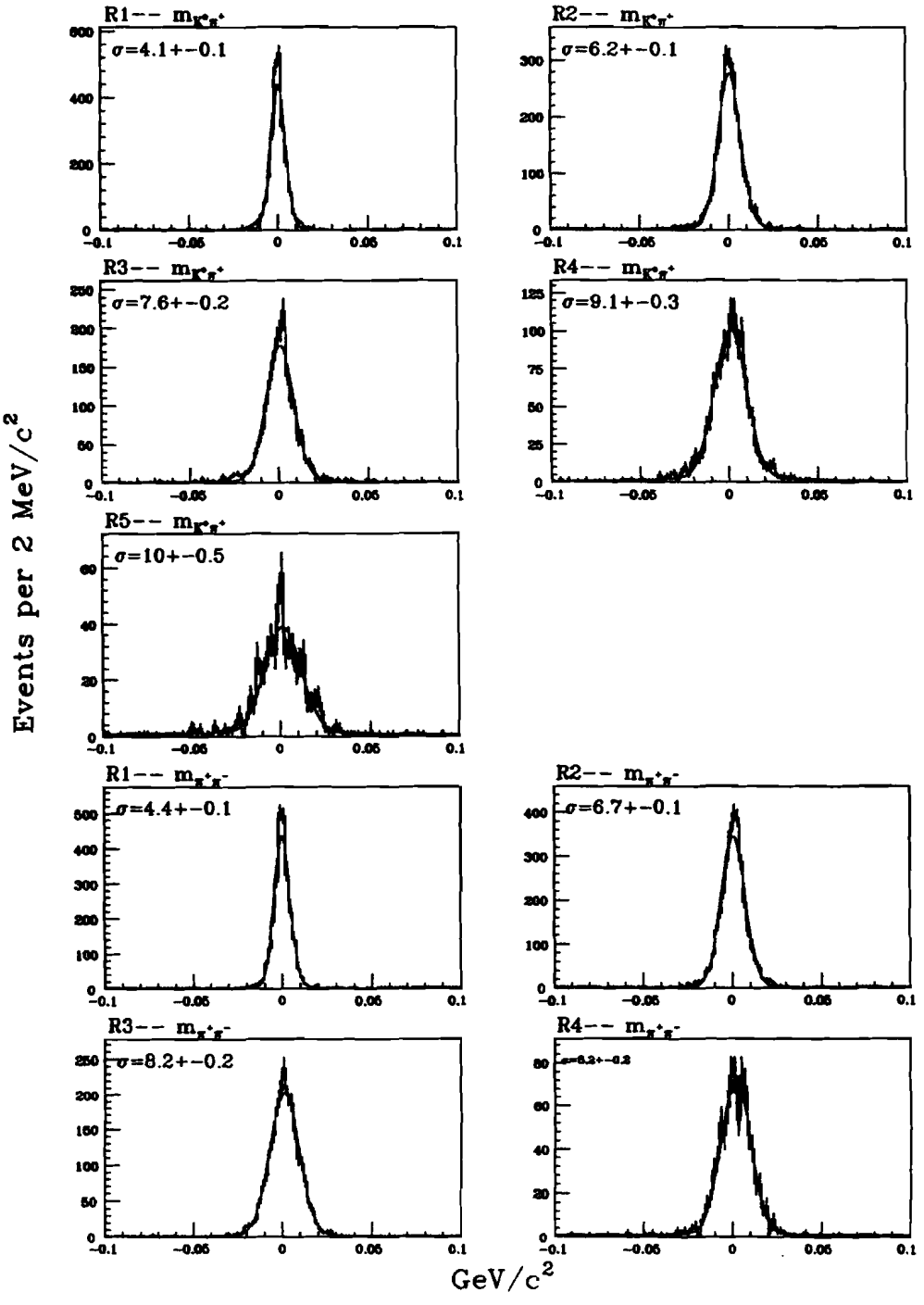

Figure 5.19. Mass residuals vs. Dalitz plot region. Plotted are the quantities for each of the bands defined in Fig. 5.18. The curves correspond to the fitted Gaussian functions and the σ's are in MeV.

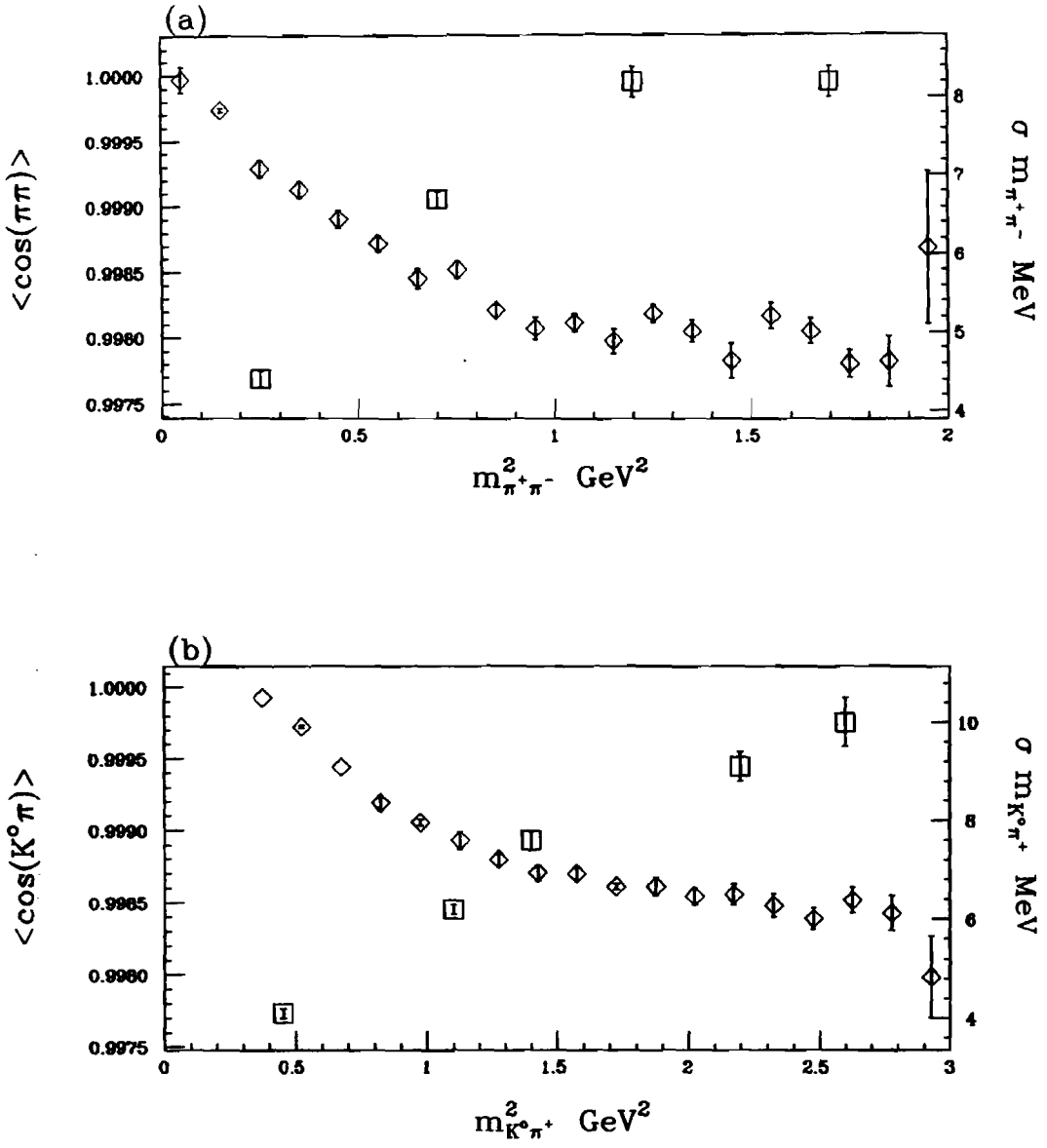

Figure 5.20. Average cosine of opening angle between particle pairs: a) π^+–π^- and b) K^o–π^- tracks, for the decay $D^o \rightarrow K^o_s\pi^+\pi^-$ (diamonds–left hand scale). The squares indicate the widths for the given mass bin (right hand scale).

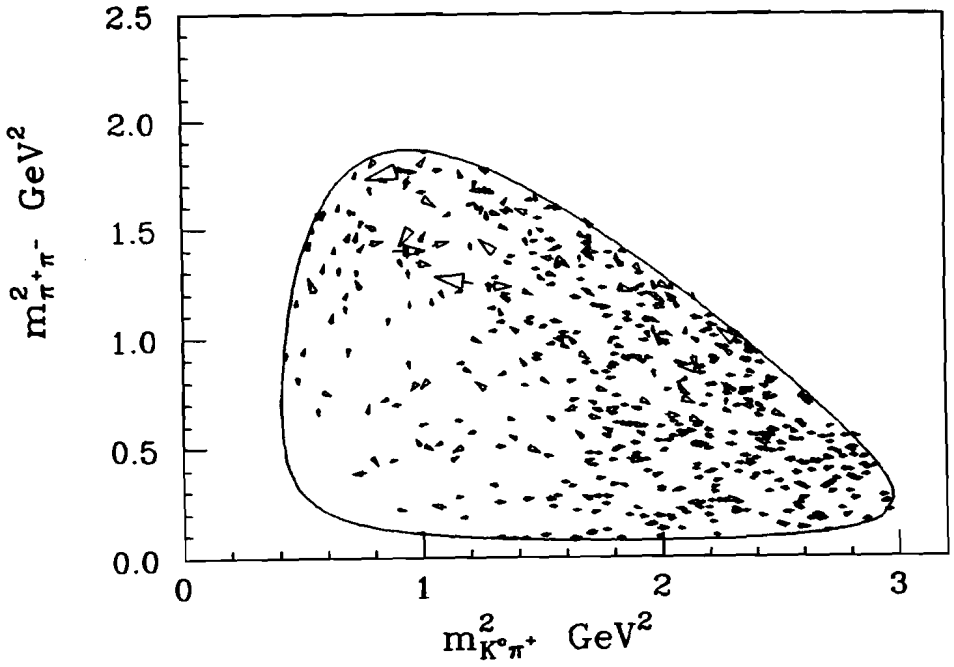

Figure 5.21. Mass measurement shifts in the Dalitz plot: the arrows point from the generated to reconstructed positions, and the size of the arrowhead is proportional to the shift. Only events with shifts greater than 0.03 GeV^2 are plotted.

5.7 *Fit Results on Data*

In the same manner as the Monte Carlo tests, the data were fit by incoherent or coherent sums of the three decay amplitudes, $\overline{K}^0\pi^+\pi^-_{\text{nonres}}$, $K^{*-}\pi^+$, and $\overline{K}^0\rho^0$. The fit results for the inclusive sample using a fully coherent sum of amplitudes and the two methods for efficiency correction are shown in Fig. 5.22. In these figures, the data are represented by points, and in each projection the upper histogram represents the fitted signal plus backgound function, while the lower histogram represents only the background; the dotted curve represents the interference contribution, plotted as the interference plus background term. In Fig. 5.23, plots illustrating the two dimensional χ^2 calcluations are shown in which symbols are drawn to scale according to the size of the χ^2 contribution for a particular bin, thus indicating specifically where the function results disagree with the data.

In Table 5.5 a summary of the corresponding fit parameters is given and in Table 5.6 the goodness of fit indicators from the fits are listed. The systematic errors,

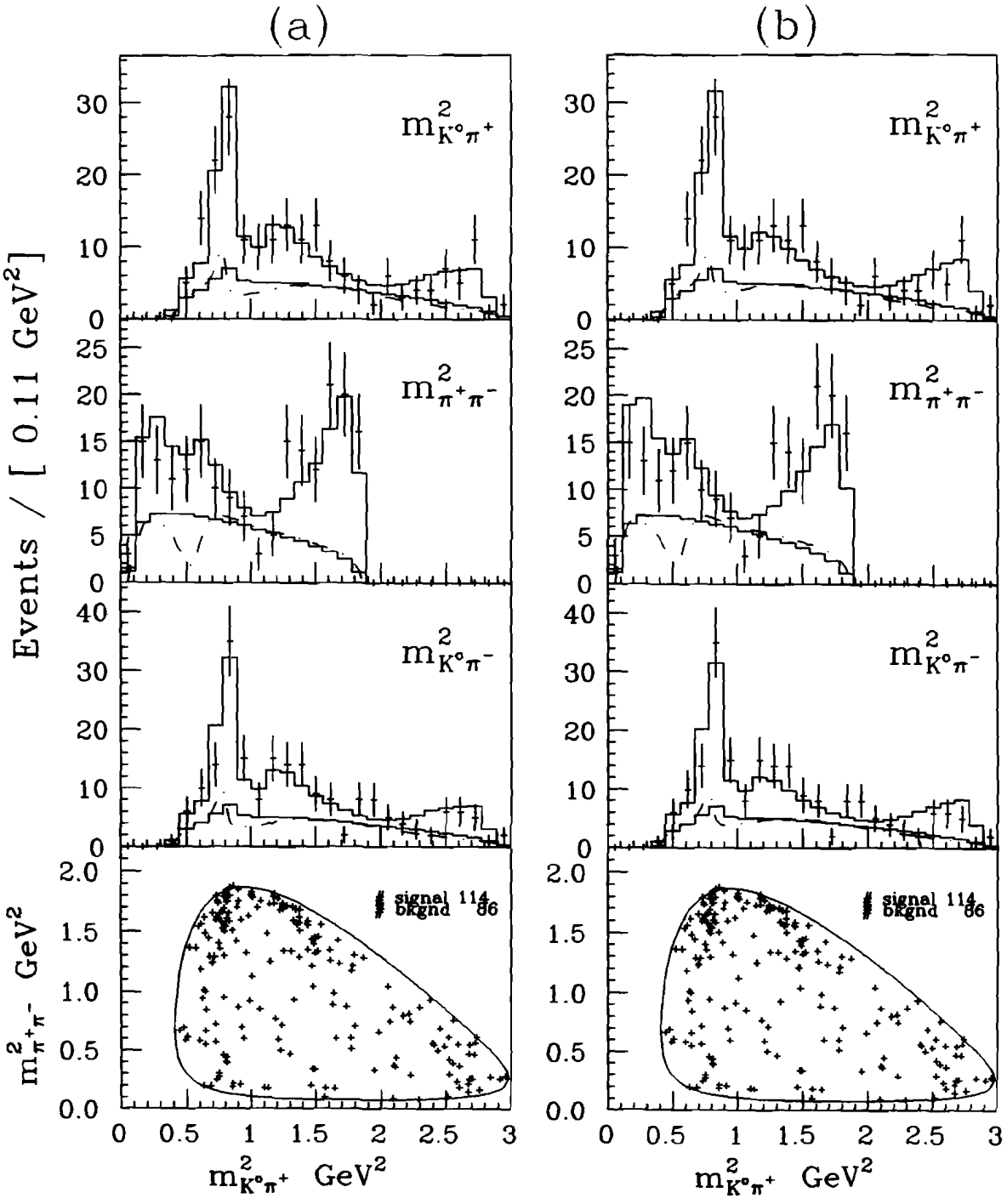

Figure 5.22. Fully coherent fit to the inclusive $L/\sigma > 10$ data set: a) using the bin-by-bin efficiency correction technique; b) the polynomial fit efficiency correction technique.

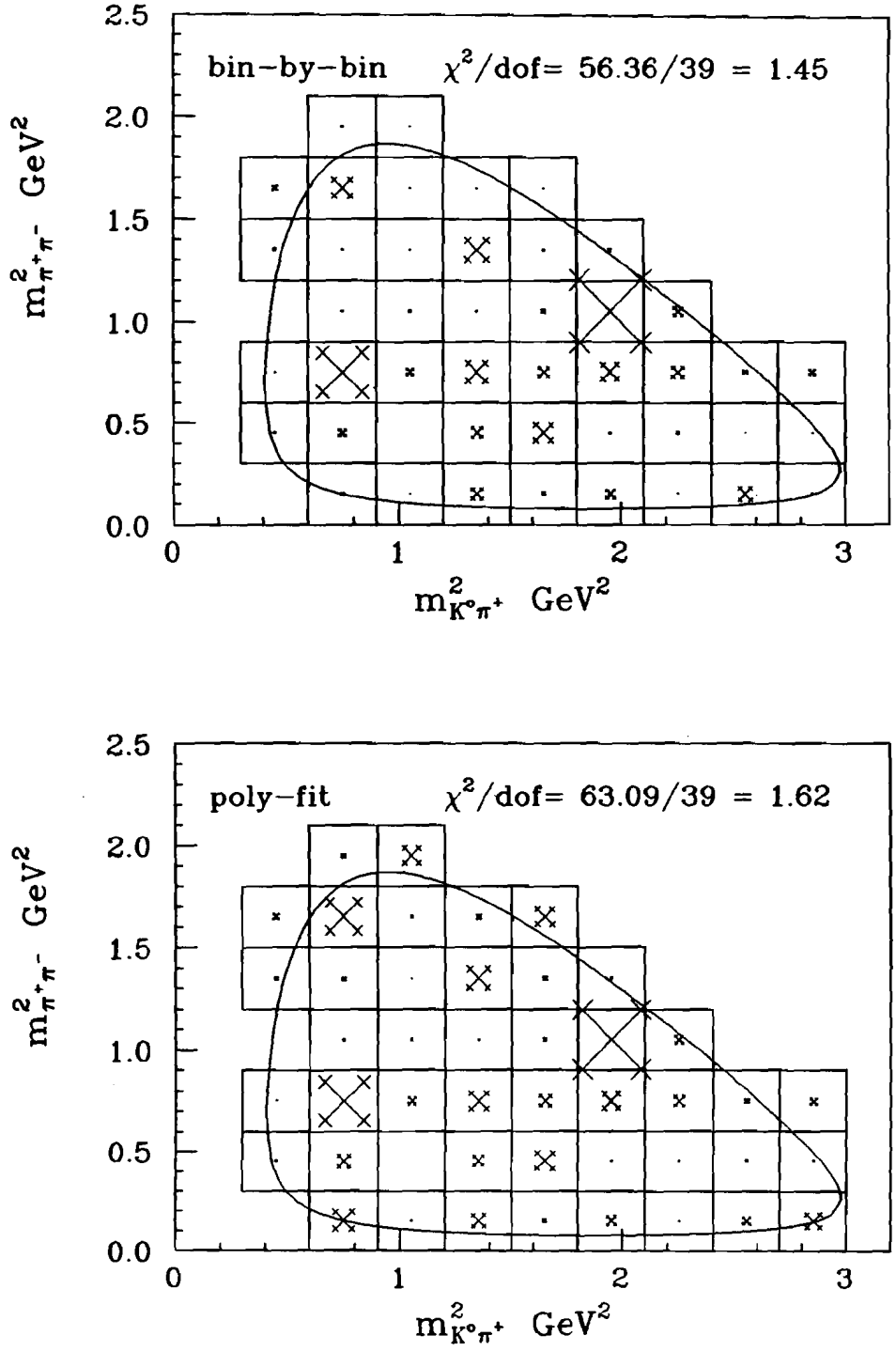

Figure 5.23. Two dimensional χ^2 evaluation for the fully coherent fit to the inclusive $L/\sigma > 10$ data set: a) bin-by-bin efficiency correction; b) polynomial fit efficiency correction.

the contributions of which are discussed in the following section, were estimated for the fit which used the bin-by-bin efficiency correction method. The fit results from Table 5.5 can be used to derive branching fractions using the known total decay fraction for $D^o \to \overline{K}^o\pi^+\pi^-$ (see Chapter 7).

Table 5.5. Dalitz plot fit results for $D^o \to K^o_s\pi^+\pi^-$ using two methods of efficiency correction. For the bin-by-bin corrected data, the first errors are statistical while the second are systematic.

(a) $D^o \to K^o_s\pi^+\pi^-$ (bin-by-bin)		
Mode	fit fraction (%)	phase (radians)
$\overline{K}^o\pi^+\pi^-_{\text{nonres}}$	$7\ ^{+12}_{-8} \pm 9$	$0.7\ ^{+0.8}_{-1.1} \pm 0.4$
$K^{*-}\pi^+$	$85\ ^{+13}_{-15} \pm 12$	0.0 (fixed)
$\overline{K}^o\rho^o$	$17\ ^{+11}_{-9} \pm 5$	$-2.51\ ^{+0.55}_{-0.50} \pm 0.48$

(b) $D^o \to K^o_s\pi^+\pi^-$ (poly-fit correction)		
Mode	fit fraction (%)	phase (radians)
$\overline{K}^o\pi^+\pi^-_{\text{nonres}}$	4 ± 8	1.0 ± 1.0
$K^{*-}\pi^+$	84 ± 14	0.0 (fixed)
$\overline{K}^o\rho^o$	17 ± 9	-2.3 ± 0.5

There are many options available to fit the data and many details to be considered when attempting to obtain the optimal fit results. The important points are discussed below.

Fit Parameters

The number of parameters of the fit were four: two coefficients and two interference angles. The fit coefficient of the most dominate mode, the $K^{*-}\pi^+$ mode, was fixed at one, and its phase angle fixed at zero radians. In Table 5.5, the "fit fractions" are

Table 5.6. Goodness of fit indicators final fits using the two methods of efficiency correction.

(a) $D^o \to K^o_s\pi^+\pi^-$ (bin-by-bin)			
$\chi^2(m^2_{K^o\pi^+})$	$\chi^2(m^2_{\pi^+\pi^-})$	$\chi^2(m^2_{K^o\pi^-})$	χ^2(2D)
1.07	1.12	1.63	1.45

(b) $D^o \to K^o_s\pi^+\pi^-$ (poly-fit correction)			
$\chi^2(m^2_{K^o\pi^+})$	$\chi^2(m^2_{\pi^+\pi^-})$	$\chi^2(m^2_{K^o\pi^-})$	χ^2(2D)
1.29	1.55	1.90	1.62

determined from the fit coefficients f_i^s of the likelihood function by dividing by the normalization constant, $\mathcal{N}^S$ of Eqn. 5.4, computed with all fit parameters set to their final values. Since the amplitudes are allowed to interfere these fractions do not sum to one.

Fit Coherence

Several types of fits were attempted: completely incoherent, partially coherent combinations between pairs, and the fully coherent fit. The best fit was chosen through comparison of the relative values taken by the negative log-likelihood, $-ln(L)$, and by judgement of the χ^2 quantities of the projection comparisons and the two dimensional comparison. Each type of fit can describe the data with some degree of consistency. However, this fitting technique prefers some level of coherence between the decay amplitudes (i.e. the completely incoherent returns the poorest set of χ^2 values), but it cannot distinguish whether or not the decay is completely coherent or partially coherent. In the latter case, the fraction of three-body non-resonant decays is reduced significantly to a value of $\simeq$ 1% from the fully coherent result of 7%. Thus, the fraction of three-body non-resonant decays observed is correlated with

the nature of the amplitude interference. If the three-body non-resonant amplitude is added incoherently with the amplitudes for the vector resonances, the fraction becomes smaller than what the fit process can reliably determine. This is considered a source of systematic error in the branching fraction determination.

Efficiency Correction

As discussed in the preceeding section, two techniques were employed in order to correct for the spectrometer acceptance. The best fit was obtained with the bin-by-bin method (Fig. 5.22a) in which the binning size was 0.2 GeV^2 by 0.2 GeV^2. The results using the bin-by-bin correction technique are listed in Table 5.5a. Acceptable fits were also obtained with the fitted polynomial correction function and are shown in Fig. 5.22b; however, the overall goodness of fit indicators, listed in Table 5.6 for the two techniques, were slightly worse.

Background Fractions

During the fitting process the background parameters, as determined from the sideband studies, were not allowed to vary. The systematic error incurred by this was small, as discussed below.

f_D Parameter

The data sample contained approximately equal numbers of D^o and $\overline{D}^o$ mesons, as determined by the parameter f_D of Eqn. 5.13. Allowing this parameter to vary, a value of $f_D = 0.49 \pm 0.05$ was obtained. In the final fits we did not allow this parameter to vary and assumed equal numbers of produced D^o and $\overline{D}^o$ mesons.

Interference Angles

The determination of the phase angles was not sensitive to the starting values they assumed in the fit. The relative differences between the amplitudes was always

returned as the same value within statistical error.

Statistical Errors

The statistical errors from the fitting process are determined by taking into account correlations between the fit parameters as well as the detailed shape of the likelihood function in the neighborhood of the determined minimum. Each parameter is varied about its minimum in steps chosen to be small enough so that several are needed until the negative log-likelihood reaches its minimum plus one half. At each of these intermediate steps, the remaining variables are allowed to vary and a new minimum is found. The amount by which each of the variables must be varied, in the positive and negative directions separately, until the function reaches its minmum plus one half determines the one standard deviation statistical errors.

In addition, the number of signal events (given in terms of the quantity f_{sig}) was not a parameter of the fit but was constrained from fits made to the $K^o_s\pi^+\pi^-$ invariant mass histograms of Fig. 5.1. This number itself has an uncertainty which is statistical in origin. To account for this statistical source of error, which is not included by the method outline above, the fraction of signal events was varied 1.5 standard deviations above and below its nominal value. The resulting changes in the parameters are added in quadrature to the error returned by varying the parameters individually until the negative log-likelihood function increases by one half. The fits using f_{sig} replaced by $f_{sig}+1.5\sigma(f_{sig})$ resulted in an increase of about about 6% in the fraction of three-body non-resonant events while decreasing the fraction into the $K^{*-}\pi^+$ channel by $\sim 11\%$. The effect on the $\overline{K}^o\rho^o$ channel was a few percent increase in the fit fraction.

The error determination for the $K^{*-}\pi^+$ fit fraction was made in a way similar to the others, with one exception. The fit coefficient of the three-body non-resonant decay channel was fixed to its final fit value. Then, as for the other fit coefficients, the value for the $K^{*-}\pi^+$ fit coefficient was stepped about its minimum and the remaining

parameters, with the exception of the fixed three-body coefficient, were allowed to vary to find an new intermediate minimum. The determination of the asymmetric errors on the $K^{*-}\pi^+$ fit fraction is illustrated in Fig. 5.24a. The strong correlation between the fit parameters can be illustrated by computing the resulting fit fraction for the three-body non-resonant channel as the $K^{*-}\pi^+$ fit fraction is varied about its minimum. This is shown in Fig. 5.24b.

Dalitz plot fit for $D^{*\pm} \to (K^o_s\pi^+\pi^-)\pi^\pm$

The D*-tagged sample suffered from poor statistics such that conclusive fits to all variables could not be obtained. This can be appreciated by considering the three-body non-resonant channel, which in the inclusive fit above was found to $\simeq 7\%$, would thus only have of order 10 events to determine its fraction and phase in the D*-tagged $L/\sigma_L > 5$ data set. We thus removed one parameter, the phase associated with the three-body non-resonant amplitude, and performed a partially coherent Dalitz plot fit to the sample. The fit results, shown in Fig. 5.25 and Table 5.7 show good agreement with the inclusive results. For this fit a similar bin-by-bin correction to that for the inclusive decay was used. Since the signal to background is very high for this data set ($\simeq 3$), this result provides a significant check to the inclusive Dalitz plot fit.

The Decay $D^o \to K^{*-}_o(1430)\pi^+$

A study was made to check for contributions from the $K^{*-}_o(1430)\pi^+$ decay channel, allowing for interference with the other amplitudes as well. In Fig. 5.26a a Monte Carlo event sample containing only the $K^{*-}_o(1430)\pi^+$ decay channel is shown for illustrative purposes. The fit result in which this amplitude was included in the likelihood function is presented in Fig. 5.26b. The data prefers a fit fraction for this mode of $2.2 \pm 5\%$, while the χ^2 comparisons (two-dimensional and also for the mass-squared projections) returned higher values than the fits with the amplitude excluded. The results thus suggest no conclusive evidence for $D^o \to K^{*-}_o(1430)\pi^+$ decays, even

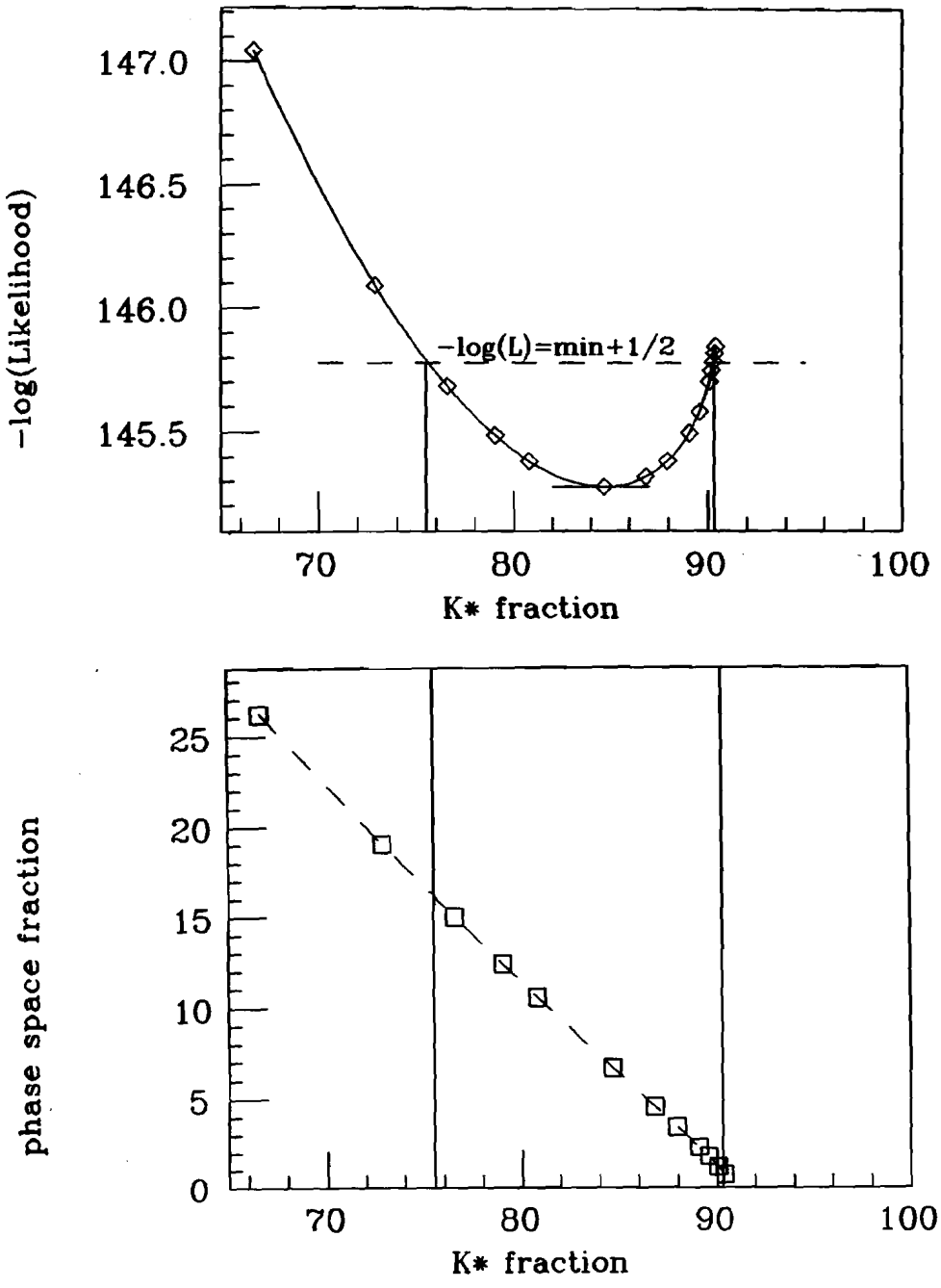

Figure 5.24. Error determination for $f(K^{*-}\pi^+)$ and correlations: a) the $K^{*-}\pi^+$ fit fraction is varied about is minimum; b) correpsonding three-body non-resonant fraction at these intermediate minima.

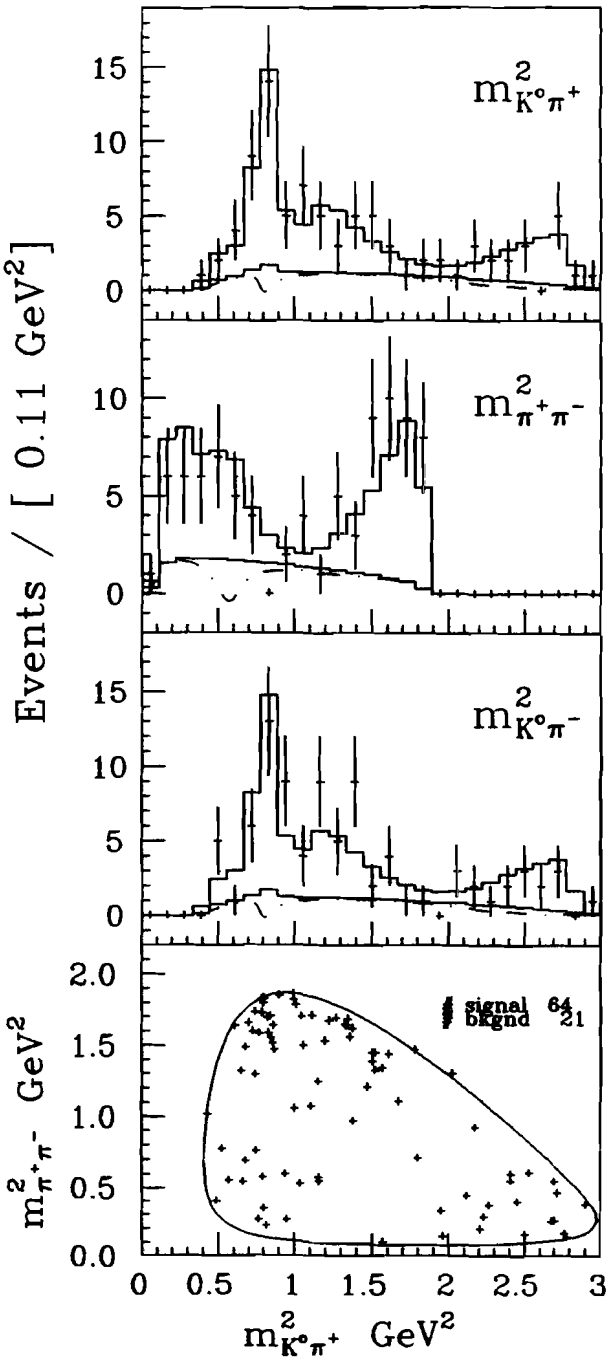

Figure 5.25. Partially coherent fit to the D*-tagged sample.

Table 5.7. Dalitz plot fit results for $D^{*\pm} \rightarrow (K^{\circ}_{s}\pi^{+}\pi^{-})\pi^{\pm}$.

(a) $D^{*\pm} \rightarrow (K^{\circ}_{s}\pi^{+}\pi^{-})\pi^{\pm}$ results		
Mode	fit fraction (%)	phase (radians)
$\overline{K}^{\circ}\pi^{+}\pi^{-}_{\text{nonres}}$	10 ± 12	—
$K^{*-}\pi^{+}$	80 ± 15	0.0 (fixed)
$\overline{K}^{\circ}\rho^{\circ}$	21 ± 9	-2.7 ± 0.6

(b) goodness of fit indicators for $D^{*\pm} \rightarrow (K^{\circ}_{s}\pi^{+}\pi^{-})\pi^{\pm}$			
$\chi^2(m^2_{K^{\circ}\pi^{+}})$	$\chi^2(m^2_{\pi^{+}\pi^{-}})$	$\chi^2(m^2_{K^{\circ}\pi^{-}})$	$\chi^2(2D)$
1.00	1.35	1.33	0.86

when interference is allowed with the other amplitudes.

5.8 *Systematic Error Estimates*

There are a number of important considerations concerning the systematic errors associated with the fit fractions and phase angles, and thus the branching ratios. Each of the uncertainties discussed below were added in quadrature to the total systematic error.

Background Parameterization

To gauge the extent to which the background parameterization can affect the results, the sample was refit after fixing the K* background fraction to the most extreme values it could reasonably take while giving good fits to the sidebands. The result was an increase in the fit fraction attributed to the three-body non-resonant decays of 1-2%, while the $K^{*-}\pi^{+}$ fit fraction decreased by 3-4% and the $\overline{K}^{\circ}\rho^{\circ}$ increased by 2%. The relative phase of the three-body non-resonant amplitude shifted positively

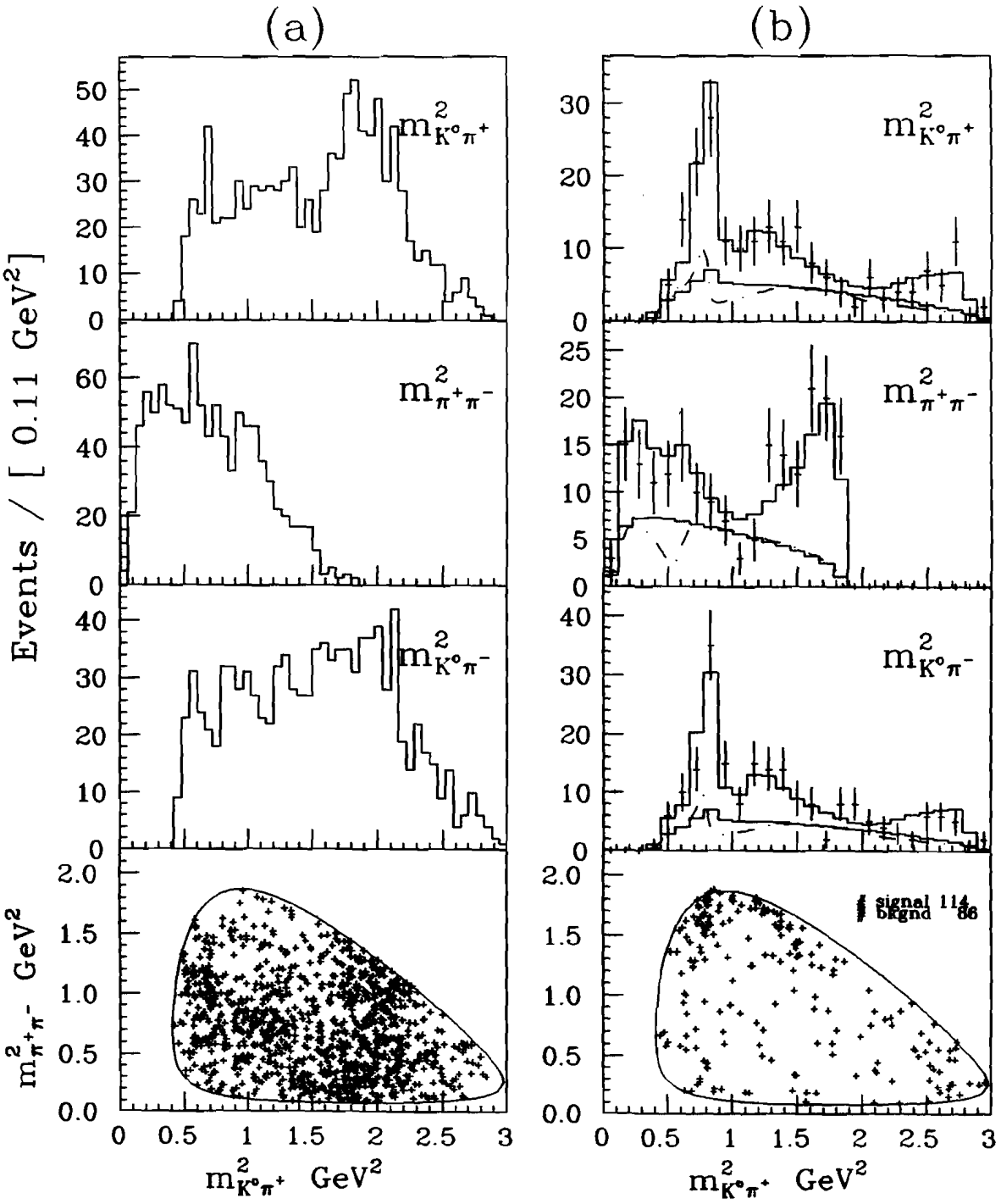

Figure 5.26. Dalitz plot fit including to the amplitude for $D^0 \to K_0^{*-}(1430)\pi^+$: a) a Monte Carlo sample of 1000 $D^0 \to K_0^{*-}(1430)\pi^+$ events; b) fully coherent fit on the data sample including the amplitude for $D^0 \to K_0^{*-}(1430)\pi^+$.

by 30% of its fit value.

Efficiency Correction

For this uncertainty we simply took the differences between the bin-by-bin method and the fitted mass-squared polynomial methods, and the results obtained with no efficiency corrections applied. The stability of the bin-by-bin method was checked by varying the binning size. The range of differences between methods were ~5% for the three-body non-resonant channel, ~5% the $K^{*-}\pi^+$ channel, while the effect was much less on the $\overline{K}^o\rho^o$ channel, < 1%. These results are consistent with the contours of the efficiency accross the Dalitz plot in which the $m^2_{\pi\pi}$ variations were much stronger than those in $m^2_{K^o\pi}$.

Coherent Fit Uncertainty

As mentioned above, the results from incoherent and partially coherent fits differ significantly from those of the completely coherent fit, affecting mostly the three-body non-resonant channel. The tendency of these fit combinations is to attribute all of the data to the two-body resonance decays, leaving a three-body fraction of about 1%. Most of the decays feed into the $K^{*-}\pi^+$ channel, increasing its fraction. The shifts in values from the different techniques were approximately 6% for the three-body non-resonant, ~5% the $K^{*-}\pi^+$ amplitude, and for the $\overline{K}^o\rho^o$ channel, ~ 3%. The difference in the relative phase angle between the $\overline{K}^o\rho^o$ and $K^{*-}\pi^+$ amplitudes using the completely coherent or partially coherent fit was approximately 0.4 radians.

L/σ_L Selection

Data samples selected with L/σ_L requirements near that of the $L/\sigma_L > 10$ data set were studied to find shifts from the final results of Table 5.5. This can be an important source of error, since the nature of the background may not be constant as a function of L/σ_L . In addition, this provides an additional variation of the efficiency correction

factors, since they depend on the value of L/σ_L used. Reasonable fits (resulting in good confidence levels) could obtained for the values $L/\sigma_L > 8,9,11$. The effect was most significant for the $K^{*-}\pi^+$ channel, in which values differed by 9% between the samples. In addition, the three-body non-resonant channel spread was about 5% between fits. As with the efficiency correction, the $\overline{K}^0\rho^0$ channel was affected the least: variations of only 2% were observed.

CHAPTER 6

THE DECAY $D^o \rightarrow K^o_s K^+ K^-$

This chapter describes a study of the decay $D^o \rightarrow K^o_s K^+ K^-$. The final state is of interest since it contains the decay mode $D^o \rightarrow \overline{K}^o \phi$, which in principle is a test of non-spectator processes in weak decays. Also of interest is the remaining or competing fraction of decays leading to the $K^o_s K^+ K^-$ final state; in this study the decay rate $D^o \rightarrow \overline{K}^o (K^+ K^-)_{non-\phi}$ is measured as well.

The $D^o \rightarrow \overline{K}^o K^+ K^-$ (inclusive), $D^o \rightarrow \overline{K}^o \phi$, and $D^o \rightarrow \overline{K}^o (K^+ K^-)_{non-\phi}$ branching ratios were measured through comparison to the $D^o \rightarrow \overline{K}^o \pi^+ \pi^-$ decay channel. The observed event yields into these channels were corrected for spectrometer acceptance and detector inefficiencies using Monte Carlo simulations. In addition, factors derived from studies of the response of the E687 spectrometer using the actual data sample were used to correct the event yields. For the decay mode in question, the relative branching ratio was obtained by dividing the corrected number of events into that mode by the corrected yield of decays $D^o \rightarrow K^o_s \pi^+ \pi^-$. The $K^o_s \pi^+ \pi^-$ channel was chosen as the comparison channel due to its larger branching ratio and similar decay topology. The feature that all the modes contain a K^o_s meson will tend to reduce the systematic uncertainties associated with correcting for vee detection inefficiency. Also, as each final state contains two charged tracks emerging from a vertex upstream of the SSD detectors, systematic differences between corrections due to the vertex reconstruction will be lessened. This also holds for PWC-SSD track linking efficiency,

where again each mode has the same linking requirements.

The resulting relative branching ratios can then be used to infer absolute branching fractions using the known $D^o \rightarrow \overline{K}^o\pi^+\pi^-$ branching fraction. The method of acceptance correction is discussed first, followed by the results for the three branching ratios.

6.1 Acceptance Corrections

We discuss first the acceptance correction for the decay $D^o \rightarrow \overline{K}^o\pi^+\pi^-$. Using the methods outlined in Section 4.5, a sample of Monte Carlo events was generated using the E687 GENERIC charm production and decay generator and the ROGUE spectrometer simulation package. The details of the generation and simulation were similar to those of Section 4.5, namely, a photon-gluon fusion cross section was used to model the charm quark production, and a 'dressing' function was used to describe the subsequent hadronization of the charm quarks into the final state mesons. This function was specified by a flat distribution in the variable z, defined in the quark-gluon rest frame as the fraction of the charm quark momentum given to the the charm meson. As will be seen shortly, the model dependence of the generator was effectively removed during the acceptance correction.

From the Monte Carlo sample of events an acceptance function was derived by counting the number of events passing each of the analysis cuts used to isolate the charm candidates and dividing by the generated number. A summary of the selection requirements that were needed for the decay $D^o \rightarrow K^o_s\pi^+\pi^-$ was given in Section 4.7.2. The measurement of the acceptance function was the subject of considerable study.

It was suggested [44] that dependence on the production and decay models implemented in the Monte Carlo generator could be avoided if the acceptance corrections were applied as a function of a suitable scaling variable of the candidate (eg. the Feynman variable x_F or the D^o energy or momentum). In this way, precise agree-

ment between the Monte Carlo models and the actual production and decay dynamics need not be assumed, and thus the chance of introducing systematic biases into the corrected yields would be reduced. Following this suggestion, D^o momentum dependent acceptance corrections for each of the decay modes were made as follows. The generated events were binned in D^o momentum intervals which were chosen to be small enough to account for the regions in which the acceptance was rapidly varying, but large enough to acquire adequate statistics. The bin size thus chosen was $\delta p = 10$ GeV/c. The distribution of the fraction of generated events, binned in momentum, passing all the analysis cuts was fitted to a polynomial curve, suitably restricted in momentum to ensure a good fit. In Fig. 6.1 the fitted acceptance functions for the $K^o_s\pi^+\pi^-$ mode for various values of the L/σ_L cut shown. For events satisfying the $L/\sigma_L > 10$ requirement, the acceptance below 30 GeV/c is approximately zero. After that point, the acceptance steadily rises, leveling off at around 7% at a candidate momentum $P(D^o) \simeq 100$ GeV/c. Beyond this point the acceptance drops, more slowly, to 3% at $P(D^o) \simeq 200$ GeV/c. The general shape of theses curves was governed by the acceptance of the RESH detector and the hadron calorimeter efficiency in forming the second level trigger.

Using these acceptance functions, candidate momentum dependent acceptance corrections were applied on an event-by-event basis. Each entry into the invariant mass histogram was weighted by an acceptance factor taken as the inverse of the acceptance function evaluated at the candidate momentum. Thus a weighting function was applied, given as a function of the D^o momentum $P(D^o)$,

$$w(P) = \frac{1}{\epsilon(P)} \tag{6.1}$$

where $\epsilon(P)$ is the acceptance function. The actual weights used on the data are shown in Fig. 6.2 for the (a) $L/\sigma_L > 3$, (b) $L/\sigma_L > 5$, and (c) $L/\sigma_L > 10$ data sets.

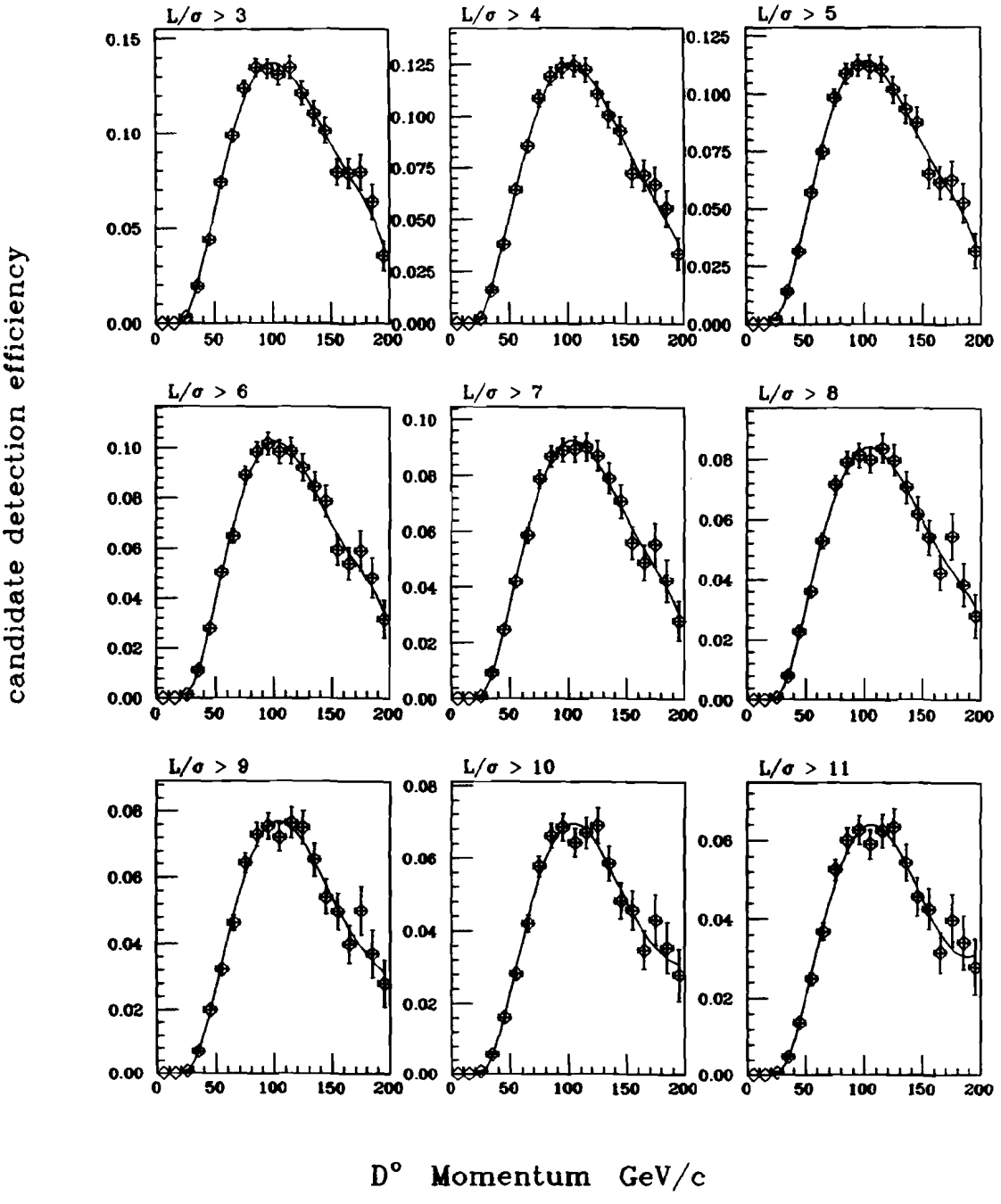

Figure 6.1. Acceptance curves for $D^o \rightarrow K^o_s\pi^+\pi^-$ events.

These figures illustrate that the average weights were constant as a function of the invariant mass $M(K_s^o K^+ K^-)$ for a given set of analysis cuts. Note using this weighting technique, the background events are weighted with the same factors as the charm data; if the general features of the signal (eg. width, signal to noise) are retained then weighting procedure should be valid. For the $L/\sigma_L > 10$ events, the mean weighting factor was $\simeq 25$. The result of applying these weighting factors to the data is a corrected invariant mass distribution from which the true number of events produced in the experiment can be derived. As corrections applied to each of data sets having different L/σ_L requirements should produce the (same) true yield of events, the yields derived from these weighted histograms should be equal to within errors accounting for fluctuations in the data as well as the weighting factors themselves. After the data sets of Figs. 4.11 for the $K_s^o \pi^+ \pi^-$ decay mode were corrected with the appropriate (event-by-event) factors, the invariant mass distributions of Fig. 6.3 were produced.

The weighted histograms were fit to Gaussian functions representing the signal contributions and straight line curves for the background. A quick glance at the fitted yields marked on the figures indicates good agreement (within the quoted statistical errors) across a large range in L/σ_L . The yields from Fig. 6.3 are plotted in Fig. 6.4 where the uniformity of the correction is quite evident.

As mentioned above, it is important to check that the correction technique does not alter the properties of the signal in unexpected (or unwanted) ways. The signal parameters of the raw and corrected events can be judged for consistency. For example, the fitted signal parameters corresponding to curve superimposed on the histogram of Fig. 6.3 for the $L/\sigma_L > 10$ data set are summarized in Table 6.1 and can be compared with the uncorrected result. Note that fitted mass peak retains a central value consistent with that of the unweighted histogram fit while the width is very nearly consistent with the expected mass resolution for this state, which was determined from a Monte Carlo study of the E687 detector to be 12 MeV. Although the

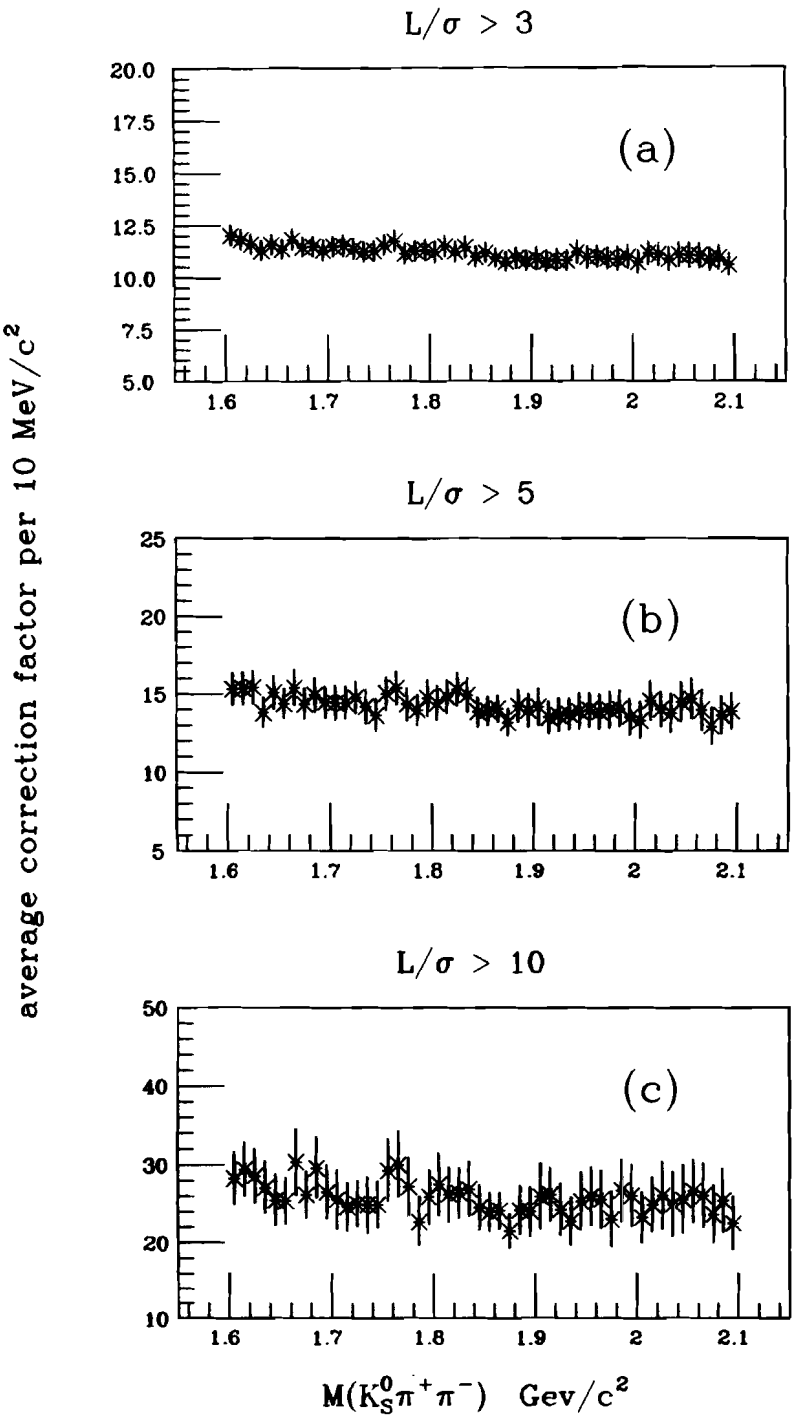

Figure 6.2. Weighting factors for the $D^0 \to K^0_s\pi^+\pi^-$ events for three values of the L/σ_L requirement.

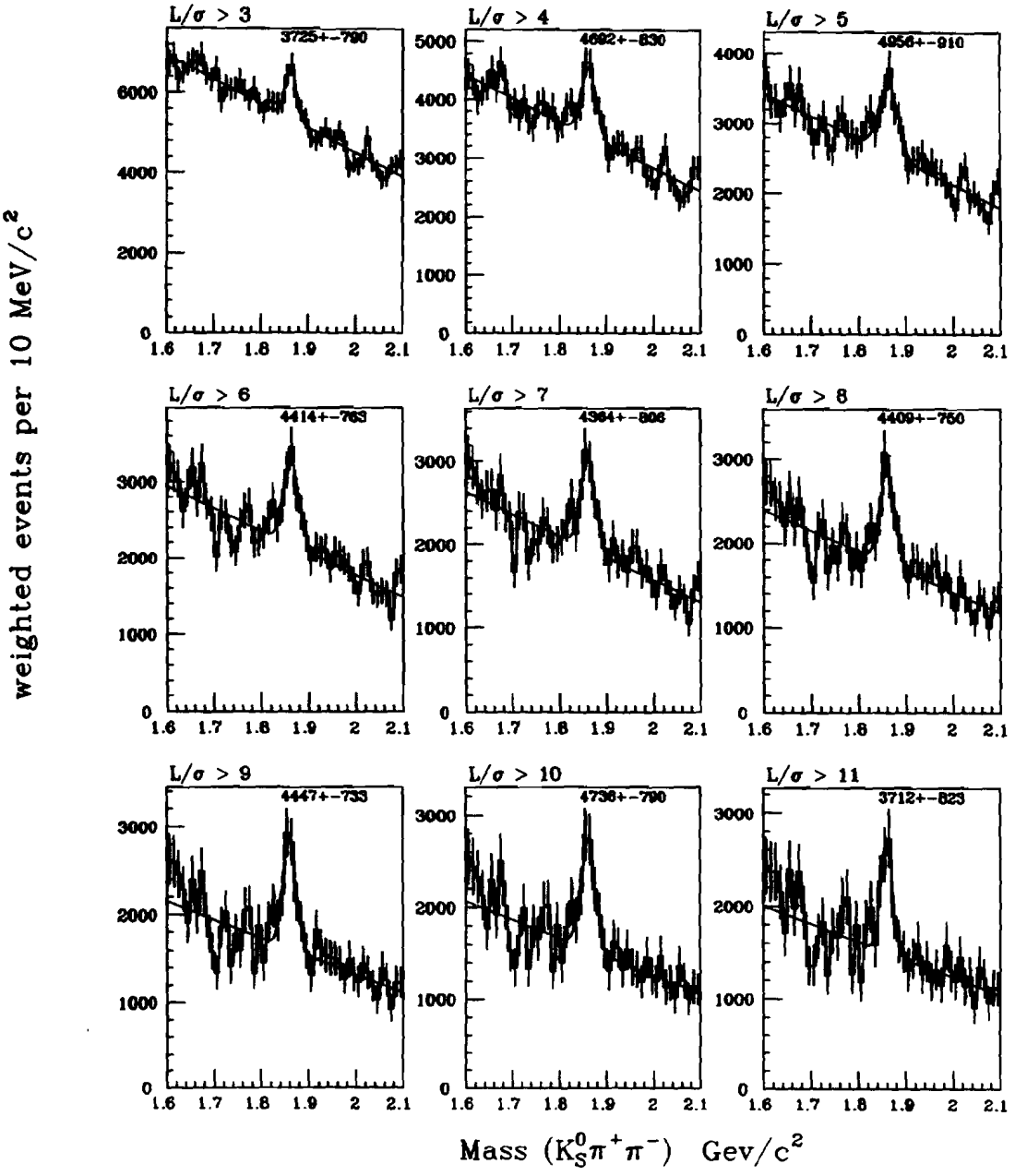

Figure 6.3. Weighted $K_s^o\pi^+\pi^-$ mass distributions.

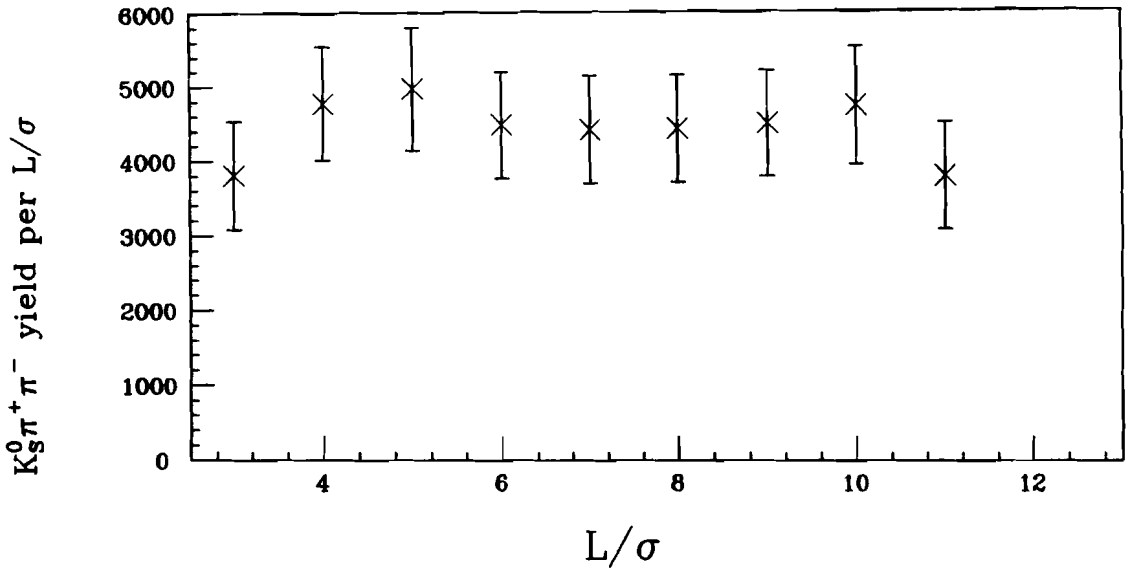

Figure 6.4. Corrected $D^o \rightarrow K^o_s\pi^+\pi^-$ yields vs. L/σ_L .

weighting technique introduced a slight degradation in the signal to background ratio, the value is consistent with the unweighted ratio to within one standard deviation (see for reference Table 4.4).

One issue that needs to be dealt with in the weighting procedure is the correct assignment of statistical errors for each of the bin entries. As a result of the weighting procedure, additional uncertainties are introduced from the random fluctuations in the weights, owing mainly to finite Monte Carlo statistics. These fluctuations can be added in quadrature to the statistical fluctuation in the raw number of bin entries. Thus, errors to the weighted histograms are assigned by

$$\sigma_w = \sqrt{\Sigma_i w_i^2} \tag{6.2}$$

so that the statistical error on the bin is given simply by the square root of the sum of squared weights for that bin. The statistical error for each bin entry can also be computed by scaling the weighted bin contents by the fractional error of the

unweighted bins. In practice slight differences between the two methods were found to occur when evaluating fit parameter errors: typically the first method gives somewhat larger fractional errors. For the discussions that follow, the first method was used to determine the errors for each histogram bin. These errors are reflected in the fitted signal parameters of the weighted histograms.

From the $L/\sigma_L > 10$ data set, the weighted yield of 4736 ± 790 events was used as a reference in computing the relative branching ratios of the $K_s^o K^+ K^-$ decay channels.

Table 6.1. Weighted $D^o \rightarrow K_s^o \pi^+ \pi^-$ signal parameters for $L/\sigma_L > 10$.

Yield	4736 ± 790
Mass	1860 ± 3 MeV/c^2
Width	16 ± 3 MeV/c^2
Signal/Noise	0.6

For the $K_s^o K^+ K^-$ decay modes, a similar procedure was followed. An important complication, however, involved the method of correcting for the kaon identification inefficiency of the E687 Čerenkov system. Acceptance weighting functions were determined using two methods to account for this inefficiency. The first assumed an efficiency derived from the ROGUE Monte Carlo program which took into account detection features such as the mirror geometry, Čerenkov light emission thresholds, and the detection efficiencies for the cells of each of the detectors C1, C2, and C3. The fitted acceptance curves for all cuts pertaining to the inclusive $K_s^o K^+ K^-$ final state are shown in Fig. 6.5a for five values of the L/σ_L requirement. Note that in these plots the stringent cuts imposed by the kaon identification are found to be compensated by the less restrictive $L/\sigma_L > 3$ requirement, resulting in an overall acceptance comparable to the $K_s^o \pi^+ \pi^-$ state subject to the $L/\sigma_L > 10$ requirement.

The second method ignored all aspects of the kaon identification in the Monte

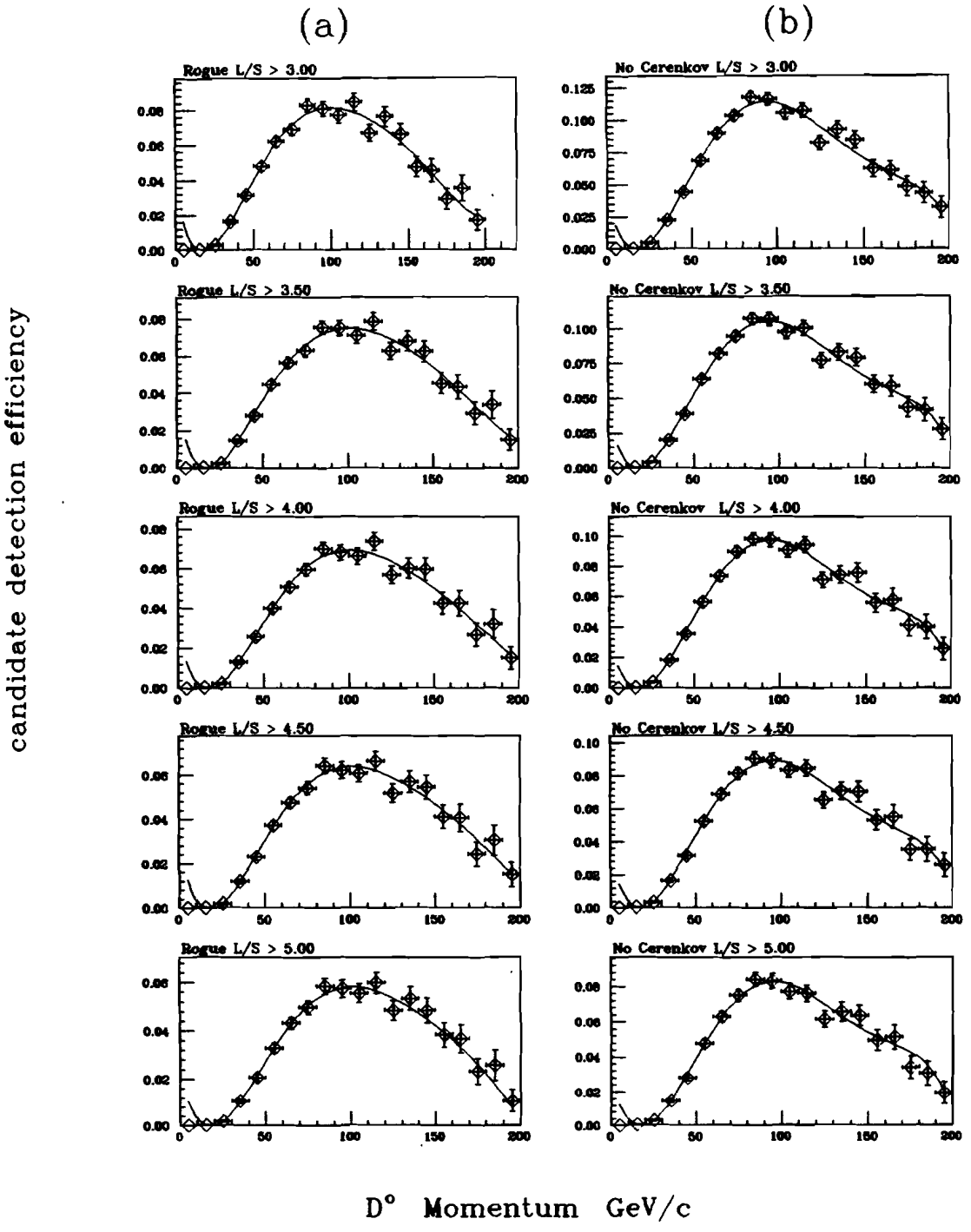

Figure 6.5. Acceptance functions for the decay $D^o \rightarrow K_s^o K^+ K^-$: a) the kaon identification requirements using the ROGUE Monte Carlo are included; b) they are not included.

Carlo, but took advantage of measurements of single kaon detection efficiency derived from studies of large samples of D-meson decays $D^o \rightarrow K^-\pi^+$,$K^-\pi^+\pi^+\pi^-$, and $D^+ \rightarrow K^-\pi^+\pi^+$ [45]. Unlike the decay $D^o \rightarrow K^o_s K^+ K^-$, very clean samples of these decays were obtainable from the experimental data sample using only decay length cuts based on topologically identified vertices. The signal peaks were fitted to obtain yields before and after the kaon identification cuts were applied. The efficiency for the positive kaon identification was then calculated both as a function of the kaon momentum and whether it was detected as a 5-chamber track or 3-chamber stub. Within either the track or stub category the momentum dependence is slight. The efficiencies for the identification category of 'kaon definite', 'kaon/proton ambiguous', and 'kaon/pion/electron ambiguous' (for $P(K)$ >60 GeV/c) are listed in Table 6.2 for reference. The efficiencies listed the Table 6.2 may even be replaced by two overall correction factors: one for tracks and one for stubs [35]. However, in this analysis the values directly from Table 6.2 were used.

Table 6.2. Data-derived kaon identification [45].

kaon momentum (GeV/c)	tracks	stubs
4.95 < P(K) < 17.5	.74 ± .10	.66 ± .07
17.5 < P(K) < 23.3	.54 ± .10	.55 ± .08
23.3 < P(K) < 44.3	.71 ± .08	.50 ± .07
44.3 < P(K) < 60.8	.71 ± .11	.50 ± .07
P(K) > 60.8	.82 ± .09	.50 ± .07

The correction method, using these data-derived efficiencies, then entails determining the overall acceptance as a function of the D^o momentum for all cuts up to, but excluding, the Čerenkov identification cuts. The acceptance curves as a function of D^o momentum corresponding to this circumstance are shown in Fig. 6.5b. The

incoming D^o candidate events are then weighted using this acceptance function and a product of two kaon identification weights, given by the inverse of the efficiency listed in Table 6.2, for each of the kaons in the candidate combination. The resulting $K^o_s K^+ K^-$ mass distributions after the corrections have been applied are shown in Fig. 6.6 for each of the two weighting methods.

The weighted mass histograms were fit using Gaussian functions for the signal events and a second order polynomial for the background events. The best fit could be obtained when the widths were constrained to have the values of the corresponding unweighted histograms, in this case 7.0 MeV/c^2. The resulting weighted signal parameters are listed in Table 6.3 for the $L/\sigma_L > 3$ data set, and as before the corrected yield in steps of L/σ_L is shown in Fig. 6.7 for the two methods. The difference in the corrected yield between the two correction methods is significant ($\simeq$ 30%), and obviously figures prominently in the $D^o \to \overline{K}^o K^+ K^-$ branching ratio measurement. The reason for the difference is due to an overestimation of the kaon identification efficiency by the Monte Carlo. As was pointed out earlier, the Monte Carlo simulation did not simulate processes such as noise within phototubes, sources of stray light (eg. embedded electrons), or fluctuating pedestals. Thus, the corrected yields of the $D^o \to K^o_s K^+ K^-$ decay using the data-derived weights are considered to be the more accurate determination of the true yield. The discrepancy is considered when estimating the systematic error on the branching ratio.

6.2 Inclusive Branching Ratio

Using the corrected yields of the previous section, the inclusive branching ratio for $D^o \to \overline{K}^o K^+ K^-$ is computed by taking the ratio of the weighted yield of events into the $K^o_s K^+ K^-$ mode to the weighted yield of events into the $K^o_s \pi^+ \pi^-$ mode. The measurement obtained, using the results from the data-derived weighting technique

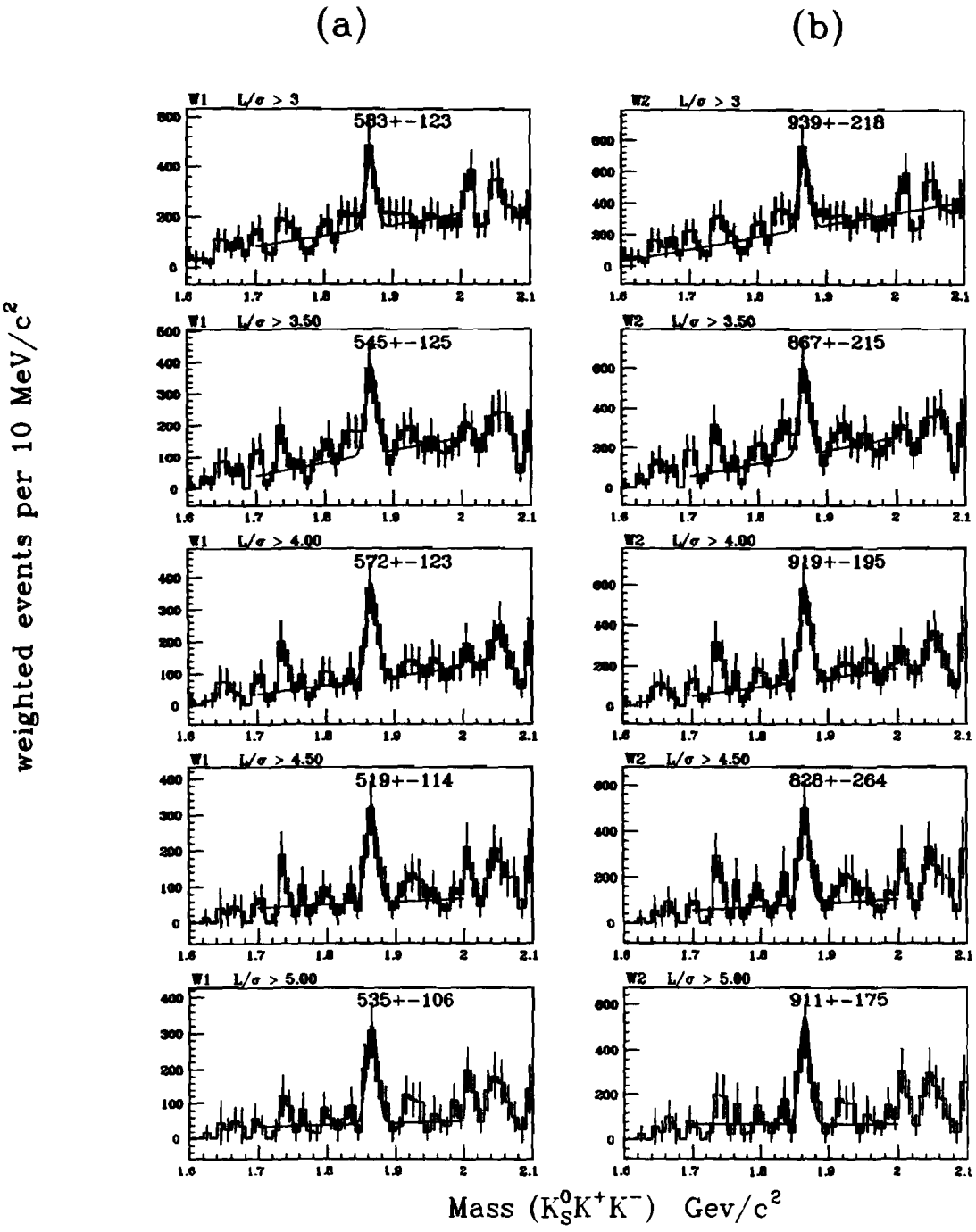

Figure 6.6. Weighted mass distributions for the decay $D^o \rightarrow K^o_s K^+ K^-$: a) using Monte Carlo kaon identification efficiencies, and b) using data-derived kaon identification efficiencies.

Table 6.3. Weighted $D^o \rightarrow K^o_s K^+ K^-$ signal parameters for the $L/\sigma_L > 3$ data set.

	Čerenkov efficiency used	
parameter	ROGUE	data-derived
Yield	583 ± 123	939 ± 219
Mass	1867.4 ± 1.8 MeV/c^2	1867.5± 1.9 MeV/c^2
Width	7.0 MeV/c^2 fixed	7.0 MeV/c^2 fixed
Signal/Noise	0.96	0.98

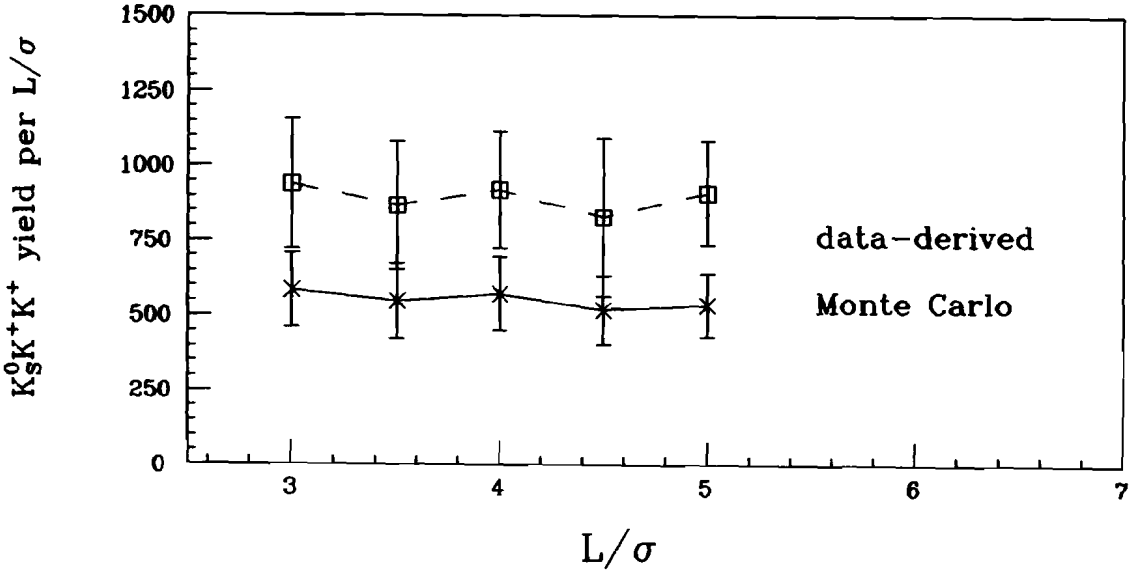

Figure 6.7. Corrected $D^o \rightarrow K^o_s K^+ K^-$ yields vs. L/σ_L for the two methods of Čerenkov identification correction discussed in the text.

for the $K^o_s K^+ K^-$ mode, is:

$$\frac{Br(D^o \to \overline{K}^o K^+ K^-)}{Br(D^o \to \overline{K}^o \pi^+ \pi^-)} = \frac{\tilde{N}(D^o \to K^o_s K^+ K^-)}{\tilde{N}(D^o \to K^o_s \pi^+ \pi^-)}$$

$$= 0.198 \pm 0.057 \pm 0.078 \qquad (6.3)$$

where the first error is statistical and the second systematic. The absolute branching ratio can be derived using the known branching ratio for $D^o \to \overline{K}^o \pi^+ \pi^-$ ($6.4 \pm 0.5 \pm 1.0\%$) [46]. Multiplying the above result one obtains the absolute branching fraction:

$$Br(D^o \to \overline{K}^o K^+ K^-) = (1.27 \pm 0.37 \pm 0.50)\% \qquad (6.4)$$

where the largest contribution to the systematic error comes from the uncertainty in the Čerenkov identification correction factor (38%), followed by uncertainties of 12% for the choice of L/σ_L cut and 1% for the branching ratio $Br(D^o \to \overline{K}^o \pi^+ \pi^-)$ uncertainty.

6.3 The $D^o \to \overline{K}^o \phi$ Branching Ratio

The inclusive signal can be analyzed to extract the fraction of events in which the D^o decay is a quasi two-body decay with the K^+K^- pair resonating as a ϕ meson. A study of the K^+K^- mass component of the inclusive $K^o_s K^+ K^-$ final state was initiated to search for possible resonance structures. In Fig. 6.8a the invariant mass of the D^o meson candidates passing the $L/\sigma_L > 3$ selection requirements is plotted against the K^+K^- invariant mass of the candidates. Along the $M(K^o_s K^+ K^-)$ mass coordinate, a band is seen corresponding to the observed signal peak at the nominal D^o mass. Likewise, along the $M(K^+K^-)$ mass coordinate a narrow band is seen corresponding to the ϕ meson mass. Where the two bands overlap an enhancement is seen, which can be interpreted as evidence for the decay $D^o \to K^o_s \phi$. A three

dimensional representation is shown in Fig. 6.8b.

Using this event sample as the starting point for the analysis, the K^+K^- mass distribution (the projection from Fig. 6.8a above) is displayed in Fig. 6.9a. To select $D^o \rightarrow K^o_s\phi$ decays, events are required to have a K^+K^- invariant mass lying within 10 MeV of the nominal ϕ meson mass:

$$1.010 < M(K^+K^-) < 1.030 \text{ GeV}/c^2$$

This cut is indicated in the expanded scale of Fig. 6.9b, along with side band selections of

$$0.988 < M(K^+K^-) < 1.008 \text{ GeV}/c^2 \text{ (lower)}$$
$$1.050 < M(K^+K^-) < 1.070 \text{ GeV}/c^2 \text{ (upper)}$$

The upper sideband was chosen to be further away from the ϕ meson signal region in order to avoid contamination resulting from the extended tail of the ϕ invariant mass. As will be seen below, the events falling into these regions were studied to determine the number of D^o mesons falling into each region, and thus to infer the number actually proceeding through the $K^o_s\phi$ channel. However, an additional check was made to study the nature of decay process, which is discussed next.

The $D^o \rightarrow K^o_s\phi$ decay sequence is known to be of the type pseudoscalar $\rightarrow$ vector + pseudoscalar, a fact which can (but need not necessarily) be exploited in isolating the decays. To check the selected events against this decay hypothesis the sample of combinations falling within 20 MeV of the nominal D^o meson mass were subjected to an analysis of the decay angle correlations among the daughter particles. A simple plot of the cosine of the helicity angle, ϑ^*, defined as the angle between the K^+ from the ϕ meson and the recoiling K^o_s direction, each evaluated in the rest frame of the ϕ, can distinguish uncorrelated, or nonresonant decays from those emerging with definite angular momentum quantum numbers. This observed distribution is shown

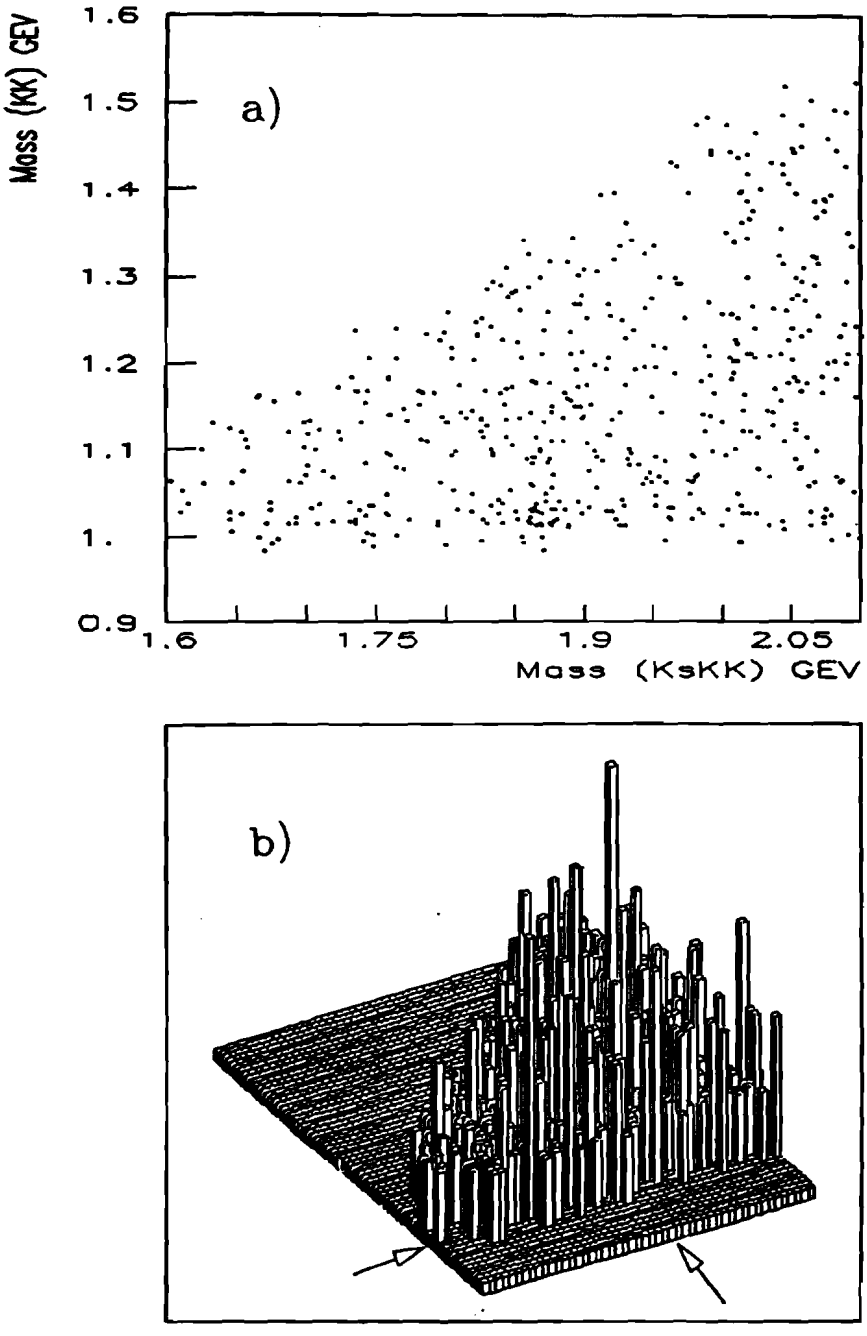

Figure 6.8. $M(K^+K^-)$ vs. $M(K^0_sK^+K^-)$ for $D^o \to K^0_sK^+K^-$ candidates passing the $L/\sigma_L > 3$ requirement: a) two-dimensional scatter plot; b) three-dimensional histogram.

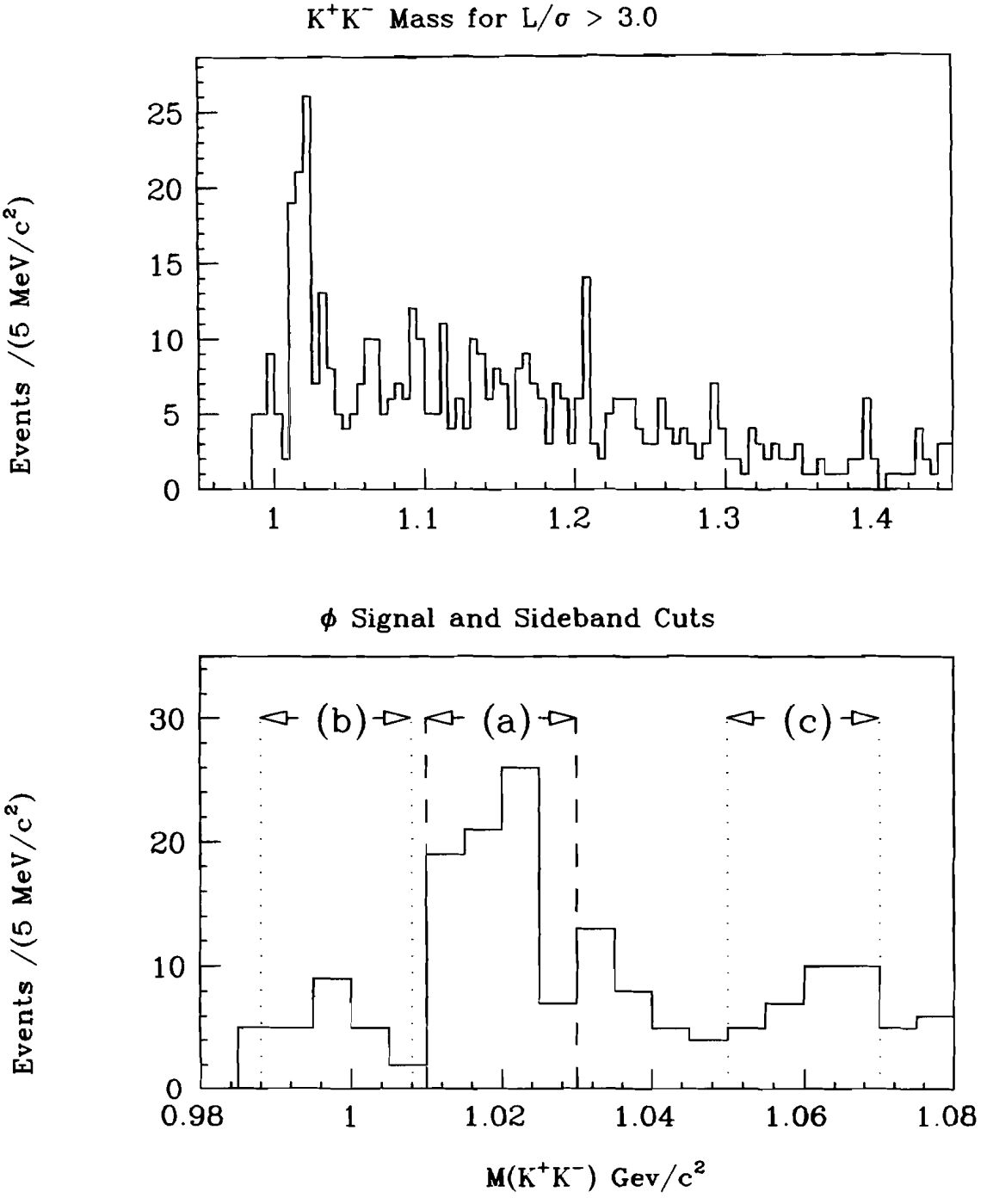

Figure 6.9. The K^+K^- invariant mass for $K^o_s K^+K^-$ candidate events: a) the K^+K^- invariant mass for all combinations in in the $K^o_s K^+K^-$ signal plot; b) expanded scale of the above.

in Fig. 6.10 for events satisfying the ϕ signal region mass cut. The distribution was fit to a functional form expected from angular momentum conservation:

$$\frac{dN}{d(cos\vartheta^*)} = bcos^2\vartheta^* \tag{6.5}$$

returning a confidence level of 87% and thus satisfying the decay hypothesis.

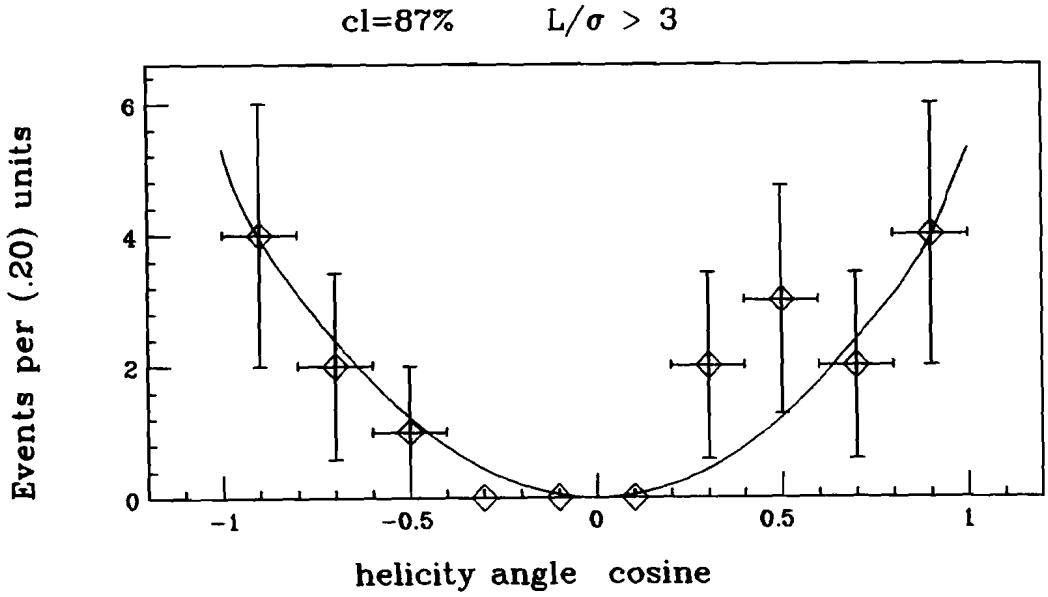

Figure 6.10. Cosine of the helicity angle distribution for $K^o_sK^+K^-$ events with K^+K^- mass in the ϕ signal region.

The events satisfying the restrictions for the K^+K^- invariant mass as specified above were studied to extract the yield into the decay channel $D^o \rightarrow \overline{K}^o\phi$. These events are shown in the upper plots of Fig. 6.11 and Fig. 6.12 for the signal and sidebands, respectively. In the same manner as before, candidate momentum dependent corrections were applied on an event-by-event basis to the combinations in upper plots of these two figures. In the lower plots the weighted histograms from which the corrected yields may be derived are given using the "data-derived" technique for the kaon identification corrections as was described in Section 6.1. The uncorrected

plot, without background subtraction, indicates observation of 13.8 ± 4.3 events into the decay channel $D^o \rightarrow K_s^o\phi$. The corresponding plots for the ϕ-mass sidebands, as shown in Fig. 6.12, indicate that some of the inclusive decays $D^o \rightarrow K_s^oK^+K^-$ may be found in nearby K^+K^- mass intervals, close to the K^+K^- threshold. The curves superimposed onto the histograms require some explanation. They were obtained by constraining Gaussian functions to have the nominal D^o mass and width, while allowing the number of events to vary. In addition, the background was constrained to be flat across the $M(K_s^oK^+K^-)$ mass region, which of course is purely assumptive but clearly is not a bad approximation. These curves may be useful for obtaining background subtraction estimates. Each sideband indicates the possible presence of signal events, though both contain considerable background and could also be consistent with zero events within one standard deviation error. The background subtracted raw event yield, using an average of sideband yields obtained from these fits, indicates observation of 11.0 ± 4.7 $D^o \rightarrow K_s^o\phi$ events. The results of the fits, including the corrected yields, are summarized in Table 6.4.

Table 6.4. Sideband subtracted raw and efficiency corrected $D^o \rightarrow K_s^o\phi$ events.

parameter	raw	corrected
Yield	11.0 ± 4.7	284 ± 126
Mass MeV/c^2	1867.7 ± 2.3	1868.0 ± 2.9
Width MeV/c^2	6.2 ± 2.3	7.1 ± 2.6
Signal/Noise	2.2	2.4

Following the previous outline for calculation of the relative branching ratio, the relative $D^o \rightarrow K_s^o\phi$ branching ratio is taken to be the ratio of the weighted yield of events into the $K_s^o\phi$ mode (sideband subtracted) to the weighted yield into the $K_s^o\pi^+\pi^-$ mode. Accounting also for the $\phi \rightarrow K^+K^-$ branching ratio of 49.5±1.0% [40]

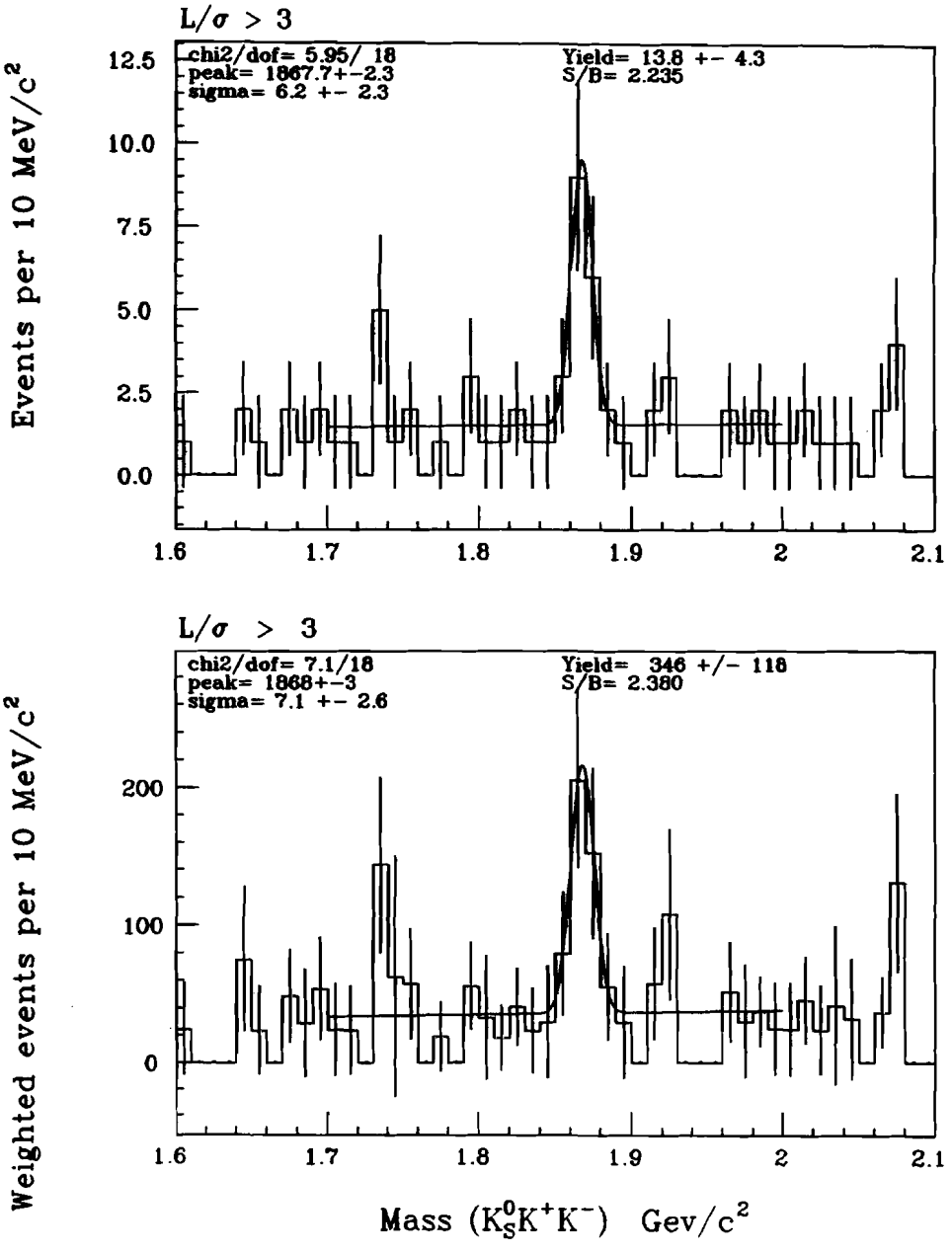

Figure 6.11. $K^0_S K^+ K^-$ Invariant mass with "ϕ"-mass requirements: the upper plot is the uncorrected signal, while the lower plot has been corrected using the "data-derived" method of Section 6.1.

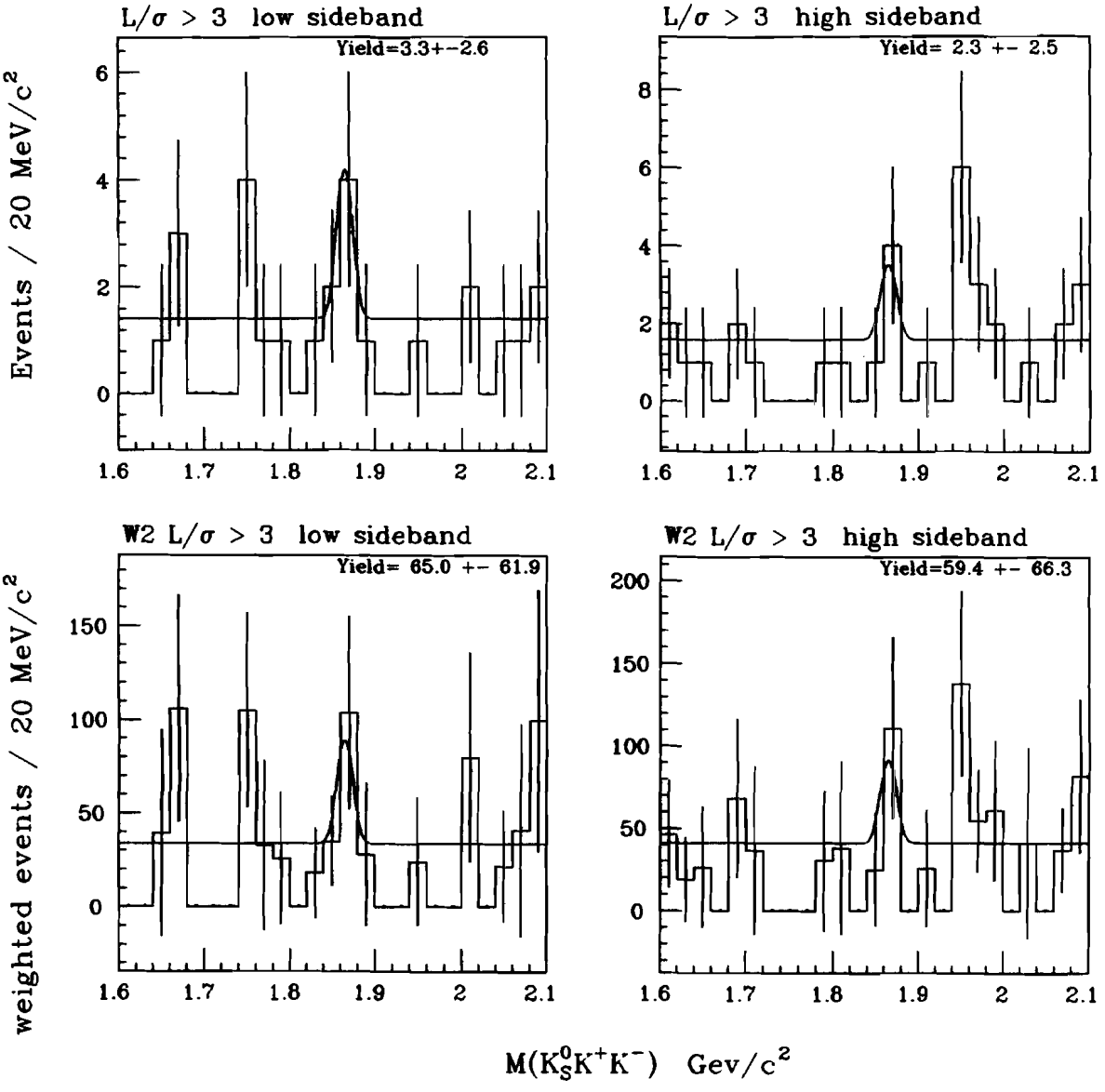

Figure 6.12. $K^{\circ}_{s}K^{+}K^{-}$ Invariant mass with "ϕ"-mass sideband selection: the upper plots are the uncorrected sidebands, while the lower plots have been corrected using the "data-derived" method of Section 6.1.

one obtains,

$$\frac{Br(D^o \to \overline{K}^o\phi)}{Br(D^o \to \overline{K}^o\pi^+\pi^-)} = \frac{\bar{N}(D^o \to K^o_s K^+K^-)^{\phi mass-cut}}{\bar{N}(D^o \to K^o_s\pi^+\pi^-)Br(\phi \to K^+K^-)}$$

$$= 0.121 \pm 0.057 \pm .090 \qquad (6.6)$$

The systematic uncertainty includes contributions from the Čerenkov identification correction (16%), the choice of L/σ_L (60%—the variation is depicted in Fig. 6.13), the sideband subtraction of events (22%), and the very small contribution due to $Br(\phi \to K^+K^-)$. As before, the absolute branching ratio can be computed using the Mark III branching ratio for $D^o \to \overline{K}^o\pi^+\pi^-$ to obtain

$$Br(D^o \to \overline{K}^o\phi) = (\ 0.77 \pm 0.37 \pm 0.58\ )\%. \qquad (6.7)$$

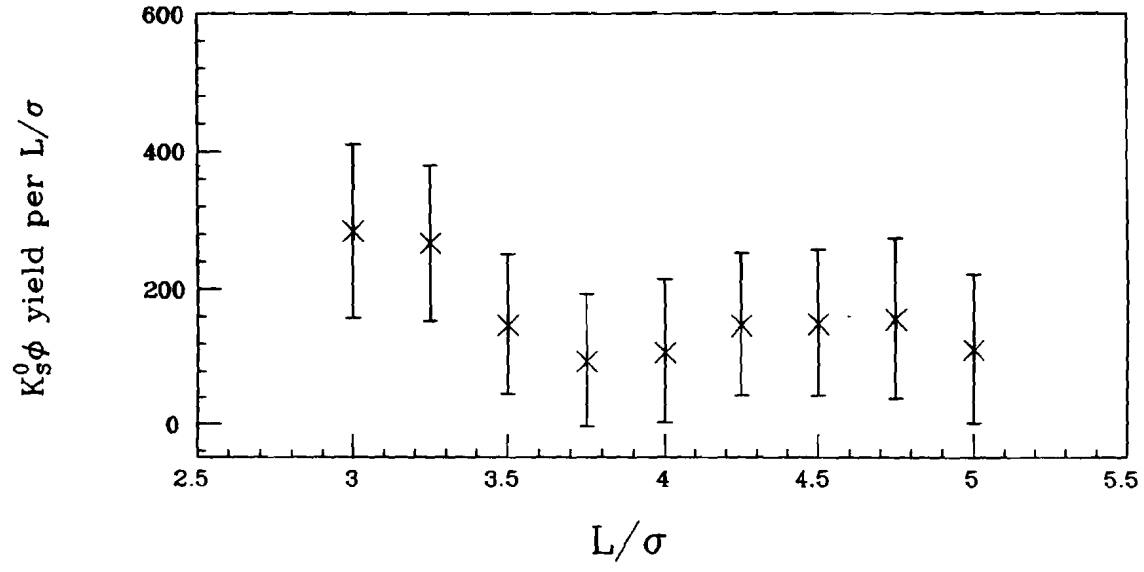

Figure 6.13. The corrected $K^o_s\phi$ yield vs. the L/σ_L cut.

6.4 The $D^o \to \overline{K}^o(K^+K^-)_{non-\phi}$ Branching Ratio

Finally, an estimate of the $D^o \to \overline{K}^o(K^+K^-)_{non-\phi}$ may be obtained by simply excluding the K^+K^- pairs which fall in the ϕ meson signal region, and assuming all other resonance contributions (such as the $a_0(980)$ or $f_0(975)$) are small in the ϕ signal region. Fig. 6.14 shows the $K^o_s K^+K^-$ invariant mass in which the ϕ signal region, specified above, is excluded. Note that for this mode the $L/\sigma_L > 4.0$ data set has been utilized for its improved signal to background ratio. The weighted signal parameters are given in Table 6.5. The result using the data-derived Čerenkov ID efficiency correction is:

$$\frac{Br(D^o \to \overline{K}^o(K^+K^-)_{non-\phi})}{Br(D^o \to \overline{K}^o\pi^+\pi^-)} = \frac{\tilde{N}(D^o \to \overline{K}^o K^+K^-)^{non-\phi}}{\tilde{N}(D^o \to K^o_s\pi^+\pi^-)}$$

$$= 0.136 \pm 0.042 \pm 0.068 \qquad (6.8)$$

which, when multiplied by the Mark III branching ratio for $D^o \to \overline{K}^o\pi^+\pi^-$ gives $Br(D^o \to \overline{K}^o(K^+K^-)_{non-\phi}) = (0.87 \pm 0.27 \pm 0.44)\%$. The systematic error reflects contributions from the choice of L/σ_L requirement (23%) and the Čerenkov identification correction (45%).

Table 6.5. Raw and weighted $D^o \to \overline{K}^o(K^+K^-)_{non-\phi}$ signal parameters.

parameter	raw	corrected
Yield	19.2 ± 5.9	641.8 ± 169.0
Mass MeV/c^2	1867.4 ± 2.5	1867.3 ± 2.4
Width MeV/c^2	6.4 ± 2.0	6.7 ± 1.7
Signal/Noise	1.1	1.4

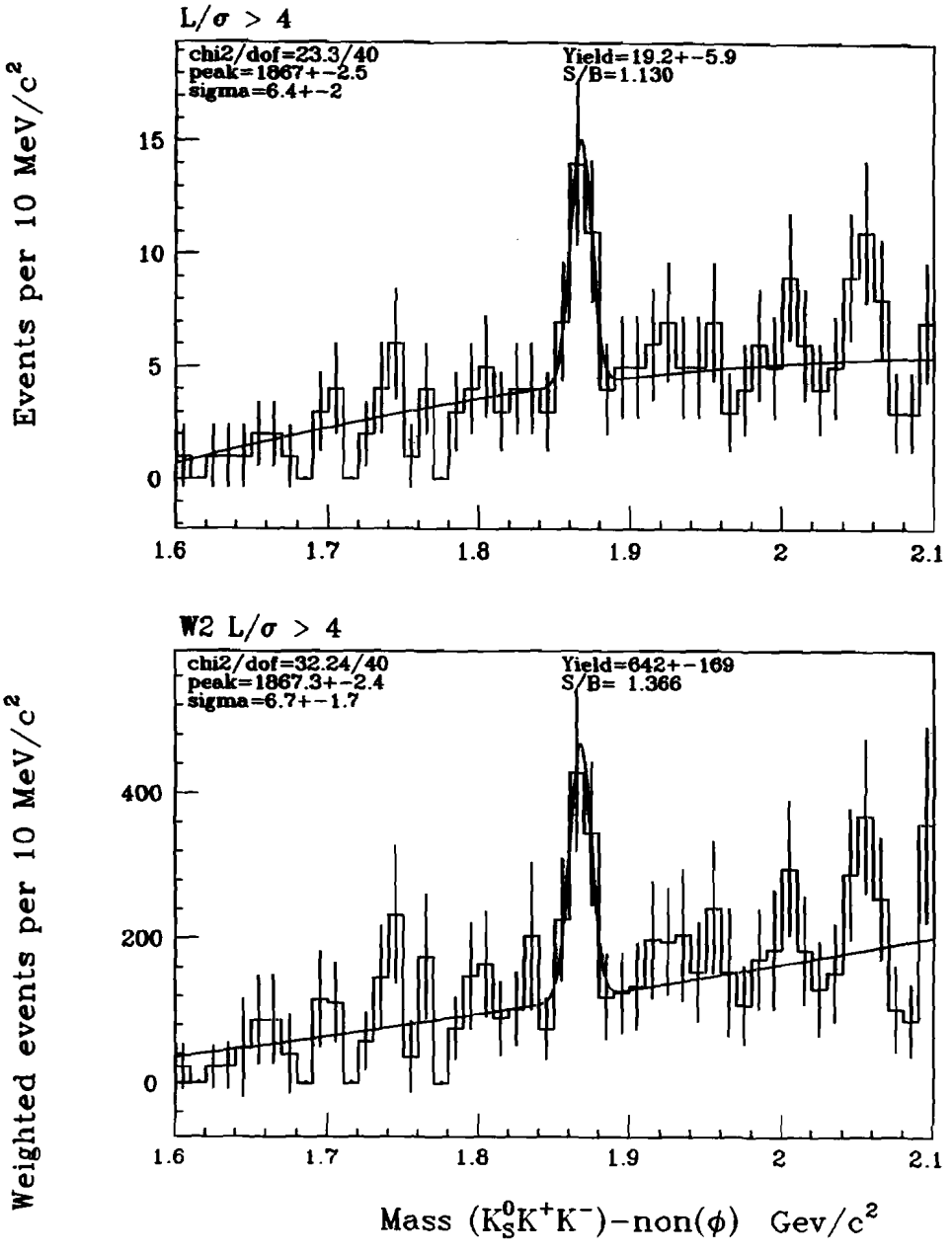

Figure 6.14. Invariant mass distribution for $\overline{K}^{o}(K^{+}K^{-})_{non-\phi}$: a) un-corrected, and b) corrected for acceptance.

CHAPTER 7

SUMMARY AND CONCLUSIONS

In summary, studies of several decay topologies of the D^o meson produced in high energy photoproduction have been presented. In this brief chapter we compare results to previous experiments, and where possible to theoretical models of heavy quark decay.

7.1 The Decay $D^o \to K^o_s\pi^+\pi^-$

The results of the Dalitz plot analysis presented in Chapter 5 are summarized in Table 7.1 below.

Table 7.1. Final results for $D^o \to K^o_s\pi^+\pi^-$.

Mode	fit fraction (%)	phase (radians)
$\overline{K}^o\pi^+\pi^-_{nonres}$	$7\ ^{+12}_{-8} \pm 9$	$0.7\ ^{+0.8}_{-1.1} \pm 0.4$
$K^{*-}\pi^+$	$85\ ^{+13}_{-15} \pm 12$	0.0 (fixed)
$\overline{K}^o\rho^o$	$17\ ^{+11}_{-9} \pm 5$	$-2.51\ ^{+0.55}_{-0.50} \pm 0.48$

A comparison can be made to a similar analysis performed by the Mark III group operating at the SPEAR e^+e^- collider at the Stanford Linear Accelerator Center. Since our experiment measured only the relative fractions of the intermediate decay channels, a comparison can be made using the absolute branching fraction

$Br(D^o \to \overline{K}^o\pi^+\pi^-) = 6.4 \pm 0.5 \pm 1.0$ %, as measured by the Mark III group [46]. The resulting branching fractions are listed in Table 7.2 below, together with the fractions and amplitude phases measured by the Mark III group.

Table 7.2. Dalitz plot fit comparisons for branching fractions and phase angles.

branching fraction (%)		
Mode	Mark III†	this work
$\overline{K}^o\pi^+\pi^-_{nonres}$	$2.1 \pm 0.3 \pm 0.7$	$0.45\ ^{+0.79}_{-0.53} \pm 0.59$
$K^{*-}\pi^+ \times Br(K^{*-}\to\overline{K}^o\pi^-)$	$3.5 \pm 0.27 \pm .67$	$5.4\ ^{+0.8}_{-1.0} \pm 0.8$
$\overline{K}^o\rho^o$	$0.8 \pm 0.1 \pm 0.5$	$1.1\ ^{+0.7}_{-0.5} \pm 0.3$

phase angles (radians)		
Mode	Mark III‡	this work
$\overline{K}^o\pi^+\pi^-_{nonres}$	—	$0.7\ ^{+0.8}_{-1.1} \pm 0.4$
$K^{*-}\pi^+$	0.0 (fixed)	0.0 (fixed)
$\overline{K}^o\rho^o$	1.62 ± 0.52	$-2.51\ ^{+0.55}_{-0.50} \pm 0.48$

† The $K^{*-}\pi^+$ result has been multiplied by $Br(K^{*-}\to\overline{K}^o\pi^-)$.
‡ The $\overline{K}^o\rho^o$ angle has been converted to radians.

The measurements by the two groups show qualified agreement, in particular the $K^{*-}\pi^+$ channel is found to dominate in both experiments. The branching fractions for the $D^o \to \overline{K}^o\rho^o$ channel show agreement within one standard deviation error. For the three-body non-resonant and $K^{*-}\pi^+$ decay channels, however, the agreement does not appear as satisfactory. The disparity between the results may not be large when correlated errors are taken into account. In fact, the $K^{*-}\pi^+$ and three-body non-resonant channels were found to be negatively correlated, meaning that increases in the three-body channels were accompanied by depletions in the $K^{*-}\pi^+$ channel. When the $K^{*-}\pi^+$ fraction was lowered to its one standard deviation limit and the likelihood

function minimized again, the branching fraction for three-body non-resonant decays increased to $1.1 \pm 0.6\%$, in better agreement with the Mark III result.

In the Mark III analysis the most favorable decay hypothesis was a partially coherent decay between the two-body vector-pseudoscalar channels. As mentioned previously, our result could not distinguish between partial coherence and complete coherence, although the result for the $\overline{K}^{o}\rho^{o}$ phase angle was consistent within error between both methods. Our result for this phase difference between the two vector-pseudoscalar decay amplitudes disagrees with the Mark III result by $\simeq 3$ standard deviations. The effect may be understood as a consequence of the destructive interference the two amplitudes experience in the region of the Dalitz plot where the resonance bands overlap. This is indicated in the E687 data by the dashed curve plotted along the $m^2_{\pi^+\pi^-}$ projection of Fig. 5.22a. Evidently, no such negative interference was observed in the Mark III data.

7.2 *The Decay $D^o \rightarrow K^o_s K^+ K^-$*

The relative branching ratio

$$\frac{\mathrm{Br}(\mathrm{D}^{o} \rightarrow \overline{\mathrm{K}}^{o}\mathrm{K}^{+}\mathrm{K}^{-})}{\mathrm{Br}(\mathrm{D}^{o} \rightarrow \overline{\mathrm{K}}^{o}\pi^{+}\pi^{-})} = 0.182 \pm 0.055 \pm 0.078 \qquad (7.1)$$

is in excellent agreement with the the world average [40] of 0.20 ± 0.05. The result

$$\frac{\mathrm{Br}(\mathrm{D}^{o} \rightarrow \overline{\mathrm{K}}^{o}(\mathrm{K}^{+}\mathrm{K}^{-})_{\mathrm{non}-\phi})}{\mathrm{Br}(\mathrm{D}^{o} \rightarrow \overline{\mathrm{K}}^{o}\pi^{+}\pi^{-})} = 0.136 \pm 0.042 \pm 0.038 \qquad (7.2)$$

leads to

$$\mathrm{Br}(\mathrm{D}^{o} \rightarrow \overline{\mathrm{K}}^{o}(\mathrm{K}^{+}\mathrm{K}^{-})_{\mathrm{non}-\phi}) = (0.87 \pm 0.27 \pm 0.24)\% \qquad (7.3)$$

when the known branching fraction $Br(D^o \rightarrow \overline{K}^o\pi^+\pi^-)$ is used. This result can be compared to the ARGUS [9] result[1] of $Br(D^o \rightarrow \overline{K}^o(K^+K^-)_{non-\phi}) = (0.54 \pm 0.13)\%$. It is also of interest to compare this result to the world average [40] for $Br(D^o \rightarrow \overline{K}^o(K^+K^-)_{nonres})$ which is $\simeq 0.76\%$.

The measurement

$$\frac{Br(D^o \rightarrow \overline{K}^o\phi)}{Br(D^o \rightarrow \overline{K}^o\pi^+\pi^-)} = 0.121 \pm 0.057 \pm 0.090 \qquad (7.4)$$

is consistent with the ARGUS result [9] of 0.155 ± 0.033 for this ratio. The derived result of

$$Br(D^o \rightarrow \overline{K}^o\phi) = (0.77 \pm 0.37 \pm 0.58)\% \qquad (7.5)$$

can be compared to the average of the three other experiments [9][10][11] which have reported observations of this mode [2]:

$$Br(D^o \rightarrow \overline{K}^o\phi) = 0.83 \,^{+0.18}_{-0.16}\,\% \text{ (ARGUS, CLEO, Mark III average).}$$

This result has been the subject of much discussion concerning the interpretation of its relatively large value. Since normal spectator processes cannot contribute directly to the $\overline{K}^o\phi$ final state, it was first pointed out by Bigi *et al.* [7] that this mode could be a first direct evidence for exchange diagram contributions. There are other possibilities, however, including final state interactions and channel mixing. In Table 7.3 the result presented here is compared to to the factorization approach of Bauer, Stech and Wirbel (BSW)[15], to applications of QCD sum rules (Blok and Shifman [17]), and to the 1/N expansion phenomenology of Buras, Gerard and Ruckl [16].

In conclusion, these results, obtained from high energy hadronic photon interactions, have added to the experimental determination of some decay branching fractions for D^o mesons. Previous high statistics experiments studying these decays were

[1] This result has been rescaled with the more recent value for $Br(D^o \rightarrow \overline{K}^o\pi^+\pi^-)$.

Table 7.3. Comparison of experimental results to models.

Model	$B(D^o \rightarrow \overline{K}^o \phi)$
Spectator Model	≈ 0 %
BSW	0.75 %
QCD Sum Rules	1.3 %
1/N Expansion	0.1-0.2 %
This work	0.77 ± 0.37 %

performed at e^+e^- colliders where the measurement systematics are rather different. Regardless of the experimental technique used, it is clear that more experimental and theoretical work is needed to understand the non-leptonic decays.

BIBLIOGRAPHY

[1] I.I. Bigi, Nuc. Phys. B. 7A, 318 (1989).

[2] R. J. Morrison, M. S. Witherell, Ann. Rev. Nucl. Part. Sci. 39, 183 (1989).

[3] G.H. Trilling, Phys. Rep. 75, 57 (1981).

[4] S. Barlag *et al.*, (ACCMOR Collaboration) CERN-EP/90-47 (April, 1990).
P.L. Frabetti *et al.*, (E687 Collaboration) FERMILAB-FN-557 (October, 1990).

[5] M.K. Gaillard, B.W. Lee, J.L. Rosner, Rev. Mod. Phys. 47, No. 2, 277 (1975).

[6] D.G. Hitlin, *Weak Decays of Charmed Quarks– An Experimental Review*, Proceedings of the Charm Physics Symposium/Workshop, Beijing, China, CALT-68-1463 (June, 1987).

[7] I.I. Bigi and M. Fukugita, Phys. Lett. 91B, 121 (1980).

[8] G. Zweig, CERN Report No. 8419/TH 412 (1964).

[9] H. Albrecht *et al.*, (ARGUS Collaboration), Z. Phys. C33, 359 (1987).

[10] C. Bebek *et al.*, (CLEO Collaboration), Phys. Rev. Lett., 56, 1983 (1986).

[11] R.M. Baltrusitus *et al.*, (Mark III Collaboration), Phys. Rev. Lett. 56, 2136 (1986).

[12] H. Lipkin, Phys. Rev. Lett. 44, 710 (1980).

[13] J. Donoghue, Phys. Rev. D33, No. 5, 1516 (1986).

[14] J. Ellis, M.K. Gaillard, D.V. Nanopolulos, Nuc. Phys. B100 313 (1975);
M.K. Gaillard, B.W. Lee, Phys. Rev. Lett. 33, 108 (1974);
G. Altarelli *et al.*, Phys. Lett. 99B, 141 (1981).

[15] M. Bauer, B. Stech, M. Wirbel, Z. Phys. C34, 103 (1987);
M. Bauer, B. Stech, Phys. Lett. 152B, 380 (1985).

[16] A.J. Buras, J.M. Gerard, R. Ruckl, Nucl. Phys. B268, 16 (1986).

[17] B.Yu. Blok, M.A. Shifman, Soviet Journal Nucl. Phys. 45, 135,301,522 (1987).

[18] D. Binnie, J. Kirkby, R. Ruchti, *Precise, Compact Tracking in SSC Detectors Using Compact Scintillating Glass Fibers*, Proceedings of the 1984 Summer Study on the Design and Utilization of the SSC, Snowmass, CO, R. Donaldson and G. J. Morfin, Eds., 593 (1984).

[19] Submitted to Nuclear Instruments and Methods (1991).

[20] S. Park *et al.*, IEEE Trans. Nucl. Sci. 34, 516 (1987).

[21] R. Ruchti *et al.*, IEEE Trans. Nucl. Sci. 34, 544 (1987).

[22] K. Knickerbocker *et al.*, IEEE Trans. Nucl. Sci. 34, 245 (1987).

[23] R. Gardner *et al.*, Proc. International Electronic Imaging Conference, Institute for Graphic Communication, Inc., Boston MA; 757 (1987).

[24] Corning glass '467' was used.

[25] C.G.A. Hill, Levy-Hill Laboratories Ltd., Cheshunt, Waltham, Hertfordshire EN8 9TJ, England.

[26] R. Mead, Collimated Holes, Inc., Campbell, CA.

[27] B. Baumbaugh *et al.*, Proc. IEEE Nuc. Sci. Sym., San Francisco CA (1988).

[28] T. Nash *et al.*, FERMILAB-Conf-85/94 (1985).

[29] L. Moroni, D. Pedrini, *Everything You Always Wanted to Know About Microrico but Were Afraid to Ask*, E687 internal note (1989).

[30] J. Wiss, *Analytic Calculations Related to Microlinking*, E687 internal note (1989).

[31] J. Wiss, *Vee Primary Vertex Arbitration Studies*, E687 internal note (1989).

[32] J. Wilson, J. Wiss, *Generalized Vee Fitting*, E687 internal note (1989).

[33] C. Bogart, *DOWNV3-Reconstruction Vee Analysis Program*, E687 internal note (1989).

[34] J. Wiss, *The Logic Cerenkov Algorithm*, E687 internal note (1988).

[35] G. Jaross, PhD Thesis, University of Illinois (1990).

[36] K. Lingel, PhD Thesis, University of Illinois (1990).

[37] K. Lingel, *Rogue Targeting Corrections*, E687 internal note (1989).

[38] J. Wiss, R. Culbertson, *DVERT*, E687 internal note (1989).

[39] J. James, M. Roos, *MINUIT: Functional Minimization and Error Analysis*, CERN Computer Centre Program Library, D506 (1983).

[40] J.J. Hernandez *et al.* (Particle Data Group), Phys. Lett. B239 1 (1990).

[41] M. Rath, Ph.D. Thesis, University of Notre Dame (1988).

[42] C. Zemach, Phys. Rev. 133 Vol 5B, 1201 (1964);
C. Zemach, Phys. Rev. 140 Vol 1B, 97 (1965);
C. Zemach, Phys. Rev. 140 Vol 1B, 109 (1965).

[43] J.D. Jackson, Nuovo Ciemento 34 No. 6, 1644 (1964).

[44] J. Wiss, personal communication.

[45] G. Jaross, E687 internal note (1990).

[46] J. Adler *et al.*, Phys. Lett. B196, 107 (1987).